PEOPLE'S DEMOCRATIC REPUBLIC OF ALGERIA
MINISTRY OF HIGHER EDUCATION AND SCIENTIFIC RESEARCH
UNIVERSITY 20 AUGUST 1955 SKIKDA
FACULTY OF TECHNOLOGY
DEPARTMENT OF MECHANICAL ENGINEERING

Affiliation: Mechanical Engineering Ref: D012125033D

Specialization: Renewable Energies in Mechanical Engineering

LGMM Laboratory, 20 August 1955 University, Skikda- Algeria

Presented by

ABDELLATIF Houssam Eddine

Theme

Numerical study of stable phase change materials based on polymers and renewable resources for thermal energy storage

Thesis Supervisor

Prof. BELAADI Ahmed

Co-Supervisor:

Dr. MAKHLOUF Azzedine

Members of Juries

Fateh Mebarek-Oudina	President	University of Skikda
Salah Amroune	Examiner	University of M'sila
Bachir Bouchehit	Examiner	University of Skikda
Saaidia Aziz	Examiner	ENSET Skikda

Skikda 2024/2025

Contents

LIST OF FIGURES

Chapter I: Comprehensive review and bibliographic synthesis of PCMs

Chapter II. Mathematical Modeling and Numerical Methods for PCM-Based Thermal Energy Storage

Chapter III: Numerical analysis of varying aspect ratios (*L/D*) in a hybrid Thermal Energy Storage Tank

Chapter IV: Enhancing thermal storage efficiency in hybrid tanks with baffle design

Chapter VI: Enhancing TES Efficiency with Wedge-Shaped Geometries and Fins in PCM Heat Exchangers

LIST OF TABLES

Chapter I. Comprehensive review and bibliographic synthesis of PCMs

Chapter II. Mathematical Modeling and Numerical Methods for PCM-Based Thermal Energy Storage

Chapter III: Numerical analysis of varying aspect ratios (*L/D*) in a hybrid Thermal Energy Storage Tank

Chapter IV: Enhancing thermal storage efficiency in hybrid tanks with baffle design

Chapter V: Impact of oval inner tube shape on PCM thermal storage performance in shell-and-tube systems

Chapter VI: Enhancing TES Efficiency with Wedge-Shaped Geometries and Fins in PCM Heat Exchangers

ACKNOWLEDGMENTS

First and foremost, I thank God for His countless blessings and guidance throughout this journey, giving me the strength, patience, and perseverance needed to accomplish this work. Alhamdulillah.

I am deeply grateful to my supervisor, Professor Belaadi, for his invaluable guidance, continuous support, and encouragement during my research. His expertise, insights, and unwavering dedication have profoundly shaped this thesis, and I am truly honored to have had the opportunity to work under his supervision.

I would like to extend my sincere thanks to the Mechanical and Materials Engineering Laboratory (LGMM) for providing me with the opportunity and resources to complete my PhD. The support and environment at LGMM have been instrumental in my academic journey. I also want to acknowledge the collaboration and assistance of Shan Ali Khan and Adeel Arshad, whose contributions have been invaluable.

I am also grateful to the University of Exeter, United Kingdom, for their support in facilitating open-access research collaboration during the course of my PhD work.

I am also thankful to my family and friends for their endless support, love, and encouragement, which have been my foundation throughout this journey. Their belief in me has been a constant source of motivation, helping me overcome every challenge.

Finally, I extend my appreciation to everyone who has played a role in my academic and personal development, contributing to the completion of this thesis.

DEDICATION

To my beloved mother, whose love, prayers, and sacrifices have always been my guiding light.

To my father, Abdellatif Khalifa. May God have mercy on him and grant him a place in heaven.

To my dear wife, for her unwavering support, patience, and love throughout this journey.

To two of my sisters and their sons, Iyad, Ghaith, and Isaak, whose joy and affection bring light into my life.

To all my family and friends, who have supported and encouraged me in countless ways.

A special mention to: Chenta Al-Rubaie, Aymen Abdellatif, Chouaib Debili, Zin Eddine Chenta, Belgacem Abdellatif, Heithem Abdellatif, Houcin Chenta, Hichem Chenta, Nouar Chenta, Rachid Chenta, and Houcin Bouteraa.

This work is dedicated to you all

ABSTRACT

This thesis presents a comprehensive study on advanced thermal energy storage (TES) technologies, focusing on Phase Change Materials (PCMs) and their integration into hybrid systems that combine both sensible and latent heat storage, as well as pure latent heat storage systems. The research begins with an extensive exploration of methods to enhance PCM performance, including the use of fins, nanoparticles, porous matrices, multiple PCMs, encapsulation, and shape stabilization. To evaluate and optimize these enhancements, advanced simulation techniques are employed. These techniques are categorized into Numerical Methods such as Finite Difference, Finite Volume, Finite Element, and Lattice Boltzmann method and Thermal Modeling Techniques, including the Enthalpy Method, Enthalpy-Porosity Method, Heat Capacity Method, and Molecular Dynamics. Together, they provide comprehensive insights into PCM behavior and system performance. It is important to note that the numerical investigations presented in this thesis are based on experimental studies previously reported by other authors, which serve as a reference for validation and model development.

The thesis also investigates hybrid TES systems by analyzing the impact of varying the length-to-diameter (*L/D*) ratio on thermal stratification in TES tanks and the melting process of PCM, utilizing computational fluid dynamics (CFD) to evaluate system efficiency. Additionally, it explores the influence of baffle designs, particularly those with varying hole diameters, on the thermal performance of PCM-based TES tanks. Furthermore, the thesis examines how different inner tube geometries, including novel horizontal oval, inclined oval (45°), vertical oval shapes, wedge shapes, and the addition of fins, affect the melting and solidification processes within PCM units, contributing to enhanced heat transfer and energy storage efficiency.

This thesis demonstrated that enhancing design parameters significantly enhances PCM-based TES systems. Optimal *L/D* ratios improved stratification and heat transfer; baffles reduced melting time by 21.67% and enhanced economic performance; vertical oval tubes shortened solidification by ~19%; and advanced multi-wedge, parallel shell, and finned designs decreased melting time by 56.75% while boosting storage capacity and cost efficiency.

Keywords: Thermal energy storage, Phase Change Materials, Hybrid energy systems, Computational fluid dynamics, Numerical simulation techniques.

المخلص

تقدم هذه الأطروحة دراسة شاملة حول تقنيات تخزين الطاقة الحرارية المتقدمة، مع التركيز على مواد تغيير الطور ودمجها في الأنظمة الهجينة التي تجمع بين تخزين الحرارة الحساسة والكامنة، بالإضافة إلى أنظمة تخزين الحرارة الكامنة النقية. تبدأ هذه الدراسة باستكشاف شامل للطرق التي تهدف إلى تحسين أداء مواد تغيير الطور، بما في ذلك استخدام الزعانف، والجسيمات النانوية، والمصفوفات المسامية، والمواد تغيير الطور المتعددة، وعمليات التغليف، وتثبيت الشكل. ولتقييم هذه التحسينات وتحقيق أفضل أداء ممكن، يتم استخدام تقنيات متقدمة للمحاكاة العددية. يتم تصنيف هذه التقنيات إلى أساليب عددية مثل طريقة الفروق المحدودة، وطريقة الحجوم المحدودة، وطريقة العناصر المحدودة، وطريقة شبكة بولتزمان، وإلى تقنيات النمذجة الحرارية التي تشمل طريقة الإنثالبي، وطريقة الإنثالبي-المسامية، وطريقة السعة الحرارية، إضافةً إلى المحاكاة الديناميكية الجزيئية. وتوفر هذه الأساليب مجتمعةً فهماً شاملاً لسلوك مواد تغيير الطور وأداء النظام ككل. من المهم الإشارة إلى أن الدراسات العددية المقدَّمة في هذه الأطروحة تستند إلى دراسات تجريبية سبق أن نشرها مؤلفون آخرون، والتي تُعتمد كمرجع لعملية التحقق من الصحة وتطوير النموذج.

كما تبحث الأطروحة في الأنظمة الهجينة لتخزين الطاقة الحرارية من خلال تحليل تأثير تغيير نسبة الطول إلى القطر على التدرج الحراري في خزانات تخزين الطاقة الحرارية وعملية الانصهار للمواد، باستخدام الديناميكا الحركية للسوائل الحاسوبية لتقييم كفاءة النظام. بالإضافة إلى ذلك، تستكشف تأثير تصميمات الحواجز، خاصة تلك التي تحتوي على أقطار مختلفة للثقوب، على الأداء الحراري لخزانات تخزين الطاقة الحرارية القائمة على مواد تغيير الطور. علاوة على ذلك، تفحص الأطروحة كيف تؤثر الأشكال الهندسية المختلفة للأنابيب الداخلية والخارجية، بما في ذلك الأشكال البيضاوية الأفقية، والبيضاوية المائلة (45°)، والبيضاوية الرأسية، والأشكال على شكل إسفين، بالإضافة إلى إضافة الزعانف، على عمليات الانصهار والتصلب داخل وحدات مواد تغيير الطور، مما يسهم في تحسين نقل الحرارة وكفاءة تخزين الطاقة.

أظهرت هذه الأطروحة أن تحسين معلمات التصميم يعزز بشكل كبير من أداء أنظمة التخزين الحراري بالمواد متغيرة الطور. حيث حسّنت نسبة الارتفاع إلى القطر للخزان من الطبقية الحرارية وانتقال الحرارة، وقللت الحواجز زمن الانصهار بنسبة 21.67% مع تحسين الأداء الاقتصادي، في حين خفّضت الأنابيب البيضوية العمودية زمن التجمد بحوالي 19%. كما أن التعديلات الهندسية المتقدمة، مثل الأنابيب متعددة الأوتاد والأغلفة الموازية والمزودة بريش، قللت زمن الانصهار بنسبة 56.75% وزادت من السعة التخزينية والكفاءة الاقتصادية.

الكلمات المفتاحية: تخزين الطاقة الحرارية، مواد تغيير الطور، الأنظمة الهجينة للطاقة، ديناميكا السوائل الحاسوبية، تقنيات المحاكاة العددية.

RÉSUMÉ

Cette thèse présente une étude approfondie des technologies avancées de stockage d'énergie thermique, en se concentrant sur les matériaux à changement de phase (MCP) et leur intégration dans des systèmes hybrides combinant le stockage de chaleur sensible et latente, ainsi que les systèmes de stockage de chaleur latent pur. La recherche commence par une exploration approfondie des méthodes visant à améliorer les performances des matériaux à changement de phase (MCP), notamment l'utilisation d'ailettes, de nanoparticules, de matrices poreuses, de PCM multiples, de l'encapsulation et de la stabilisation de forme. Pour évaluer et optimiser ces améliorations, des techniques de simulation avancées sont utilisées. Ces techniques sont classées en méthodes numériques telles que la méthode des différences finies, la méthode des volumes finis, la méthode des éléments finis et la méthode de Boltzmann sur réseau et en techniques de modélisation thermique, incluant la méthode de l'enthalpie, la méthode enthalpie-porosité, la méthode de la capacité calorifique et la dynamique moléculaire. Ensemble, elles offrent une compréhension approfondie du comportement des PCM et de la performance globale du système. Il est important de noter que les investigations numériques présentées dans cette thèse sont basées sur des études expérimentales précédemment rapportées par d'autres auteurs, qui servent de référence pour la validation et le développement du modèle.

La thèse examine également les systèmes hybrides TES en analysant l'impact de la variation du rapport longueur/diamètre (*L/D*) sur la stratification thermique dans les réservoirs TES et sur le processus de fusion des MCP, en utilisant la dynamique des fluides numérique pour évaluer l'efficacité du système. Elle explore aussi l'influence des conceptions de chicanes, en particulier celles avec des diamètres de trous variés, sur les performances thermiques des réservoirs TES à base de MCP. De plus, la thèse examine comment différentes géométries de tubes internes, y compris les formes ovales horizontale, ovale inclinée (45°) et ovale verticale, les formes en coin, et l'ajout d'ailettes, affectent les processus de fusion et de solidification des unités de PCM, contribuant à améliorer le transfert de chaleur et l'efficacité du stockage d'énergie.

Cette thèse a démontré que l'optimisation des paramètres de conception améliore considérablement les performances des systèmes de stockage thermique à base de matériaux à changement de phase (PCM). Des rapports *L/D* optimaux ont amélioré la stratification thermique

et le transfert de chaleur ; l'ajout de chicanes a réduit le temps de fusion de 21,67 % tout en améliorant la performance économique ; les tubes ovales verticaux ont diminué le temps de solidification d'environ 19 % ; et les conceptions avancées, incluant des tubes multi-calés, des enveloppes parallèles et des ailettes intégrées, ont réduit le temps de fusion de 56,75 % tout en augmentant la capacité de stockage et l'efficacité économique.

Mots clés : Stockage d'énergie thermique, Matériaux à changement de phase, Systèmes énergétiques hybrides, Dynamique des fluides computationnelle, Techniques de simulation numérique.

PUBLICATIONS AND COMMUNICATIONS

1-International Publications

1. Modeling three-dimensional flow in a thermal energy tank: Numerical analysis of the impact of tank shape on the melting and solidification of phase change material.

DOI: 10.1016/j.est.2023.108286

2. Efficiency enhancement in solar energy storage: Impact of oval inner tube geometries on phase change material units.

DOI: 10.1080/10407782.2024.2332478

3. Enhanced solar energy utilization of thermal energy storage tanks with phase change material and baffle incorporating holes.

DOI: 10.1016/j.tsep.2024.102674

4. Comparative analysis of tube designs in heat exchangers: A numerical simulation study for enhanced thermal-flow efficiency, "optimizing wavy tubes bundle geometries for enhanced heat transfer in underwater application".

DOI : 10.1080/10407782.2024.2369943

5. Numerical study of shell and tube thermal energy storage system: Enhancing solidification performance with single-walled carbon nanotubes in phase change material.

DOI : 10.1016/j.icheatmasstransfer.2024.108338

6. Enhancing Thermal Energy Storage System Efficiency: Geometric Analysis of Phase Change Material Integrated Wedge-shaped Heat Exchangers.

DOI : 10.1016/j.applthermaleng.2024.125268

7. Enhancing Thermal Energy Storage: The Impact of Inclined Enclosure Geometry and Artificial Neural Network Based Modeling on Phase Change Material Melting Performance.

DOI: 10.1016/j.est.2025.115750

8. Numerical Assessment of Heat Transfer and Entropy Generation of a Mixed Convection Ferrofluid Flow under the Effect of a Non-uniform Magnetic Field.

DOI: 10.1016/j.csite.2025.105788

9. Advancing Thermal Energy Storage: Unravelling the Optimal Orientation of Annular Phase Change Material Containers within the Tank.

DOI: 10.1016/j.csite.2025.105931

2- International Communications

1. **Numerical study of the performance of phase change materials (PCMs) in a storage tank.**
   - 2nd INTERNATIONAL SEMINAR IN INDUSTRIAL ENGINEERING AND APPLIED MATHEMATICS (ISIEAM'22) IN SKIKDA (ALGERIA). 23-25 October 2022.
2. **Improving phase change material melting efficiency: A comparative study of shape variations in tank geometries for thermal energy storage.**
   - 1st International Seminar on Chemical Processes and Sustainable Development, (ISCPSD'23) Skikda, 23 - 25 Octobre 2023. At: Skikda.
3. **Enhancing solar energy efficiency through thermal energy storage tank utilizing phase change materials.**
   - The International Conference on Petrochemistry and Energy Transition (ICPET23.), 21-23 November 2023. At: Skikda.
4. **Numerical Analysis of Solidification Behavior in Phase Change Material Cylinders: Impact on Energy Storage Systems.**
   - 1ST INTERNATIONAL CONFERENCE ON PHYSICO-CHEMISTRY, MATERIALS SCIENCES & APPLIED MATHEMATICS (ICPMSAM'23) on 27-28 November 2023, Skikda, Algeria.

3- National Communications

1. **Improving Solar Energy Efficiency with Phase Change Material-Based Thermal Energy Storage Tanks.**
   - The First National Conference of Materials Sciences and Renewable Energy CMSRE23 on November 22-23, 2023 in Relizane, Algeria.

Nomenclature

A_m	The mushy zone (kg/s m^3)
C_{PCM}	PCM cost ($/kg)
C_{Al}	Aluminum cost ($/kg)
C_p	Thermal capacity (J/K)
$C_{P,\,eff}$	Equivalent specific heat capacity (J/kg.K)
D	The tank's diameter (mm)
d	The cylindrical containers' diameter (mm)
D_h	Hydraulic diameter (mm)
d_P	Nanoparticles diameter (m)
E	Diameter of the tank's inlet and outlet (mm)
f	Liquid fraction of PCM (%)
g	Gravity(m/s^2)
H	Enthalpy of the PCM(J/kg)
h	Sensible enthalpy (J/kg)
h_{ref}	Reference enthalpy (J/kg)
L	Length of the tank (mm)
L_{pcm}, ℓ	Length of PCM cylinder(mm)
L_f	Latent heat capacity
M	The inlet and outlet's length (mm)
r, θ, z	Cylindrical coordinates
Q	Thermal energy storage (KJ)
Ra	Rayleigh number
Re	Reynolds number
Ri	Richardson number
S	Source term
t	Time (s)
T_{ref}	Reference temperature (K)
T_{cold}	Cold water temperature(K)
T_{hot}	Hot water temperature (K)

T_{in}	Inlet temperature (K)
$T_{M\ ini}$	Initial melting temperature (K)
T_{out}	Outlet temperature (K)
$T_{S\ ini}$	Initial solidification temperature (K)
$\|\Delta T\|$	Temperature differences (K)
U	Velocity(m/s)
U_{in}	Inlet velocity(m/s)
U_{outlet}	Outlet velocity(m/s)
u_r	Velocity in the radial direction (m/s)
u_θ	Velocity in theta direction (m/s)
u_ϕ	Velocity in azimuthal direction (m/s)
u_f	PCM velocity

Greek symbols

α	Thermal Diffusivity (m^2/s)
β	Thermal expansion coefficient (1/K)
ν	Kinematic viscosity (m^2/s)
λ	Thermal conductivity (W/K m)
μ_w	Dynamic viscosity of water (Pa·s)
ρ	The Density (kg/m^3)
ρ_{PCM}	Density of PCM (kg/m^3)
ρ_{Al}	Density of Aluminum (kg/m^3)
ξ	Constant

Abbreviations

CFD	Computational Fluid Dynamics
CPU	Central Processing Unit
DHW	Domestic hot water
EPCM	Encapsulated PCM
HTF	Heat Transfer Fluid
LBM	Lattice Boltzmann method
LHTES	Latent Heat Thermal Energy Storage
MDS	Molecular Dynamics Simulation
MF	Metal foam
NePCM	Nano-enhanced PCM
H oval	Horizontal oval
In oval	Inclined oval
V oval	Vertical oval
SIMPLE	Semi-Implicit Method for Pressure-Coupled Equations
SIMPLEC	Semi-Implicit Method for Pressure Linked Equations-Consistent
SHS	Sensible Heat Storage
TES	Thermal Energy Storage

General introduction

1-General introduction

The improvement in living conditions and the acceleration of technological development have significantly increased global energy demand, leading to greater reliance on fossil fuels. However, this dependency has severe environmental consequences, particularly the emission of greenhouse gases that contribute to global warming. Moreover, fossil fuel resources are finite and subject to eventual exhaustion. These challenges have encouraged a worldwide transition toward renewable energy alternatives. Among these, solar energy emerges as a highly promising option for meeting heating and cooling demands in buildings, as well as supplying hot water for both industrial and household applications [1]. TES has become a key solution in large-scale industrial thermal processes and power generation, offering an effective means to mitigate the intermittent nature of solar energy while supporting a wide range of energy demands [2]. A crucial component of solar energy systems is the hot water storage tank, which stores thermal energy collected during the day and delivers it when needed [3] , [4]. Thermal energy can be stored using three main techniques: sensible heat storage, latent heat storage, and thermochemical storage. Each method relies on different physical or chemical processes ranging from temperature changes to phase transitions and chemical reactionsto fulfill specific roles in energy storage applications [5]. Among the available technologies, Phase Change Materials (PCMs) are particularly effective for latent TES due to their high energy storage density and consistent phase transition behavior [6].

This thesis employed the VOSviewer literature analysis software to analyze the keywords in publications related to thermal energy storage tanks utilizing PCMs technology. The study identified and highlighted frequently occurring keywords, as depicted in **Figure 1**. The analysis underscores the pivotal role of PCMs in the domain of thermal energy storage tanks. Specifically, it emphasizes their significance in facilitating efficient thermal heat storage processes. This observation elucidates the critical influence of PCMs on the overall performance of such systems. Furthermore, the research revealed that the predominant methods employed in this field are experimental research (often referred to as experimental study) [7], [8], [9] and numerical simulation (commonly referred to as numerical model) [4], [10], [11], [12], as illustrated in **Figure 1**. These methodologies are essential in investigating and optimizing the operational aspects of thermal energy storage tanks utilizing PCMs technology, as well as PCM shell and tube heat exchangers.

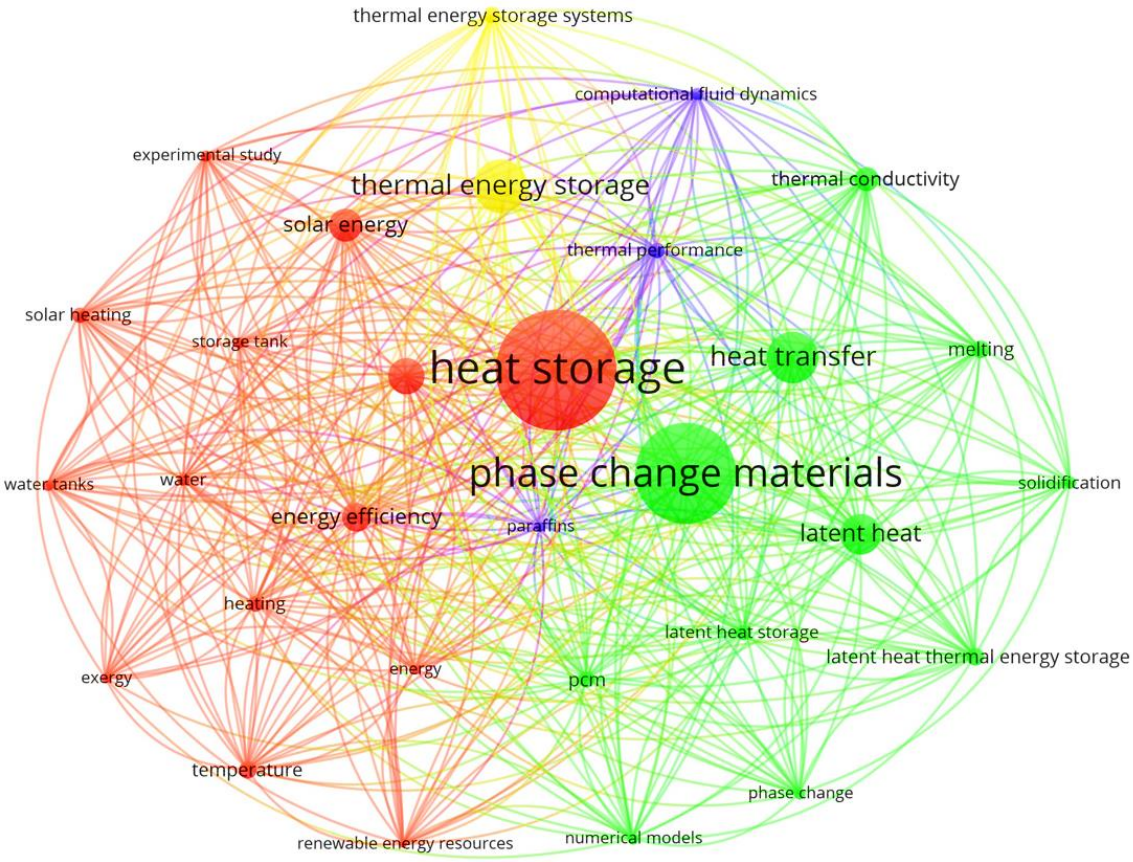

Figure 1: Co-occurrence analysis of keywords in research papers about thermal energy storage tanks utilizing PCMs.

Latent heat thermal energy storage (LHTES) is a core approach within TES systems, notable for its ability to store large amounts of energy while maintaining a nearly constant operating temperature [13]. PCMs utilize latent heat to store and release thermal energy efficiently, thereby improving the effectiveness of solar energy systems. Due to their affordability, broad operating temperature range, and availability, PCMs significantly enhance the TES capacity of thermal systems. Incorporating PCMs into thermal storage units especially hot water tanks plays a vital role in optimizing both energy retention and discharge performance [14]. Optimizing the configuration of hot water storage tanks plays a vital role in enhancing the performance and efficiency of TES systems [15], [16]. **Figure 2** illustrates a solar thermal energy storage system incorporating PCM (water tank) for hybrid storage, while **Figure 3** presents the configuration of a PCM shell-and-tube heat exchanger system for latent storage, designed to enhance heat transfer

and storage efficiency. These systems are integral to improving overall thermal management and energy utilization in various applications.

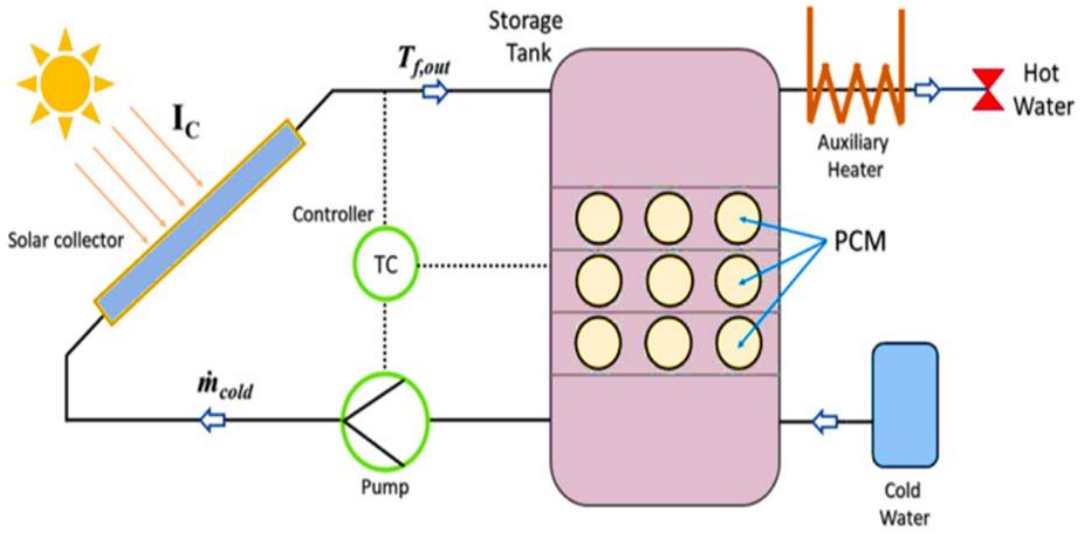

Figure 2 : Hybrid thermal energy storage tank system[12].

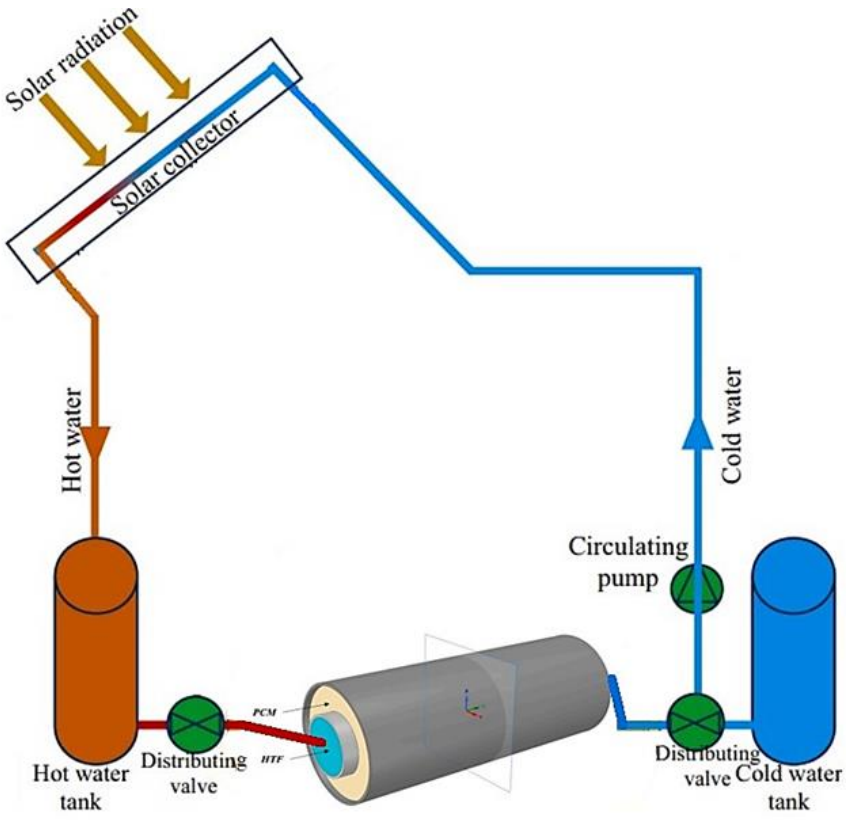

Figure 3 : PCM shell-and-tube heat exchanger system for thermal energy storage.

PCMs are generally classified into three types: organic, inorganic, and composite [13] Organic PCMs such as paraffins, fatty acids, esters, and alcohols are valued for their wide phase transition temperature range, chemical stability, and resistance to phase separation. Nonetheless, they also present certain limitations, including low thermal conductivity, noticeable volume expansion during phase change, and high flammability [14]. Inorganic PCMs such as salts, hydrated salts, molten salts, and metal alloys are recognized for their affordability and high latent heat storage capacity. However, their practical use is often limited by issues like phase segregation, corrosiveness, and inadequate thermal stability [15]. To address these challenges, composite PCMs have been developed by combining two or more materials. These composites typically exhibit lower melting points than their individual components and function by absorbing heat during melting and releasing it during solidification. Their eutectic nature ensures a distinct and consistent melting temperature, which enhances the efficiency of thermal energy storage and retrieval. By integrating the strengths of different PCM types, composites can offer improved overall performance while minimizing inherent disadvantages. **Figure 4** shows the relationship between melting temperature and specific latent heat for various organic, inorganic, and eutectic PCMs [16].

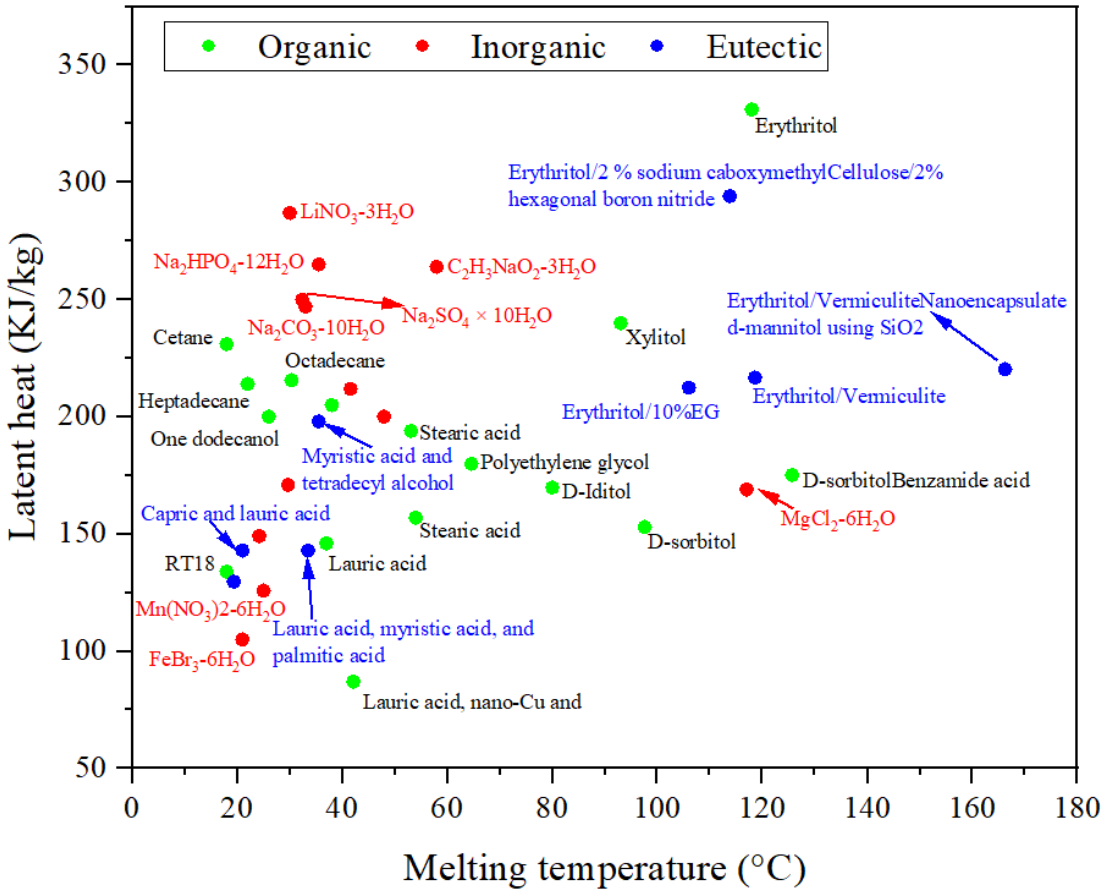

Figure 4 : Variation of specific latent heat of common PCMs as a function of melting temperature [16], [17].

Key criteria for selecting suitable PCMs for specific applications include their thermal conductivity, phase transition temperature, latent heat storage capacity, and durability over repeated thermal cycles [18]. Paraffin wax is extensively studied for its favorable thermal properties, especially its high latent heat capacity, low vapor pressure when melted, and strong thermal and chemical stability. Despite these benefits, one major limitation is its inherently low thermal conductivity, typically ranging between 0.15 and 0.24 W/m·K [19]. **Figure 5** presents the relationship between specific latent heat and thermal conductivity for various common PCMs, including organic, inorganic, and eutectic types [16].

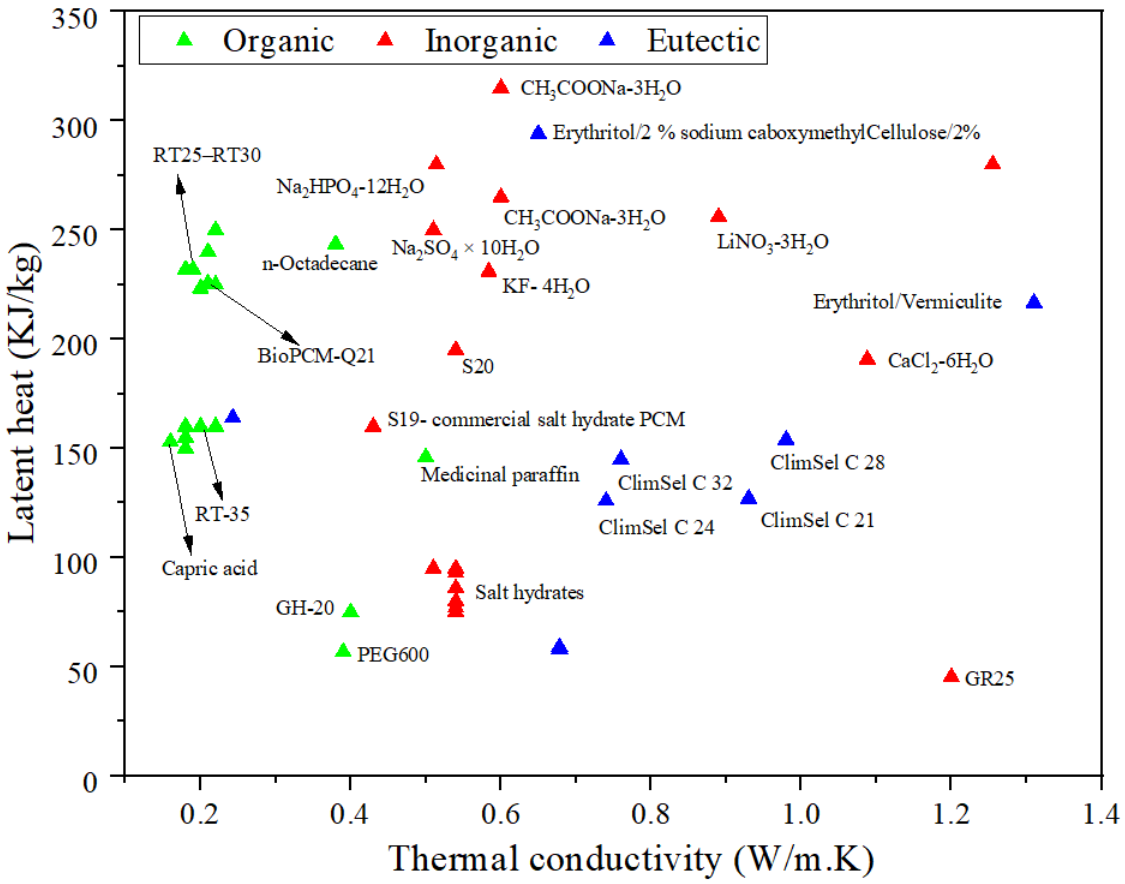

Figure 5 : Variation of specific latent heat of common PCMs as a function of their solid phase thermal conductivity [16], [17].

To improve heat transfer during the melting process, several methods have been developed to enhance the thermal conductivity of PCMs. These enhancement techniques are generally categorized into two main approaches. The first involves integrating extended surfaces such as fins [19] or incorporating high-conductivity porous structures like metal foams [20] to increase the effective surface area. The second strategy focuses on the addition of thermally conductive nanoparticles to the PCM matrix [21]. Both approaches aim to address the intrinsic low conductivity of PCMs and significantly improve their effectiveness in TES systems.

Artificial intelligence (AI) and machine learning (ML) tools provide powerful capabilities for analyzing complex factors in system-level deployment. These technologies enable efficient PCM selection by processing large datasets and predicting performance across various applications. Furthermore, achieving large-scale implementation of thermal energy storage requires advancements in manufacturing and automation. Recent developments in polymer and metal

additive manufacturing especially when integrated with topological optimization (TO) have facilitated the creation of novel geometries and complex structures customized for specific thermal management needs [22].

A wide range of research has explored TES systems incorporating PCMs. For instance, Nazari et al. [21] examined the influence of nanotechnology on PCM performance, demonstrating improved heat transfer efficiency and shorter charging and discharging durations. Their findings highlighted that both nanoparticle concentration and operating conditions play a crucial role in influencing the melting behavior of nano-enhanced PCMs. Asgharian et al. [23] presented an extensive review of PCM-integrated systems for solar energy storage, focusing on various mathematical modeling approaches and numerical simulation techniques. Their work highlighted existing research gaps and reinforced the adaptability of PCMs in diverse applications. Similarly, Kalapala et al. [24] conducted an in-depth analysis of PCM-based heat exchangers, with particular attention to shell-and-tube and triple concentric tube configurations. Their review examined the influence of operating conditions, design variables, and heat transfer enhancement methods, offering practical guidance for optimizing system performance. Xiong et al. [25] reviewed recent numerical investigations on NePCMs for TES, focusing on simulation methodologies, phase change dynamics, and identifying key research gaps to guide future studies. In a related effort, Cui et al. [26] examined the role of metal foams in improving heat transfer within LHTES systems. Their review provided scientometric analyses, discussed influential factors, and explored practical applications, while highlighting the ongoing need for research and innovation in the field. Zhang et al. [27] conducted a review focused on numerical approaches for modeling phase change processes, with particular attention to the application of CFD tools such as FLUENT. Their study addressed the influence of natural convection and nanoparticle inclusion on melting duration, while also outlining current challenges and future opportunities in simulation techniques.

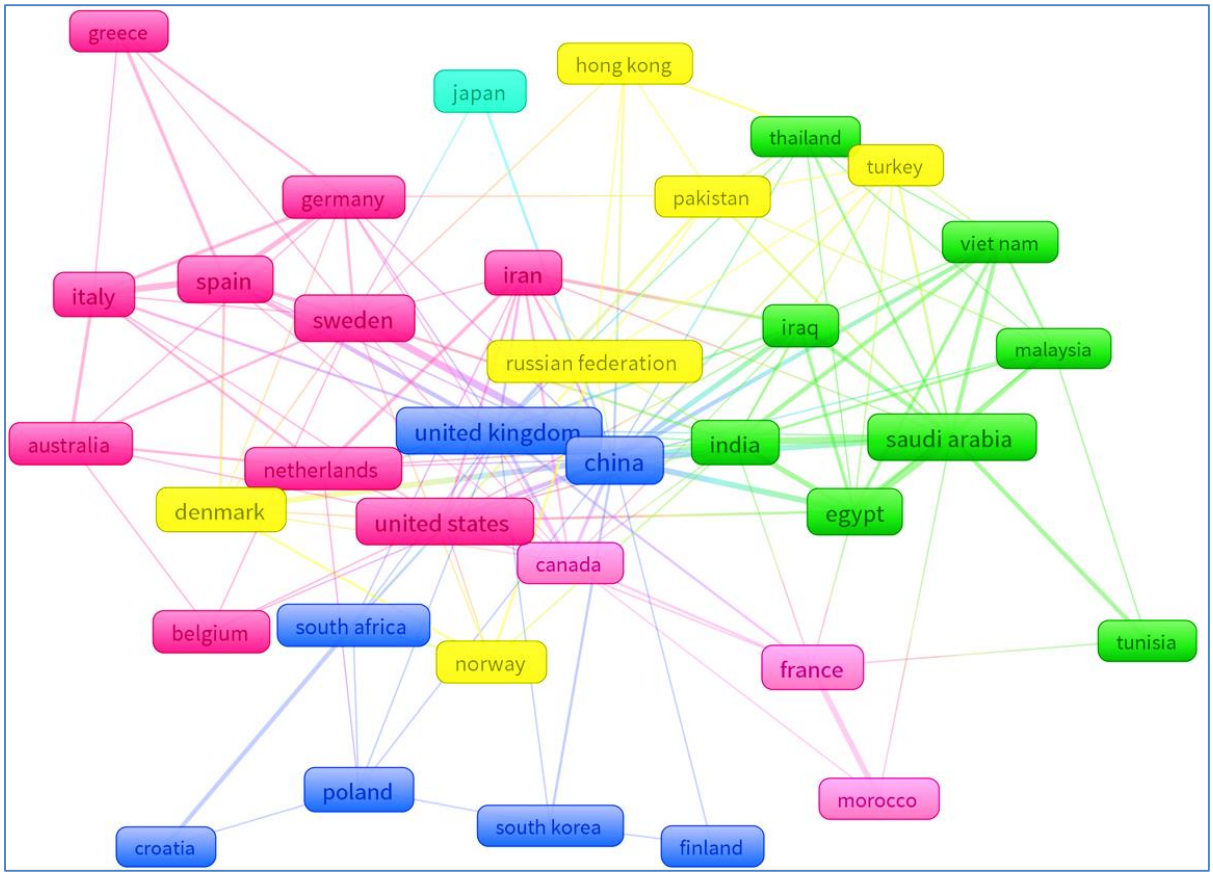

Figure.6 : The leading countries in research on TES tanks with PCM.

On the other hand, **Figure 6** in this paper highlights the global interest in studying TES tanks utilizing phase change materials. The analysis conducted through VOSviewer reveals the leading countries in this field. China emerges as the frontrunner in research and development in this domain [28], followed closely by India [4], Iran [29], USA[30], UK [31]..... etc. This observation underscores the international significance and collaborative nature of research about TES tanks with PCMs. Key factors in PCM material selection for any application encompass thermal conductivity, phase change temperature, high latent heat capacity, and long-term cycle stability [32].

In **Chapter 01**, this thesis laid the foundation by thoroughly examining innovative TES technologies, with a particular focus on latent heat storage and hybrid systems that combine both sensible and latent heat storage. The chapter examined innovative methods to enhance PCM performance, including the use of fins, nanoparticles, porous matrices, multiple PCMs, encapsulation, and shape stabilization.

Chapter 02 opens with an overview of the mathematical modeling and numerical simulation approaches employed to investigate the phase change behavior of PCM-based TES systems. The chapter highlights the fundamental governing equations, as well as the numerical schemes and solution techniques widely adopted in both existing literature and the current study. Emphasis is placed on how these models are utilized to capture the complex thermal and phase transition dynamics of PCMs, providing a foundation for accurate and efficient simulation of latent heat storage processes.

Chapter 03 shifts the focus to hybrid TES systems, specifically examining the effect of the *L/D* ratio on thermal stratification within TES tanks. A series of three-dimensional models were developed and analyzed using CFD to assess how changes in the *L/D* ratio influence system performance. The study demonstrates that increasing the *L/D* ratio can enhance thermal stratification, shorten charging and discharging durations, and ultimately improve the efficiency of solar thermal collector systems.

In **Chapter 04**, our study explored the introduction of baffles with holes at the bottom of TES tanks, which served to enhance thermal stratification and improve heat transfer within the system. We closely analyzed the effects of hole diameter on buoyant forces and temperature distribution. By evaluating temperature contours, liquid fraction, heat flow, velocity vectors, Richardson numbers, and overall thermal storage efficiency, we demonstrated that the introduction of baffles with specific hole diameters significantly improved the thermal performance of PCM-based TES systems. We focused on the relationship between baffle designs, specifically the hole diameters, and their effect on melting behavior and heat transfer in PCM units. Our work revealed the importance of baffle designs in achieving uniform temperature distribution, thus enhancing the thermal performance of the TES system. By carefully optimizing the baffle configurations, our research offers unique insights into maximizing efficiency in TES systems, particularly in solar thermal applications.

In **Chapter 05**, we investigated the melting and solidification processes in PCM units, specifically focusing on the impact of various inner tube geometries. We introduced and analyzed novel inner tube configurations, including H oval, In oval (45°), and V oval shapes, comparing them to the traditional circular inner tube design. This innovative approach provided valuable insights into how these different geometries affect the efficiency and performance of PCM units during phase

change processes. Our study demonstrated that inner tube design plays a crucial role in optimizing heat transfer and overall system performance, contributing to more reliable and effective solar energy storage solutions. By advancing the understanding of inner tube geometry's impact on PCM behavior, this research offers practical innovations aimed at enhancing heat storage and retrieval in solar energy systems.

Chapter 06, explores the impact of geometric modifications on TES systems using PCMs. Ten configurations were analyzed, introducing wedge-shaped inner tubes, parallel shells, and fins. Results showed significant improvements, with melting time reduced by 56.75% and enhanced energy storage capacity. The optimized design demonstrated superior performance, efficient convection currents, and cost-effectiveness, highlighting the importance of geometric innovations for improving TES efficiency and economic feasibility.

Chapter I. Comprehensive review and bibliographic synthesis of PCMs

I.1- Introduction

Phase Change Materials (PCMs) play a vital role in TES systems, yet their application is limited by challenges such as low thermal conductivity, limited latent heat capacity, and leakage issues. This chapter reviews advanced TES technologies, with an emphasis on latent heat and hybrid systems. It highlights innovative enhancement strategies, including the integration of fins, nanoparticles, porous metal matrices, and encapsulation methods. Additionally, it examines numerical simulation approaches, like the finite volume and finite difference methods for their effectiveness in accurately modeling phase change processes. The chapter also evaluates different composite PCMs, like nano-enhanced and encapsulated types, for their potential to improve energy efficiency. **Figure I.1** summarizes the chapter's content.

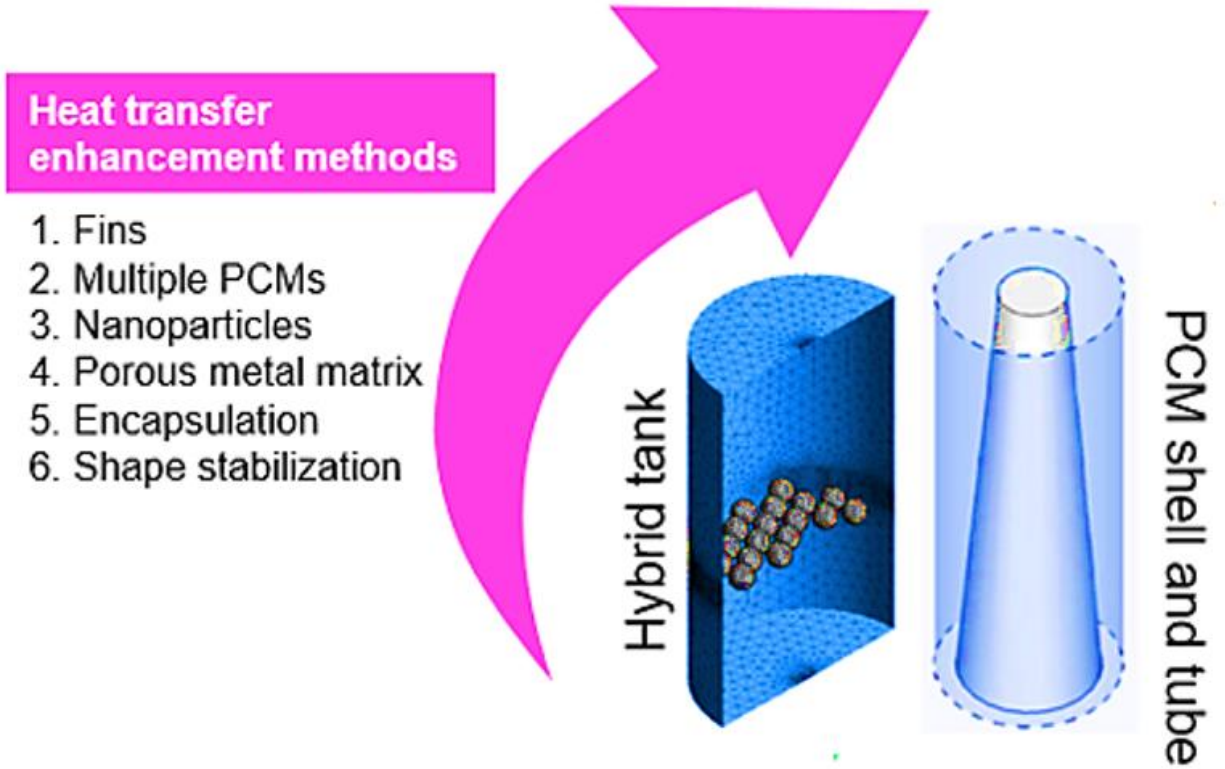

Figure I. 1 : Summary of performance enhancement methods described in this chapter.

I.2-Thermal energy storage

Solar energy holds significant potential as a renewable energy due to its versatility in being converted into both thermal and electrical forms [33]. Nevertheless, its reliance on sunlight and

inconsistent availability pose considerable challenges [34]. TES plays a key role in overcoming these limitations by capturing excess solar energy during daylight hours and making it available for use at night [35]. TES systems are generally categorized based on their heat storage and release mechanisms into three main types: sensible heat storage, latent heat storage, and thermochemical storage, as illustrated in **Figure I.2** [36].

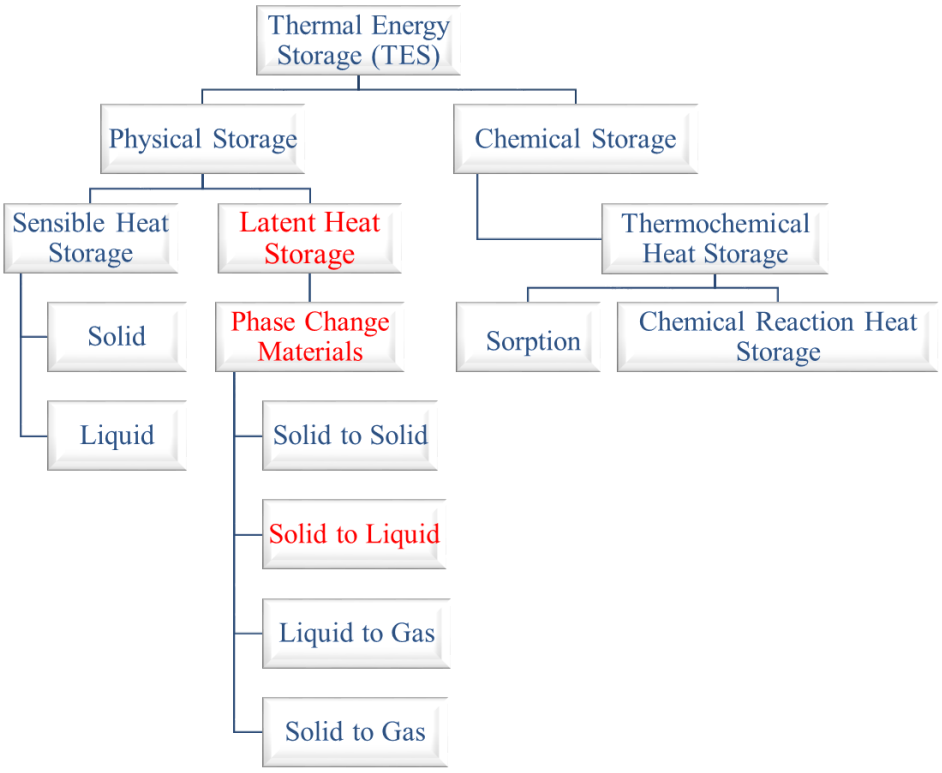

Figure I. 2 : Classifications of thermal energy storage methods.

I.2.1-Sensible heat storage

Sensible TES retains heat by raising the temperature of a material without undergoing any phase change [37]. Sensible heat storage can be achieved using either solid or liquid materials as the storage medium [38]. STES systems typically utilize substances with high specific heat capacities and considerable volume. For efficient operation, a substantial temperature difference between the heat transfer fluid (HTF) and the storage medium is essential [15]. As a non-isothermal process, the amount of stored heat is directly related to the material's mass and specific heat capacity, as expressed in the equation (I.1) [39]:

$$Q = m.C_p.\Delta T \qquad \text{(I.1)}$$

Where:

In this context, Q denotes the stored heat, m represents the mass of the material, C_p is the specific heat capacity at constant pressure, and ΔT refers to the temperature difference between the initial and final states.

TES can be categorized into three primary methods: storage in fluids, solids, and hybrid systems combining both phases.

I.2.1.1-Thermal storage in fluids

Thermocline storage systems operate by maintaining a temperature gradient within a single tank, where hot and cold fluids are naturally stratified. When hot fluid is introduced at the top, it pushes the cooler fluid downward, which is then extracted from the bottom. Conversely, injecting cold fluid at the bottom displaces the warmer fluid upward for collection at the top. A key challenge in this system is preserving the thermal stratification during the charging and discharging processes[40].

I.2.1.2-Thermal storage in solids

In low-temperature thermal energy storage, one common approach involves storing heat directly in the ground using systems like Borehole Thermal Energy Storage (BTES) or geothermal probes. Alternatively, thermal energy can be stored in solid materials such as rock beds or vitrified waste. These systems operate by circulating a hot fluid through or around the solid medium to deposit heat. Later, a cooler fluid is passed in the reverse direction to recover the stored energy. [40], [41].

I.2.1.3-Hybrid thermal storage technologies

Hybrid storage systems combine both solid and liquid media, as demonstrated in solar thermal energy plants that utilize a mixture of oil and rock for energy storage [42]. To minimize the cost associated with thermal oil, the storage tank is filled with rocks that possess a similar volumetric heat storage capacity. During the charging phase, hot oil is introduced at the top of the reservoir, while in the discharging phase, cooler oil enters from the bottom taking advantage of thermocline behavior[43].

I.2.2-Latent heat storage

Latent heat storage captures thermal energy during phase transitions, such as solid-to-liquid, liquid-to-gas, or solid-to-solid transformations, by utilizing the material's ability to absorb or release heat without a change in temperature. In this process, the material is heated to its phase change temperature, where it absorbs latent heat such as the heat of fusion or vaporization. When the material cools, it returns to its original phase and releases the stored latent energy [44]. PCMs are widely adopted in latent heat storage systems due to their ability to store substantial energy at nearly constant temperatures. Among these, solid-liquid PCMs are the most prevalent, as they feature high latent heat of melting and exhibit limited volume changes during phase transitions typically less than 10% making them well-suited for thermal management applications [18]. To ensure efficient operation of a latent heat TES system, three key elements are necessary: a PCM with a suitable melting temperature, an effective heat transfer surface, and a compatible storage container [45].

For a given PCM, the melting temperature (T_m) represents the idealized point it undergoes a transition from the solid phase to the liquid phase. In practical engineering scenarios, this phase change is often assumed to occur isothermally, particularly for pure PCMs [46]. However, in practical scenarios, most PCMs used in thermal systems exhibit a phase transition over a small temperature range surrounding the nominal melting point, as illustrated in **Figure I.3**.

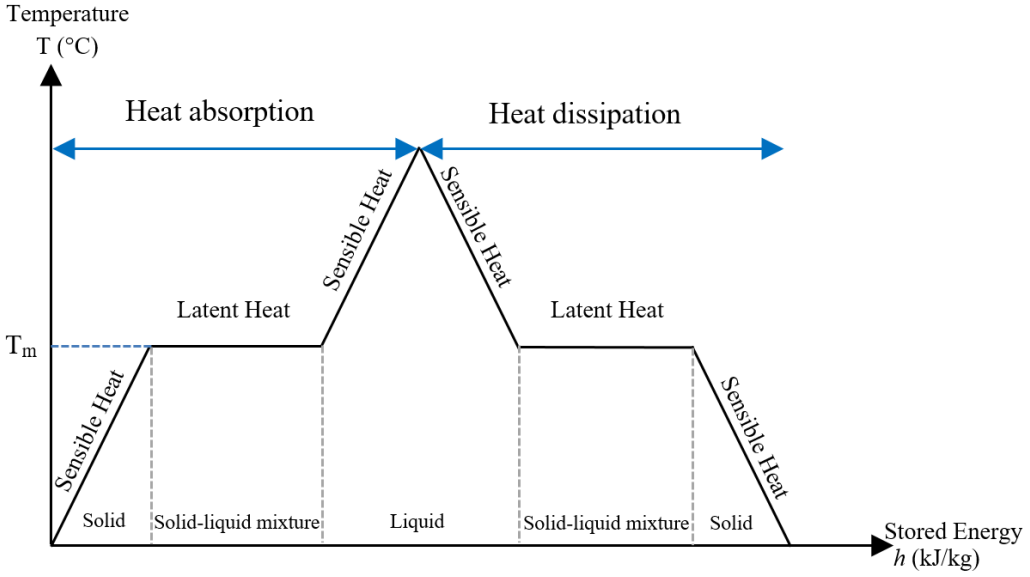

Figure I. 3 : PCM phase change transition.

Figure I.4 presents an idealized phase change diagram. At lower energy levels, the PCM undergoes a solid–solid transition, such as a structural shift from the β-phase to the α-phase, occurring below the melting point. The mushy zone represents a mixed state primarily composed of α-phase with a small fraction of liquid. As energy input increases, the material progresses toward a predominantly liquid state, retaining only traces of the α-phase. The total heat storage capacity of the PCM essential for efficient thermal energy storage comprises three key components: pre-sensible heat, latent heat during the phase change, and post-sensible heat [47]. At lower temperatures, the PCM undergoes a solid–solid phase transition, where the β-phase converts into the high-temperature α-phase [48]. As the temperature increases, the mushy zone emerges, containing a mix of α-phase and liquid until full melting occurs, marking the completion of the solid-to-liquid transformation also known as the heat of fusion. For simplification in analysis, both the latent heat associated with the solid–solid transformation and the heat of fusion are combined to represent the total latent heat involved in the thermal storage or release process. In essence, the phase change behavior of PCMs spans two temperature intervals: the initial solid–solid transition temperature and the melting point, which finalizes the transformation into a fully liquid state [49].

I.2.3-Thermochemical heat storage

Thermochemical energy storage relies on reversible chemical reactions to capture and store heat, typically through the dissociation of chemical compounds. The stored energy is released when the original compounds are reformed. For high energy density and compact storage, the reactants are generally in solid or liquid form, while the resulting products can be gases, liquids, or solids. In cases involving gaseous reactions, fluidized bed reactors are often employed. This approach enables long-term storage of reaction products, making it particularly suitable for applications such as seasonal energy storage [50]. Let *A*, *B*, and *C* be three distinct chemical compounds, and let *Q* a quantity of thermal energy. The reaction can be expressed as follows:

$$A + Q \rightleftarrows B + C \qquad \text{(I.2)}$$

The reaction products in thermochemical storage systems can be maintained at ambient temperature and, when properly sealed, are subject to minimal chemical degradation. Unlike sensible and latent heat storage, which are constrained by thermal losses over time, thermochemical storage is far less affected by storage duration, making it ideal for long-term or

seasonal energy storage. Schmidt et al. [51] demonstrated this concept by using a thermochemical reaction to store solar thermal energy across seasons, employing the reversible conversion of calcium hydroxide into calcium oxide and water. The reaction is represented as follows:

$$Ca(OH)_2 \longleftrightarrow CaO + H_2O \quad \text{(I.3)}$$

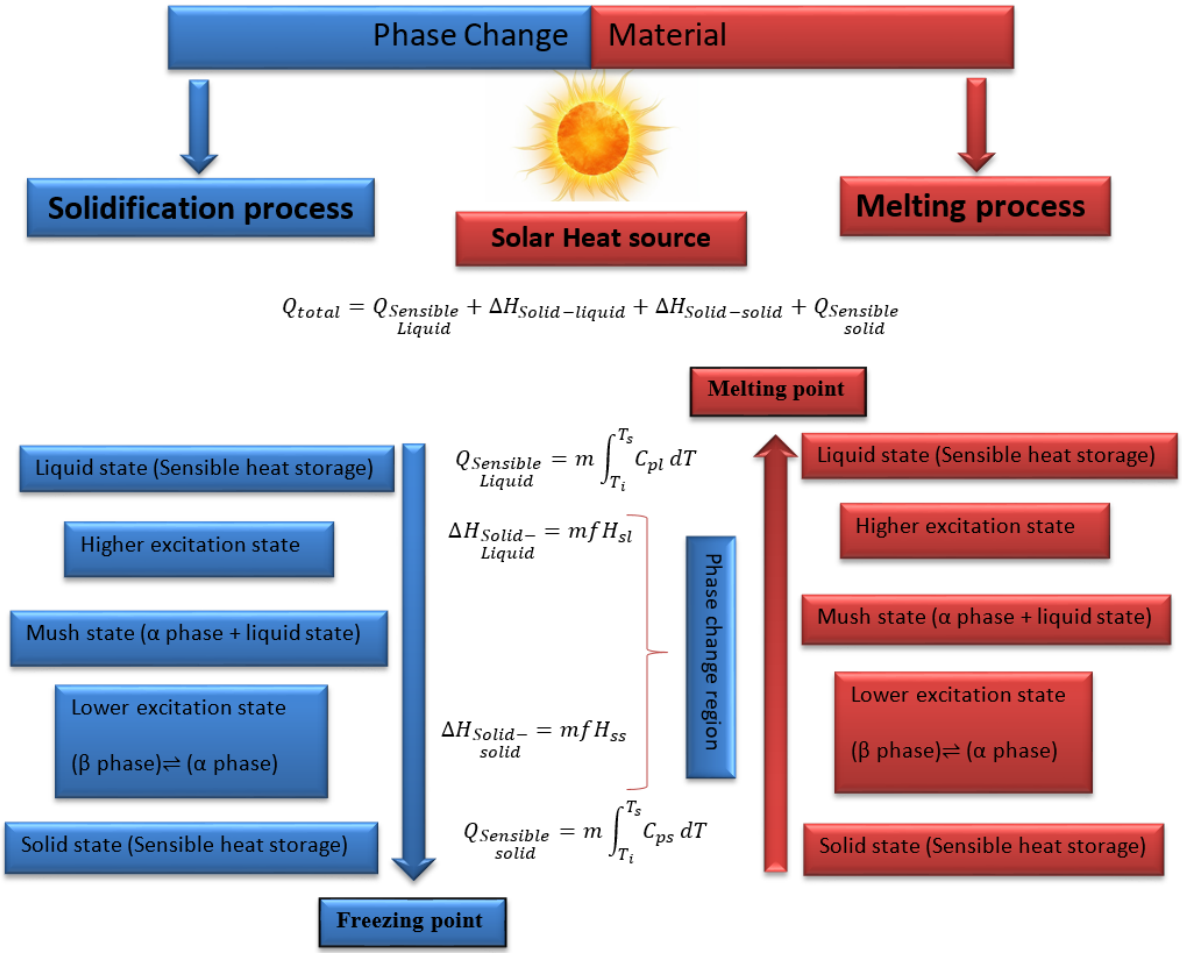

Figure I. 4 : Optimal phase transition diagram for PCM.

I.2.4-Comparison of Storage Systems

Thermochemical storage systems offer a significantly higher energy density approximately five times greater than that of phase change materials. Furthermore, latent heat systems possess a heat capacity that is about 5 to 14 times higher than that of sensible heat storage [52], resulting in overall storage densities that exceed those of sensible systems by a factor of two to three. Thermochemical storage provides several notable advantages, such as nearly unlimited storage duration, easier transportation, and superior energy density compared to other storage methods.

Nonetheless, a major limitation lies in the difficulty of implementing continuous charging and discharging cycles, as current systems typically operate in batch or discrete modes. In industrial settings, sensible heat storage systems are currently the most mature and widely implemented, particularly effective when there is a significant temperature difference between the hot and cold working fluids. However, to reduce thermal losses, these systems require large thermal masses, resulting in a relatively low surface-to-volume ratio. In contrast, phase change storage systems are still in the developmental stage, with progress primarily demonstrated through laboratory research and early prototypes. These systems are especially advantageous in applications with smaller temperature gradients, where sensible heat systems may be less efficient. Incorporating thermal energy storage into district heating networks can offer several operational and economic benefits. However, to achieve optimal performance, careful planning is needed regarding the type of storage system used and its location within the network. **Table I.1** outlines the key advantages and limitations of different thermal storage technologies and provides comparative energy densities for selected materials.

I.3-Phase change materials

PCMs are essential components in LHTES systems, allowing for efficient heat storage during phase transitions. These materials, which can be either pure substances or mixtures, are integral to matching thermal storage requirements. However, the limited availability of pure compounds with specific melting points poses challenges, particularly in applications requiring storage temperatures between 60–90 °C common in domestic and space heating systems [53]. PCMs function by absorbing or releasing latent heat during phase changes such as solid–liquid or liquid–gas transitions. Recognized for their clean energy potential and energy-saving capabilities, PCMs are categorized according to their phase transition type: solid–solid, solid–liquid, gas–solid, and liquid–gas. Of these, solid–liquid PCMs are most widely applied in thermal energy systems due to their high latent heat capacity, low volume variation during phase change, environmental compatibility, wide availability, and cost-effectiveness [54].

Table I. 1 : Comparison of thermal storage and energy densities [55], [56].

Sensible TES	**Specific heat capacity Cp (KJ/kg.k)**	**Energy density (Kw.h/m^3)**	**Advantages**	**Disadvantages**
Sands - rock Mineral oil Water Reinforced concrete	1.3 2.6 4.18 0.85	61 56 70 52	• Inexpensive • Simple engineering	• Low energy density • Insulation is essential
Latent TES	**Latent heat L (KJ/kg)**	**Energy density (Kw.h/m^3)**	**Advantages**	**Disadvantages**
Maleic acid Erythritol NaNO3	235 340 172	103 137 108	• Medium to high energy density • Absorption and release of energy at constant temperature	• Insulation is essential • Complex at a technical level
Thermochemical TES	**Enthalpy of reaction ΔH_r (KJ/mol)**	**Energy density (Kw.h/m^3)**	**Advantages**	**Disadvantages**
$MgH_2 + \Delta H_r \leftrightarrow Mg + H_2$ $CaCO_3 + \Delta H_r \leftrightarrow CaO + CO_2$	-75 (for a charging pressure changing from 380 to 1 bar, and for discharge, it changes from 230 to 4 bar) -178 (for a charging pressure of 700 bar, and discharge of 650 bar)	430 110	• Possesses an exceptionally high energy density, surpassing both sensible and latent heat • No insulation is needed	• Expensive • Restricted reversibility • Complicated engineering

I.3.1-PCM classifications

Thermal energy can be stored in multiple forms: as sensible heat in inert materials, as latent heat using PCMs during phase transitions, and as thermochemical energy through reversible chemical and absorption reactions. **Figure I.5** presents a detailed classification of PCMs, which can be expanded as follows:

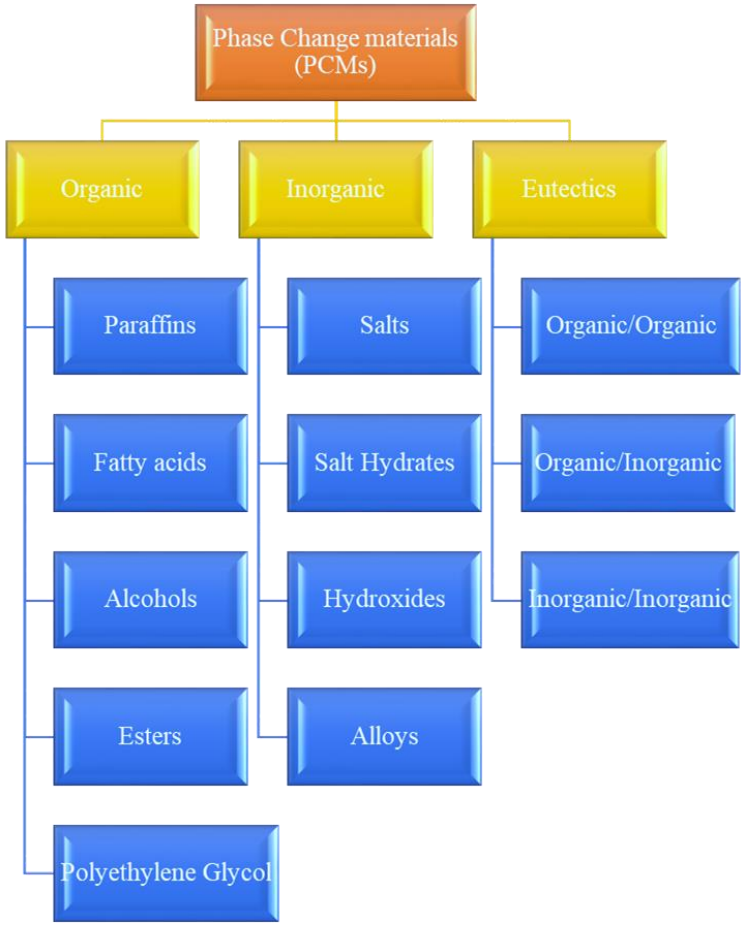

Figure I. 5 : Classification of PCMs.

I.3.1.1-Organic PCMs

Organic PCMs can be broadly classified into paraffin-based and non-paraffin-based compounds. Paraffin waxes, typically represented by the empirical formula C_nH_{2n+2} (where n indicates the number of carbon atoms) [57], and non-paraffin materials, such as polyethylene glycols and fatty acids are among the most widely researched and applied. Paraffin waxes and fatty acids, in particular, have gained prominence due to their well-defined melting ranges, making them

highly suitable for solar hot water systems. These PCMs undergo solid–liquid phase transitions, allowing for consistent melting temperatures and substantial latent heat absorption or release. While they benefit from minimal phase separation and negligible subcooling, they are hindered by drawbacks such as low thermal conductivity, limited latent heat values, and the risk of leakage during the liquid phase. Hydrocarbon-based PCMs, including both paraffin waxes and fatty acids, offer high heat of fusion, making them effective for TES during melting and freezing. Though they are generally non-toxic and non-corrosive [58], their flammability poses safety concerns in certain applications. Furthermore, their low thermal conductivity can slow heat exchange, despite their wide range of melting points, which enhances their applicability across diverse thermal systems. **Table I.2** lists common organic PCMs along with their corresponding melting temperatures

I.3.1.2-Inorganic PCMs

Inorganic PCMs are composed of non-carbon-based compounds, including metals, salts, and ceramics [59]. These substances, particularly salts and metals, are capable of storing substantial amounts of thermal energy due to their high heat of fusion and superior thermal conductivity, which enables quick heat absorption and release. Despite these strengths, inorganic PCMs face several challenges. A common issue is supercooling, where the material cools below its freezing point before beginning to solidify, which can hinder performance in certain applications. Other drawbacks include corrosiveness and phase segregation, where components may separate during repeated use, reducing long-term reliability. Salt hydrates, a major subgroup of inorganic PCMs, are composed of salt and water molecules. They are known for their high latent heat capacity, good thermal conductivity, and relatively low cost. However, their limitations such as thermal instability, corrosive nature, and recrystallization after multiple cycles can impair their ability to store and release heat effectively. On the other hand, metallic PCMs like gallium offer low melting points and fast thermal responses due to high thermal diffusivity, making them attractive alternatives to salt hydrates. Compared to organic PCMs, metals exhibit higher thermal conductivity and minimal volume change. Nevertheless, their low heat of fusion per unit mass results in greater overall system weight, limiting their practical use in lightweight thermal storage applications.

Table I. 2 : List of organic PCM.

Material	Latent heat (J/g)	Temperature range (°C)	Ref
Paraffin	~ 200	20-60	[60]
Lauric acid	146	37	[61]
Myristic acid	168	50-70	[61]
Stearic acid	181	52-58	[61]
Palmitic acid	206	59-64	[62]
Sebacic acid	222	128-133	[63]
Hexadecane	236	28	[64]
Heptadecane	214	22	[64]
Cetane	231	18	[65]
Paraffin RT18	134	18	[66]
n-Nonadecane	243.5	27-32	[67]
n-Tetradecane (C-14)	229	6	[68], [69]
n-Pentadecane (C-15)	206	10	
n-Octadecane (C-18)	28.4	244	
n-Eicozane (C-20)	36.5	247	
Heneicozane (C-21)	40.2	213	
n-Docozane (C-22)	44	249	
n-Tetracozane (C-24)	50.6	255	
n-Pentacozane (C-25)	53.5	238	
n-Hexacozane (C-26)	56.3	256	
n-Heptacozane (C-27)	58.8	236	
n-Oktacozane (C-28)	41.2	254	

I.3.1.3-Eutectic PCMs

Eutectic PCMs are formed by combining two or more components to create a mixture with a melting point lower than that of the individual substances. This characteristic allows for efficient energy absorption and release during phase transitions. Eutectic compositions exhibit a sharp, well-defined melting point, which enhances their effectiveness in TES applications. By blending

the favorable traits of both organic and inorganic PCMs, eutectic materials aim to address the limitations inherent in each category. By precisely adjusting the mass ratios of constituent materials, researchers can tailor key thermophysical properties of eutectic PCMs, such as melting point, latent heat capacity, and thermal conductivity thus expanding their usability across a wider range of applications. Despite these advantages, eutectic PCMs continue to face significant challenges, including reduced thermal efficiency at high temperatures, diminished latent heat after eutectic formation, leakage issues, and relatively high manufacturing costs. To overcome these limitations, recent studies have focused on the integration of carbon-based additives. These enhancements not only improve thermal conductivity and minimize leakage but also contribute to better dispersion in both phases and offer environmentally friendly alternatives. While challenges remain, incorporating carbon materials represents a promising pathway for boosting the performance and reliability of eutectic PCMs in modern thermal energy storage technologies [70].

I.3.2-PCM selection criteria and applications across temperature ranges

PCMs span a broad spectrum of transition temperatures and possess diverse thermophysical characteristics that directly impact their effectiveness in TES systems. Therefore, selecting an appropriate PCM is a critical step in optimizing system performance. This selection involves a comprehensive assessment of multiple parameters, including thermal properties, phase transition behavior, chemical and thermal stability, environmental considerations, and economic feasibility. Key selection criteria encompass the phase change temperature, thermal conductivity, latent heat storage capacity, material compatibility, and safety aspects such as flammability. A balanced evaluation of these factors ensures the PCM aligns well with the specific requirements of the intended TES application [54]. Among the various selection criteria, the phase change temperature is the most critical, as it directly determines the suitability of a PCM for a particular application. It is essential to match the PCM's transition temperature with the operational range of the system for example, domestic refrigeration typically requires PCMs with melting points between -20 °C and 5 °C [71], and buildings and electronics typically require 5 to 40 °C [72], and solar water heating functions around 40 to 80 °C [73]. The diversity in operating temperature requirements underscores the importance of selecting PCMs that are specifically tailored to the thermal demands of each application. **Figure I.6** summarizes the key criteria for PCM selection, highlighting the most influential parameters that guide material choice across a wide range of uses. Furthermore,

Figure I.7 categorizes PCM applications into four distinct temperature ranges, offering a comprehensive overview of their deployment in various thermal energy storage contexts [74].

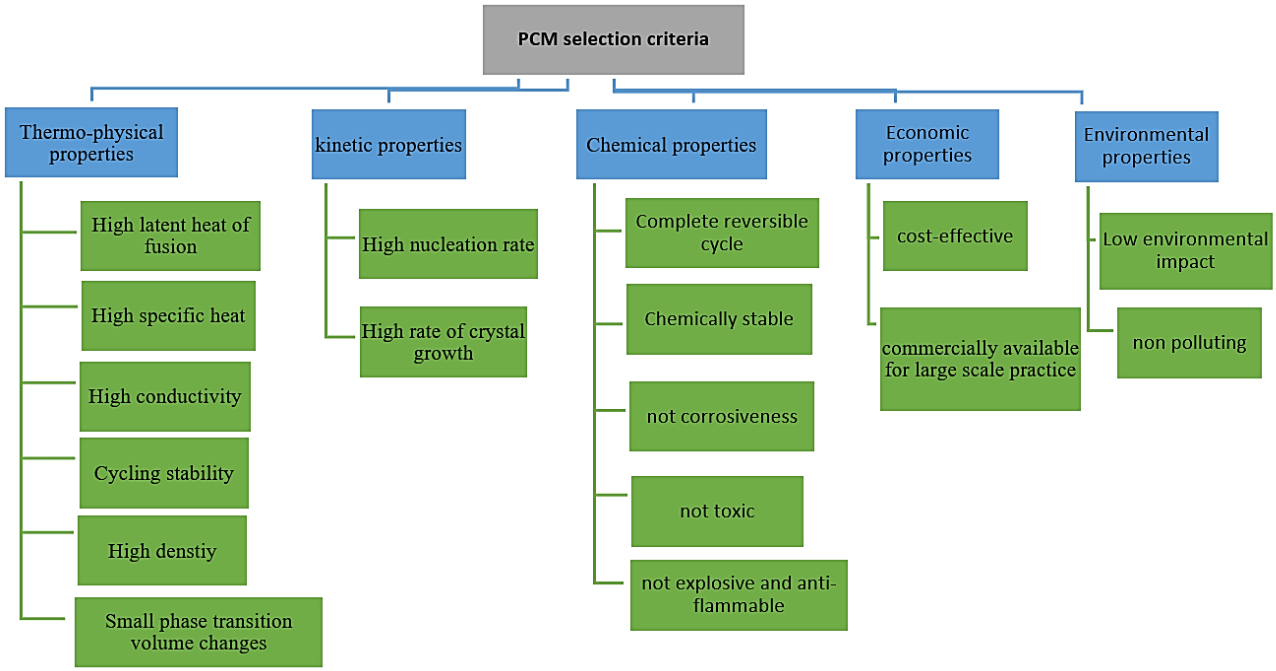

Figure I. 6 : Criteria for PCM selection in thermal energy storage systems [75], [76].

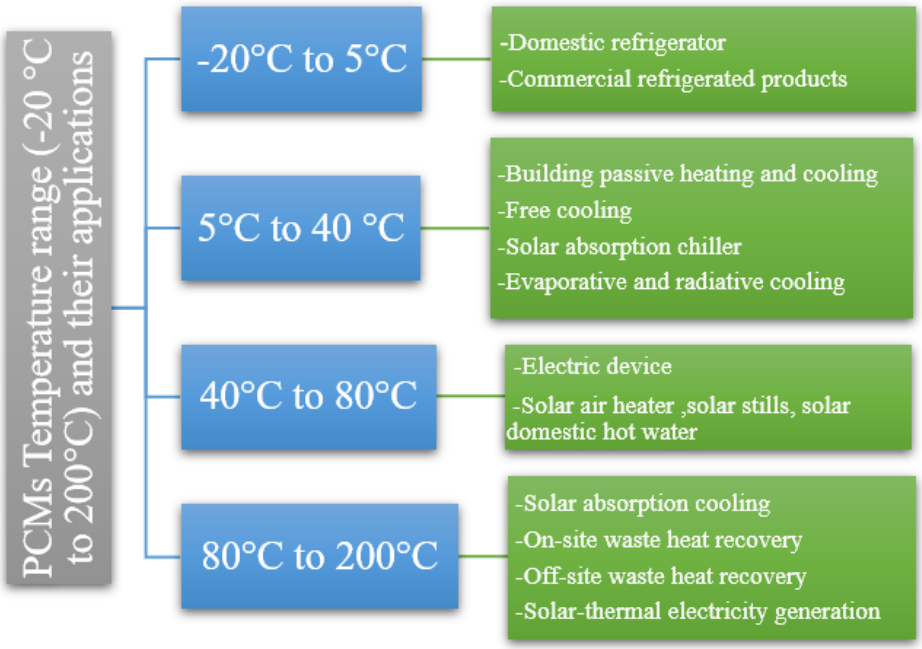

Figure I. 7 : Categorization of PCM applications across four temperature ranges [74].

I.4-Heat transfer enhancement methods of PCMs

Although PCMs offer significant advantages and diverse applications in thermal energy systems, their large-scale deployment remains limited due to three primary challenges: inherently low thermal conductivity [77], potential leakage during phase transitions [78], and limited solar-to-thermal energy conversion efficiency [79]. These limitations restrict their performance and versatility in various applications. However, several strategies have been developed to address these issues. Improving thermal conductivity and minimizing leakage are particularly critical. As illustrated in **Figure I.8**, common enhancement methods include the use of extended surfaces such as fins [80], the deployment of multi-PCM configurations [81], the addition of nanoparticles [49], the integration of porous metal structures [82], encapsulation [78], and Shape stabilization of PCMs [83]. These approaches not only help to overcome existing limitations but also broaden the practical applications of PCMs across a wide range of thermal energy systems.

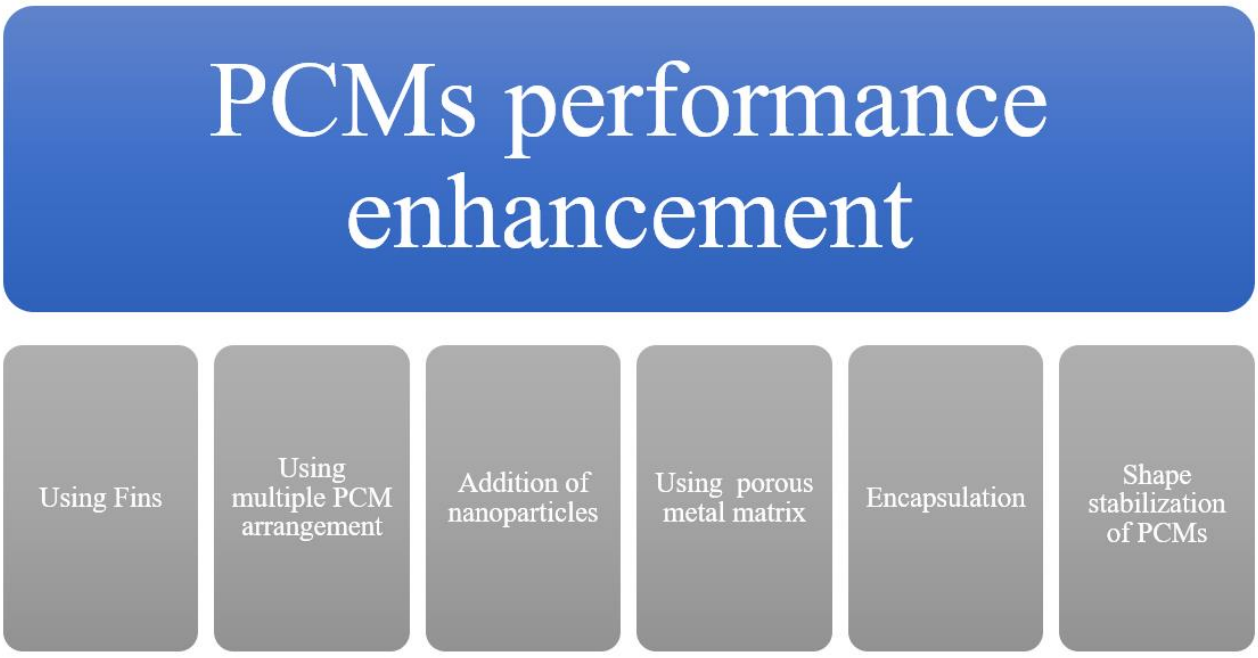

Figure I.8 : Improving PCM performance [84].

I.4.1-Fins

PCMs are characterized by high energy storage capacity and a stable phase change temperature. However, a key limitation particularly in organic PCMs is their low thermal conductivity, which leads to inefficient heat transfer during melting and solidification. To

overcome this issue, researchers have extensively investigated the integration of fins to increase the surface area in contact with the PCM, thereby enhancing heat transfer rates and reducing response time [85]. This approach has gained substantial attention due to its superior performance compared to finless configurations [86]. Numerous studies have demonstrated the effectiveness of finned structures in accelerating thermal exchange during phase transitions [24]. **Tables I.3** and **I.4** provide a comprehensive overview of different fin configurations available for implementation in PCM systems.

Kirincic et al. [87] examined a shell-and-tube system utilizing paraffin and water, enhanced with longitudinal fins on the inner tube. Their findings revealed notable improvements, with melting and solidification times reduced by 52% and 43%, respectively, compared to systems without fins. In a related study. Nie et al.'s [88] explored phase change behavior in a double-tube thermal system with fins, concluding that straight, fewer, and longer fins yielded better heat transfer performance, particularly in applications involving low-conductivity PCMs. Similarly, Mhood et al. [89] investigated melting processes in horizontal LHTS systems, emphasizing the importance of optimizing fin geometry. Their results indicated that increasing fin height and using specific angular placements could reduce melting time by up to 50%, significantly enhancing heat transfer in thermally critical areas.

Table I. 3: Various geometries of fins for PCM storage.

Authors	Geometry	Dimension type	Study	Types of fins	Main Research Focus
Wu et al[90]		2D	Numerical	Spiderweb-like fins	Improving solidification performance in LHTES using spiderweb-structured fins
Oskouei et al[91]	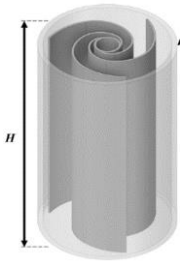	3D	Experimental and numerical	Fibonacci-inspired fins (tree-like fins)	Improving LHTES performance using fins designed based on the Fibonacci sequence
Liu et al[92]	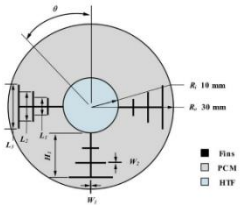	2D	Numerical	Gradient fins	Improving LHTES performance through gradient fin structures and natural convection evaluation
Nakhchi et al [93]	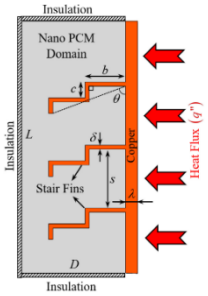	2D	Numerical	Stair fins	Improving LHTES performance using nano-enhanced PCMs combined with stair-shaped fins

Ge et al [94]	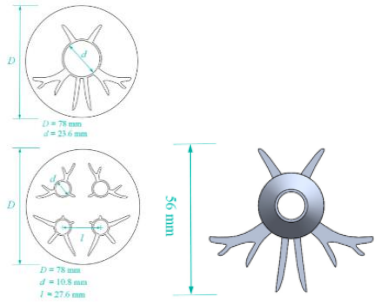	2D	Experimental and numerical	Topology optimized fins	Enhancing the efficiency of LHTES using topology-optimized fin structures

Table I. 4 : (*continued*)

Authors	The model	Dimension type	Study	Fins name	Principal investigation
Vogel et al [95]	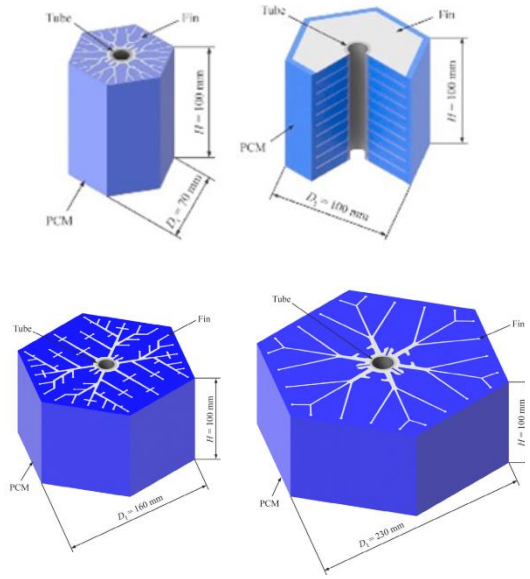	3D	Numerical	Organic shape, Plate shape, Snow-flake shape, Eco shape	Influence of Natural Convection on Extended Fins in Shell-and-Tube Thermal Storage Units
Sciacovelli et al [96]	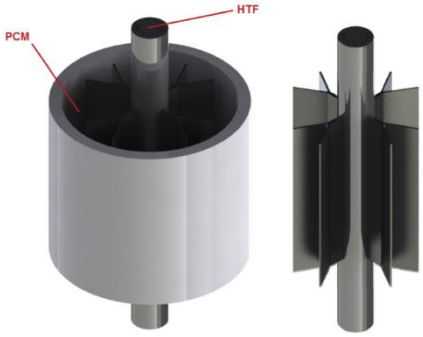	2D	Numerical	Tree-shaped	Enhancing LHTES Performance Using Y-Shaped Fin Configurations

Ghalambaz et al [97]	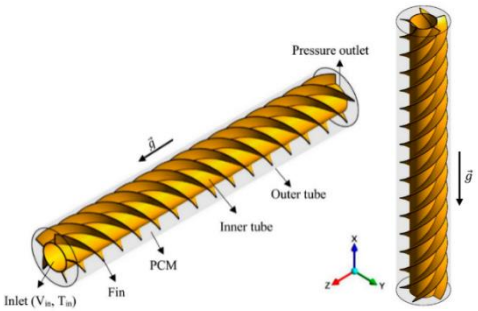	3D	Numerical	Twisted fins	Improving PCM Charging Performance through Twisted Fin Array Configurations

I.4.2-Multiple PCMs

Multi-PCM LHTS systems incorporate two or more PCMs with different melting points or thermal properties, distinguishing them from traditional single-PCM units. While single-PCM systems are simpler in design, they often exhibit longer melting and solidification durations, which limits their thermal performance [98]. By contrast, multi-PCM configurations improve heat transfer efficiency by strategically layering PCMs, allowing for more effective energy storage and release across a broader temperature range. Researchers have explored various multi-PCM arrangements, including differing the number of materials and adjusting the orientation of the heat exchanger to further optimize performance [99].

Kurnia et al. [100] investigated a range of PCM thermal storage designs, highlighting a novel festoon-shaped channel that demonstrated improved heat transfer performance. Their study also explored the use of multiple PCM configurations to further enhance system efficiency, as illustrated in **Figure I.9**.

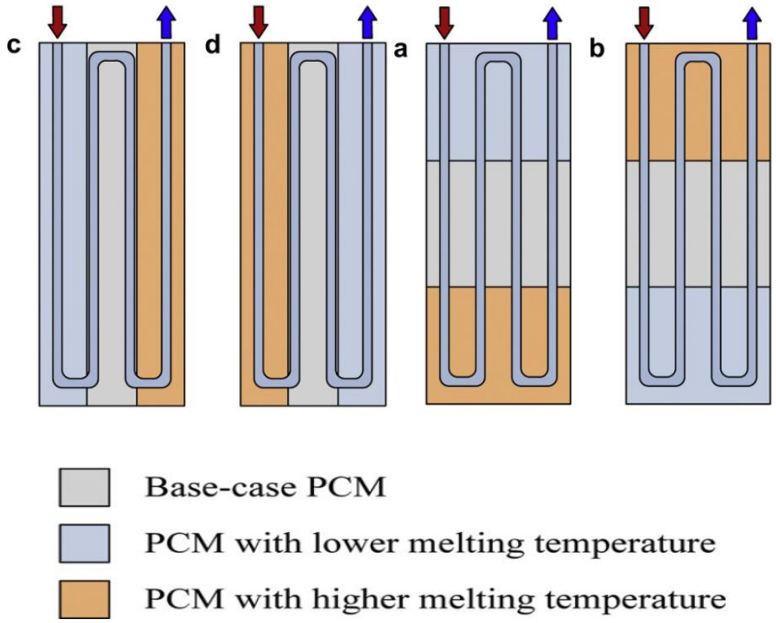

Figure I. 9 : Configurations of multi-PCM thermal energy storage [100].

Gao et al. [101] developed a three-stage cascaded packed bed thermal energy storage (CPBTES) system utilizing PCMs for solar heating applications. They constructed a thermal resistance-based model and validated it experimentally. Through multi-objective optimization, the system achieved a 5% improvement in exergy efficiency and a 4% reduction in storage capacity. The results demonstrated superior temperature distribution and optimized design parameters, offering practical insights for enhancing the performance of similar thermal storage systems. These findings are illustrated in **Figure I.10**.

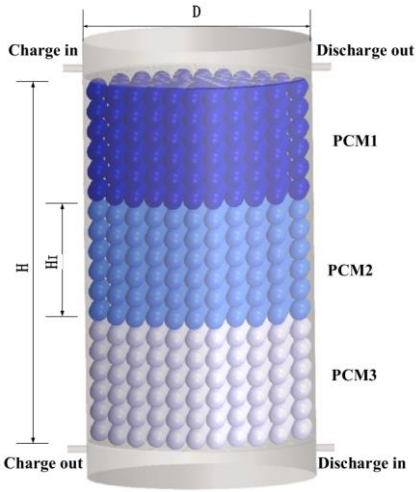

Figure I. 10 : Packed cascaded structure for thermal energy storage [101].

I.4.3- Nanoparticles

Nanoparticles have been incorporated into PCMs to enhance their thermal conductivity, leveraging their high surface-to-volume ratio. The degree of conductivity improvement in shape-stabilized PCMs containing nanoparticles depends on several key factors, including the concentration and size of the nanoparticles, their aspect ratio, intermolecular interactions, Brownian motion, clustering behavior, material purity, and interfacial thermal resistance [50]. **Figure I.11** presents a summary of widely used nanoparticles integrated with PCMs. The addition of metals, metal oxides, and carbon-based nanomaterials to PCM composites has been shown to significantly improve thermal conductivity and overall heat transfer performance [102]. Khodadadi and Hosseinizadeh. [103] were pioneers in enhancing LHTES systems through the introduction of nanoparticles. Their study demonstrated significant performance improvements by dispersing copper nanoparticles into a water-based PCM during solidification, a technique known as nanoparticle-enhanced PCM (NEPCM). This approach effectively increases thermal conductivity, resulting in faster melting and solidification processes compared to conventional PCMs. Table I.5 provides a detailed summary of the thermal properties of various nanoparticles used in numerical PCM studies, including parameters such as thermal conductivity, particle size, density, and specific heat capacity.

Table I. 5: Thermal properties of nanoparticles used in numerical studies with PCM [104], [105], [106].

Nanoparticles Materials	Symbol	Size	Density (kg/m^3)	Thermal conductivity (W/m.K)	Specific heat capacity (J/kg.K)
Aluminum Oxide	Al_2O_3	20 nm	3980	38.493	778
Silver	Ag	-	10500	429	235
Carbon nanofiber	CNF	D :400 nm; L :50µm	2100	-	-
Cerium (IV) Oxide	CeO_2	15-30 nm	6100	11.715	352
Cobalt Oxide	CoO	30 nm	6460	10.042	703
Copper	Cu	90 nm	8954	400	383
Copper Oxide	CuO	40-80 nm	6500	17.991	536
Gadolinium Oxide	Gd_2O_3	20-80 nm	7640	10.042	290
Graphene	GN	-	2200	5000	790.1
Graphene oxide	GO	-	1800	5000	717
Graphite nanopowder	Grp	APS:50 nm	2200	-	-
Graphene nano-platelets	GNP	Thickness: 7 nm APS: 15 µm	100	-	-
Iron oxide	Fe_2O_3	20-40 nm	5240	12.552	628
Multi-walled carbon nanotube	MWCNT	-	1600	3000	796
Magnesium Oxide	MgO	35 nm	3580	61.923	921
Nickel Oxide	NiO	20 nm	6400	12.970	603
Single-walled carbon nanotube	SWCNT	-	2600	6600	425
Silicon Oxide	SiO_2	10-20 nm	2650	11.715	753
Strontium Titanate	$SrO.TiO_3$	100 nm	5110	05.858	536
Tin Oxide	SnO_2	100 nm	5560	31.380	343
Titanium Oxide	TiO_2	100 nm	4250	08.954	686
Yttrium Oxide	Y_2O_3	30-50 nm	5000	14.226	448
Zinc Oxide	ZNO	100 nm	5630	27.196	494

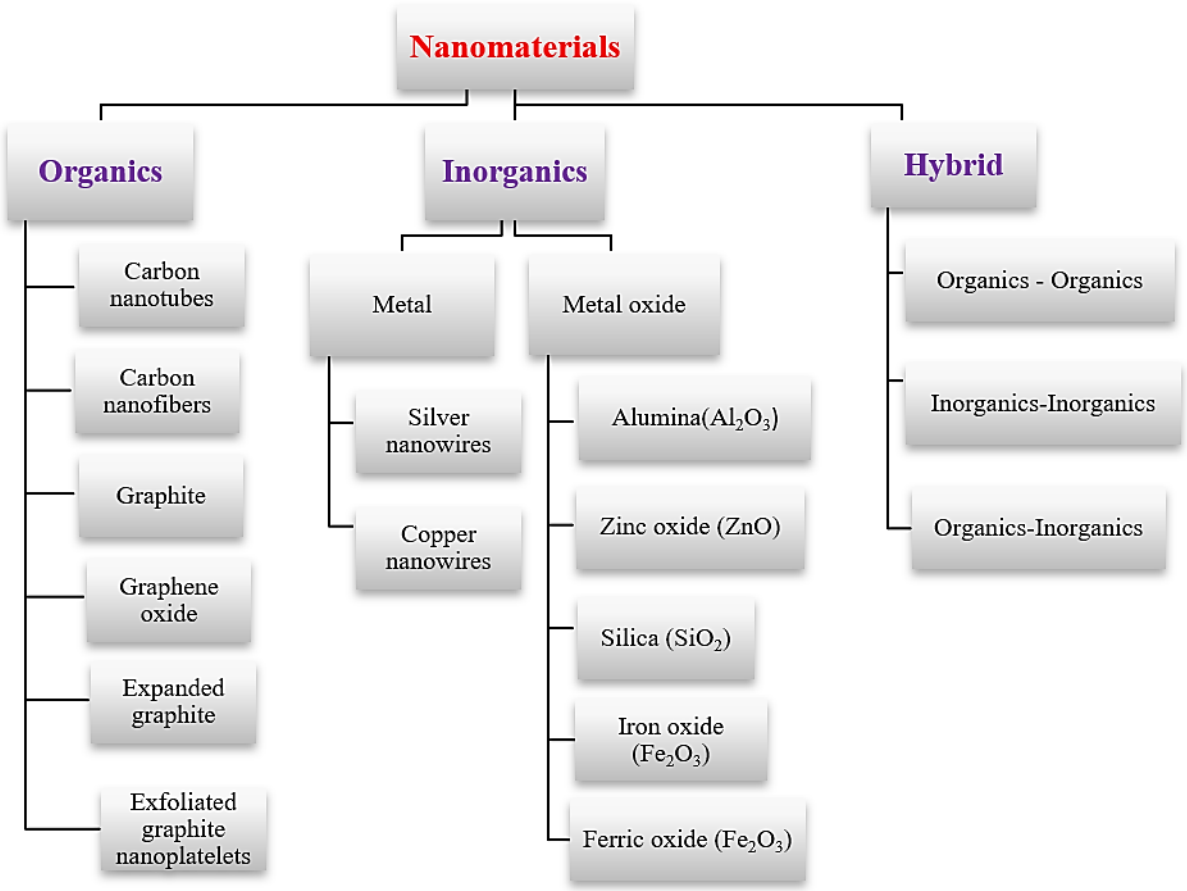

Figure I. 11 : Widely employed nanomaterials in composite PCM [107], [108].

Nakhchi et al. [93] investigated the combined effects of CuO nanoparticles and stair-shaped fins on TES performance, reporting a 9.1% increase in stored energy and achieving a total capacity of 474.1 kJ. The integration of descending stair fins and nanoparticles was found to enhance melting performance by improving both thermal conductivity and natural convection within the PCM. In a related study, Singh et al. [109] performed a numerical analysis of the melting behavior in a finned latent heat storage unit incorporating varying volume fractions of graphene nanoplatelets (GNPs). Their research examined the influence of fins, GNPs, and their synergy on effective thermal conductivity, accounting for parameters such as anisotropy and aspect ratio. Experimental characterization of sugar alcohol was conducted to determine phase change properties, and transient simulations were used to support the design of medium-temperature thermal storage systems. The optimized configuration, featuring fins and 5% GNP, resulted in a substantial 68% decrease in total melting time, as shown in **Figure I.12**.

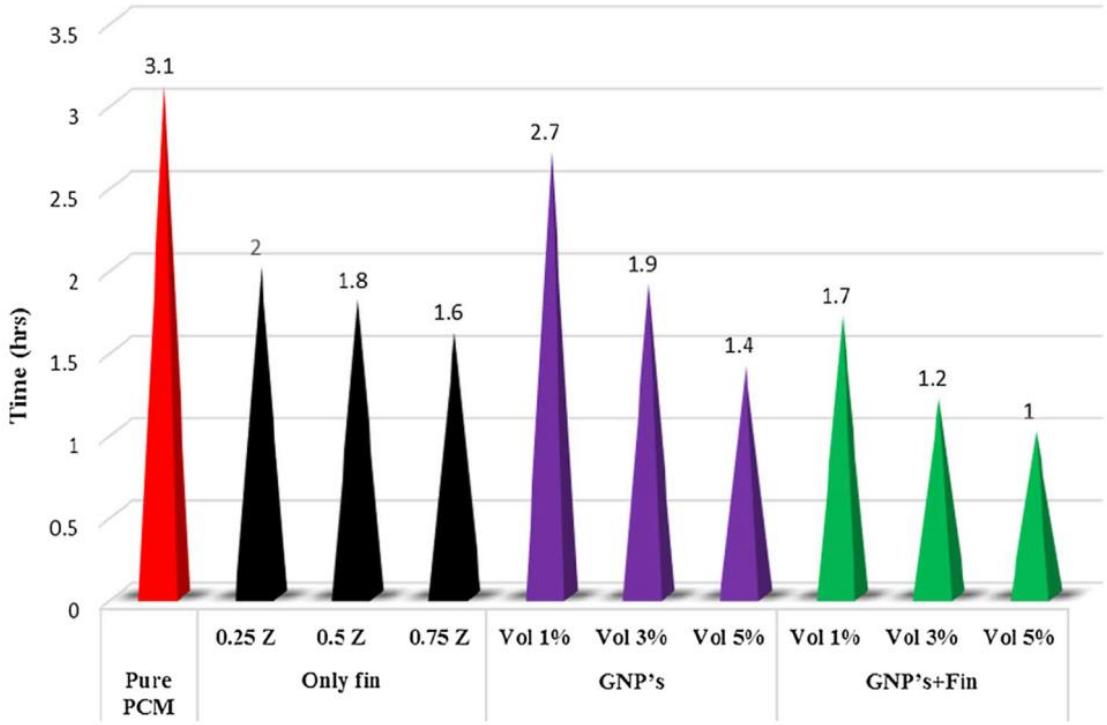

Figure I. 12 : Overall melting time with various heat transfer enhancement techniques [109].

I.4.4- Porous metal matrix

One common strategy to improve the thermal conductivity of PCMs is the incorporation of high-conductivity additives [110]. Composite PCMs enhanced with such fillers ranging from nanoparticles [111], and extended surfaces like fins [112], to porous materials [111]. show great promise in boosting heat transfer performance. Among these, metal foam (MF) is particularly notable due to its high thermal conductivity, interconnected porous structure, and excellent compatibility with PCMs [113]. The porous architecture of MF allows it to hold the PCM efficiently while significantly improving thermal diffusion, positioning it as a highly effective solution for overcoming the inherent low conductivity of PCMs [114].

Parida et al. [115] introduced a pore-scale numerical approach to examine the melting process of PCMs within metal foams, successfully highlighting how foam geometry affects local heat transfer characteristics. By incorporating convection effects, the study revealed that higher porosity and larger pore sizes promote natural convection, thus enhancing the overall thermal performance. Similarly, Yang et al. [116] explored the melting behavior of paraffin infiltrated into metal foam at various inclination angles (0°, 30°, 60°, and 90°). Their results indicated that lower

inclination angles notably accelerated the melting process reducing the total melting time by 12.28% at 0°, 22.81% at 30°, and 34.21% at 60° due to stronger convective currents. However, the inclination angle exhibited limited impact on the melting behavior within the foam matrix itself. These observations are visually summarized in **Figure I.13**.

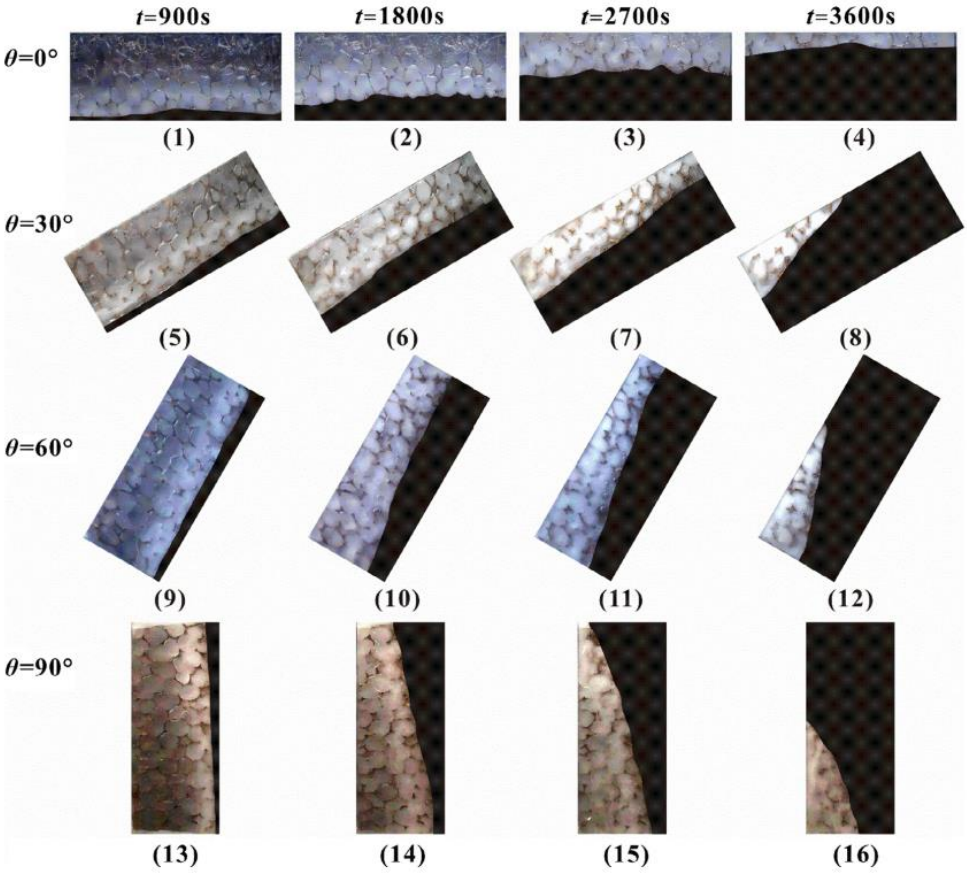

Figure I. 13 : Evolution of melting front in paraffin-embedded within metal foam at different time intervals and inclination angles [116].

Yang et al.[117] performed a detailed comparative study of melting heat transfer in PCMs embedded with metal foam, using both the volume-averaged method and direct numerical simulation. By incorporating a two-temperature model into the VAM framework, the researchers effectively captured macroscopic behaviors such as interface movement and temperature distribution, while highlighting the influence of natural convection. Although the VAM approach does not resolve pore-scale details, the study demonstrates its practicality and cost-effectiveness for evaluating the use of metal foam in applications like residential heating and domestic hot water systems utilizing waste heat. The key findings are illustrated in **Figure I.14**.

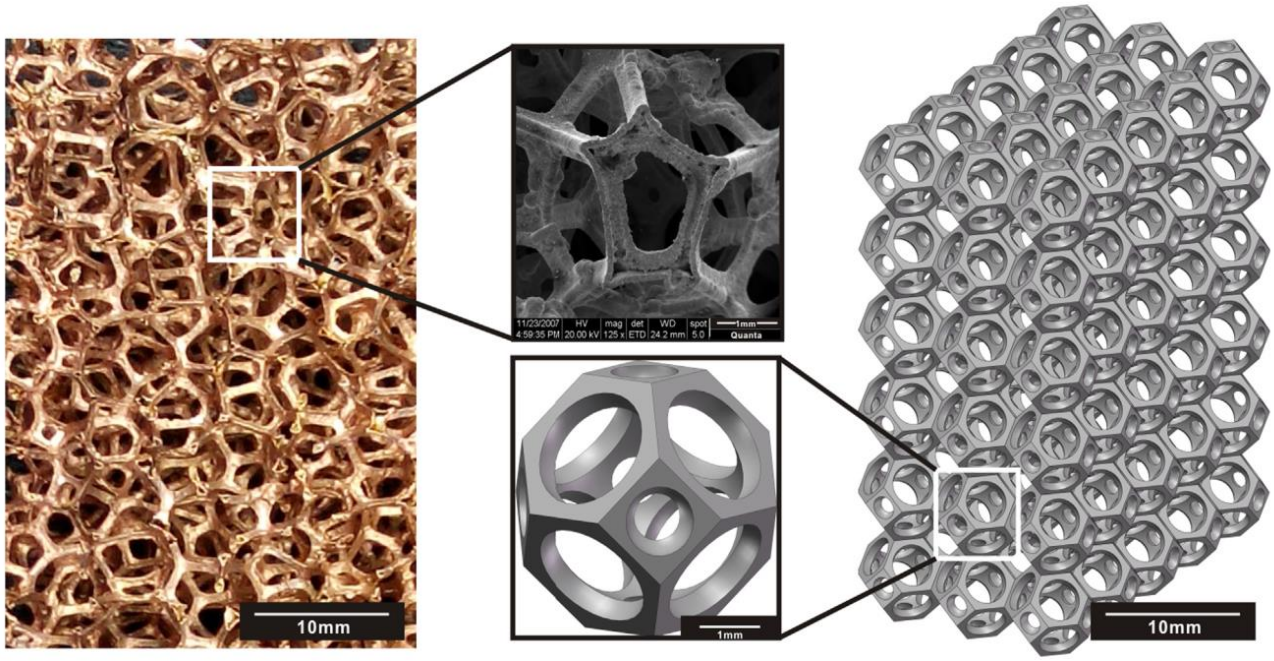

Figure I. 14 : Copper foam with open-cell structure and reconstructed tetkaidechedron-shaped cut [117].

I.4.5-Encapsulation

The effectiveness of PCMs can be compromised by issues such as chemical reactivity and volumetric changes during phase transitions. Encapsulation addresses these challenges by enclosing PCMs within a protective shell, reducing reactivity and mechanical stress, thereby improving durability and functional reliability [118]. Various encapsulation methods have been developed to tackle problems like leakage, stability, and poor thermal conductivity. These include macro-encapsulation (particle sizes >1 mm), which can take several forms such as spherical [119], rectangular [120], tubular [121], or cylindrical [122]. Micro-encapsulation (ranging from 0 to 1000 μm) provides a higher surface-to-volume ratio, leading to more efficient heat transfer [68], while nano-encapsulation (0 to 1000 nm) offers exceptional structural integrity and is considered highly promising for advanced TES applications [123].

Neri et al. [124] evaluated a hybrid thermal energy storage system combining a hot water tank with macro-encapsulated PCMs (**Figure I.15**). Utilizing three numerical models validated by experiments, they aimed to increase the system's overall thermal storage capacity. However, results indicated that only about 40% of the PCM's latent heat potential was utilized, primarily due to thermal transport limitations that hinder effective heat exchange.

Figure I. 15 : The top view of the tank incorporates macro-encapsulated PCM [124].

Su et al. [125] utilized melamine-formaldehyde (MF-3) resin to microencapsulate paraffin wax, producing five different encapsulation variants (**Figure I.16**). Their investigation demonstrated enhanced thermal stability, primarily attributed to the influence of binary emulsifiers, as confirmed through thermogravimetric analysis. While these findings highlight promising thermal performance, further research is needed to explore the practical integration of these microcapsules into TES systems.

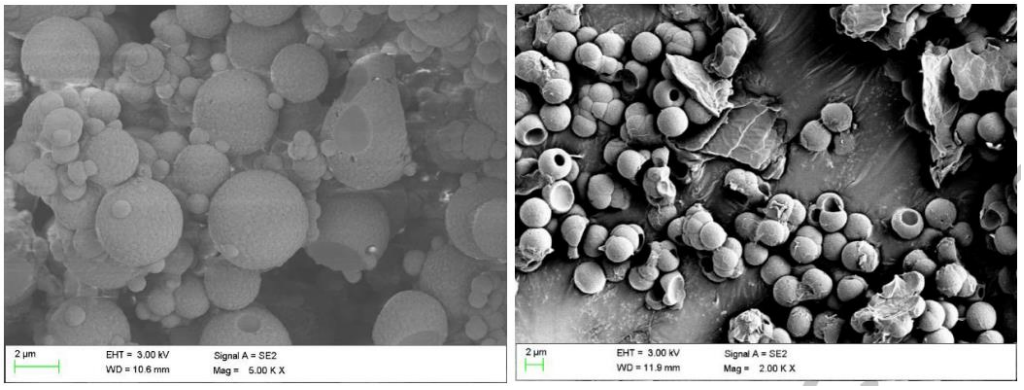

Figure I. 16 : SEM analysis of Micro-encapsulated PCM (MEPCM) samples [125].

In their study, Ghalambaz et al. [126] conducted a study on the convective heat transfer and fluid flow behavior of nanoencapsulated phase change materials (NEPCMs) inside a thermally insulated square cavity, as illustrated in **Figure I.17**.

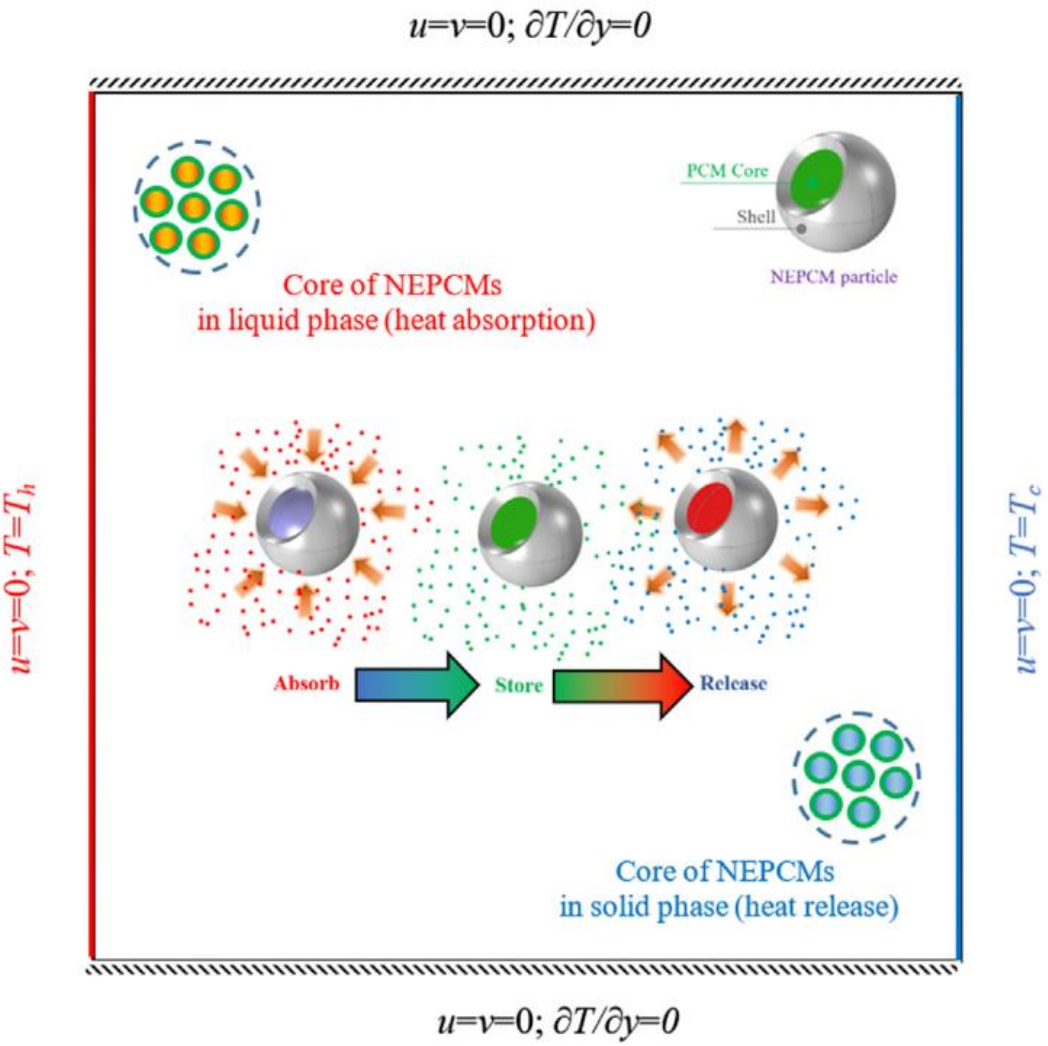

Figure I. 17 : Schematic representation of the physical model of nano-enhanced PCM (NEPCM) [126].

I.4.5.1-Encapsulation methods

Encapsulation techniques for PCMs are generally grouped into three main categories physical, physico-chemical, and chemical based on the synthesis approach used for producing encapsulated PCMs (EPCMs). An overview of these classification methods is presented in **Figure I.18**.

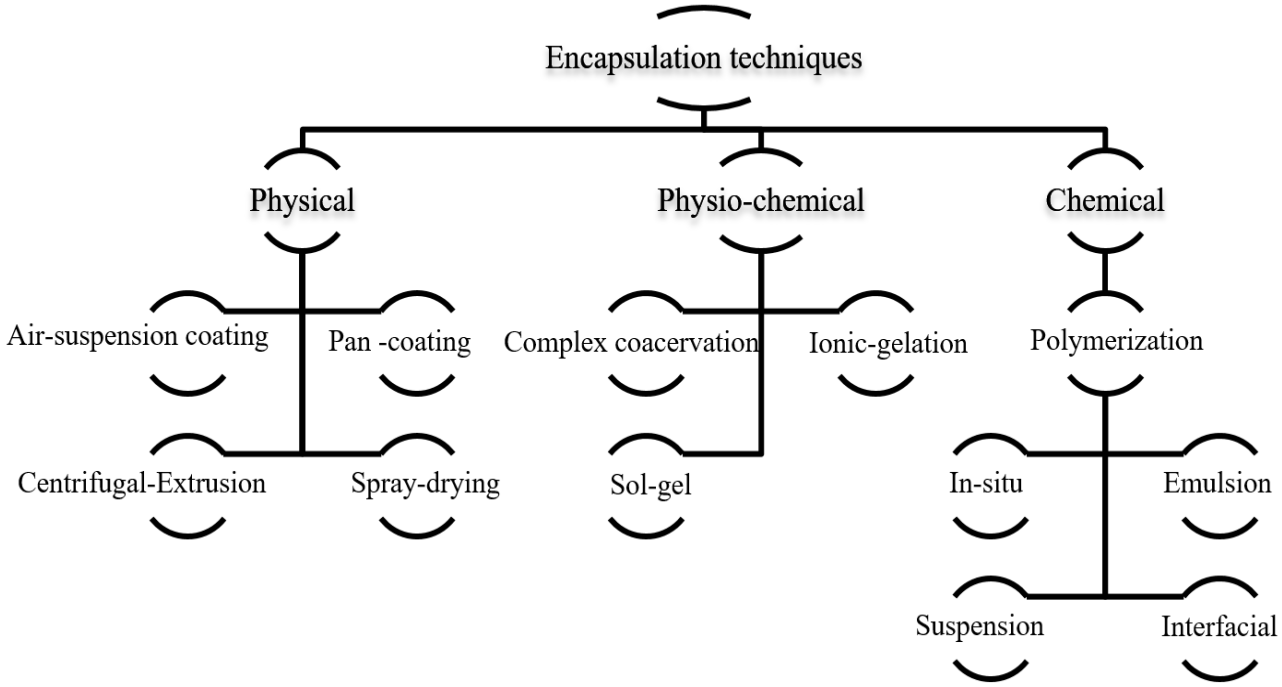

Figure I. 18 : PCM encapsulation methods [127].

I.4.6-Shape stabilization

To enhance the thermal performance of PCMs, various additives referred to as thermal reinforcements are incorporated to form optimized thermal composites. These reinforcements are typically classified as thermal conductivity enhancers (TCEs), shape stabilizers (SSs), or multifunctional agents serving both purposes. Materials such as graphene are often employed for their dual-functionality, resulting in duplex thermal composites. Based on their intrinsic structural characteristics, these reinforcements are further categorized into organic and inorganic types, as depicted in **Figure I.19**. Effective additives are characterized by their high thermophysical properties and robust morphology, which encapsulate PCM molecules to prevent leakage and maintain structural integrity during phase transitions.

While triplex composites offer enhanced thermal performance, they can reduce the overall latent heat capacity of the system. To address PCM drawbacks such as low thermal conductivity and

leakage, shape-stabilized composite PCMs (SS-CPCMs) are created by blending PCMs with structural supports like porous or nanomaterials (**Figure I.20**). Although these composite systems significantly improve stability and thermal conductivity, the thermal storage capacity may be compromised, as the support materials generally contribute minimally to the latent heat storage process[128].

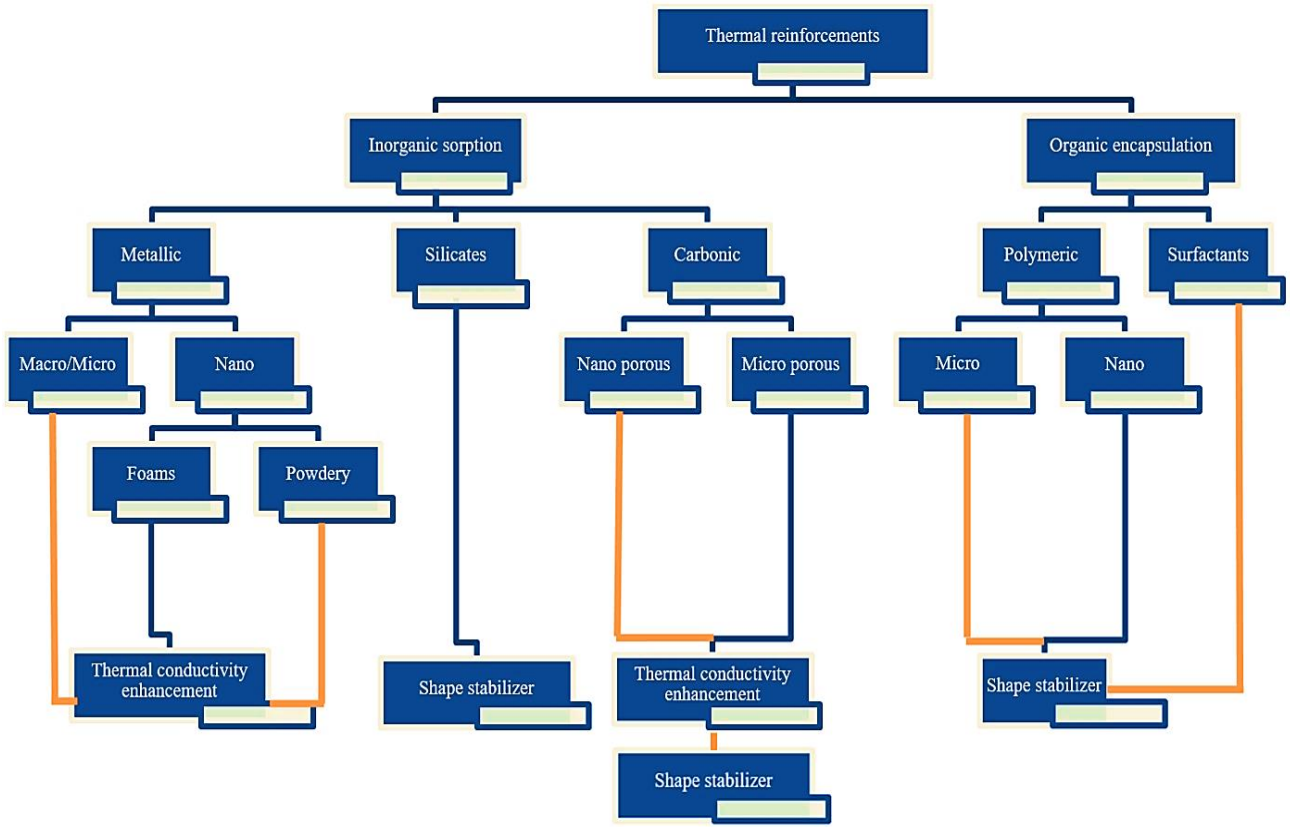

Figure I. 19 : Classification of additives for PCM [129].

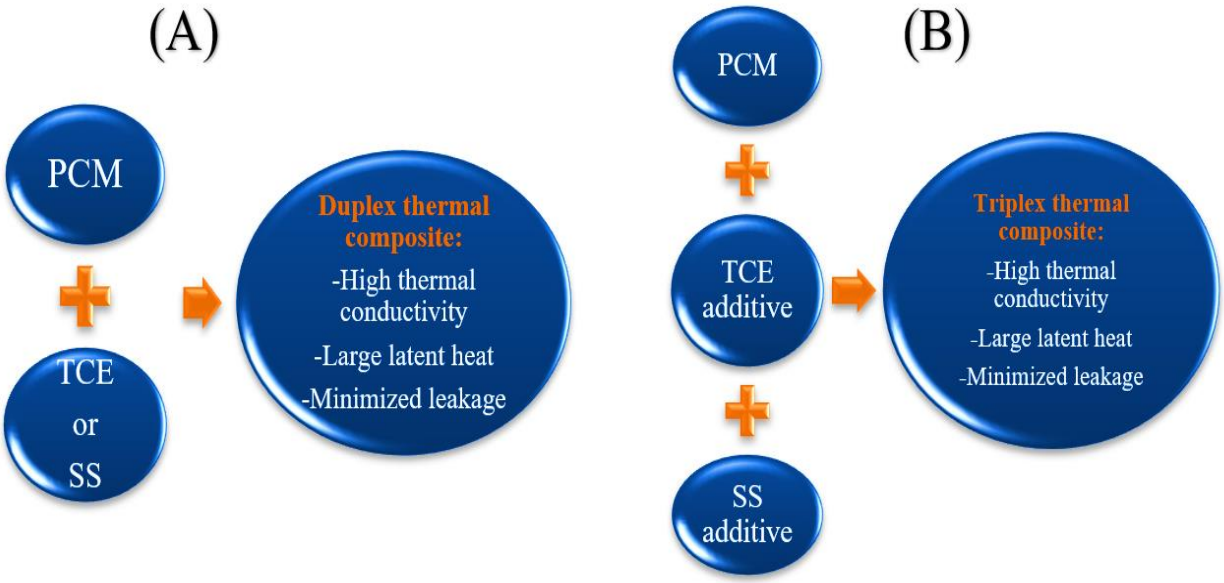

Figure I. 20 : (A)-Duplex thermal composite (b)-triplex thermal composite.

Zhang et al. [130] developed a form-stable composite PCM by integrating 80 wt% RT100 with expanded graphite (EG), tailored for medium-temperature latent heat thermal energy storage (TES). This composite demonstrated significantly improved thermal conductivity compared to pure RT100, with conductivity rising proportionally to its packing density. Additionally, the RT100/EG blend showed strong photothermal responsiveness, maintained thermal conductivity throughout the melting process, and retained structural integrity and reliability over 200 thermal cycles highlighting its suitability for medium-range TES applications.

In a related study, Xiao et al. [131] engineered a shape-stabilized composite PCM composed of 72.5 wt% sodium acetate trihydrate ($CH_3COONa \cdot 3H_2O$), 0.4 wt% disodium hydrogen phosphate (Na_2HPO_4), 17.1 wt% expanded graphite, and 10 wt% copper sulfide (CuS). The inclusion of Na_2HPO_4 promoted effective crystallization of the salt hydrate, while EG mitigated leakage, and CuS significantly enhanced the light-to-thermal energy conversion efficiency from 66.9% to 94.1%. This composite retained a high phase change enthalpy of 194.8 J/g and showed only minimal losses (5.9% in enthalpy and 2.6% in conversion efficiency) after 150 thermal cycles, marking it as a strong candidate for solar-driven TES systems.

I.5-Latent and hybrid thermal energy storage

I.5.1- Latent heat TES

Shell-and-tube heat exchangers are central components in LHTES systems, effectively utilizing PCMs to absorb and release energy during solid–liquid transitions. The melting process in these systems is predominantly governed by natural convection, which significantly affects heat transfer dynamics. Owing to their structural adaptability and thermal efficiency, shell-and-tube designs are extensively employed in applications that demand precise thermal regulation. Numerous studies have proposed enhancements to such configurations by altering the geometry of the shell, the tube, or both, to improve thermal performance. **Tables I.6** and **I.7** summarize selected investigations, categorizing them according to the specific shell and tube modifications applied.

I.5.2- Hybrid TES

Hybrid thermal storage systems incorporate PCMs into conventional water tanks to significantly boost their overall thermal storage capacity. By combining sensible heat and LHS mechanisms, these systems offer more efficient energy management across a wide range of applications, including residential heating, hot water supply, and industrial thermal processes. Current research efforts are directed toward designing innovative hybrid configurations that maximize thermal efficiency and responsiveness. **Tables I.8** and **I.9** provide an overview of numerical investigations on hybrid storage systems.

Table I. 6: Summary of studies that show shell-and-tube heat exchanger modifications involving geometrical alterations.

Authors	Geometry	Model Approach	PCM type	Main Research	Main Conclusions
Hu et al [132]		The enthalpy–porosity formulation	Paraffin	Enhancing melting heat transfer and minimizing TES time in frustum-shaped units using multi-PCM configurations	Minimizing TES duration using optimized frustum-shaped designs integrated with multi-PCM configurations
Rabienataj Darzi et al [133]	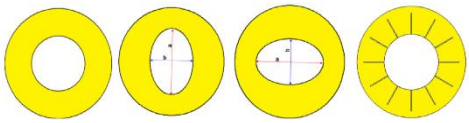	The enthalpy–porosity technique	N-eicosane	Boosting PCM heat transfer through annular design variations and nanoparticle enhancement for faster phase change	Enhanced PCM phase change performance using annular designs and nanoparticle integration
Dwi Korawan et al [134]	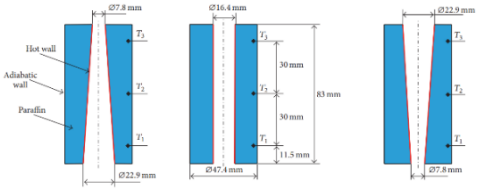	The enthalpy-porosity technique	Paraffin	3D Numerical Comparison of Paraffin Melting Across Various TES Configurations.	The nozzle-and-shell configuration exhibits the highest melting efficiency among the evaluated models
Faghani et al [135]	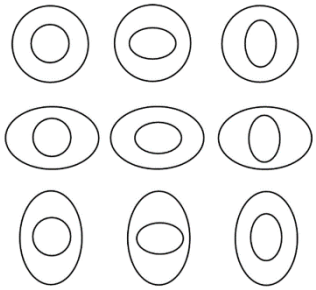	The enthalpy-porosity method	RT 25	Analysis of melting behavior in heat exchangers with elliptical geometries to identify optimal orientations for enhanced heat absorption	Comprehensive analysis reveals optimal heat absorption in elliptical-tube heat exchangers during melting

Table I. 7: (*continued*).

Authors	Geometry	Model Approach	PCM type	Main Research	Main Conclusions
Pourakabaret et al [136]	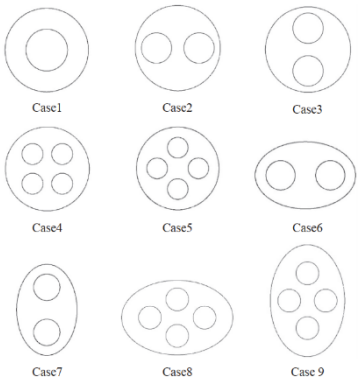	The enthalpy–porosity technique	N-eicosane	Investigation of PCM phase change in cylindrical containers with diverse inner tube layouts and copper foam enhancement	Different tube configurations affect melting rates, while copper foam enhances phase change speed but dampens natural convection, especially during melting
Kursun et al [137]	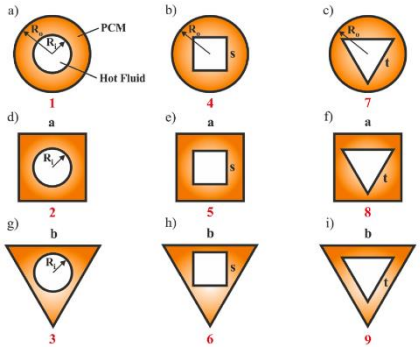	The enthalpy-porosity approach	N-eicosane	Enhancing energy storage efficiency in double-pipe TES systems via geometric optimization of inner and outer flow channels	Improved energy storage efficiency through optimized inner and outer channel geometries
Chatterjee et al [138]	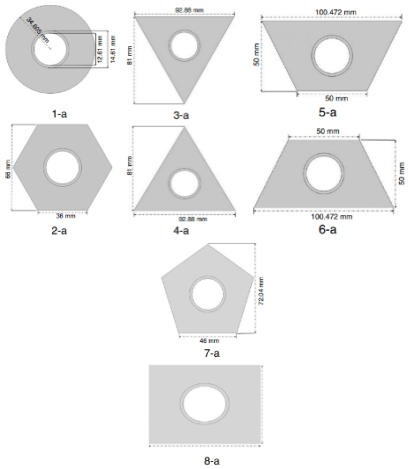	The heat capacity approach	lauric acid	Numerical analysis of cavity geometry and inner tube placement effects on PCM melting behavior to improve charging rates	Cavity geometry and optimal inner tube placement significantly affect the melting process, leading to improved charging rates

Table I. 8: Numerical studies on hybrid TES tanks.

Authors	Geometry	Dimension type	Solver	Subject
Wang et al. [139]	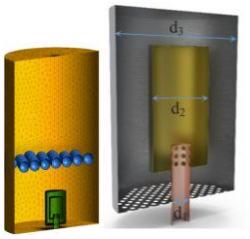	3D	The CFD commercial code Fluent 18	Assessment of inlet structure effects on thermal stratification in PCM-based heat storage tanks
Qin et al. [2]	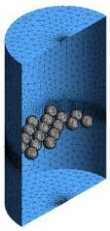	3D	The commercial CFD, code ANSYS 14.5	Investigation of PCM ball integration and its effects on thermal performance in hot water storage tanks
Fertahi et al [9]	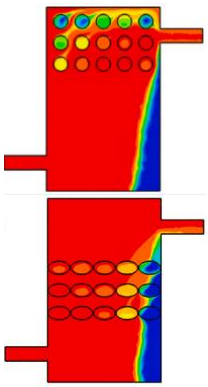	2D	OpenFOAM	The study explored PCM encapsulation using cylindrical and elliptical capsules within a vertical water storage tank
Bouhal et al [140]	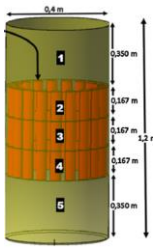	1D	The Fortran programming code	Examining the effect of PCM integration on water temperature distribution within the storage tank

Table I. 9: (*continued*).

Authors	Geometry	Dimension type	Solver	Subject
Feng et al [7]	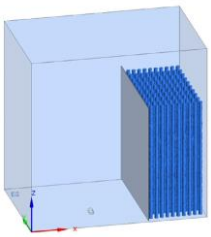	3D	FLUENT 19.0 software (ANSYS)	This study simulated a novel phase change water tank design featuring a vertical baffle
Feng et al [141]	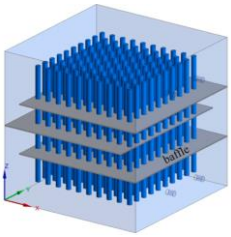	3D	Fluent software	Developed a latent heat storage tank incorporating baffles and two PCMs with distinct phase-change temperatures
Wu et al [142]	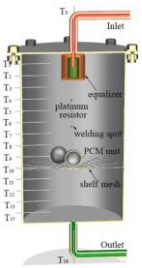	3D	Fluent 19.2	Evaluates the thermal stratification performance of a newly designed domestic hot water (DHW) tank equipped with a porous equalizer under varying operating conditions.

I.6-Applications of PCM in various fields

Thermal energy plays a critical role in a wide array of applications, ranging from power generation to maintaining optimal environmental conditions. TES systems are integral components in technologies that involve the generation or transfer of heat, offering tailored benefits depending on the application. These benefits include improved energy efficiency, reduced greenhouse gas emissions, effective load balancing, and enhanced thermal managementall contributing to safe and stable operation within required temperature ranges [143]. Given forecasts indicating a 28% rise in global energy demand by 2050 [144], PCMs have emerged as promising candidates for advanced TES systems. Numerous studies [76] have comprehensively evaluated the strengths and

limitations of PCMs, highlighting their advantages such as compactness, high latent heat capacity, excellent chemical stability, and notable energy storage density, as summarized in **Figure I.24**.

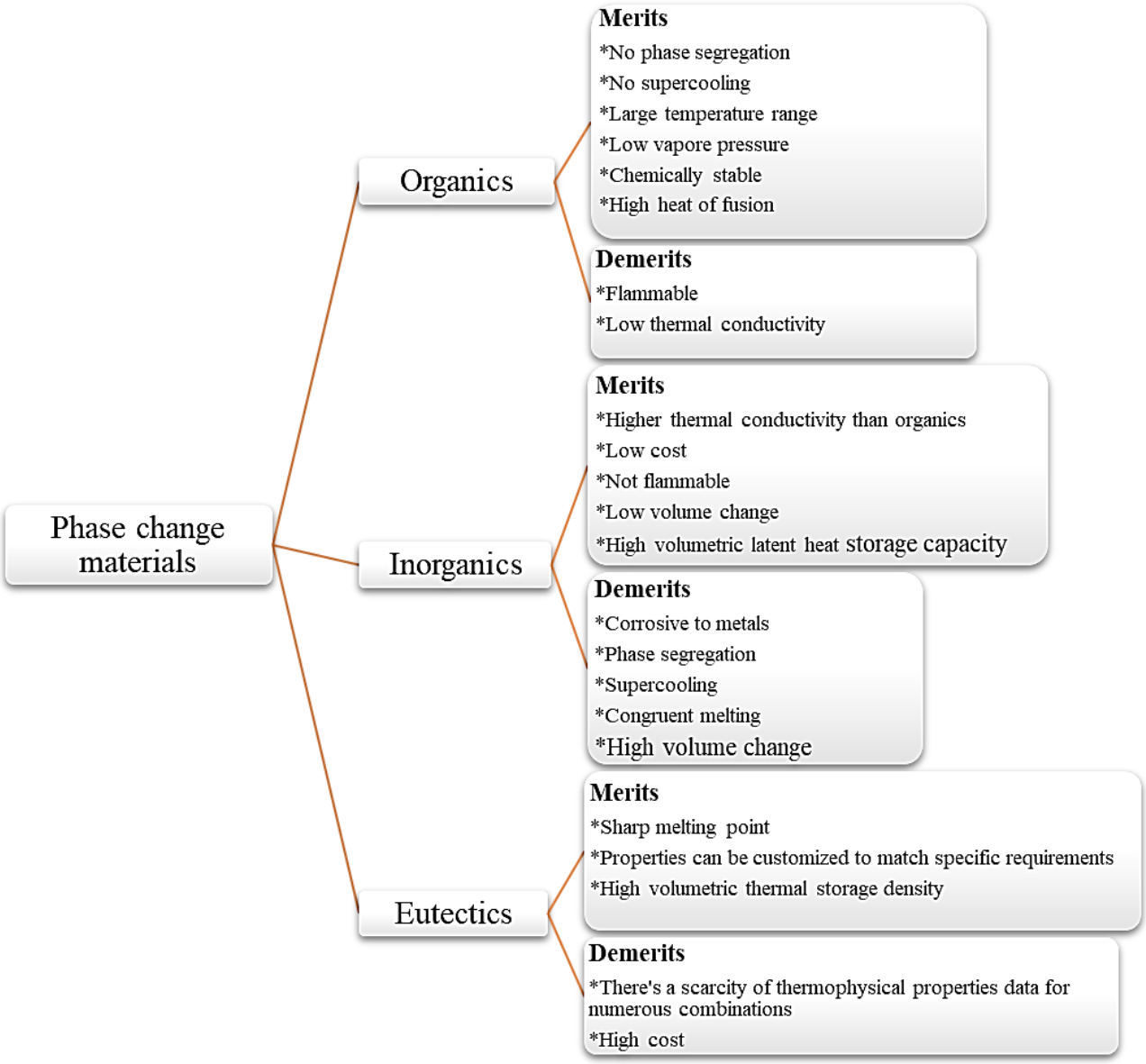

Figure I. 21: Overview of the merits and demerits of three distinct PCM categories [76], [145].

Due to their unique thermal properties, PCMs have been successfully integrated into a wide range of applications, including building energy management [146], food preservation [147], thermal energy storage systems [148], greenhouse agriculture [149], cooling and refrigeration technologies [150], smart textiles [151], solar thermal systems [152], heat sinks [153], battery thermal regulation [154], and waste heat recovery [155], as depicted in **Figure I.25**. This broad applicability

highlights the versatility of PCMs in addressing critical challenges in energy conservation, environmental sustainability, and climate resilience. In industrial settings, thermal energy is often generated intermittently and locally, making its immediate use challenging. To address this, efficient storage and redistribution strategies are essential [156]. For consumers located nearby, integrating LHTES into district heating systems offers a cost-effective and dependable solution for heat supply [157]. In contrast, for remote users, the concept of mobile LHTES units has emerged as a promising strategy, enabling the collection and transportation of low-grade industrial waste heat via specially designed vehicles [158]. By utilizing PCMs with high thermal energy density, these systems support the rapid deployment of district and mobile heating networks, enhancing the flexibility and efficiency of long-term thermal energy storage and distribution.

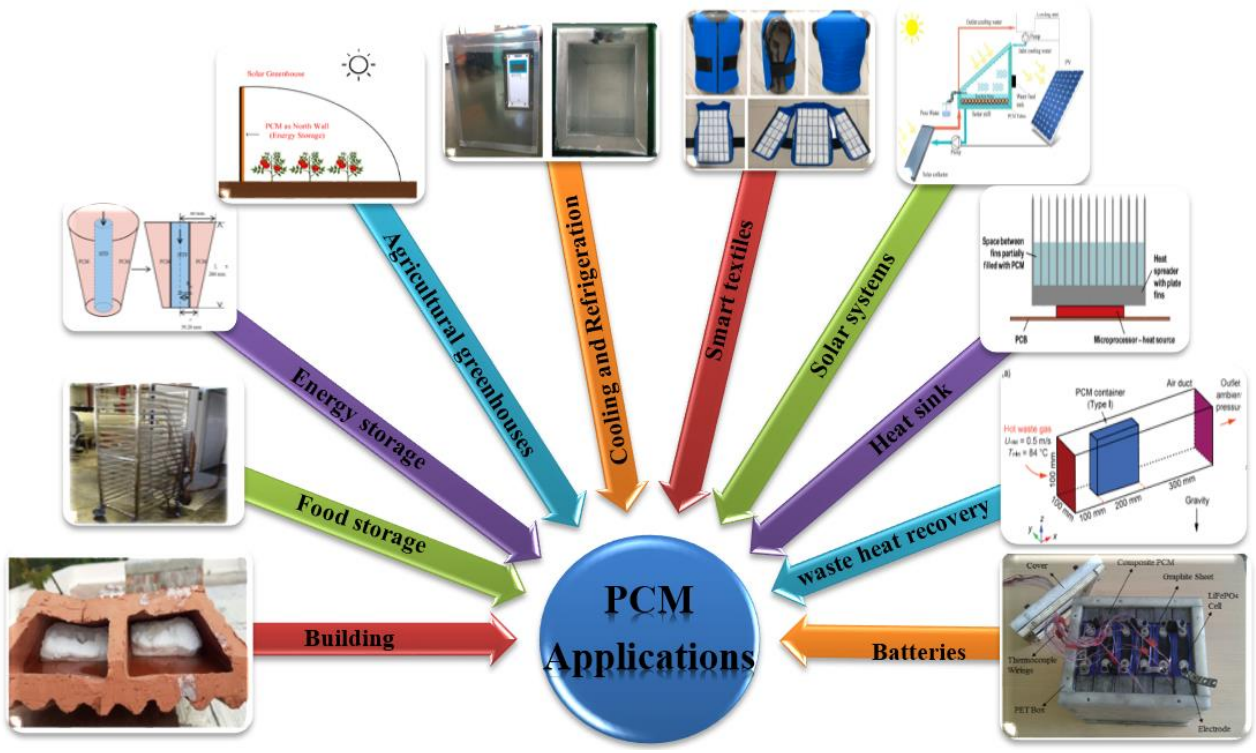

Figure I. 22 : Application of phase change materials.

I.7- Conclusion

This chapter highlights the vital role of PCMs in improving the performance of TES systems, especially in renewable energy applications. PCMs enable the storage of excess energy during peak generation and its release during high-demand periods, thereby enhancing grid stability and system reliability. The chapter offers a comprehensive overview of TES technologies, with a focus on latent heat storage due to its high energy density and minimal volume change, making it ideal for diverse thermal applications.

The integration of PCMs into hybrid TES systems combining sensible and latent heat storage further improves thermal performance and operational flexibility. Additionally, the chapter details the classification of PCMs, outlines the criteria for their selection across various temperature ranges, and explores their practical applications. To address inherent limitations such as low thermal conductivity and phase instability, advanced enhancement techniques such as finned structures, nanoparticle incorporation, and encapsulation are discussed. Finally, the importance of numerical simulation tools, including the enthalpy method and effective heat capacity approach, is emphasized for the accurate design and optimization of PCM-based TES systems, with precise meshing techniques highlighted as a key factor for achieving reliable simulation outcomes.

Chapter II. Mathematical Modeling and Numerical Methods for PCM-Based Thermal Energy Storage

II.1-Introduction

This chapter introduces the mathematical and numerical methods used to analyze PCMs in TES systems. Due to the complexity of phase change such as melting, solidification, and natural convection numerical simulation is a powerful alternative to experimental studies, offering flexibility and cost-efficiency.

The chapter presents the key governing equations and explores major numerical methods, including the finite difference method (FDM), finite volume method (FVM), finite element method (FEM), and lattice Boltzmann method (LBM). It also discusses thermal modeling approaches like the enthalpy method, enthalpy-porosity model, and heat capacity method. Additionally, the treatment of the mushy zone and the importance of mesh quality in simulations are highlighted. Commercial tools like ANSYS Fluent, often used in PCM research, are introduced for their capabilities in handling phase change processes.

II.2-Numerical simulations of PCMs

Numerical simulations serve as a foundational tool in the analysis of PCMs, offering a reliable, efficient, and cost-effective means of evaluating thermal performance. When investigating the behavior of PCMs in TES systems, it is essential to consider critical aspects such as the dynamics of the solid-liquid interface, conductive heat transfer in both solid and liquid phases, and the influence of liquid PCM flow on overall heat transfer performance [23]. To address these complex thermal processes, a variety of numerical approaches have been developed and applied in PCM research, particularly within solar energy applications. These include the enthalpy method, enthalpy-porosity technique, finite difference method (FDM), and finite volume method (FVM), each tailored to specific configurations and demands. Such methods have been effectively employed in a wide range of PCM-integrated systems, including photovoltaic panels, solar thermal collectors, and building envelopes [159].

II.2.1-Numerical Methods

II.2.1.1-Finite difference method

The finite difference method (FDM) is a classical numerical approach used for solving partial differential equations (PDEs) by discretizing the computational domain into a grid of discrete nodes. Within this framework, derivatives in the governing equations are approximated using finite differences, allowing the transformation of PDEs into solvable algebraic equations. FDM is especially known for its simplicity, high accuracy, stability, and fast convergence rates, making it a practical choice for problems requiring computational efficiency [160]. Although it is a conventional and effective technique, FDM is generally more suited for structured grids and regular geometries. While it can be adapted to irregular regions, this typically results in increased computational effort and complexity. Additionally, when applied to complex fluid flow and heat transfer scenarios, FDM may lack the robustness and flexibility of the FVM, which is often preferred in computational fluid dynamics due to its conservative formulation and better treatment of boundary conditions [27]. Nevertheless, FDM remains a valuable method, particularly in applications with simple geometries and where computational speed is a priority, as illustrated in **Figure II.1-(A)**.

II.2.1.2-Finite volume method

The finite volume method (FVM) is a widely utilized numerical approach for solving partial differential equations by transforming them into algebraic equations over discrete control volumes. In this method, the computational domain is subdivided into small control volumes, each centered around a computational node. One of the key strengths of FVM lies in its ability to ensure the conservation of mass, momentum, and energy across each control volume, which provides physical accuracy and stability to the solution process. FVM is particularly well-suited for handling complex geometries and is highly adaptable to unstructured meshes, making it an effective choice for problems involving irregular domains. This flexibility, combined with its conservation properties, renders the method especially effective in modeling phase change processes such as melting and solidification in LHTES systems. Moreover, FVM enhances computational efficiency while maintaining accuracy, avoiding numerical errors often associated with non-conservative schemes. Due to these advantages, the finite volume method (**Annex 5**) has

become the dominant numerical strategy in CFD and is employed as the foundational approach in commercial simulation tools such as ANSYS FLUENT [27] , as illustrated in **Figure II.1-(B)**.

II.2.1.3-Finite element method

The finite element method (FEM) is a powerful numerical technique that partitions the computational domain into discrete elements, often referred to as unit bodies. Within each element, nodes are strategically placed, and the governing differential equations are transformed into algebraic equations through weighted residual techniques and numerical integration. This method is especially well-suited for complex and irregular geometries, offering high flexibility in meshing and the ability to model intricate boundary conditions. Despite its versatility, FEM is often characterized by high computational demands, especially in large-scale simulations, due to the substantial number of elements and degrees of freedom involved. Furthermore, while FEM excels in structural mechanics and stress analysis, its application in fluid flow and heat transfer problems can present challenges, as the solution strategies for these domains are less mature compared to those established in the finite volume method (FVM). Nevertheless, FEM remains widely adopted in engineering and scientific disciplines for the simulation of structural deformation, thermal conduction, fluid dynamics, and electromagnetic fields. Its adaptability and robust mathematical foundation continue to make it a fundamental tool in numerical modeling, particularly for problems requiring high spatial accuracy [23], as illustrated in **Figure II.1-(C)**.

II.2.1.4-Lattice Boltzmann method

The Lattice Boltzmann Method (LBM) is a relatively modern CFD approach that has gained considerable attention in recent years for simulating complex fluid flow and heat transfer phenomena. Unlike conventional CFD techniques, which solve the macroscopic Navier–Stokes equations directly, LBM adopts a mesoscopic perspective, modeling the fluid as a collection of fictitious particles that propagate and interact on a discrete lattice grid through streaming and collision processes. This particle-based framework enables LBM to naturally handle complex boundary conditions, multiphase flows, and flows in porous media with enhanced computational efficiency. **Figure II.1-(D)** presents a visual depiction of a standard 2D lattice model. The standard LBM formulation is based on the discretization of the Boltzmann transport equation, and the evolution of particle distribution functions is governed by the lattice Boltzmann equation [161]:

$$g_i(x+\vec{c}_i\Delta t, t+\Delta t) = g_i(x,t) - \frac{1}{\tau_T}\left(g_i(x,t) - g_i^{eq}(x,t)\right) + R_i\Delta t \quad \text{(II.1)}$$

Here, τ_T denotes the relaxation time associated with the temperature field, while *Ri* represents the source term in the temperature distribution function.

LBM presents several compelling advantages over traditional numerical approaches, making it particularly attractive for simulating fluid flow and heat transfer in complex systems. Its explicit algorithmic structure simplifies the solution process by avoiding the need to solve large systems of nonlinear equations, instead relying on linear operations that facilitate ease of programming and implementation. Furthermore, the local nature of particle interactions and the method's inherent spatial uniformity make LBM especially well-suited for parallel computing architectures, enabling high computational efficiency in large-scale simulations [162]. In addition to these strengths, LBM demonstrates robust capabilities in handling intricate boundary conditions and is inherently flexible in simulating multiphase and multicomponent flows, as well as fluid-solid interactions frequently encountered in PCM applications. However, despite these advantages, several challenges persist in the application of LBM to phase change problems. One major limitation is the occurrence of deviation terms that arise when recovering the macroscopic governing equations particularly the energy equation from the mesoscopic LBM framework. These deviation terms can introduce accuracy and stability issues, especially in latent heat simulations where precise energy conservation is critical. Numerous studies have attempted to address these discrepancies by developing improved equilibrium distribution functions, modifying source term formulations, or implementing enthalpy-based LBM schemes [163].

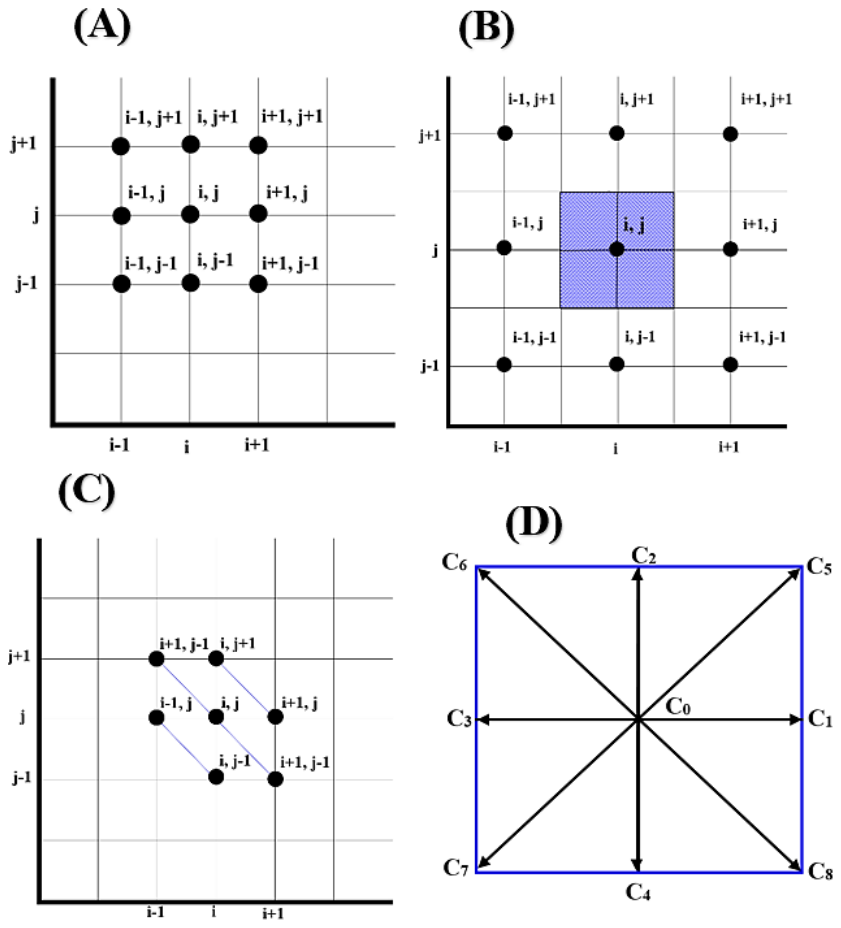

Figure II. 23 : CFD numerical approaches : (A)- Finite difference method; (B)-Finite volume method; (C)-Finite element method; (D)- LBM method (D2Q9 MODEL).

II.2.2-Thermal Modeling Techniques

II.2.2.1-Enthalpy method

The enthalpy method, initially proposed by Voller et al. [164] in 1987, is a widely used numerical approach for simulating phase change phenomena. It reformulates the energy conservation equation by expressing enthalpy as a function of temperature, thereby inherently incorporating both sensible and latent heat components into a single energy equation [165]. This unified formulation eliminates the need to explicitly track the solid-liquid interface, making the method particularly advantageous for simulating phase change in complex geometries and multi-dimensional domains

By calculating the enthalpy field throughout the computational domain, the method indirectly identifies the phase boundaries, thus significantly simplifying the modeling of phase transitions. Its versatility and computational stability have led to its broad adoption in TES applications, especially in systems using PCMs. Researchers have successfully utilized the enthalpy method to model temperature distribution, phase interface evolution, natural convection, and thermal diffusion during melting and solidification processes [166].

Furthermore, the transient form of the enthalpy method plays a critical role in accurately capturing the unsteady thermal behavior of PCMs, particularly in time-dependent storage and discharge cycles typical of solar energy and building applications [167]. Its robustness and simplicity continue to make it a preferred technique for simulating LHTES systems under various operational conditions.

The enthalpy method offers multiple advantages that contribute to its widespread use in simulating phase change problems. It enables fast computation when implemented with an appropriate numerical scheme and can effectively model both abrupt and gradual phase transitions. Its simplicity and scalability make it readily adaptable to various thermal applications, including complex multi-dimensional geometries and TES systems. Moreover, the method's unified treatment of energy conservation simplifies implementation by avoiding explicit tracking of the phase boundary.

Despite these strengths, the method is not without limitations. One key drawback is its inability to accurately model supercooling effects, which are present in many real-world PCMs. Additionally, the method may suffer from temperature oscillations at specific grid points over time, especially when coarse meshes are used. Such discretization can also lead to ambiguity in locating the phase change interface, reducing the accuracy of the phase boundary prediction. Another notable challenge is the uncertainty of thermophysical parameters in the mushy zone, where the phase is partially solid and partially liquid. Furthermore, the standard enthalpy method typically incorporates only heat conduction and latent heat absorption or release, neglecting the convective flow of melted PCM, which significantly affects the overall thermal performance of LHTES systems [168].

According to Voller et al.[169], the energy conservation during a melting or freezing process can be expressed as:

$$\frac{\partial H}{\partial t} = \nabla(k(\nabla T)) \tag{II.2}$$

Here, "H" represents the total volumetric enthalpy, and "k" denotes the thermal conductivity. The enthalpy "H" is a temperature-dependent function, described concerning the latent heat "L" and the local liquid fraction "$f(T)$" [169]:

$$H(T) = h(T) + \rho f(T) L \tag{II.3}$$

Where $h(T)$ denotes the sensible enthalpy, which is defined as follows:

$$h(T) = \int_{T_m}^{T} \rho C dT \tag{II.4}$$

In this equation, "T_m" denotes the reference isothermal phase change temperature characteristic of a given PCM. A critical component of equation (II.5) is the function "$f(T)$ ", which links the PCM's liquid fraction to its temperature. Under the assumption of an isothermal phase change where T=T_m and no temperature variation occurs during the phase transition $f(T)$, is defined using the Heaviside step function.

$$f(T) = \begin{cases} L, & \mathrm{T} > \mathrm{T}_m \\ 0, & T < T_m \end{cases} \tag{II.5}$$

Based on the governing equations, when the PCM undergoes a phase transition to the liquid state, the total volumetric enthalpy comprises both latent and sensible heat components. In contrast, if the PCM remains in the solid phase, the enthalpy is considered zero. By applying Equations (II.4) and (II.5), an alternative expression for heat transfer within the PCM domain can be formulated as follows:

$$\frac{\partial h}{\partial t} = \nabla.(\alpha \nabla h) - \rho L \frac{\partial f}{\partial t} \tag{II.6}$$

where α is the thermal diffusivity.

Fang et al. [170] employed the enthalpy method to model a shell-and-tube LTES system utilizing multiple PCMs. Their study underscored the critical impact of PCM fraction distribution and melting temperatures on both the system's TES capacity and the outlet temperature of the heat transfer fluid. The findings highlight the importance of precise PCM selection to optimize LTES system performance. Similarly, Basal et al. [171] conducted a numerical investigation of a novel triple concentric-tube thermal storage system with an annular PCM configuration, also using the enthalpy method. Their results demonstrate the system's improved thermal efficiency and emphasize the design sensitivity to PCM layer geometry, reinforcing the annular PCM's role in influencing key performance parameters. In a related study, Santos et al. [172] explored the solidification process around radial finned tubes, combining experimental work with a validated numerical code based on the enthalpy method. They developed empirical correlations for predicting interface characteristics during phase change, enabling rapid performance assessment of fin-enhanced solidification in PCM systems.

II.2.2.2.-Enthalpy-porosity method

The enthalpy-porosity method, extensively applied in heat transfer simulations involving PCMs, simplifies the modeling process by utilizing a fixed computational grid, eliminating the need for explicit tracking of the solid-liquid interface. Unlike traditional techniques that require continuous monitoring of the phase boundary, this method introduces the concept of the liquid fraction, which quantifies the proportion of the PCM in the liquid state within a control volume during the melting or solidification process [173]. The phase interface movement is thus captured indirectly through variations in the liquid fraction, which ranges from 0% (fully solid) to 100% (fully liquid) and is computed using an enthalpy balance [174]. This approach provides a continuous transition between solid and liquid phases, enhancing numerical stability and reducing computational complexity. The governing equations employed in the enthalpy-porosity model consist of the continuity, momentum, and energy conservation equations, which can be formulated as follows:

Continuity

$$Div(\rho U) = 0 \tag{II.7}$$

Momentum

$$\frac{\partial(\rho u)}{\partial t}+\nabla.(\rho u)=-\nabla p+\mu\nabla^2 u-\rho_0\beta(T-T_{ref})+S \tag{II.8}$$

Energy

$$\frac{\partial(\rho H)}{\partial t}+\nabla.(\rho uH)=k\nabla^2 T-\rho L_f\frac{\partial f}{\partial t} \tag{II.9}$$

II.2.2.2.1-Cylindrical

The governing equations in **3D cylindrical** coordinates can be expressed as follows:

1. **Continuity**

$$\frac{1}{r}\frac{\partial(r\rho u_r)}{\partial r}+\frac{1}{r}\frac{\partial(\rho u_\theta)}{\partial\theta}+\frac{\partial(\rho u_z)}{\partial z}=0 \tag{II.10}$$

2. **Momentum**

The radial component of the momentum conservation equations is given by the following expression:

$$\frac{\partial u_r}{\partial t}+u_r\frac{\partial u_r}{\partial r}+\frac{u_\theta}{r}\frac{\partial u_r}{\partial\theta}-\frac{u_\theta^2}{r}+u_z\frac{\partial u_r}{\partial z}=-\frac{1}{\rho}\frac{\partial p}{\partial r}+\nu\left[\begin{array}{l}\frac{1}{r}\frac{\partial}{\partial r}\left(r\frac{\partial u_r}{\partial r}\right)\\-\frac{u_r}{r^2}+\frac{1}{r^2}\frac{\partial^2 u_r}{\partial\theta^2}\\-\frac{2}{r^2}\frac{\partial u_\theta}{\partial\theta}+\frac{\partial^2 u_r}{\partial z^2}\end{array}\right]+A_m\frac{(1-f)^2}{(f^3+\delta)}u_r \tag{II.11}$$

The momentum conservation equations projected in the circumferential (θ) direction are expressed as follows:

$$\frac{\partial u_\theta}{\partial t}+u_r\frac{\partial u_\theta}{\partial r}+\frac{u_\theta}{r}\frac{\partial u_\theta}{\partial\theta}+\frac{u_\theta u_r}{r}+u_z\frac{\partial u_\theta}{\partial z}=-\frac{1}{\rho r}\frac{\partial p}{\partial\theta}+\nu\left[\begin{array}{l}\frac{1}{r}\frac{\partial}{\partial r}\left(r\frac{\partial u_\theta}{\partial r}\right)\\-\frac{u_\theta}{r^2}+\frac{1}{r^2}\frac{\partial^2 u_\theta}{\partial\theta^2}\\+\frac{2}{r^2}\frac{\partial u_r}{\partial\theta}+\frac{\partial^2 u_\theta}{\partial z^2}\end{array}\right]+A_m\frac{(1-f)^2}{(f^3+\delta)}u_\theta \tag{II.12}$$

The axial component of the momentum conservation equations is expressed as follows:

$$\frac{\partial u_z}{\partial t}+u_r\frac{\partial u_z}{\partial r}+\frac{u_\theta}{r}\frac{\partial u_z}{\partial \theta}+u_z\frac{\partial u_z}{\partial z}=-\frac{1}{\rho}\frac{\partial p}{\partial z}-g\beta(T-T_{ref})+\nu\begin{bmatrix}\frac{1}{r}\frac{\partial}{\partial r}\left(r\frac{\partial u_z}{\partial r}\right)\\+\frac{1}{r^2}\frac{\partial^2 u_z}{\partial \theta^2}\\+\frac{\partial^2 u_z}{\partial z^2}\end{bmatrix}+A_m\frac{(1-f)^2}{(f^3+\delta)}u_z \quad \text{(II.13)}$$

3. Energy

$$\frac{\partial T}{\partial t}+u_r\frac{\partial T}{\partial r}+\frac{u_\theta}{r}\frac{\partial T}{\partial \theta}+u_z\frac{\partial T}{\partial z}=\frac{\lambda}{\rho C_P}\left(\frac{1}{r}\frac{\partial}{\partial r}\left(r\frac{\partial T}{\partial r}\right)+\frac{1}{r^2}\frac{\partial^2 T}{\partial \theta^2}+\frac{\partial^2 T}{\partial z^2}\right)-\rho L_f\frac{\partial f}{\partial t} \quad \text{(II.14)}$$

The phase transitions of the PCM are determined by employing enthalpy as a key governing parameter [175]:

$$\frac{\partial(\rho \mathrm{H})}{\partial t}+\nabla.\left(\rho u \mathrm{H}\right)=k\nabla^2-\rho L_f\frac{\partial f}{\partial t} \quad \text{(II.15)}$$

The enthalpy function is formulated by integrating the temperature-dependent latent heat of phase transition with the sensible heat capacity, and is expressed as:

$$\begin{cases}H=h+\Delta H,\\ h=h_{ref}+\int_{T_{ref}}^{T_{solid}}C_P dT\\ \Delta H=fL_f\end{cases} \quad \text{(II.16)}$$

$$f=\begin{cases}0, & \mathrm{T}<\mathrm{T}_{solid}\\ \dfrac{T-T_{solid}}{T_{liquid}-T_{solid}}, & T_{solid}\le T\le T_{liquid}\\ 1 & T\ge T_{liquid}\end{cases} \quad \text{(II.17)}$$

In these equations, the variables represent the following parameters: h_{ref} denotes the sensible enthalpy of PCM at the reference temperature T_{ref}, f is the liquid fraction, ρ is the density, k represents thermal conductivity, μ is for dynamic viscosity, u is velocity, T represents temperature,

P represents pressure, H is specific enthalpy, g denotes gravitational acceleration, and δ is a small value introduced to prevent division by zero.

Lee et al. [176] employed the enthalpy-porosity method to investigate the melting behavior of PCMs within a cold thermal energy storage (CTES) tank equipped with internal fins. By combining numerical simulations with experimental validation, the study evaluated the influence of various fin configurations. Notably, a stratified fin design was proposed, which significantly enhanced the average power output by 156.3%, demonstrating its strong potential for improving CTES system performance. Similarly, Bouzennada et al. [177] applied the enthalpy-porosity method to assess the thermal performance of RT-27 PCM contained within a rectangular capsule featuring fins inclined at 0°, 45°, and 90°. The results revealed that decreasing the fin inclination angle accelerated the melting process and improved energy storage efficiency, with melting time reductions ranging from 1.28% to 20.52% and energy storage enhancements between 14.75% and 36.88%. Among the tested configurations, the horizontal fin at 0° demonstrated the highest thermal performance. In another study, Xu et al. [178] analyzed a horizontal latent thermal energy storage (LTES) system incorporating triplex-layer PCMs and metal fins, using the enthalpy-porosity method. A novel Composite Solid–Diffusion–Enthalpy (CSDE) criterion was introduced to evaluate the melting efficiency. Their optimized fin configurations led to a melting time reduction of up to 71%, offering valuable design insights for enhancing LTES systems.

II.2.2.3-Heat capacity method

In the apparent heat capacity method, the heat capacity of the material is modeled as a temperature-dependent function over the phase change interval. This approach effectively incorporates the latent heat by treating it as a significantly elevated apparent heat capacity within a narrow temperature range around the phase transition point. Consequently, the phase change process is reformulated as a nonlinear thermal conduction problem within a single computational domain. The governing energy equation is established across the entire region, with temperature as the only primary variable to be solved. This method simplifies the numerical procedure, eliminates the need to explicitly track the moving phase front, and enhances the ease and efficiency of computations, making it particularly suitable for complex geometries and multi-dimensional simulations [179]. The effective heat capacity, $C_{P,eff}$, can be defined as a temperature-dependent function, expressed as:

$$C_{P,eff}(T) = \frac{1}{\rho}\frac{\partial h}{\partial T} \tag{II.18}$$

Here, $C_{P,eff}$ denotes the effective heat capacity, which includes both sensible and latent heat components.

By applying Equation (II.19), a heat transfer equation can be derived using the effective heat capacity approach to account for the phase change within the thermal analysis:

$$\rho C_{P,eff}\frac{\partial T}{\partial t} = \nabla.(k\nabla T) \tag{II.19}$$

Han et al. [180] conducted numerical simulations using the apparent heat capacity method to analyze the thermal charging and discharging behavior of phase change microcapsules with multi-cavity structures. Their findings showed that a higher number of cavities notably enhances the rates of both heat storage and release. In a related study, Artinov et al. [181] analyzed the impact of latent heat on the temperature distribution using the sensible heat capacity method, illustrating how the inclusion of latent heat effects can alter the thermal response and evolution of the temperature field.

II.2.2.4- Molecular dynamics simulation

Molecular Dynamics Simulation (MDS) is a robust computational method used to study atomic and molecular interactions at the nanoscale. First introduced by Alder and Wainwright in 1950, MDS solves Newton's laws of motion to track the dynamic behavior of atoms and molecules over time within a virtual system [25]. Through these simulations, researchers can investigate a wide range of properties including molecular structure, thermodynamic behavior, chemical reactivity, and material performance across various applications [182].

Because of the rapid nature of atomic movements, MDS generally require extremely small-time steps on the order of femtoseconds (10^{-15} s) to accurately model the system's behavior. The interactions between atoms are determined through interatomic potentials or molecular mechanics force fields, enabling the calculation of potential energy surfaces and the resulting atomic trajectories. These principles are essential for generating simulations that closely replicate actual physical processes. [183].

In the context of nano-enhanced phase change materials (NePCMs), MDS is particularly advantageous for exploring thermophysical properties that may be difficult to measure experimentally. Although uncertainties can arise due to variable influencing factors, MDS provides valuable insights into the thermal behavior, structural stability, and energy storage potential of NePCMs, thereby complementing experimental and continuum-scale models [25].

Zhao et al. [184] explored the influence of CuO nanoparticles on the melting enthalpy of paraffin-based PCMs through MD simulations (**Figure II.2**). Their findings revealed a substantial reduction in latent heat with increasing nanoparticle concentrations, reporting a 51.5% decrease in melting enthalpy at 19.72 wt.% CuO content. The primary mechanisms identified were the strong interfacial interactions between nanoparticles and paraffin molecules, along with the formation of a dense, structured paraffin layer surrounding the nanoparticles. These interactions restricted molecular mobility and phase transition dynamics, thereby diminishing the effective heat storage capacity of the composite.

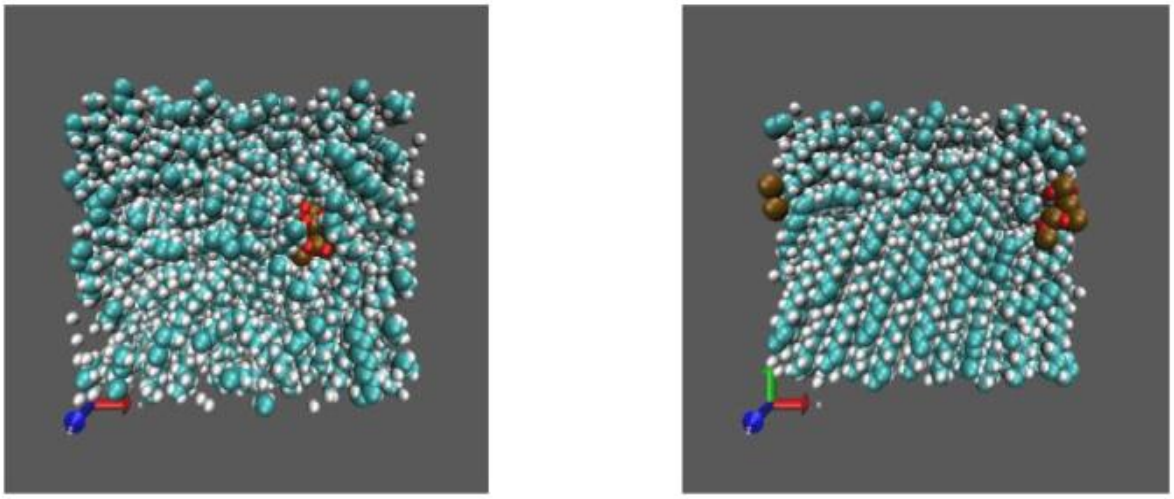

Figure II. 24 : Molecular distribution states in PCM simulation systems: Visualization of carbon and hydrogen atoms (cyan and white, respectively), along with copper and oxygen atoms (ochre and red, respectively) [184].

II.3- Mushy Zone and Mesh Quality

II.3.1- Mushy Zone

The mushy region a transitional zone between the fully solid and fully liquid states of PCMs represents a semi-solid state during phase transitions [185]. A critical parameter used to characterize this region is the mushy zone constant (A_{mush})**,** which governs the rate at which the fluid velocity decreases as the PCM solidifies[132]. A higher value of A_{mush} corresponds to a faster decline in velocity during solidification, significantly affecting the accuracy of heat transfer predictions during both melting and freezing processes [186].

Soliman et al. [187] numerically analyzed the melting behavior of paraffin wax in capsules of varying geometries (circular, vertical oval, and horizontal oval) at an ambient temperature of 27 °C. Their results revealed that A_{mush} significantly influences heat transfer characteristics, with optimal values identified as 2×10^6 for circular, 1×10^5 for vertical oval, and 1×10^6 for horizontal oval geometries. These findings demonstrate that the selection of A_{mush} is geometry-dependent, influencing fluid dynamics and the rate of phase change.

In another investigation, Hameter et al. [188] studied LHTES systems utilizing sodium nitrate ($NaNO_3$) as PCM. By varying the A_{mush} from 10^5 to 10^8, they observed notable differences in melting and solidification behavior. Specifically, higher values of C extended the phase transition period and altered the morphology of the melting front, shifting it vertically due to changes in convective flow dynamics.

Fadl et al. [8] explored the phase change of Lauric acid in both vertical and horizontal enclosures, emphasizing the role of A_{mush} in shaping the solid–liquid interface, affecting heat transfer efficiency and TES capacity (**Figure II.3**). Their study highlighted the necessity of careful calibration of A_{mush} to ensure accurate simulation of LHTES systems, as inappropriate values may lead to misrepresentation of interface dynamics and energy performance

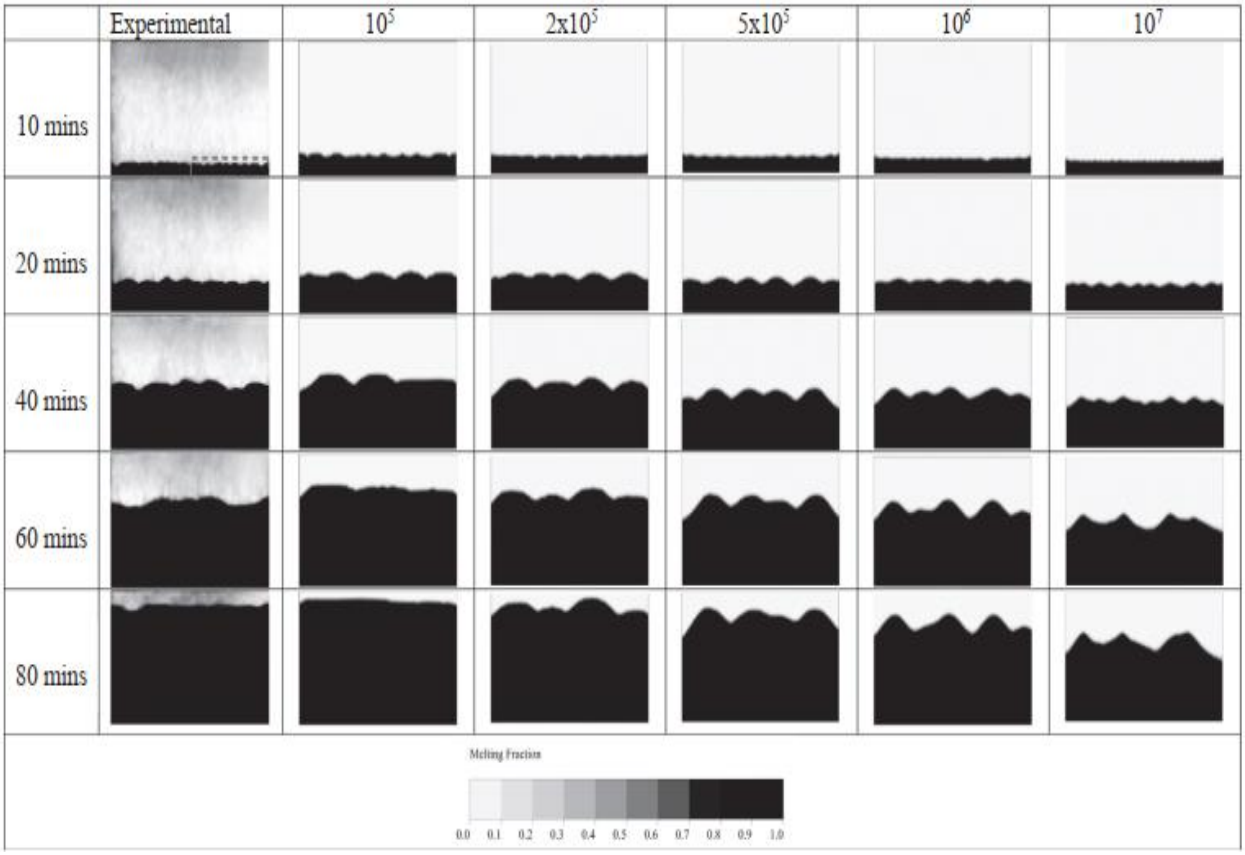

Figure II. 25 : Solid\liquid interface comparison for different A_{mush} values [8].

II.3.2-Mesh Quality

To optimize the use of computational resources and time, it is essential to implement a high-quality mesh that ensures both numerical accuracy and cost-efficiency. The quality of the mesh can be evaluated using three key indicators, each measured on a normalized scale from 0 to 1, where values closer to 1 indicate superior mesh quality [189]:

1. **Skewness**, which reflects the degree of distortion in cell shapes, should be kept as low as possible ideally with an average value below 0.7. An illustration of skewness values and corresponding cell quality is provided in **Table II.1**.

Table II. 1: Skewness values and cell quality [190].

Value of skewness	Cell quality
1	Degenerate
0.9 - <1	Bad
0.75 - 0.9	Poor
0.5 - 0.75	Fair
0.25 - 0.5	Good
>0 - 0.25	Excellent
0	Equilateral

2. **Orthogonal quality**: This metric ranges from 0 to 1, where a value of 0 indicates poor mesh quality, and 1 represents optimal quality. High orthogonal quality is essential for minimizing numerical errors and enhancing solution accuracy in CFD simulations.
3. **Element quality**: This indicator also spans from 0 to 1 and evaluates the overall shape and distortion of mesh elements. A value close to 1 (ideally ≥ 0.9) is desirable, as it signifies well-shaped elements that contribute to stable and accurate numerical computations.

For 2D simulations, equilateral triangles yield optimal mesh quality in triangular meshing, while squares are preferred for quadrilateral meshing. In 3D studies, the use of regular tetrahedra and hexahedra is recommended, as these shapes offer better uniformity and computational performance in capturing physical phenomena within PCM systems.

ANSYS Fluent is widely employed in PCM studies due to its robust computational capabilities and its strong agreement with experimental validation results. In most investigations, a pressure-based solver is utilized to model single-phase PCM systems, with the solidification/melting model activated to simulate the phase transition process. Moreover, Fluent offers flexibility through the integration of User-Defined Functions (UDFs), typically written in C++, allowing researchers to customize material properties and extend physical models to better represent complex thermal behaviors in PCM systems. In **Annex 1-(A)**, **(B)**, a flowchart outlines the step-by-step numerical solution procedure adopted for simulating the PCM melting process.

II.4- Performance Evaluation Parameters

II.4.1- Hybrid Thermal Energy Storage (Tank Systems)

- **Richardson number (*Ri*)**

When analyzing thermal stratification in a water tank under different conditions, the Richardson number (Ri) is used. The Ri measures the buoyancy force to shear forces, where a high Ri indicates a more stratified water tank and a low Ri suggests a well-mixed tank. Ri is calculated using Equation (II.20) [206].

$$Ri = \frac{g\beta H\left(T_t - T_b\right)}{v_s^2} \tag{II.20}$$

where,

$$v_s = \frac{Q}{\pi r^2} \tag{II.21}$$

where, β is denotes the thermal expansion coefficient (*1/K*), Q represents the volumetric flow rate (m^3/s), v_s is the average velocity of the water at the inlet (*m/s*) of the water at the inlet, and *r* is the inlet radius (*m*).

- **Thermal storage efficiency (η)**

The thermal storage efficiency, represented by η, is analyzed under various operating conditions to evaluate the performance of the PCM tank. As described in Equation (II.22), thermal storage efficiency is calculated as the ratio of the energy effectively stored during a given period to the maximum heat capacity of the water tank [207]:

$$\eta = \frac{\rho C_P V\left(T_W - T_{ini}\right)}{\rho C_P V\left(T_{inlet} - T_{ini}\right)} \tag{II.22}$$

- **Economic performance index (P_c)**

The economic index P_c, as defined in Eq. (IV.23) [211], signifies the heat storage efficiency of materials relative to their cost over a specified period.

$$P_c = \frac{Q}{t_m C_{total}} = \frac{Q_{latent} + Q_{sensible}}{t_m C_{total}} \quad \text{(IV.23)}$$

where,

$$Q_{latent} = m_{PCM} L_{PCM} \quad \text{(IV.24)}$$

$$Q_{sensible} = \dot{m}_{Water} \times C_{P_{Water}} \times \left(T_{in} - \left(\frac{T_{out}^{k-1} + T_{out}^{k}}{2} \right) \right) \quad \text{(IV.25)}$$

In the given Eqs. (IV.24) [211], and (IV.25)[4], the Q_{latent} represents the TES capacity of the PCM, while, $Q_{sensible}$ denotes the sensible heat storage capacity of water. T_{in} and T_{out} correspond to the inlet and outlet temperatures of the water, respectively, and $\dot{m}_{water}$ is the mass flow rate of water entering the storage tank. Additionally, $C_{P_{water}}$refers to the specific heat capacity of water within the storage tank.

The total cost (C_{total}) was calculated by summing the expenses of the PCM and the aluminum components used in the tank design. The correlation applied for this calculation is expressed as:

$$C_{total} = C_{PCM} + C_{Al} \quad \text{(IV.26)}$$

$$C_{PCM} = m_{PCM} C'_{PCM} \quad \text{(IV.27)}$$

$$m_{PCM} = \rho_{PCM} V_{PCM} \quad \text{(IV.28)}$$

$$C_{Al} = m_{Al} C'_{Al} \quad \text{(IV.29)}$$

For Tank 01

$$m_{Al} = \rho_{Al} V_{Al} = \rho_{Al} S_L e = \rho_{Al} \left(S_{\mathrm{Tan}k} + S_{PCM} \right) e \quad \text{(IV.30)}$$

For Tank 02 ~ 06

$$m_{Al} = \rho_{Al} V_{Al} = \rho_{Al} S_L e = \rho_{Al} \left(S_{\mathrm{Tan}k} + S_{PCM} \right) e + V_{Baffle} \quad \text{(IV.31)}$$

Where, S_L is the lateral surface area of the Tank and PCM cylinders, and e is the aluminum thickness, V_{Baffle} is the volume of the baffle.

II.4.2-PCM Shell-and-Tube Heat Exchanger

- **Thermal Energy Storage (*Q*)**

The energy stored during the phase change process, known as latent heat, represents a key component of TES. The stored energy of the PCM and the overall energy capacity of the TES system can be calculated using the formulation provided in [232].

$$Q = m\left(\int_{T_{ini}}^{T_m} C_{P,l}\,dT + f\,\Delta H + \int_{T_m}^{T_{f,PCM}} C_{P,s}\,dT \right) \tag{VI.32}$$

In this equation, m represents the mass of the PCM (kg), T_{ini} is the initial temperature of the PCM (K), T_m is the melting temperature, and $T_{f,PCM}$ is the average temperature of the PCM after the melting process is completed (K). The variable f indicates the liquid fraction, while ΔH is the latent heat of fusion (kJ/kg). Additionally, $C_{P,s}$ and $C_{P,l}$ correspond to the specific heat capacities of the PCM in the solid and liquid phases (kJ/kg. K), respectively. The equation consists of three terms: the first represents the sensible heat stored in the solid phase, the second accounts for the latent heat absorbed during melting, and the third reflects the sensible heat stored in the liquid phase.

- **Nusselt Number (*Nu*)**

The Nusselt number accounts for both conductive and convective heat transfer effects across the entire heated boundary. It is defined as follows [233]:

$$Nu = \frac{q'' D_h}{k\left(T_{wall} - T_{PCM}(t)\right)} \tag{VI.33}$$

In this equation, q'' denotes the heat flux (W/m^2), D_h is the hydraulic diameter (m), k represents the thermal conductivity of PCM (W/m.K), T_{wall} is the wall temperature (K), and $T_{PCM}\ (t)$ refers to the time dependent temperature of the PCM (K). This formulation enables the assessment of heat transfer efficiency at the heated surface by incorporating key parameters such as the applied heat flux, geometric characteristics, material thermal properties, and temperature gradients.

-

- **Economic performance index (P_c)**

Similar to hybrid TES but adapted to shell-and-tube geometry, including material costs for PCM and aluminum.

II.5-Conclusion

This chapter provided a comprehensive overview of the mathematical modeling and numerical methods employed in simulating phase change processes within thermal TES systems using PCMs. Various numerical techniques, such as the finite difference, finite volume, finite element, and lattice Boltzmann methods, were discussed in terms of their strengths, limitations, and application contexts. Additionally, thermal modeling strategies, including the enthalpy method, enthalpy-porosity model, and heat capacity method were analyzed for their ability to accurately capture phase transitions.

Key aspects such as mesh quality and the treatment of the mushy zone were also addressed, given their critical role in ensuring accurate and stable numerical results. The insights from this chapter form the theoretical and computational foundation for the simulation work presented in the subsequent chapters, facilitating the evaluation and optimization of PCM-based TES configurations.

Part A
Hybrid Thermal Energy Storage Systems

A.1.Validation of the Hybrid Thermal Energy Storage Models

Before presenting the numerical analysis in Chapters III and IV, it is essential to validate the computational models against experimental results to ensure the reliability of the adopted methodology. Two sets of validation studies were performed: (i) for Chapter III numerical analysis of varying aspect ratios (*L/D*) in a hybrid TES tank, and (ii) for Chapter IV enhancing thermal storage efficiency in hybrid tanks with baffle design. The following subsections summarize the validation results.

A.1.1-Validation of Hybrid TES Tank (Chapter III)

This subsection presents the validation results corresponding to Chapter III, focusing on the numerical analysis of hybrid TES tanks with varying aspect ratios (*L/D*). **Figure A.1** presents a comparison of temperature measurements at the lower parts of the TES tank (measurement points 9 and 10, as shown in **Figure III.5**) using PCM, with a flow rate of 10 L/h and inlet temperatures of 75 °C for melting and 25 °C for solidification, during both charging and discharging phases. The results indicate discrepancies between the experimental and simulation data, with maximum errors of 7.5% and 6.56% at measurement points 9 and 10, respectively, assuming identical initial temperatures for both simulation and experimental scenarios. These differences are likely due to the idealized conditions in the simulation, which may not completely replicate the actual experimental conditions. Nonetheless, the overall temperature trends in both the simulation and experiment are consistent, demonstrating the reliability of the numerical method employed in the current study.

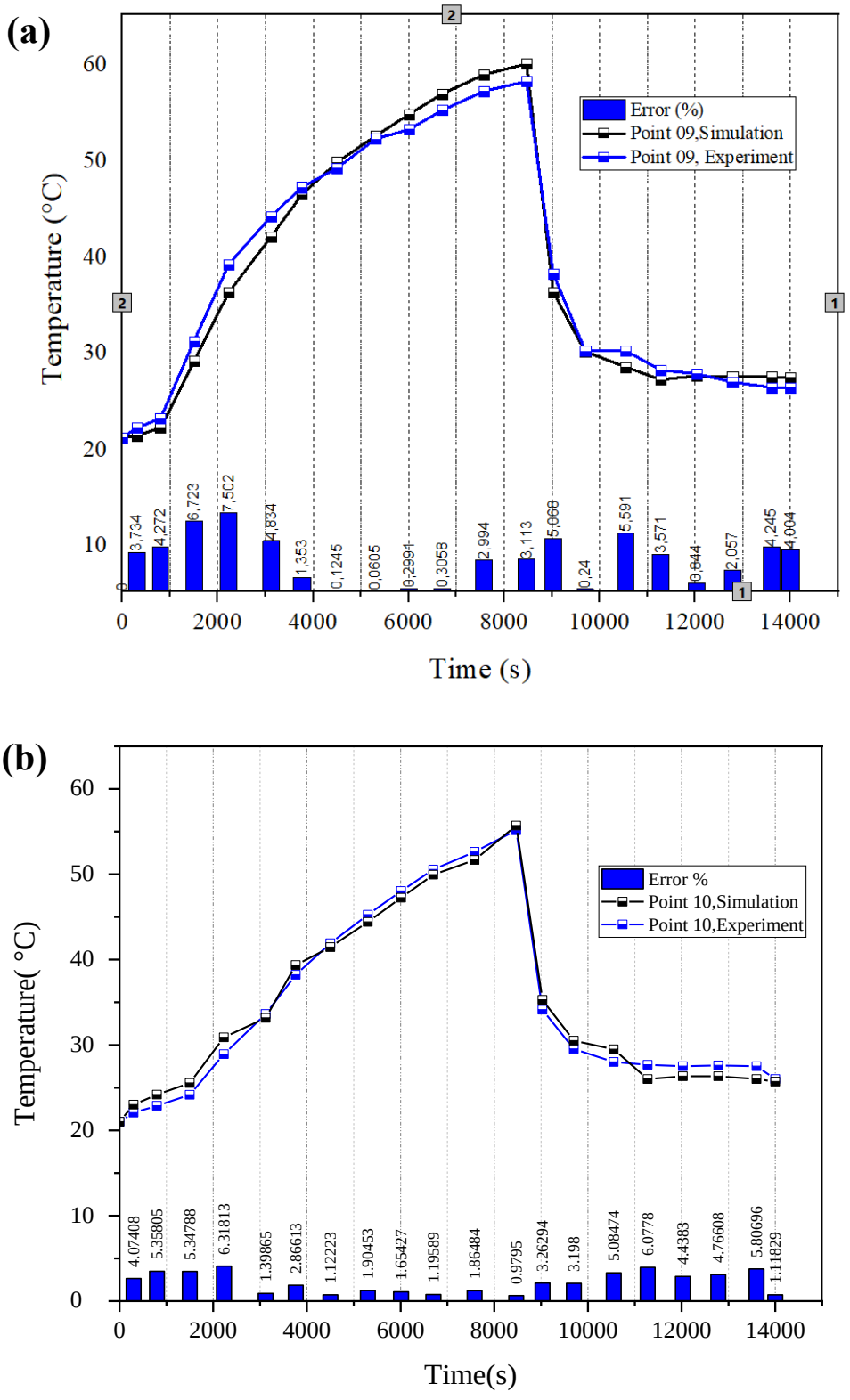

Figure A.1 : Experimental [191] and CFD results for the temperature of charging and discharging stage (A) point 09, (B) point 10.

A.1.2-Validation of PCM Tank with Baffles (Chapter IV)

This subsection details the validation results corresponding to Chapter IV. **Figure A.2-(A), (B),** and **(C)** compare experimental temperature data from Ref. with simulated results at three key locations (points 1, 3, and 5) within the PCM-based thermal storage tank. The tests were conducted at a flow rate of 10 L/h and an inlet temperature of 75°C. The figures illustrate the relative error between experimental and simulated values, with maximum discrepancies of 8.87%, 8.95%, and 8.91% observed at points 1, 3, and 5, respectively. Conversely, the minimum errors at these points were 4.054%, 4.021%, and 2.24%, respectively. Despite these discrepancies, the overall temperature variation patterns observed in the simulation closely mirrored those of the experimental data. The relative errors indicate a good level of agreement between the numerical method employed in this study and the actual experimental measurements. The consistency in temperature trends between the simulation and experimental data reinforces the reliability of the adopted numerical approach. These findings indicate that the method is robust and effectively captures the key thermal behavior within the PCM-based TES tank. Although minor localized deviations were observed, the overall agreement between the simulated and experimental results supports the validity and credibility of the developed computational model.

It is essential to clarify the interpretation of 'error' in this context. The 'true value' refers to the idealized experimental data, which inherently includes potential uncertainties such as measurement inaccuracies. This analysis focuses on assessing the agreement between numerical predictions and experimental observations, considering the limitations of both approaches. Notably, the absolute temperature differences ($|\Delta T|$) between simulated and experimental values remain within 6 K (**Figure A.2-(D)**), demonstrating a high level of consistency and highlighting the accuracy and reliability of the computational model in capturing the system's thermal behavior.

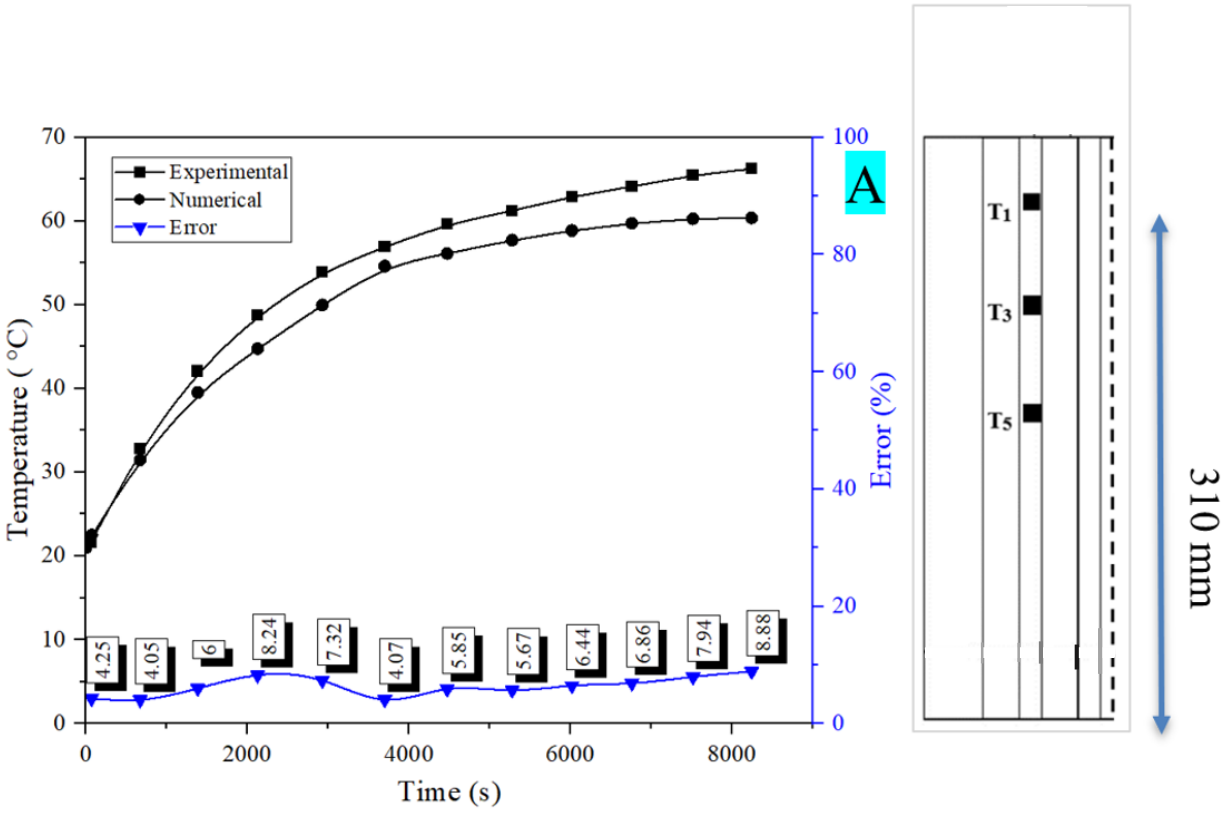
A
Experimental
Numerical
Error
Temperature (°C)
Error (%)
Time (s)
4.25
4.05
6
8.24
7.32
4.07
5.85
5.67
6.44
6.86
7.94
8.88
T1
T3
T5
310 mm

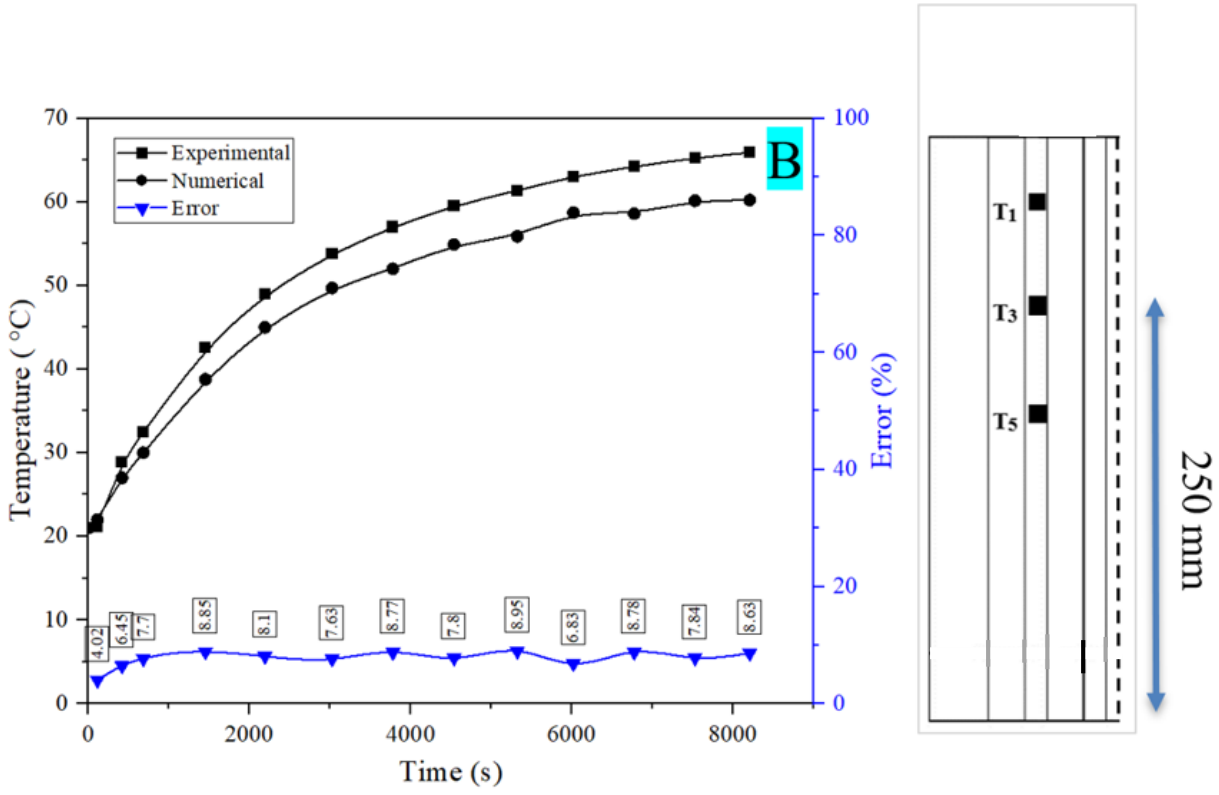
B
Experimental
Numerical
Error
Temperature (°C)
Error (%)
Time (s)
4.02
6.45
7.7
8.85
8.1
7.63
8.77
7.8
8.95
6.83
8.78
7.84
8.63
T1
T3
T5
250 mm

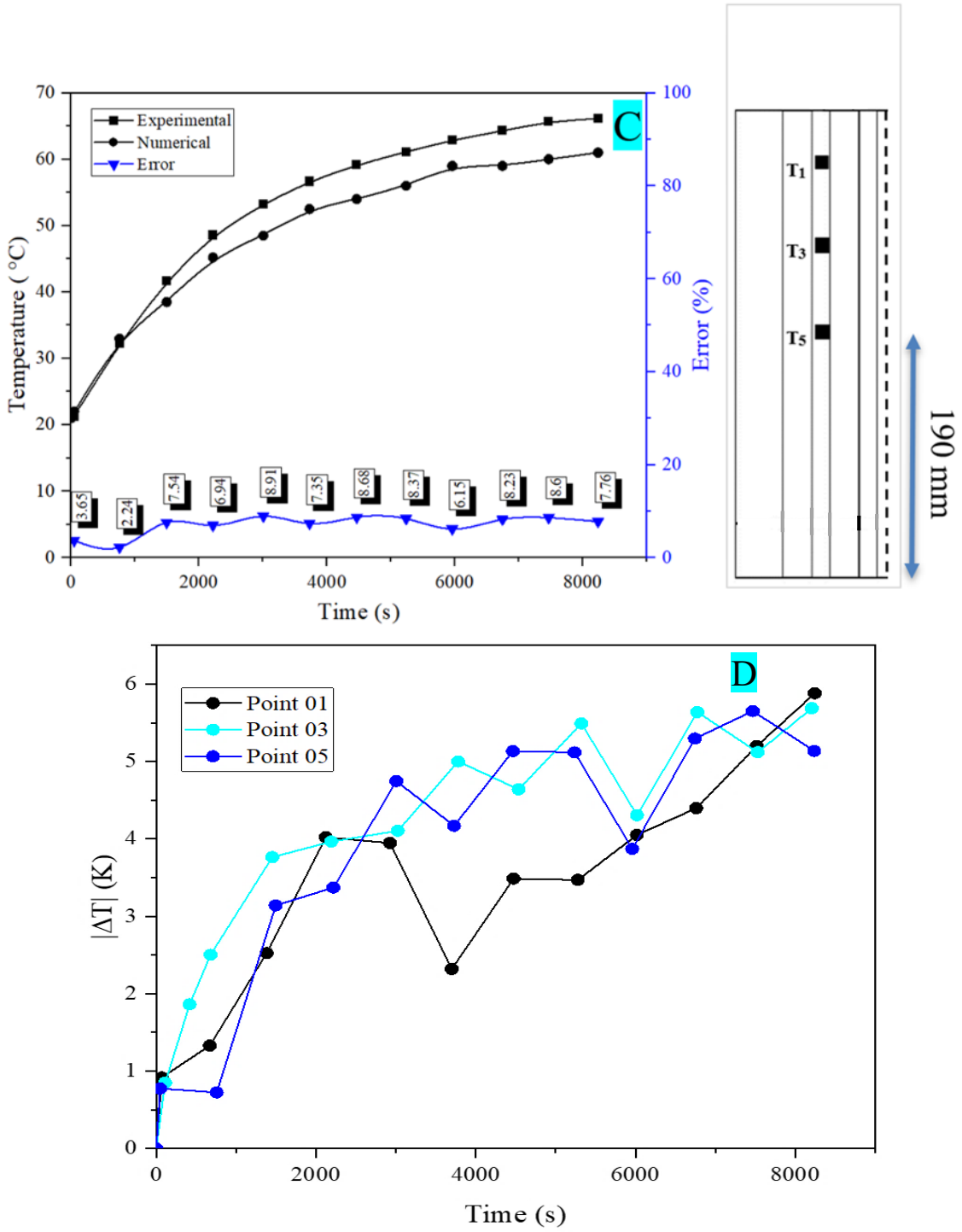

Figure A.2: Comparison of experimental and CFD temperature variations for: (A)- The point 01, (B)- The point 03, and (C)- The point 05, (D)- The temperature differences (|ΔT|).

Chapter III. Numerical analysis of varying aspect ratios (L/D) in a hybrid TES Tank

III.1-Introduction

This chapter examines the melting and solidification dynamics of PCM cylinders across five tanks with different length-to-diameter ratios (*L/D*). Through thermodynamic analysis, including liquid fraction, temperature contours, and water heat flux, the study evaluates system effectiveness. Results indicate melting times ranging from approximately 2670s in Tank 4 to 2880s in Tank 1, while solidification times vary from about 10560s in Tank 3 to 11760s in Tank 5. Tank shape significantly influences water heat flux during these processes. Higher *L/D* ratios generally enhance thermal stratification and melting rates across all tanks, except Tank 5, which exhibited unique behavior. Similarly, increased *L/D* ratios expedite solidification, with Tank 3 demonstrating the most rapid solidification. Nonetheless, optimal *L/D* ratios must be determined to avoid unintended outcomes.

III.2- Numerical Analysis

This research study explores the heat storage capacity of a 15-litre tank, expanding on the experimental setup detailed in the ref [191]. A numerical simulation was developed using experimental results to improve the thermal storage tank's performance. The configuration with the inlet positioned at the top and the outlet at the bottom demonstrated the highest efficiency. This optimal setup was selected for further analysis, focusing on improving performance by varying the *L/D* and comparing results across the four cases (**Figure III.1**). **Figures III.2-(A)** and **(B)** illustrate the dimensions of the tank 1 and the constant distance between the PCM cylinders in all tanks, respectively. **Table III.1** provides the dimensions of the modified tanks.

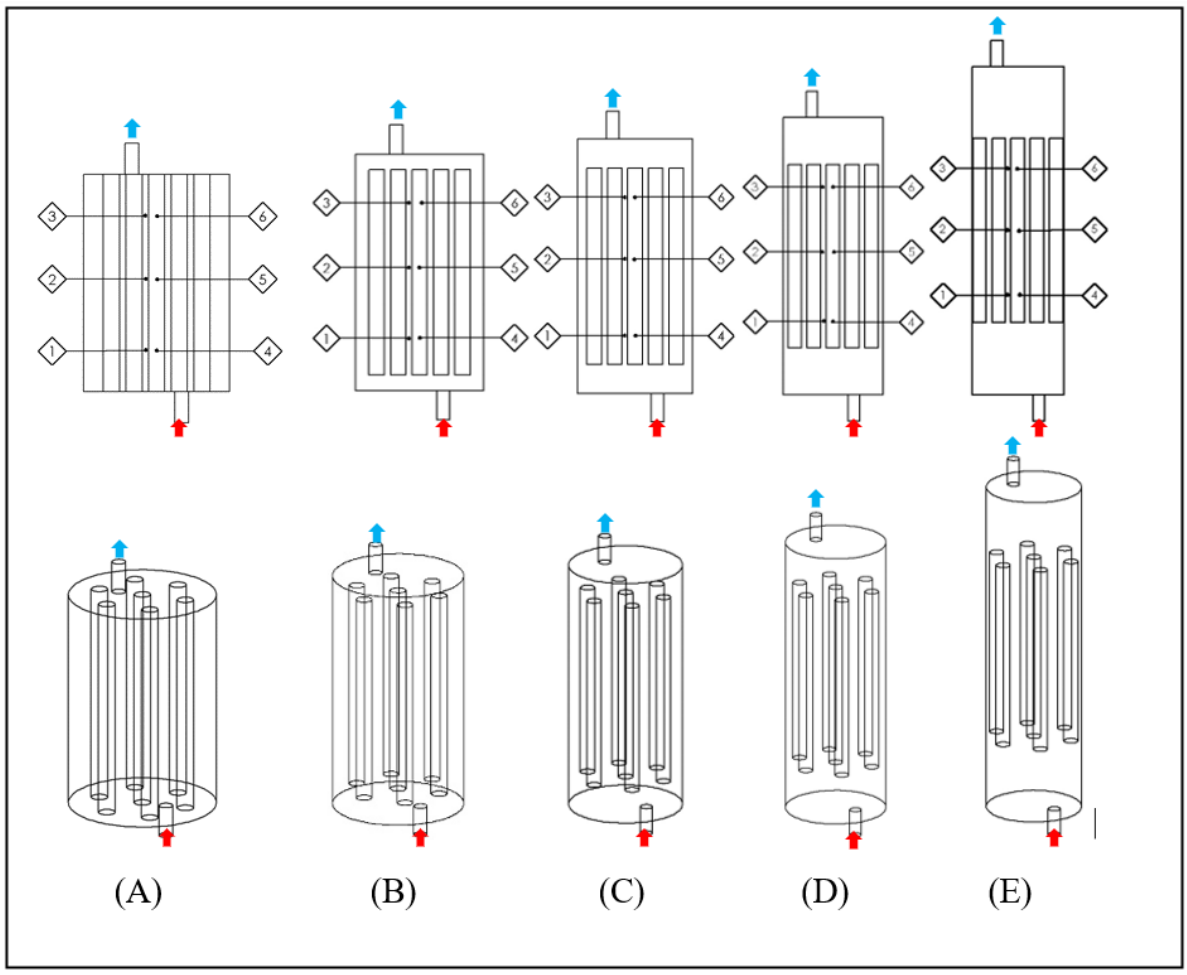

Figure III. 1 : Diagram of TES tanks: (A) — Tank 1, (B) — Tank 2, (C) — Tank 3, (D) — Tank 4, and (E) — Tank 5.

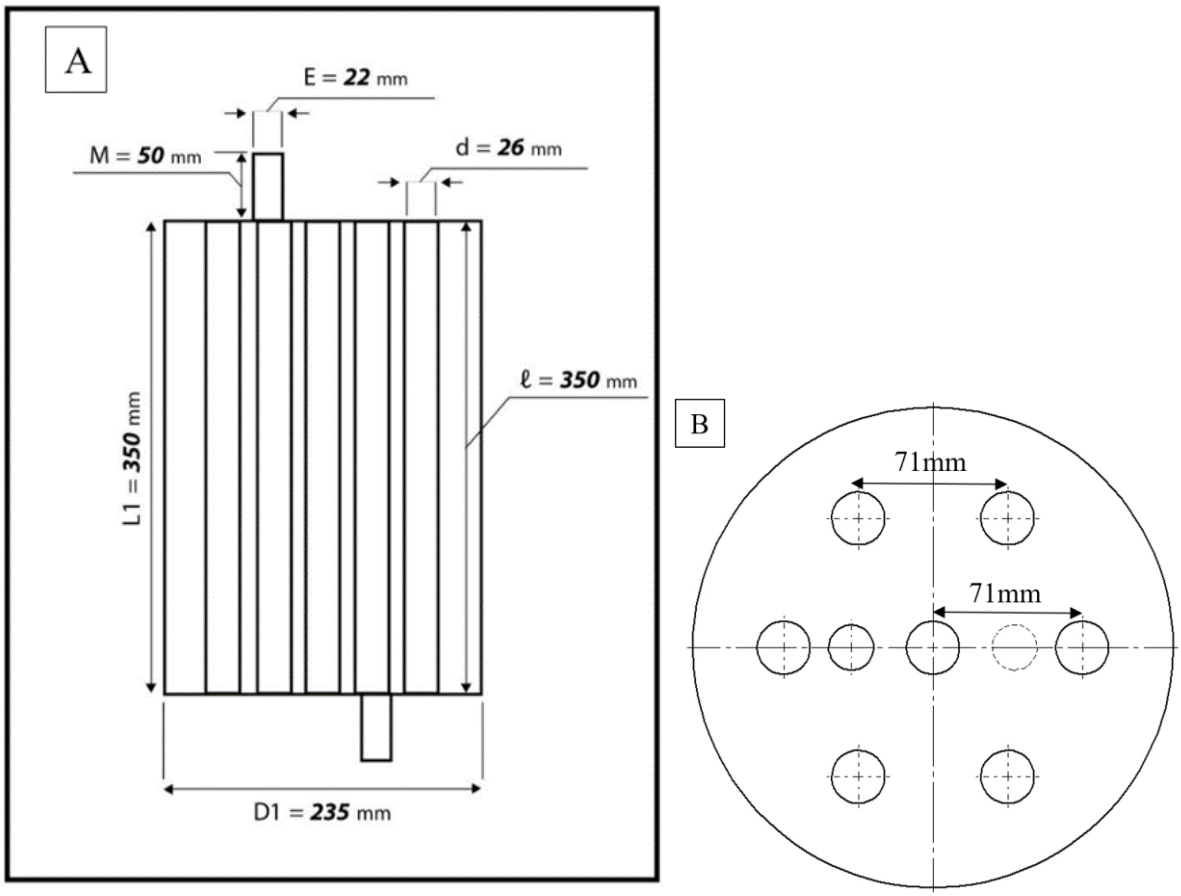

Figure III. 2 : (A)- the dimensions of tank 1, (B)- Distance between PCM cylinders for all tanks.

Table III. 1 : Tanks Dimensions.

Dimensions	Tank 2	Tank 3	Tank 4	Tank 5
L(mm)	402.5	455	530	624
D(mm)	218	205	190	175
d(mm)	26	26	26	26
ℓ(mm)	350	350	350	350
E(mm)	22	22	22	22
M(mm)	50	50	50	50
L/D	**1.846**	**2.219**	**2.789**	**3.565**

III.2.1-*Model specification*

The paper investigates the effects of modifying the dimensions of TES tanks that utilize PCMs. Specifically, the diameter of the four tanks was decreased and their height increased, while maintaining a constant volume and keeping the PCM cylinders' positions unchanged (the thermophysical characteristics of PCM are detailed in **Table III.2**). A simulation model of the tanks was developed using Fluent software version 22.2, employing a polyhedral mesh generated via Fluent Meshing, as shown in **Figure III.3**. A uniform element size of 5.4 mm was applied across all models. The total number of mesh elements for each configuration was as follows: Tank A — 202,885 elements; Tank B — 207,142; Tank C — 205,785; Tank D — 207,986; and Tank E — 204,275.

Table III. 2 : Physical properties of PCM.

Physical properties	Values
Density (liquid phase) (kg/m^3)	780
Density (solid phase) (kg/m^3)	920
Liquidus temperature (◦C)	50
Solidus Thermal conductivity (W/m K)	0.25
Liquidus Thermal conductivity (W/m K)	0.16
Latent heat of melting (kJ/kg)	130
Liquidus-specific heat capacity (J/K kg)	2100
Solidus-specific heat capacity (J/K kg)	1600

Figure III. 3 : Distribution of polyhedral mesh.

III.2.2-*The governing equations*

III.2.2.1-*Hypotheses:*

To investigate the thermal stratification characteristics of the heat-storage tank, transient 3D models were utilized. The analysis was conducted based on the following assumptions:

1. The working fluid is incompressible.
2. Viscous dissipation and pressure variations due to temperature are negligible.
3. The numerical simulation is performed in 3D.
4. The thermal properties of the PCM are constant in both solid and liquid phases [192], except for the liquid-phase density, which varies with temperature. This variation induces buoyancy forces, modeled using the Boussinesq approximation.
5. All tank walls are considered adiabatic.
6. The flow within the melted PCM zones and the water regions was characterized as laminar. A flow rate of 25 L/h, corresponding to a uniform inlet velocity of 0.018 m/s, was applied at the water tank's inlet. The flow behavior of the water inside the TES tank was assessed by calculating the maximum Reynolds number (Re), as outlined in Ref. [193].

$$\mathrm{Re} = \frac{\rho_W u_{in} D_H}{\mu_W} \qquad \text{(II.1)}$$

The maximum Re is observed at the inlet pipe due to the confined geometry and higher flow velocity, with a calculated Re of approximately 1084. As the fluid enters the larger tank volume, it spreads out and interacts with the PCM containers, leading to a reduction in local flow velocity and, consequently, a decrease in the Reynolds number. Since the inlet Re remains well below the laminar-turbulent transition threshold of 2300, the flow regime is considered laminar, which aligns with the modeling assumptions. This gradual flow expansion and obstruction by the PCM structures cause the flow regime to transition from inlet-dominated inertia to a more diffusion-controlled and buoyancy-affected regime within the storage domain (**Annex 2** presents the thermophysical properties of water at 80°C, which were used for boundary condition inputs in the simulations).

Mathematical modeling of the thermal water tank employs the Navier-Stokes and energy equations, taking gravity into account. These equations are formulated as presented in Chapter II.

III.2.3-*Boundary conditions*:

In this investigation, water was used as the working fluid, with velocity boundary conditions specified at both the inlet and outlet. The initial water temperature in the heat storage tank was set to 298.15 K and 323.15 K, with the inlet water temperature being 353.15 K for melting and 298.15 K for solidification. The flow rate at the inlet was 25 L/h (**Figure III.4**).

$t = 0 \rightarrow T(r,\theta,z,t=0) = T_{M,ini} = 298.15K$, For melting.

$t = 0 \rightarrow T(r,\theta,z,t=0) = T_{S,ini} = 323.15K$, For solidification (III.2)

The wall is constrained with a no-slip boundary condition.

The tank was assumed to be insulated from the external environment, and consequently, adiabatic boundary conditions were implemented [195].

$$\frac{\partial T}{\partial r} = \frac{\partial T}{\partial \theta} = \frac{\partial T}{\partial z} = 0 \quad \text{(III.3)}$$

The boundary conditions applied at the water inlet are as follows:

$t > 0 \rightarrow T_{M,in} = 353.15K, U_{in} = 0.018\,{}^{m}\!/_{s}$, For melting

$t > 0 \rightarrow T_{S,in} = 298.15K, U_{in} = 0.018\,{}^{m}\!/_{s}$, For solidification (III.4)

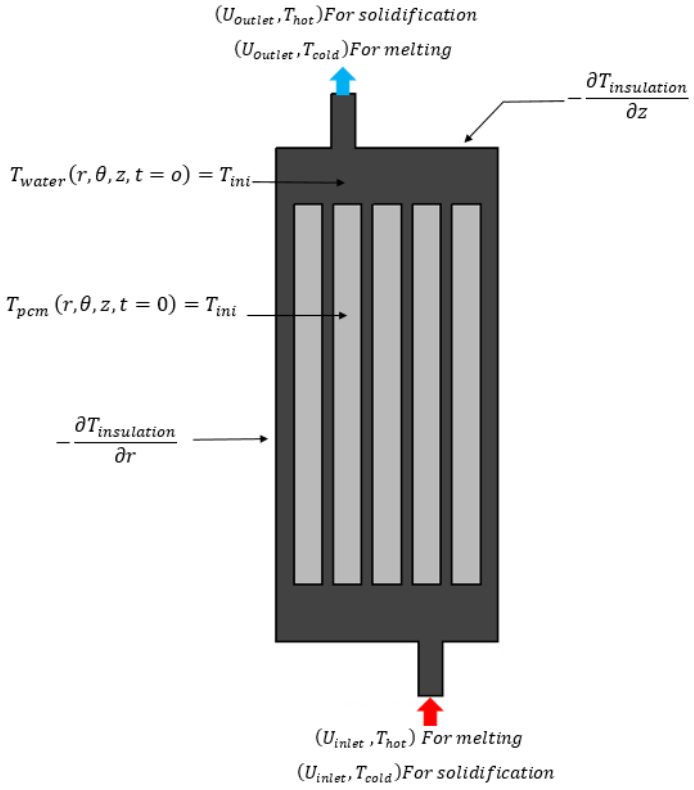

Figure III. 4 : Initial and boundary conditions.

III.2.4-*Numerical Method:*

The simulations were conducted using Fluent version 22.2. The momentum and continuity equations were solved using the pressure-based coupled solver. To simulate natural convection within the PCM, a gravitational acceleration of -9.8 m/s² was applied in the *y*-direction. The SIMPLE algorithm was used to couple the pressure and velocity fields, while second-order upwind discretization was applied for advection terms and a second-order implicit scheme was employed for the transient formulation (The general numerical solution workflow implemented in ANSYS Fluent for the present simulations is illustrated in **Annex 3**). Additionally, pressure was interpolated using a second-order scheme to ensure greater accuracy in transient calculations. The mesh was created using Fluent's meshing tool, featuring a polyhedral topology composed of connected polygonal faces and vertices. This mesh structure was selected due to its superior quality, lower overall cell count, and the enhanced user control it offers during mesh conversion. [196]. Convergence was considered achieved when the scaled residuals were below 10^{-5} for the continuity and momentum equations, and below 10^{-8} for the energy equation. Time step

independence was verified by several researchers, with only minor variations observed across a range of time steps (0.1, 0.2, 0.3, 0.5, 1, 1.5, and 2s) [197]. Consequently, a time step of 1s was selected in this study to reduce computational cost without compromising accuracy.

Figure III.6 illustrates the melting and solidification processes of the PCM in the original tank configuration, highlighting the effects of melting and solidification on the thermal layers. It is observed that the melting process is relatively time-consuming, while the solidification process is significantly longer. This discrepancy is attributed to the presence of a heat transfer blind zone, which forms due to density differences below the inlet during melting and above the outlet during solidification, as illustrated in **Figure III.5**. The significant gap between the outlet and the tank's upper wall further intensifies this issue, leading to an extended solidification duration of 74,900 seconds, in contrast to the 4,320 seconds required for the melting process.

To address this issue, Wei Li et al. [191] relocated the inlet and outlet positions within the tank, successfully eliminating the heat transfer blind zone and accelerating both melting and solidification processes. Their revised design featuring the outlet at the top and the inlet at the bottom improved thermal stratification and overall tank performance. Building upon these findings, the present study further advances tank efficiency through continued design optimization.

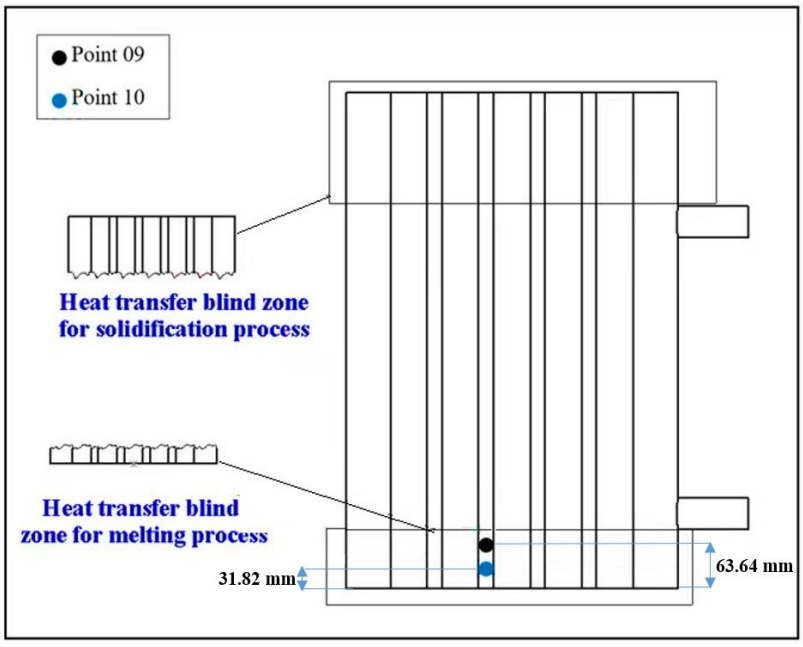

Figure III. 5: Heat transfer blind zone of experiment tank for melting and solidification processes.

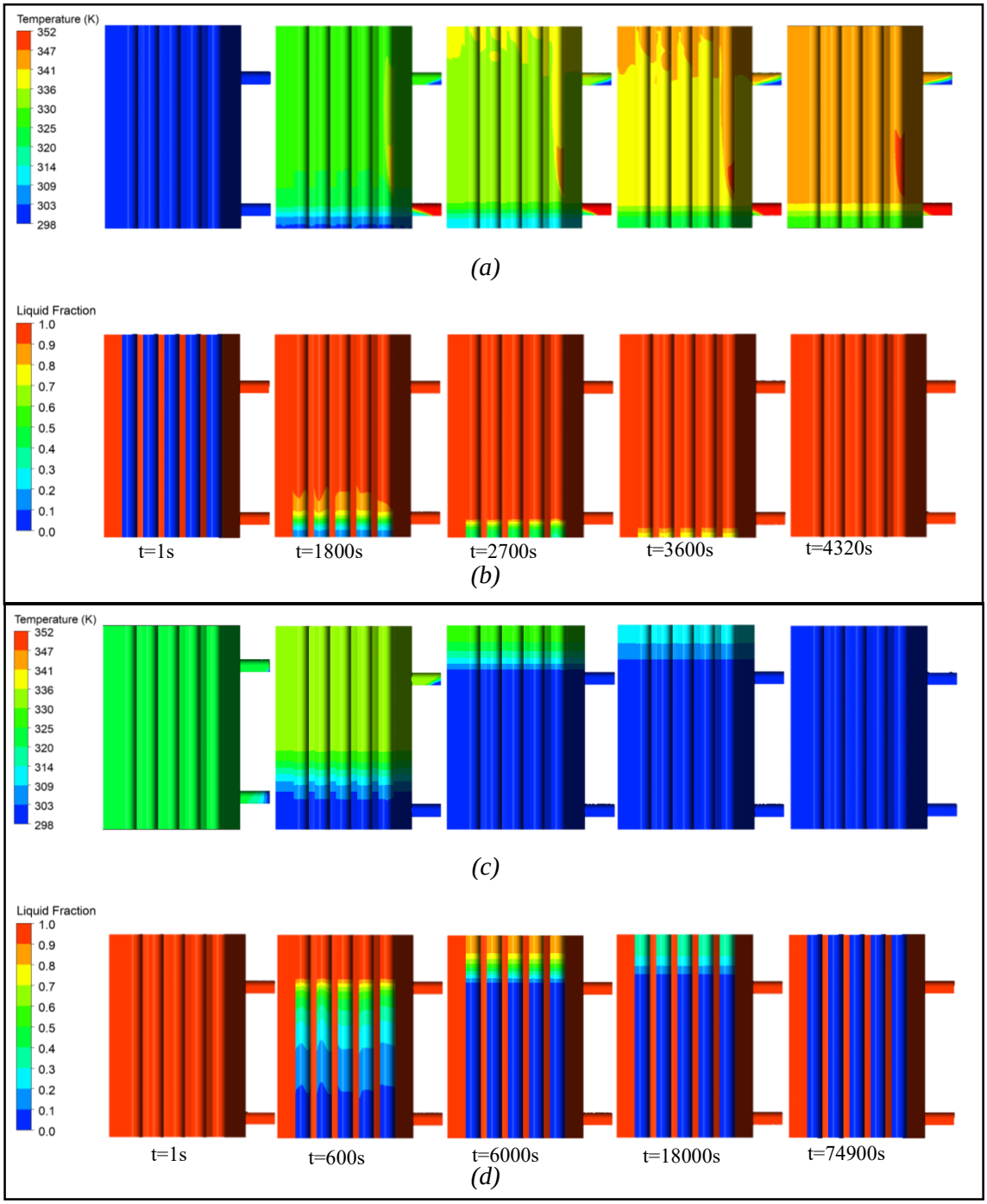

Figure III.6: Temperature and liquid fraction contours in PCM storage tank for melting and solidification processes: (a) — melting temperature contours, (b) — melting liquid fraction, (c) — solidification temperature contours, (d) — solidification liquid fraction.

This section presents the outcomes of the PCM melting and solidification processes, as well as the temperature evolution within the TES tank. Key parameters such as temperature distribution and liquid ratio are used as indicators to numerically describe the phase change events and the heat exchange between the water and PCM. These parameters help predict potential improvements to the thermal efficiency of the storage tank.

III.3.1-*The process of charging a TES system:*

III.3.1.1-*The development of temperature and liquid fraction:*

Figures III. 7-(A) and **(B**) present the average temperature of the storage tank and the PCM temperature, respectively. **Figures III.8-(A)** to **(D)** illustrate the overall liquid fraction evolution of the integrated PCMs, along with the predicted local liquid fraction at points 4, 5, and 6. These results will later serve as a basis for comparison with prior parametric studies.

Five PCM storage tanks (labeled Tank 1 through Tank 5) were designed with varying geometries but identical volumes, enabling an analysis of the effect of tank shape on melting behavior. Increasing the (*L/D*) ratio was found to significantly enhance and accelerate the PCM melting process. This improvement is attributed to the vertical orientation of the tanks, where the incoming hot water rapidly rises along the wall due to natural convection. As a result, the lower regions of the PCM cylinders receive less thermal energy from the solar heating source, as depicted in **Figures III. 7-(A)** to **(G)**.

Initially, the cold water in the tank gradually mixes with the inflowing hot water, initiating the PCM melting process once the melting temperature is reached [198], as observed in **Figure III.8-(A)**. The PCM cylinders located in the upper left region of the tank exhibit delayed melting, primarily because the outlet is positioned on the left side. This setup causes hot water in the upper left corner to exit quickly, while hot water accumulates on the upper right side, promoting faster melting in that region, as shown in **Figure III.8-(D)**.

Figures III. 7-(B) and **(C)** illustrate the temporal variation of the PCM temperature and the outlet water temperature across the five tank configurations. In addition, **Figures III. 7-(D)**, **(E)**, and **(F)** display the local water temperature evolution at points 1, 2, and 3, respectively, while **Figures III. 7-(G)**, **(H)**, and **(I)** show the corresponding PCM temperature development at points 4, 5, and 6.

During the melting process, **Figure III. 8-(A)** shows the temperature evolution across five TES tanks under identical conditions. The tanks are ranked by temperature progression from highest to lowest as follows: Tank 5, Tank 4, Tank 3, Tank 2, and Tank 1. This trend is attributed to natural convection effects governed by the Boussinesq approximation, where hot water rises and accumulates at the top. Additionally, tanks with increased length and reduced diameter promote more uniform heat dispersion, thereby mitigating thermal stratification.

Figures III.9-(A) to **(D)** display the evolution of both the total and local liquid fractions of the PCM at points 4, 5, and 6. Overall, the tanks follow a consistent trend in melting performance: Tank 5 exhibits the fastest melting, followed by Tanks 4, 3, 2, and 1. This order is also observed for the local liquid fraction at points 4 and 5. However, at point 6, the trend differs Tank 1 shows the fastest melting rate, followed by Tanks 2, 3, 4, and 5. This reversal is likely due to the localized flow and thermal distribution patterns unique to that region.

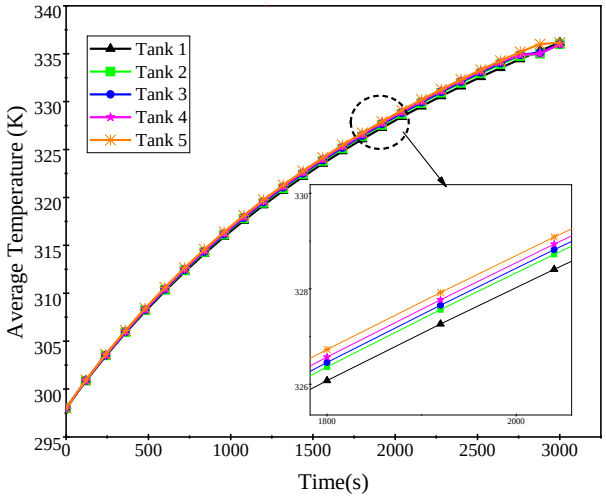

(A)

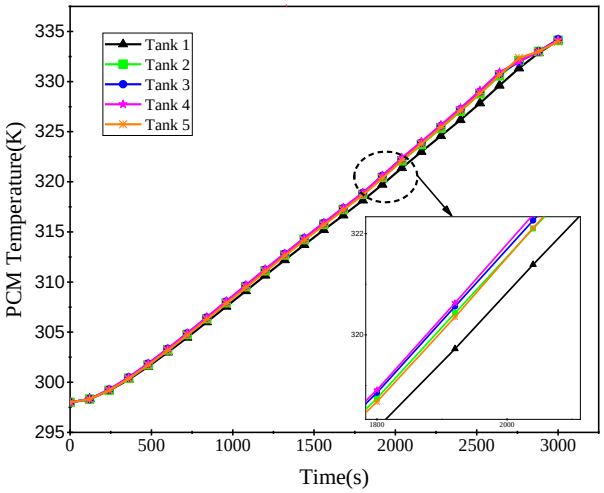

(B)

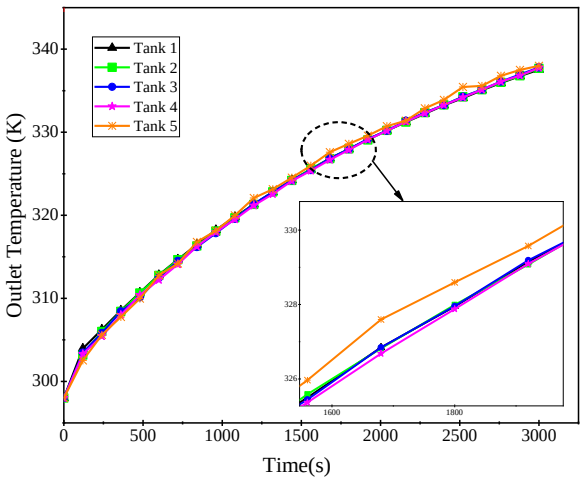
Tank 1
Tank 2
Tank 3
Tank 4
Tank 5
Outlet Temperature (K)
Time(s)

(C)

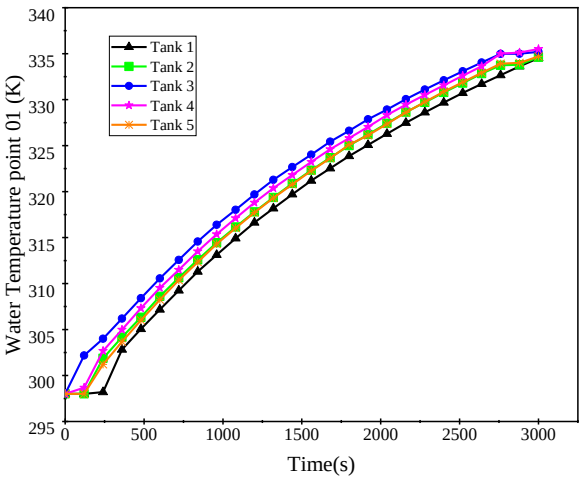
Tank 1
Tank 2
Tank 3
Tank 4
Tank 5
Water Temperature point 01 (K)
Time(s)

(D)

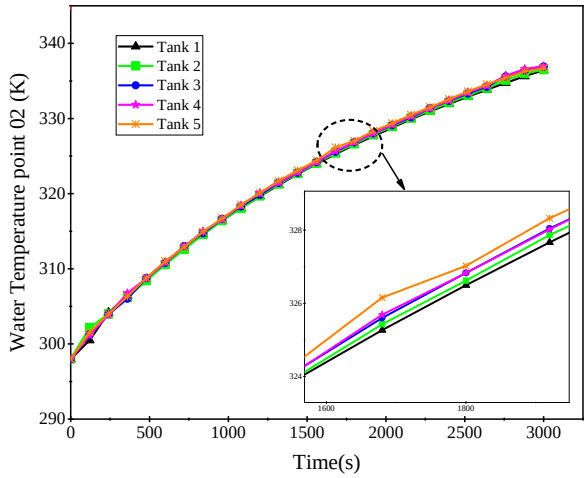
Tank 1
Tank 2
Tank 3
Tank 4
Tank 5
Water Temperature point 02 (K)
Time(s)

(E)

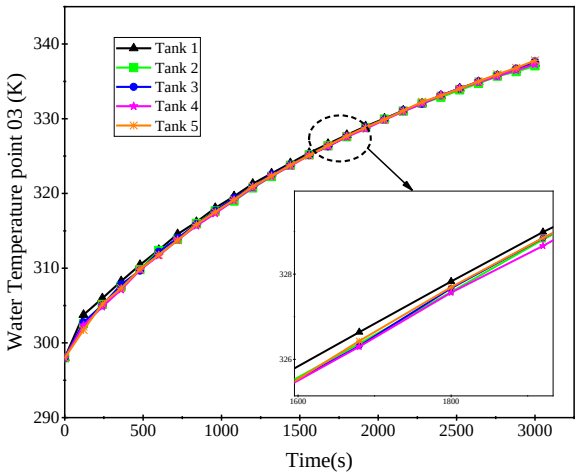
Tank 1
Tank 2
Tank 3
Tank 4
Tank 5
Water Temperature point 03 (K)
Time(s)

(F)

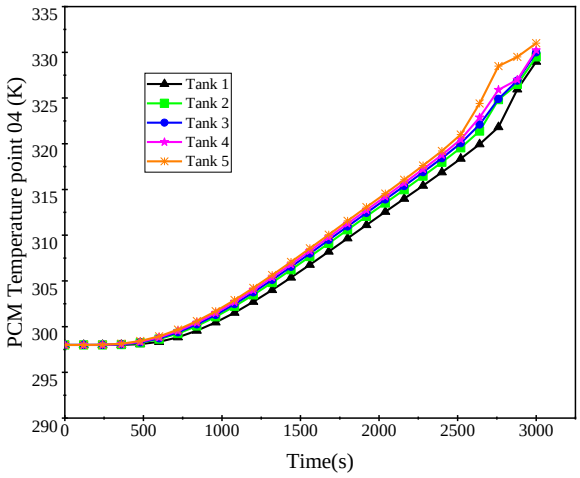
Tank 1
Tank 2
Tank 3
Tank 4
Tank 5
PCM Temperature point 04 (K)
Time(s)

(G)

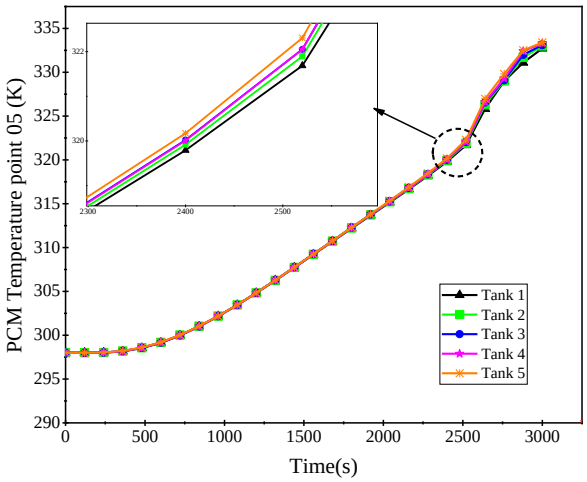
Tank 1
Tank 2
Tank 3
Tank 4
Tank 5
PCM Temperature point 05 (K)
Time(s)

(H)

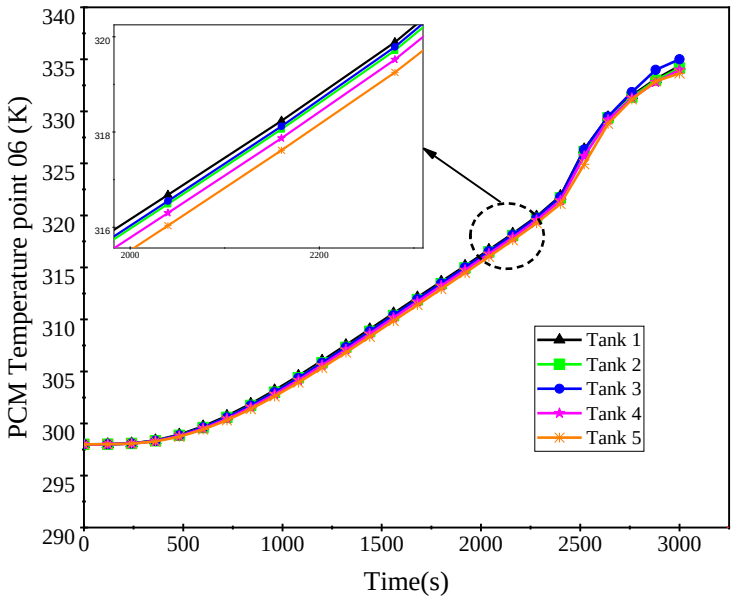

(I)

Figure III. 7: Temperature development for the melting process: (A) — average temperature, (B) — PCM temperature, (C) — outlet temperature, (D) — local temperature point 01, (E) — local temperature point 02, (F) — local temperature point 03, (G) — local temperature point 04, (H) — local temperature point 05, (I) — local temperature point 06.

As shown in **Figure III.9-(A)**, increasing the tank length while decreasing its diameter significantly enhances the PCM melting rate. This geometric configuration promotes more uniform heat distribution, reduces thermal stratification, and accelerates the phase change process. Tanks 2, 3, and 4 outperform Tank 5 in melting speed. The narrower diameter of Tank 5 creates a tighter space between the PCM cylinders and the tank wall, which restricts hot water circulation and limits lateral heat transfer. Without this geometric constraint, Tank 5 might have demonstrated the best performance, as suggested by the trends in **Figures III.9-(B)** and **(C)**, particularly at monitoring points 3 and 4. In contrast, **Figure III.9-(D)** reveals that Tank 1 achieved the highest melting rate at point 6. This is attributed to its shorter length and wider diameter, which support quicker upward flow of hot water and improved heat accumulation near the top of the tank.

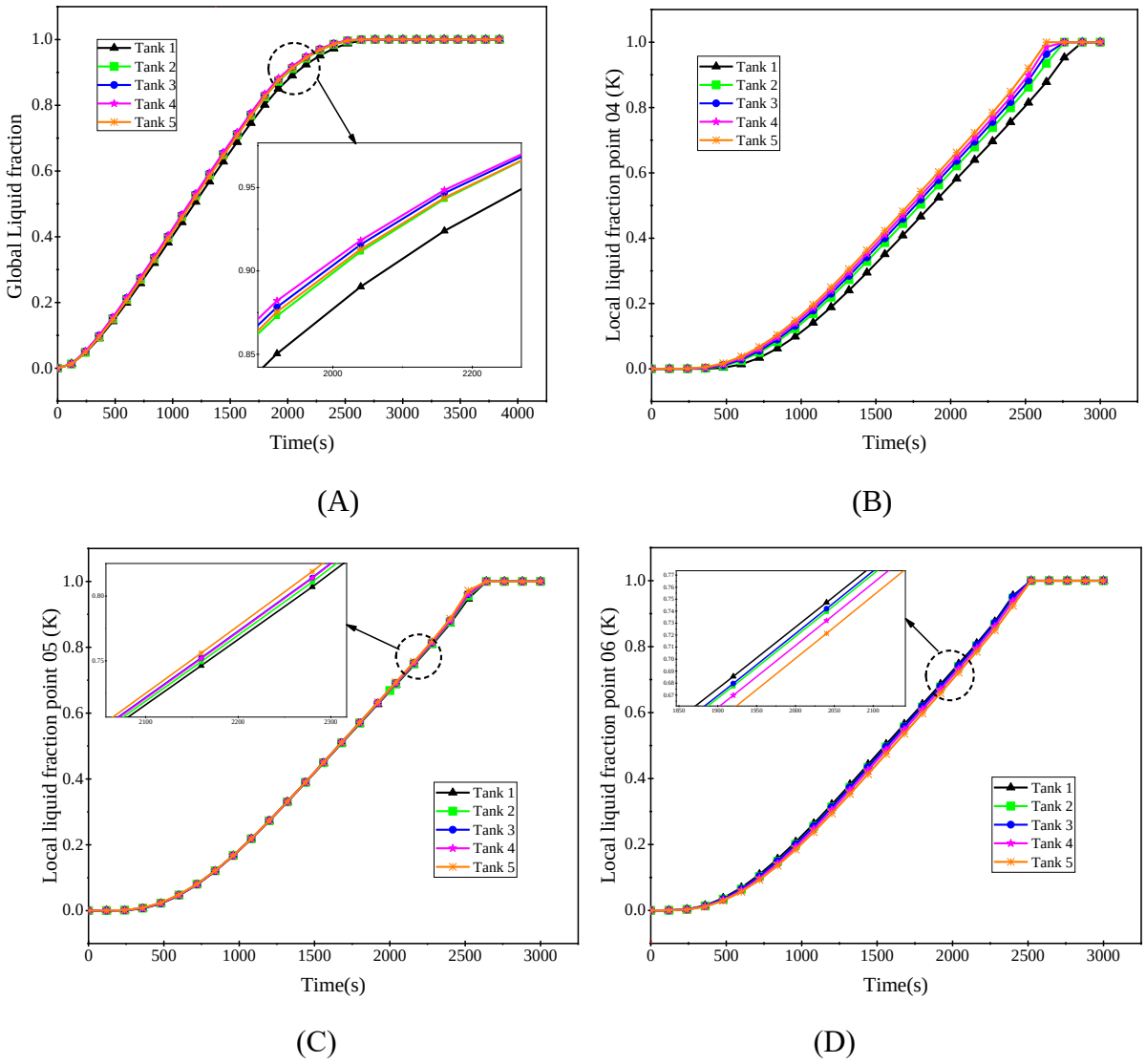

Figure III. 8 : Melting liquid fraction: (A) — global liquid fraction, (B) — local liquid fraction point 04, (C) — local liquid fraction point 05, (D) — local liquid fraction point 06.

III.3.1.2-Water heat flux for the melting process:

Heat flux refers to the amount of heat transferred per unit area [199]. In TES systems, it quantifies the energy exchanged between the hot water and the PCM inside the tank. When hot water enters the tank, it transfers heat to the PCM, triggering the melting process. As melting progresses, the PCM continues to absorb heat. This heat transfer rate is influenced by the temperature gradient between the water and PCM, the PCM's thermal conductivity, and the contact surface area between the PCM cylinders and the water.

In the analysis illustrated in **Figure III.9**, it was observed that increasing the *L/D* ratio of the tank led to a reduction in thermal flow from the water to the PCM in the final five tanks (tanks 1-5). Specifically, tanks 2-5 exhibited a more significant decrease in heat transfer compared to tank 1. This reduction is attributed to the PCM containers being positioned further from the heat accumulation point at the top of the tank as the *L/D* ratio increased. Additionally, tank 5's small diameter resulted in limited space between the tank wall and the six PCM cylinders, which restricted the flow of hot water and consequently reduced heat exchange between the hot water and the sides of the PCM cylinders facing the tank wall. As a result, tank 1 displayed the highest heat flux, while tank 5 showed the lowest. Moreover, heat transfer within a TES tank is predominantly driven by convection, where heat is transferred through the movement of fluid.

As hot water enters the tank, it circulates through the PCM cylinders, absorbing heat and causing the PCM to melt. Because of its lower density, the hot water rises to the top of the tank, transferring heat to the surrounding water. When the tank has a smaller *L/D* ratio, the hot water travels a shorter distance to reach the top. This shorter travel distance results in the hot water spending less time in contact with the PCM cylinders, leading to a higher heat flux. As *L/D* increases, heat flux from water to PCM decreases, as models 2–5 have more surface area, reducing PCM's peak heat demand.

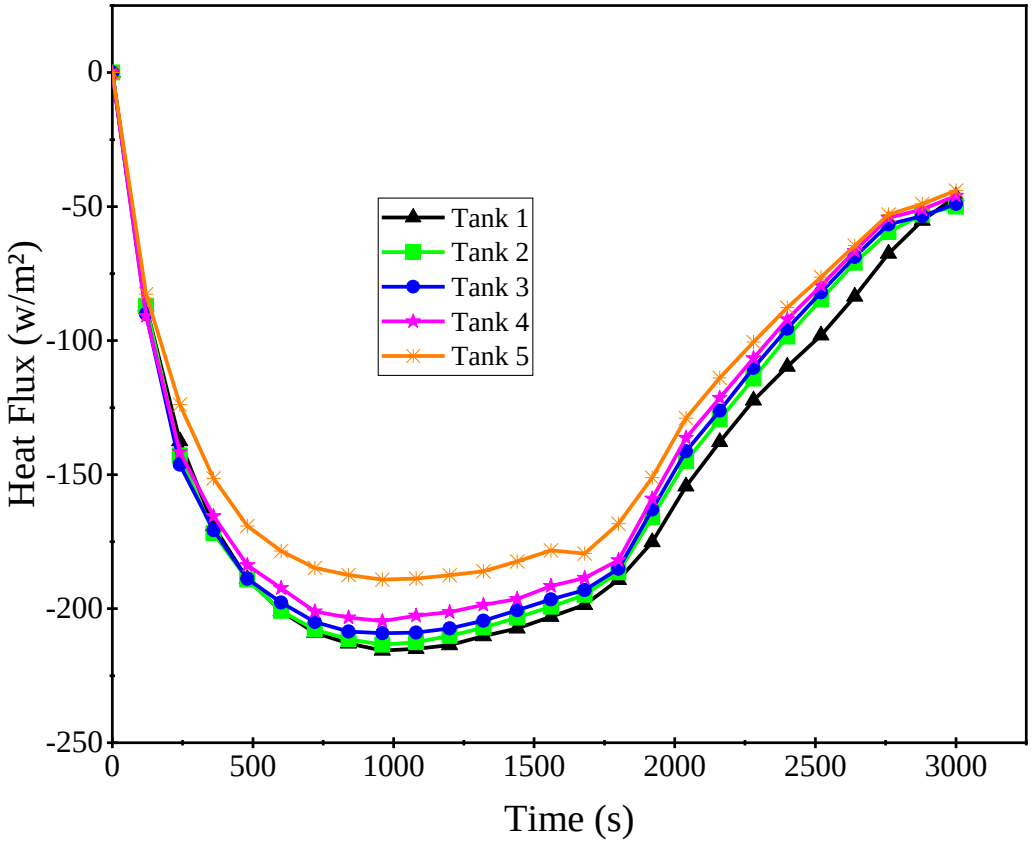

Figure III. 9: Water heat flux for the melting process.

III.3.1.3- ***Temperature and liquid fraction contours for the melting process:***

Figures III.10 and **III.11** present the temperature and liquid fraction contours at 700s intervals for all TES tanks under investigation. The results show that the highest temperature reached during the melting process is 336 K. Low-temperature regions, highlighted in blue on the temperature contours and corresponding to solid zones on the liquid fraction maps, are clearly visible. The progression of the liquid fraction contours illustrates the evolution of the melting front, with changes in shape and melting rate influenced by tank geometry. In these visualizations, the PCM appears fully solid (f = 0) in blue, fully liquid (f = 1) in red, and partially melted (mushy zone) in transitional shades, effectively representing the melting interface.

During the initial phase of the melting process (t=1-700 s), the melting front is observed to be coaxial, indicating that conduction is the dominant mode of heat transfer. However, as the process continues to 1400 and then to 2100 seconds, the liquid PCM, which becomes less dense as it heats up, begins to move upward due to its reduced density and lower temperature. This cycle repeats

several times, resulting in the formation of a vertically elongated, rotating structure that ascends in a concentric pattern. This behavior is likely influenced by the cylindrical shape of the capsules and the buoyancy effect.

The numerical analysis revealed differences in melting time across the simulated configurations. Complete melting of the PCM occurred at approximately 2880 s in Tank 1, 2740 s in Tank 2, 2720 s in Tank 3, 2670 s in Tank 4, and 2760 s in Tank 5, as summarized in **Table III.3**. These variations were influenced by factors such as tank geometry and input conditions. Upon full melting, the PCM reached its liquid state, marking the completion of the phase change. The influence of tank shape on melting performance is illustrated in **Figures III.10** and **III.11**. At t = 1 s, all tanks exhibited the initial uniform temperature of 298 K. By 700 s, stratified thermal layers had formed, with noticeable variation among tanks. Based on thermal stratification, the tanks were ranked in descending order as follows: Tank 1, Tank 2, Tank 3, Tank 4, and Tank 5. This stratification effect diminished with increasing *L/D*, indicating that taller, narrower tanks promote less temperature layering.

As shown in **Figure III.11**, the PCM remains fully solid at t = 1 s. By 700 s, melting initiates from the top due to buoyancy-driven hot water rising from density differences. The rate of PCM melting at this stage ranks the tanks in descending order as follows: Tank 4 (27.61%), Tank 3 (27.46%), Tank 5 (26.76%), Tank 2 (27.07%), and Tank 1 (25.87%) (see **Table III.3**). This trend suggests that a higher *L/D* ratio reduces thermal stratification, thereby enhancing PCM melting rates. All tanks completed melting faster than Tank 1, which recorded the slowest performance. Tank 5 followed closely, with its delayed melting attributed to its narrower diameter, which limited water flow around the PCM cylinders and reduced heat exchange on the cylinder sides adjacent to the tank wall. Similarly, Tank 1's slow melting was due to poor thermal contact between the PCM cylinder ends and the surrounding water, further impeding heat transfer.

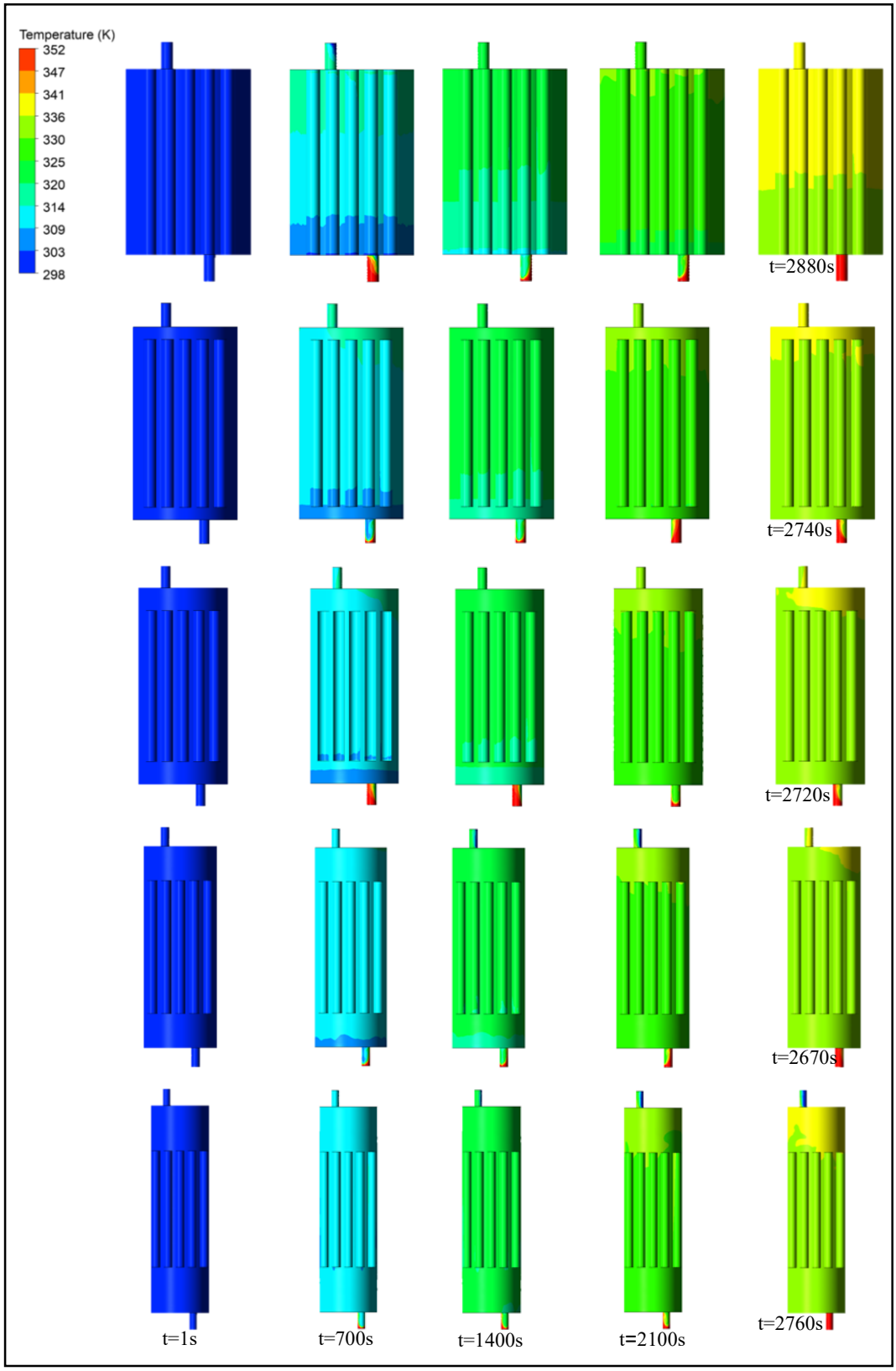

Figure III. 10 : Melting temperature contours for all PCM storage tanks.

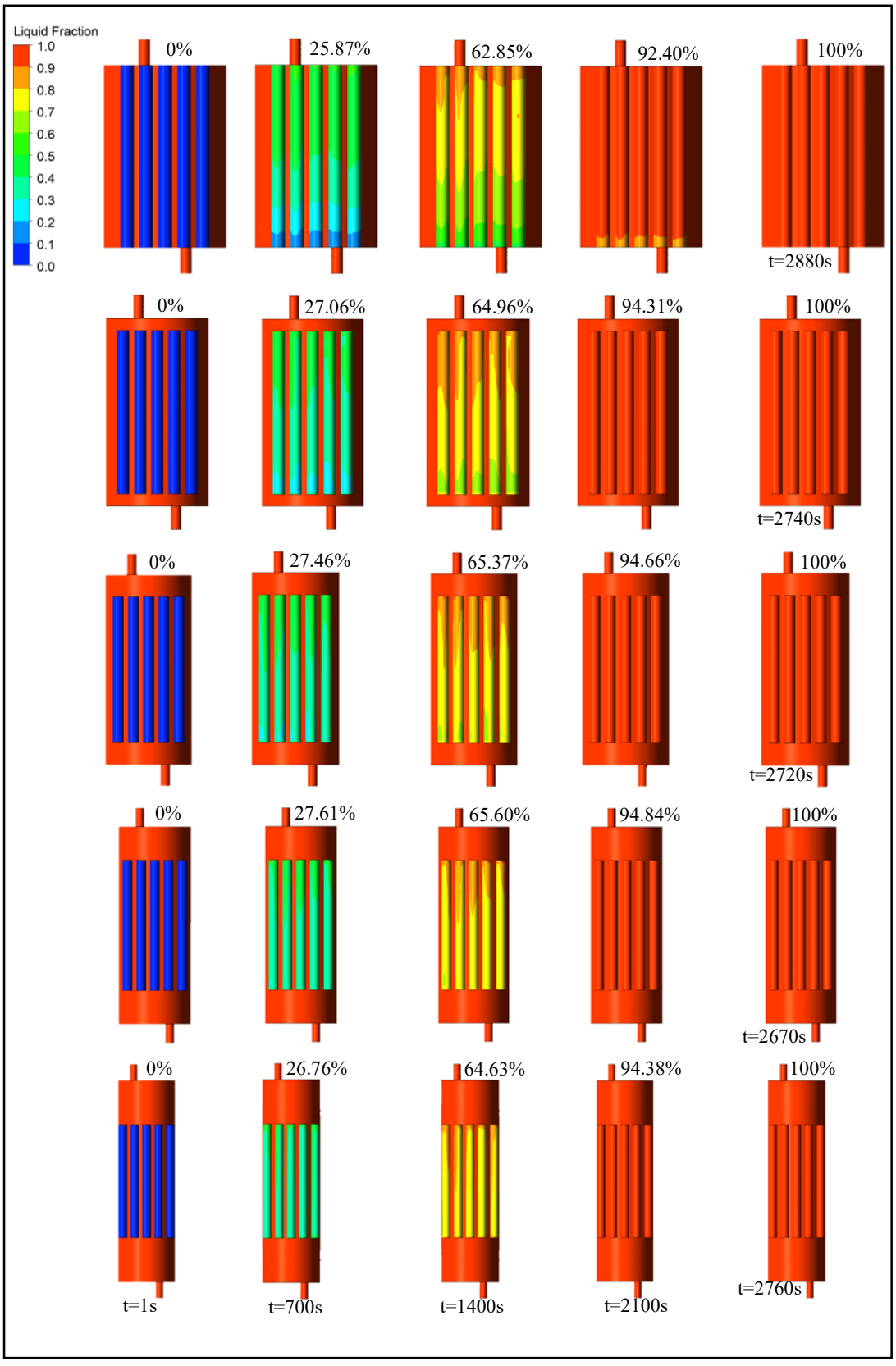

Figure III. 11 : Melting liquid fraction contours for all PCM storage tanks.

The results reveal that tank geometry significantly affects the PCM melting rate and temperature uniformity. Thermal stratification plays a key role by influencing the heat transfer efficiency between the hot water and the PCM. A higher *L/D* ratio was found to promote a more uniform temperature distribution, thereby accelerating the PCM melting process.

III.3.2-*The process of discharging a TES system*

III.3.2.1-*Development of Temperature and Liquid Fraction:*

Figure III.12-(A) presents the average water temperature within the storage tank throughout the solidification phase, while **Figure III.12-(B)** illustrates the mean temperature of the PCM. Local liquid fraction values at points 4, 5, and 6, as well as the overall liquid fraction progression in the integrated PCMs, are shown in **Figures III.13-(A)** and **(D)**. These results are compared with those from earlier parametric studies. The investigation involved five PCM tank configurations (Tank 1 to Tank 5), each designed with the same volume but distinct geometries characterized by different length-to-diameter (*L/D*) ratios. The influence of tank shape on solidification performance was examined. Tanks with higher *L/D* ratios exhibited more rapid PCM solidification, as seen in **Figure III.12-(A)**, due to the increased surface area for heat exchange at the bottom where cold fluid enters, thereby improving thermal transfer. Initially, solidification occurs at the bottom PCM cylinders exposed to the incoming cold water, as shown in **Figure III.13-(B)**. Upper cylinders solidify at a slower rate as the process continues, resulting in a vertical gradient in solidification, captured in **Figure III.13-(D)**. **Figures III.12-(C)**, **(D)**, and **(F)** provide insights into localized PCM temperature variations, while **Figures III.12-(G)**, **(H)**, and **(I)** show corresponding water temperature profiles at various positions within the tank

Throughout the solidification phase, the local PCM temperatures measured at points 5 and 6 are consistently higher than those at point 4. This temperature disparity is primarily due to the stratification effect, where hot water tends to rise and accumulate at the top of the tank, while the incoming cold water sinks to the bottom. **Figures III.12-(D)**, **(E)**, and **(F)** display the temperature profiles for five different thermal storage tank configurations during the solidification process. The temperature hierarchy across the tanks follows the trend: Tank 5 > Tank 4 > Tank 3 > Tank 2 > Tank 1. Tanks with higher *L/D* ratios demonstrated reduced thermal mixing efficiency between hot and cold water, leading to colder water settling at the base and ultimately lowering the average tank temperature, as evidenced in **Figure III.12-(A)**. Consequently, tanks with larger (*L/D*) ratios

solidified faster than those with smaller ratios (**Figures III.13-(A)**). This observation suggests that tanks with larger *L/D* ratios achieved lower temperatures and completed solidification more rapidly compared to tanks with smaller ratios during the solidification process.

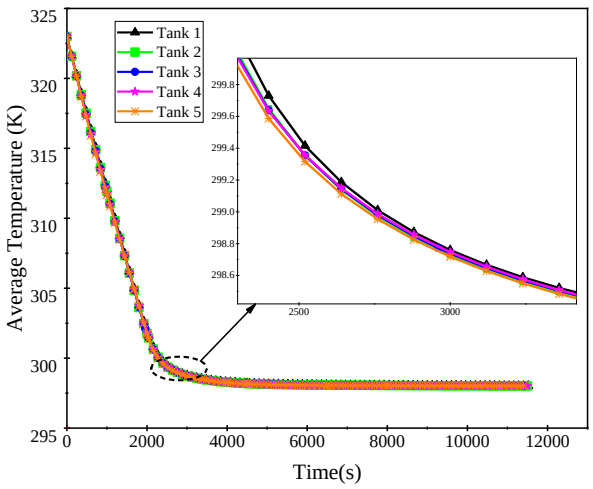

(A)

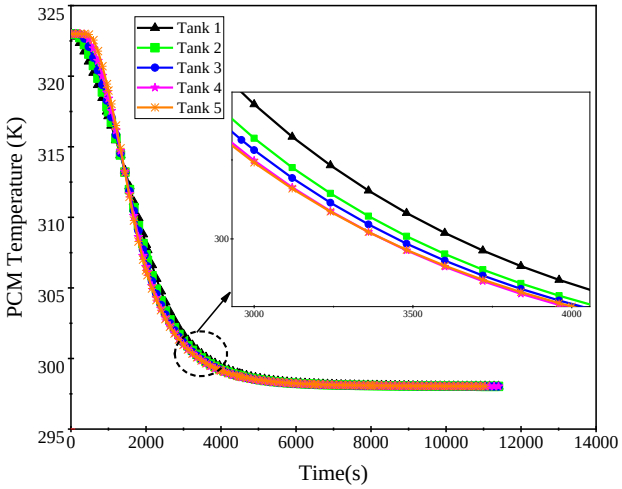

(B)

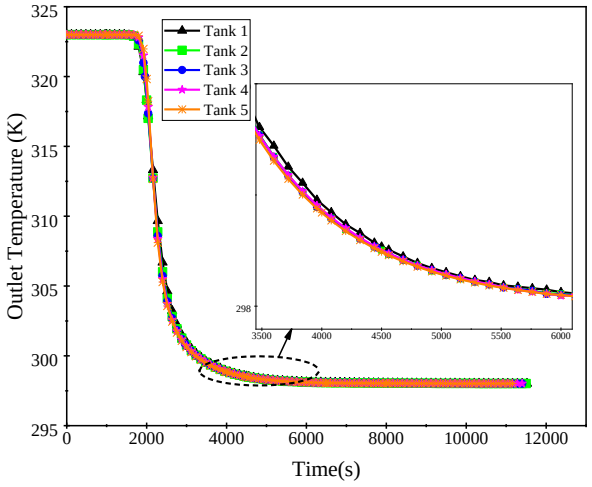

(C)

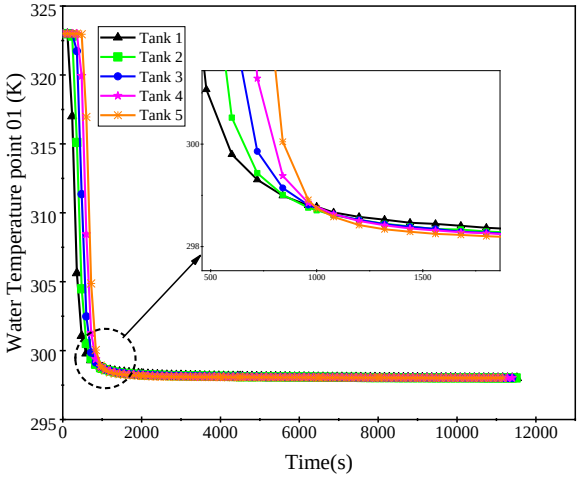

(D)

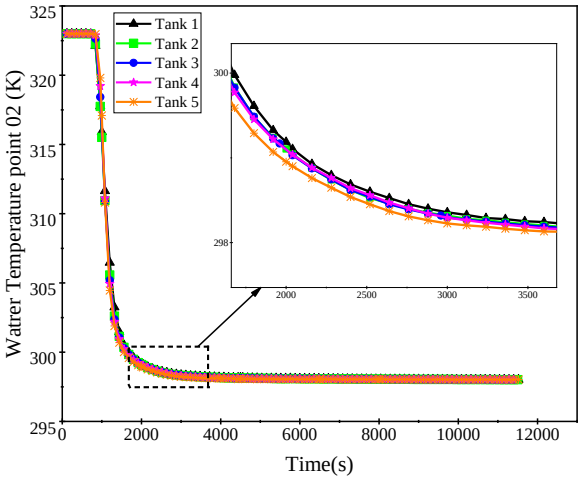
Watrer Temperature point 02 (K)
Time(s)
Tank 1
Tank 2
Tank 3
Tank 4
Tank 5

(E)

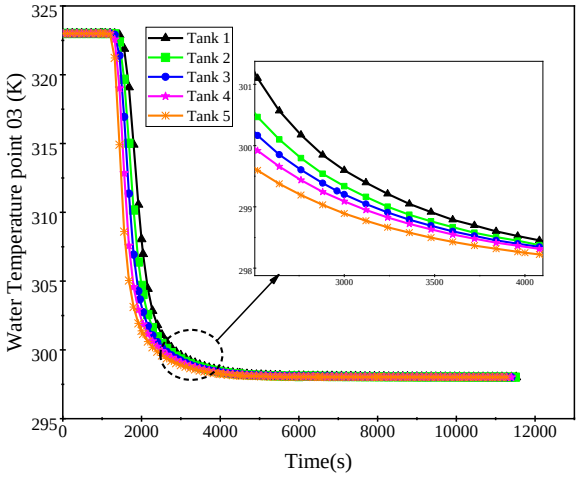
Water Temperature point 03 (K)
Time(s)
Tank 1
Tank 2
Tank 3
Tank 4
Tank 5

(F)

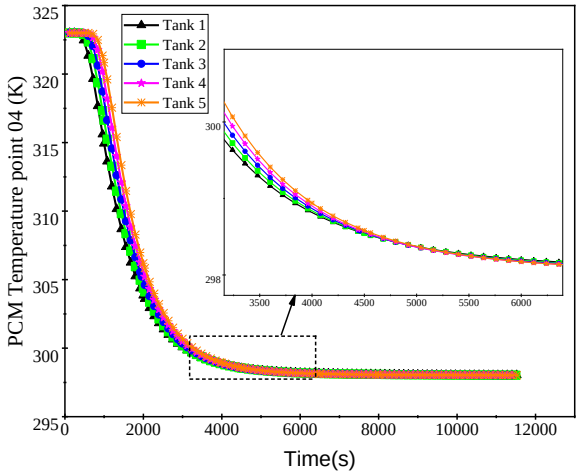
PCM Temperature point 04 (K)
Time(s)
Tank 1
Tank 2
Tank 3
Tank 4
Tank 5

(G)

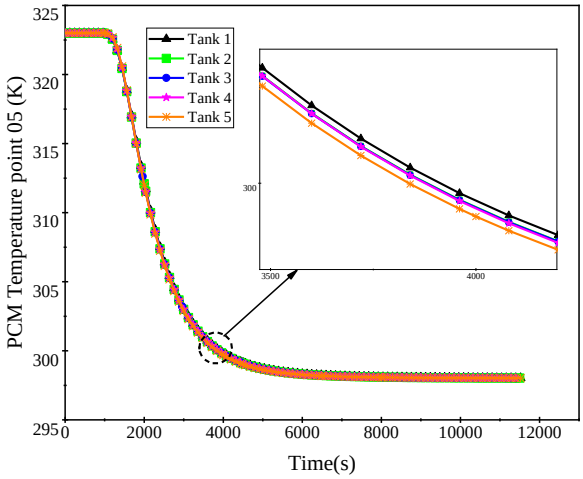
PCM Temperature point 05 (K)
Time(s)
Tank 1
Tank 2
Tank 3
Tank 4
Tank 5

(H)

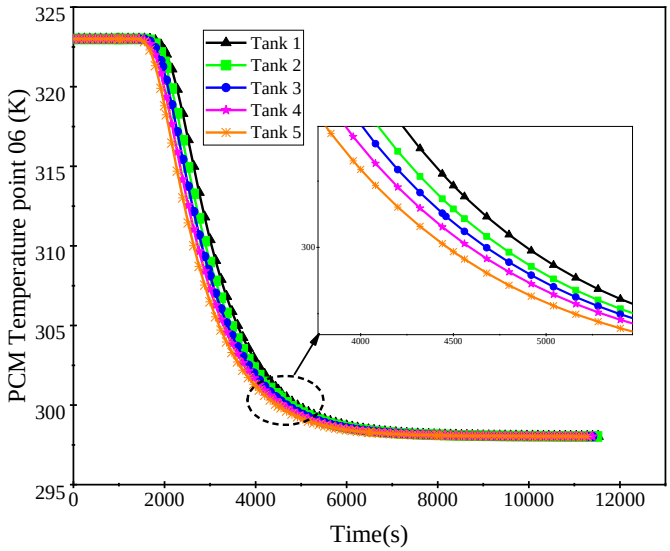

(I)

Figure III. 12 : Temperature distribution for solidification process: (A) — average temperature, (B) — PCM temperature, (C) — outlet temperature, (D) — local temperature point 01, (E) — local temperature point 02, (F) — local temperature point 03, (G) — local temperature point 04, (H) — local temperature point 05, (I) — local temperature point 06.

Figures III.13 (A–D) illustrate the evolution of local liquid fractions at monitoring points 4, 5, and 6, as well as the overall liquid fraction of integrated PCMs within the TES tanks. The tanks are ranked in descending order of global solidification speed, with Tank 1 initially showing the fastest solidification, though it slows over time. Tank 3 eventually becomes the fastest, followed by Tanks 4, 2, 1, and 5. For local solidification at point 4, the order is: Tank 5, Tank 4, Tank 3, Tank 2, and Tank 1. The same order is observed at point 5. At point 6, the ranking remains unchanged Tank 5 leads, followed by Tanks 4, 3, 2, and 1. Overall, Tank 3 demonstrates the highest solidification rate, while Tank 5 exhibits the slowest, indicating that tank geometry significantly influences both local and global solidification behavior.

Figures III.13-(A), (B), (C), and **(D)** also indicate that the solidification speed of integrated PCMs in the tanks is influenced by their design. Generally, tanks with larger (*L/D*) ratios, such as Tank 3, show higher levels of cold-water stratification, leading to faster solidification rates. Conversely, tanks that are too tall and narrow, like Tanks 4 and 5, can develop "blind zones" that impede the upward movement of the solidification front, thereby reducing performance.

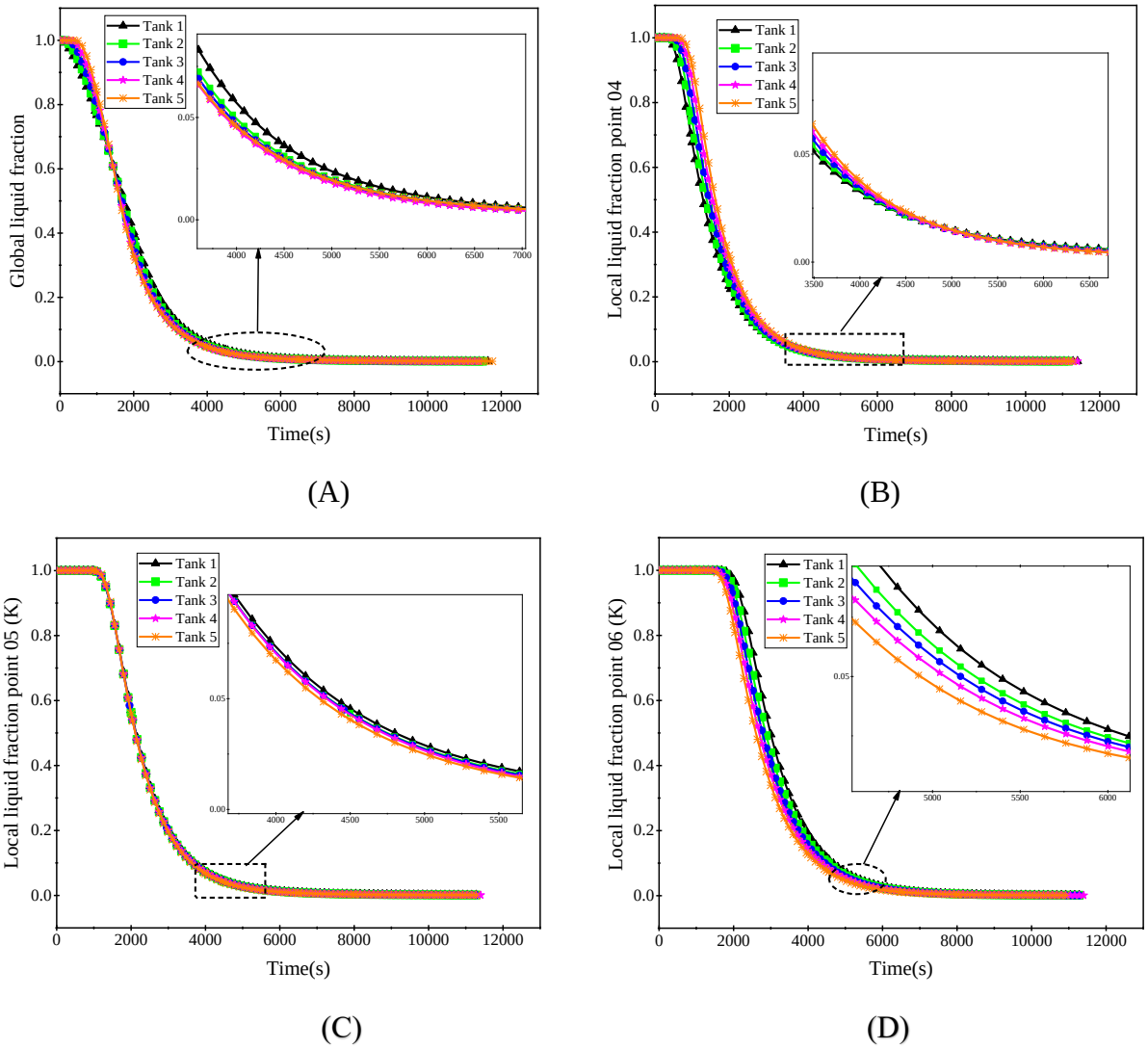

Figure III. 13 : Solidification liquid fraction: (A) — global liquid fraction, (B) — local liquid fraction point 04, (C) — local liquid fraction point 05, (D) — local liquid fraction point 06.

III.3.2.2-*Water heat flux for solidification process:*

During solidification, cold water is supplied to the tank to absorb the latent heat released by the PCM. As the cold water enters and comes into contact with the solidifying PCM, it absorbs heat and warms up before exiting through the outlet. This continuous flow of incoming cold and outgoing hot water is essential for lowering the tank's internal temperature and maintaining the solidification process until the PCM fully transitions to the solid phase.

Increasing the (*L/D*) ratio of a PCM storage tank during solidification enhances the heat flux from the PCM to the surrounding water. This effect is particularly noticeable when cold water is pumped into the tank, as tanks with a larger (*L/D*) ratio facilitate a stronger thermal distribution. The denser, colder water settles at the tank's bottom, accelerating the solidification process from the bottom to the top of the PCM cylinders. Consequently, higher levels of cold-water stratification occur with increasing (*L/D*) ratios, resulting in amplified heat flux within these tanks (**Figure III.14**).

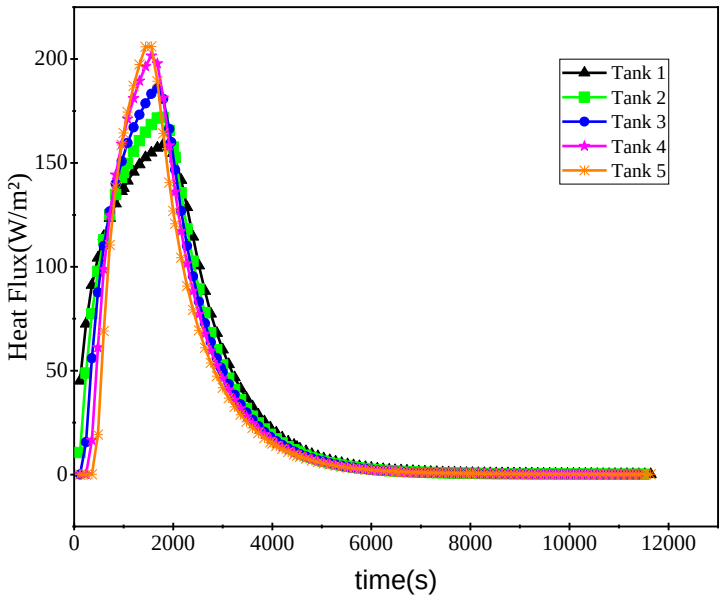

Figure III. 14 : Water heat flux for the solidification process.

III.3.2.3-*Temperature and liquid fraction contours for the solidification process:*

Critical indicators of the thermal performance and efficacy of a PCM-based TES storage system are illustrated by the temperature and liquid fraction contours. The liquid fraction contour delineates the extent of phase transition undergone by the PCM, while the temperature contour provides a visual representation of temperature distribution across the system. During the solidification process, these contours offer crucial insights into how effectively thermal energy is transferred from the PCM to the surrounding fluid. Notably, starting from an initial temperature of 323 K, the entire solidification process across all TES storage tanks in this study reached a minimum temperature of 298 K.

The evolving liquid fraction contours illustrate how the shape and movement of the solidification interface change over time. These contours provide crucial information about the

extent of PCM solidification, with blue indicating fully solid PCM (f=1) and red representing fully liquid PCM (f=0). The mushy zone, visible as the transition region, marks the solidification front. As solidification progresses, this mushy zone shrinks, and the solidification front becomes more defined.

The behavior of the solidification front is influenced by several factors, including the initial temperature of the PCM, the heat transfer coefficient at the boundary, and the thermal conductivity of the PCM. By examining the temperature and liquid fraction contours, one can gain valuable insights into the efficiency of the TES system in transferring thermal energy from the PCM to the surrounding fluid during the solidification process.

During the initial stage of solidification (t = 1–1000 s), the phase change front appears concentric, indicating that heat transfer is predominantly governed by conduction. As time progresses to 2000 s and 3000 s, the PCM's density increases with cooling, leading to the descent of the solidified material while the remaining liquid phase rises due to buoyancy-driven convection. This results in a repeating cycle that forms a vertically stretched solidification front advancing downward in a concentric fashion. Such behavior is primarily influenced by the cylindrical geometry of the capsules and the natural convective flows induced by buoyancy effects.

The numerical simulations demonstrated distinct solidification durations among the tested configurations. According to **Table III.3**, the complete solidification of PCM cylinders occurred at approximately 11,160 seconds for Tank 1, 11,040 seconds for Tank 2, 10,560 seconds for Tank 3, 10,800 seconds for Tank 4, and 11,760 seconds for Tank 5. These differences in solidification time were primarily driven by the design of each system and the specific input conditions applied in the model. Once solidification concluded, the PCM in each tank had fully transformed into the solid phase.

The influence of tank geometry on the rate of PCM solidification is illustrated in **Figures III.15** and **17**. At the initial time (1 second), the temperature in the tank is uniform at 323 K. As the process advances to 1000 and 2000 seconds, distinct thermal layers emerge, with the degree of these layers differing among the tanks. The tanks can be ranked in descending order of thermal stratification as follows: tank 1, tank 2, tank 3, tank 4, and tank 5. The differences in temperature distribution result in clear stratification, which intensifies with a decrease in the (L/D) ratio.

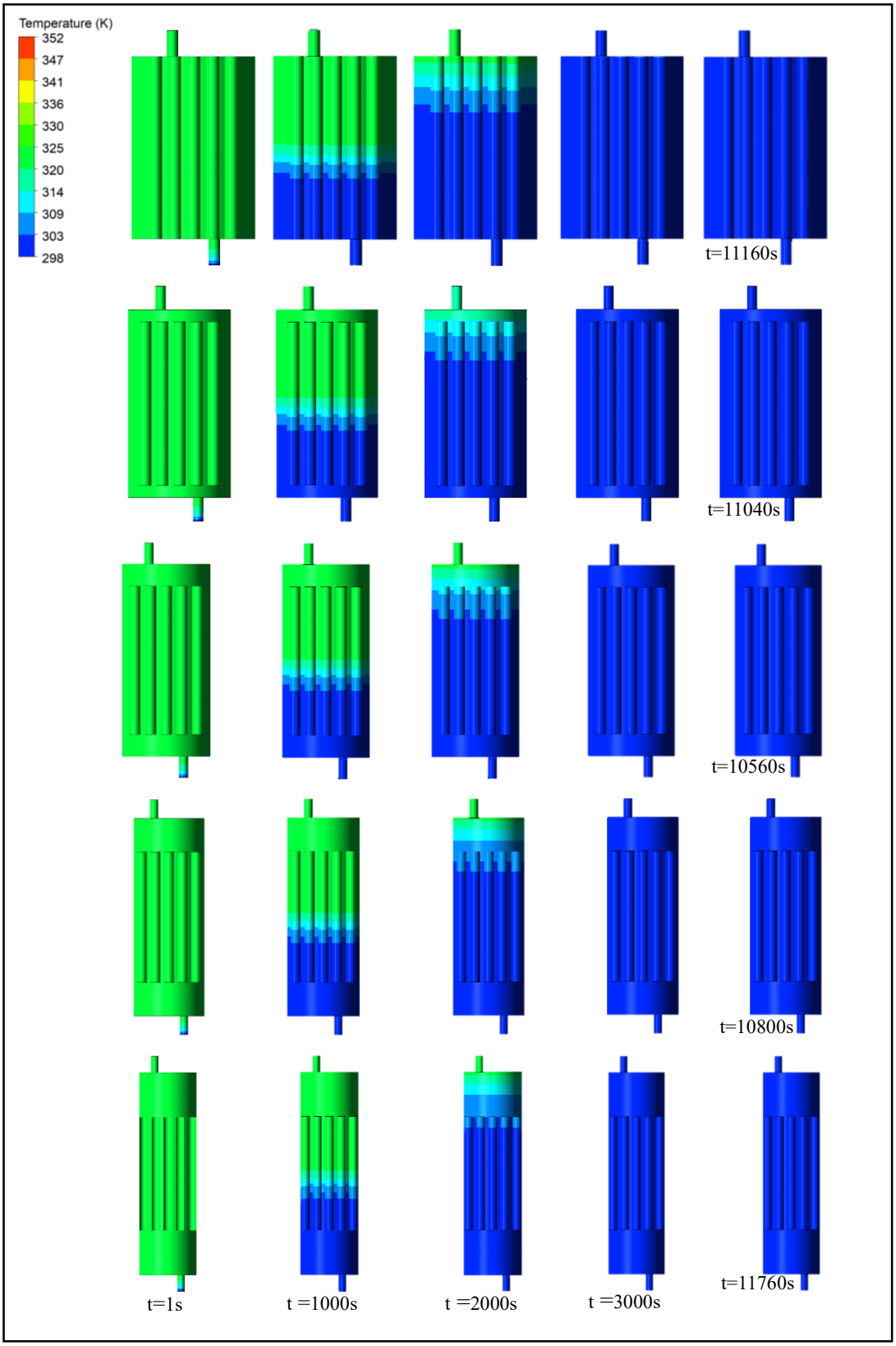

Figure III. 15 : Solidification temperature contours for all PCM storage tanks.

Table III. 3 : Duration of total melting and complete solidification of the PCM in different tanks.

Tanks	Total melting time (s)	Melting time (%)	Total solidification time (s)	Solidification time (%)
Tank 1	2880	-	11160	-
Tank 2	2740	4.86 (decrease)	11040	1.07 (decrease)
Tank 3	2720	5.55 (decrease)	10560	5.37 (decrease)
Tank 4	2670	7.30 (decrease)	10800	3.22 (decrease)
Tank 5	2760	4.16 (decrease)	11760	5.10 (increase)

In contrast, **Figure III.16** shows the initial state of the PCM at t = 1 s, where it is entirely in the liquid phase. After 1000 seconds, solidification gradually begins from the bottom of the tank, driven by the settling of cold water and the upward movement of warmer water due to density gradients. At this point, the tanks can be ranked in ascending order of PCM solidification percentage as follows: Tank 1 (76.69%), Tank 2 (77.91%), Tank 3 (78.75%), Tank 4 (81.65%), and Tank 5 (83.93%). After 2000 seconds, the solidification ranking changes, with the tanks ordered as follows: Tank 5 (11.86%), Tank 4 (11.96%), Tank 3 (12.5%), Tank 2 (13.09%), and Tank 1 (14.81%), as detailed in Table III.3.

These findings suggest that a higher *L/D* ratio enhances cold-water stratification (thermocline formation), thereby accelerating PCM solidification. When examining total solidification times, all tanks outperformed Tank 5, which exhibited the slowest solidification. This reduced efficiency is primarily due to Tank 5's smaller diameter, which results in a narrower gap between the tank wall and the PCM cylinders. This restricted space impedes cold water circulation, thereby limiting thermal exchange between the water and the sides of the PCM cylinders adjacent to the wall.

In cases with a larger *L/D* ratio, such as Tank 3, thermal stratification is reduced, with cold water remaining concentrated at the bottom and warmer water at the top. This stratification pattern facilitates the upward progression of the solidification front, leading to faster PCM solidification. However, if the tank becomes excessively tall and narrow—as seen in Tanks 4 and 5—stagnant

regions or "dead zones" may form, where water circulation is limited. These zones hinder heat exchange and slow the upward advancement of the solidification front, ultimately decreasing the system's thermal performance.

The delay in solidification in tank 1 is due to insufficient contact between the upper and lower surfaces of the PCM cylinders and the cold water, leading to decreased heat exchange and slower solidification rates. Therefore, finding an optimal balance between tank dimensions and solidification parameters is crucial to maximize thermal energy efficiency.

At specific time points during the solidification process, a small portion of PCM remained in the liquid phase across all tanks. For instance, in Tank 1 at 4320 seconds, the outlet temperature dropped to 298.1 K while the PCM temperature was slightly higher at 298.77 K, indicating about 3% of the PCM was still liquid. In Tank 2, at 5880 seconds, the PCM temperature reached 298.25 K with a remaining liquid fraction of 1.02%. Similar trends were observed in the other tanks, with Tank 3 showing 0.96%, Tank 4 showing 0.89%, and Tank 5 showing 1.01% of PCM in liquid form, despite all outlet temperatures being close to 298.1 K. These results highlight slight variations in residual liquid PCM depending on the tank configuration and thermal behavior during solidification

The findings highlight the significant impact of tank geometry on both the PCM solidification rate and the temperature distribution within the TES tank. Temperature stratification plays a key role, as it affects the efficiency of thermal exchange between the PCM and the surrounding cold water. Tanks with higher *L/D* ratios generally exhibit a more uniform temperature distribution, which facilitates more efficient heat transfer and accelerates the solidification of the PCM.

While increasing the (*L/D*) ratio can improve temperature uniformity, it may also lead to the formation of blind zones areas with poor fluid circulation which reduce heat transfer efficiency. Thus, optimizing tank dimensions is crucial to ensure balanced and effective TES system performance.

Among the tested configurations, Tank 3 with an intermediate *L/D* ratio demonstrated the most favorable performance, achieving both the good melting time (2720s) and the shortest solidification time (10560s), and can thus be considered the optimal design within this study.

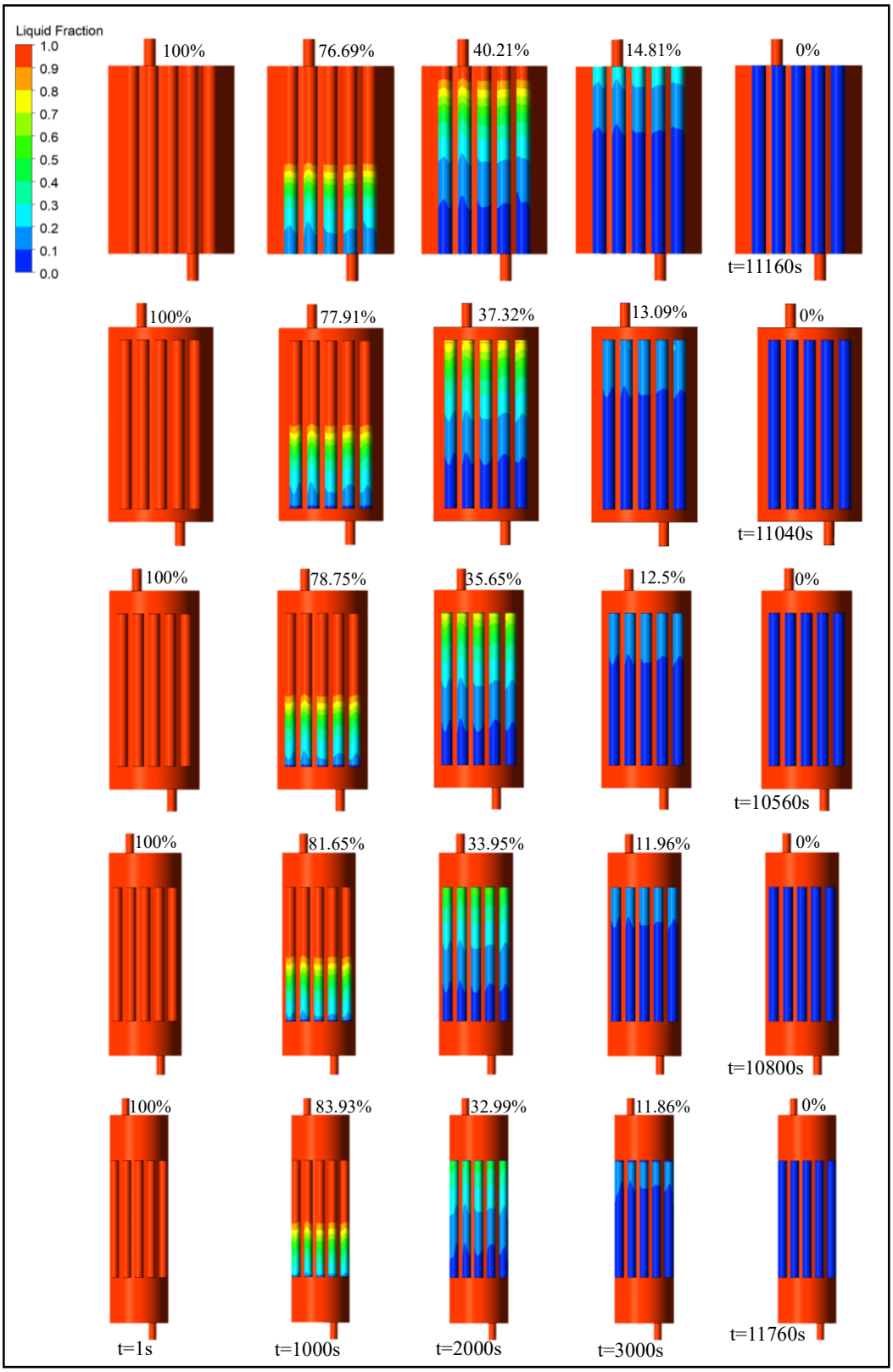

Figure III. 16 : Solidification liquid fraction contours for all PCM storage tanks.

III.4-Conclusion

In conclusion, this study underscores the critical influence of tank design, particularly the *L/D* ratio, on the solidification and melting behaviors of PCMs in TES systems. A higher *L/D* ratio promotes greater thermal stratification, facilitating faster-melting rates due to reduced stratification levels during heating. Conversely, in the solidification phase, a larger *L/D* ratio enhances cold-water stratification, leading to quicker solidification rates. The findings reveal that tanks with optimized *L/D* ratios experienced significantly reduced melting times, with Tank 4 showing the quickest melting at approximately 2670 s, compared to Tank 1 at 2880 s. Similarly, Tank 3 exhibited the fastest solidification time at around 10560 s, highlighting the benefits of enhanced thermal stratification.

Overall, the study emphasizes the potential for improving PCM-based TES systems by carefully designing tanks with appropriate *L/D* ratios to enhance efficiency and effectiveness. However, it also cautions against overly tall and narrow tanks, which may create stagnant zones that impede fluid circulation and diminish overall performance.

Chapter IV. Enhancing thermal storage efficiency in hybrid tanks with baffle design

IV.1-Introduction

In response to the growing need for efficient thermal energy storage (TES) systems, this chapter explores the integration of strategically designed baffles within PCM tanks to improve thermal performance. While PCMs are promising for TES, maintaining uniform temperature distribution remains a key challenge. To address this, horizontal baffles with varying hole diameters were introduced in Tanks 02, 03, and 04, while Tank 05 featured an inclined perforated baffle, and Tank 06 employed an inclined baffle with holes of differing sizes. A comprehensive assessment was conducted by analyzing PCM and water heat flux, static enthalpy, Richardson number, velocity fields, temperature distributions, and liquid fraction contours. Results confirm the thermal benefits of baffles: the reference Tank 01 (no baffle) exhibited a melting time of 2860 s, whereas Tanks 02 through 06 achieved significantly shorter melting times 2360 s (−17.48%), 2350 s (−17.83%), 2400 s (−16.08%), 2320 s (−18.88%), and 2240 s (−21.67%), respectively highlighting improved energy charging efficiency. An economic analysis further reveals that Tank 06, despite costing just $2 more than the baseline, delivered the best economic performance with a P_c value of 0.26. These findings demonstrate that optimized baffle configurations can markedly enhance both heat transfer and cost-effectiveness, offering a practical approach to achieving uniform temperature distribution and accelerating PCM melting in TES systems.

IV.2-Numerical methodology

IV.2.1-Systems description

Six water tank models with distinct modifications were developed to fulfill the objectives described in Ref. [201], building upon the validation of experimental results reported in Ref.[191]. These models form the foundation of our investigation and include the following designs:

Tank 01: This is the baseline model, featuring no modifications. Tank 02: The original tank is equipped with a baffle, positioned 40 mm above the tank bottom, with a diameter of 233.5 mm (**Figure IV.1**). The baffle contains seven holes, each 30 mm in diameter (**Table IV.1**), through which PCM cylinders are inserted. Tank 03: This model mirrors Tank 02, except the diameter of the baffle holes is increased to 32 mm. PCM cylinders are inserted through these 32 mm holes (**Table IV.1**). Tank 04: Based on the design of Tank 02, this tank features a baffle with seven holes, but the hole diameter is further enlarged to 35 mm. PCM cylinders are inserted through

these larger 35 mm holes (**Table IV.1**). Tank 05: Similar to Tank 03, this model includes a baffle with seven holes, each 32 mm in diameter, but with the baffle inclined at a 5-degree angle (**Figure IV.2**). PCM cylinders pass through the 32 mm holes in the inclined baffle. Tank 06: This design includes a baffle with five holes, each 32 mm in diameter, along with two additional holes near the inlet, each measuring 35 mm in diameter. The baffle is inclined at 5 ° (**Figure IV.2**), and PCM cylinders are inserted through the five 32 mm holes and the two 35 mm holes near the inlet (**Table IV.1**). The 5° inclination is the maximum angle at which the PCM cylinders remain centered within the baffle holes. Importantly, the PCM volume is consistent across all tanks, as the design allows the cylinders to pass through the baffle holes without reducing their effective volume. **Figure IV.1-(B)** illustrates the coordinate systems used in the analysis, showing the shift from Cartesian coordinates (x, y, z) to cylindrical coordinates (r, θ, z), with the origin indicated. This transformation is essential for analyzing flow around cylindrical structures such as the water tank and PCM containers. By converting Cartesian coordinates to cylindrical ones, we can more accurately capture the radial and angular components of both flow and thermal behavior.

In this study, a simulation model of the tanks was developed using ANSYS FLUENT 22.2 software. The meshing process employed a tetrahedral mesh for the tank and a hexahedral mesh for the PCM containers, created using the Meshing tool (CFD prep post). **Figure IV.3** illustrates the meshed tank along with the PCM containers. It is important to mention that the number of mesh cells used in the simulations for the heat storage tanks reached a maximum of 700,000. This high cell count ensures fine domain discretization, facilitating precise and detailed simulations of fluid flow and heat transfer processes within the tanks and PCM containers.

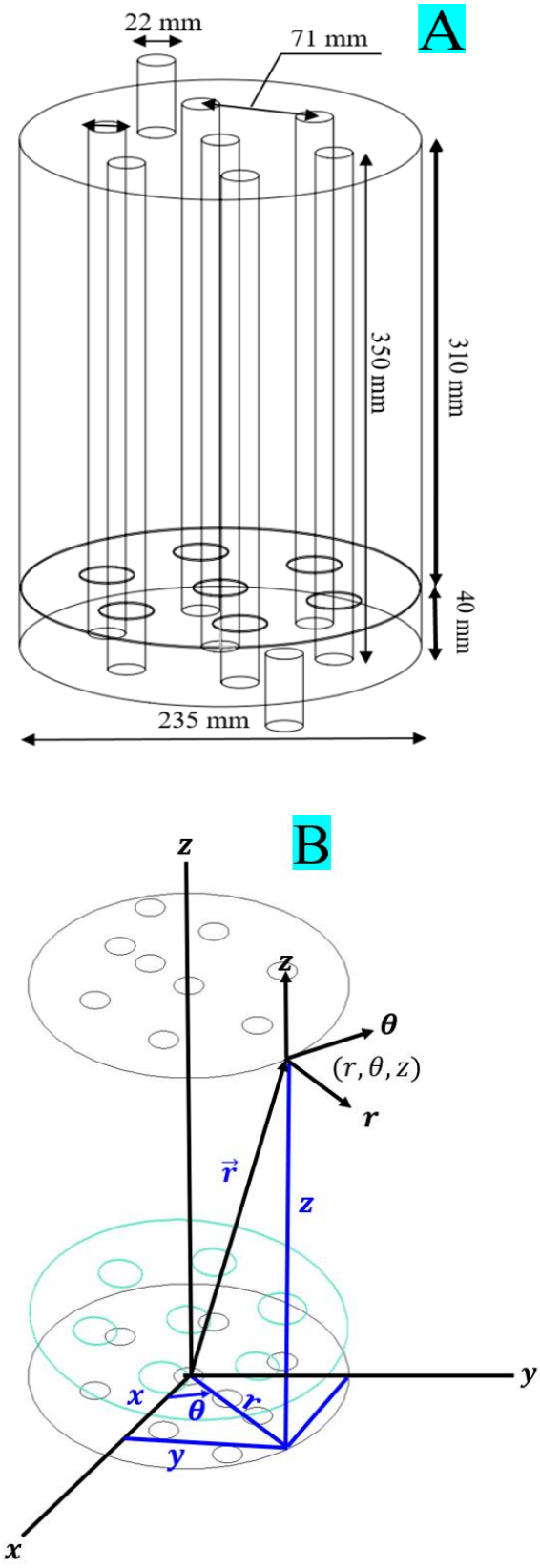

Figure IV. 1 : (A)-Tank`s dimensions used in this chapter, (B)-Illustration of cartesian and cylindrical coordinate systems used in this chapter.

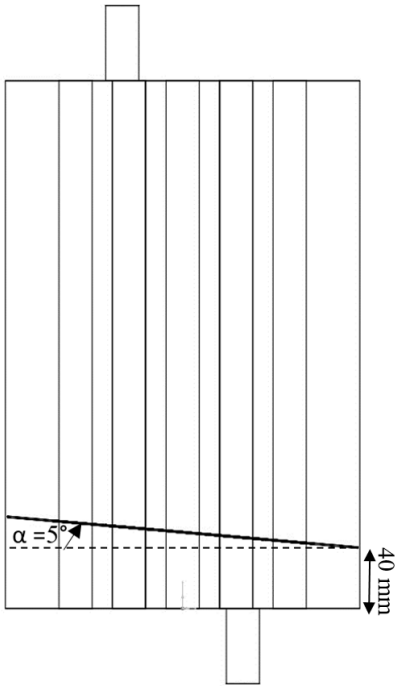

Figure IV. 2: Inclined baffle for Tanks 05 and 06.

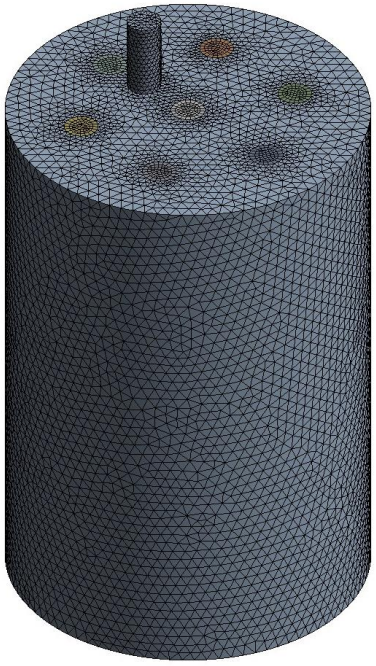

Figure IV. 3: Mesh distribution for all tanks modeling.

The simulation of the PCM utilized the enthalpy-porosity method, a widely adopted approach in PCM heat transfer studies. This method simplifies the process by using a fixed grid rather than explicitly tracking the melting front, as described in Ref.[202]. Instead of traditional methods that monitor the phase interface directly, the enthalpy-porosity approach introduces the concept of the liquid phase ratio [173], representing the percentage of liquid material within a control volume during phase change. The phase interface movement is indirectly determined by this ratio, ranging from 0% to 100% based on the enthalpy balance [174]. The simulation was executed in 3D with double precision. A pressure-based coupled technique was employed to solve the momentum and continuity equations, and the natural convection of the PCM was predicted using a gravitational vector along the y-axis with a magnitude of -9.8 m/s². To handle pressure-velocity coupling, the SIMPLEC algorithm was implemented. Advection terms were modeled using a second-order upwind approach, while transient terms were addressed with a second-order implicit discretization scheme. Additionally, second-order pressure interpolation was applied for the transient calculations. The goal of achieving rapid convergence drove these choices (The detailed numerical methods used in the CFD modeling, including discretization schemes and solver settings, are summarized in **Annex 4**).

Table IV. 1 : The dimensions of the baffles.

Name	Design	Dimensions
Baffle for tank 02		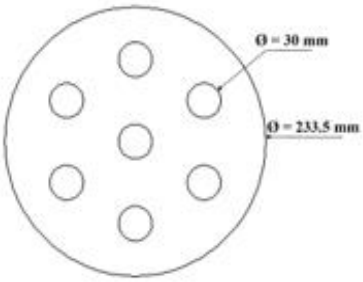
Baffle for tank 03 and tank 05		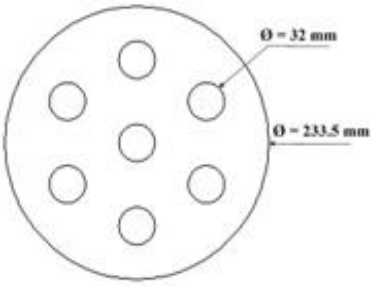
Baffle for tank 04		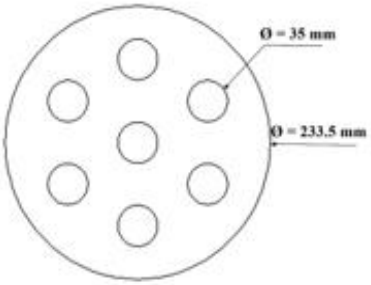
Baffle for tank 06		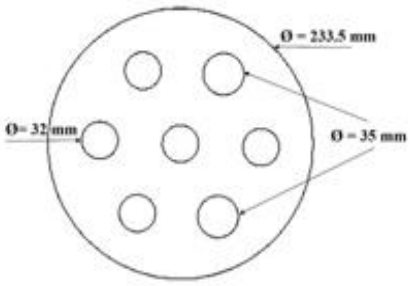

This study examined the thermal stratification characteristics of the heat storage tank using transient 3D models. The analysis was based on several key assumptions. First, the fluid in the system (water) was assumed to be incompressible. Second, the complexity of the system was addressed through numerical modeling in three dimensions. Third, the PCM (paraffin RT48) was considered isotropic, with constant thermal properties in both its solid and liquid states. However, the density of the liquid phase was treated as temperature-dependent, based on the Boussinesq approximation, allowing for temperature-driven changes in density. The tank walls were modeled as adiabatic, implying no heat exchange with the surroundings. Additionally, viscous dissipation and the effects of temperature on pressure were assumed to be negligible [203]. While the study did not directly address radiative heat transfer, these assumptions enabled the simulations to provide valuable insights into the thermal behavior of the PCM-enhanced heat storage tank. The transient 3D modeling offered a detailed analysis of the system's thermal stratification, accounting for the phase change dynamics of the PCM (paraffin RT48) (**Table IV.2**).

Table IV. 2 : Physical properties of RT 48.

Melting temperature (K)	Latent heat (J/kg)	Thermal conductivity (W/m.K)	Density (kg/m^3)	Specific heat capacity (J/kg.K)
323.15	130000	0.25 (Solid) 0.16 (Liquid)	920 (Solid) 780 (Liquid)	2100 (Solid) 1600 (Liquid)

IV.2.2-Governing equations

Using the Navier–Stokes and energy equations, this study evaluated the thermal stratification characteristics within the TES tank. Gravitational effects were also incorporated to accurately simulate natural convection phenomena. The governing equations employed in this analysis are presented in Chapter II.

IV.2.3-Boundary conditions and initial conditions

The study evaluates the impact of various operational parameters on the heat storage capabilities of the domestic hot water tank. The boundary conditions for the tank include velocity-inlet boundaries at the entrance and an outflow boundary condition for the exit. The initial water

temperature within the heat storage tank was set at 298.15 K, while the inlet water temperature was 353.15 K, with a flow rate of 25 L/h (**Figure IV.4)**.

$$t = 0 \rightarrow T(r,\theta,z,t=0) = T_{ini} = 298.15K \quad \text{(IV.1)}$$

$$\forall t \geq 0, T_{inlet} = 353.15K, Q = Q_{inlet} = 25\,{}^{L}\!/_{h} \quad \text{(IV.2)}$$

The no-slip boundary condition was implemented along the wall, ensuring that the water velocity at the wall surface approaches zero. This condition is described by Equation (IV.3):

$$\begin{cases} u_r = 0 \\ u_\theta = 0 \\ u_z = 0 \end{cases} \quad \text{(IV.3)}$$

If the tank is considered thermally insulated, the adiabatic boundary conditions of the wall can be determined [204]. The adiabatic boundary condition for the tank is expressed by Eq (IV.4):

$$\frac{\partial T}{\partial r} = \frac{\partial T}{\partial \theta} = \frac{\partial T}{\partial z} = 0 \quad \text{(IV.4)}$$

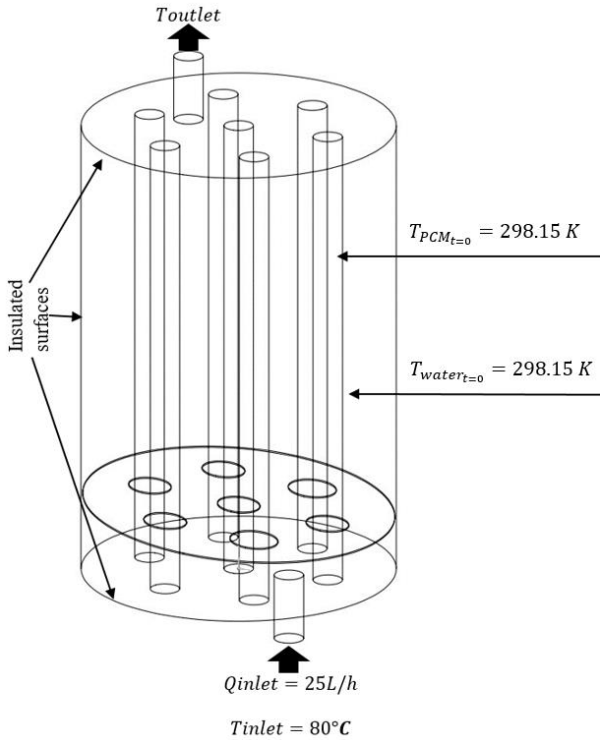

Figure IV. 4 : Initial and boundary conditions imposed in this work.

where, β represents the thermal expansion coefficient (1/K), g is the gravitational acceleration, L_{PCM} denotes the characteristic length of PCM cylinders, ν_{PCM} is the kinematic viscosity of the PCM, and α_{PCM} is the thermal diffusivity of the PCM.

IV.2.4-Time step independence

Ensuring time step independence is essential in transient simulations, as it directly affects the balance between numerical accuracy and computational efficiency. Larger time steps can lead to convergence issues, while smaller steps increase computation time significantly. This study evaluated time step intervals of 0.25, 0.5, and 1 second for temperature variations in Tank 06. **Figure IV.6-(A)** shows only minor differences in the results, leading us to select a time step of 1 second. This choice was made to balance accuracy with computational efficiency, reducing simulation time while still ensuring reliable results. A time step of *dt = 1*s resulted in a Courant-Friedrichs-Lewy (CFL) number of 2.25, which is within the optimal range of 0.5 to 10, as indicated by the study [205]. Several studies have explored time step independence in TES tanks with PCM.

IV.2.5-Mesh independence

The grid number is a critical factor in determining calculation accuracy. This study investigated three different mesh sizes for analyzing water temperature in Tank 06: 741,553, 790,820, and 850,522. **Figure IV.6-(B)** shows the subtle differences in results across these mesh sizes. To balance computational efficiency and accuracy, we chose the smaller mesh size of 741,553. This choice allowed us to optimize computational performance while maintaining the required accuracy.

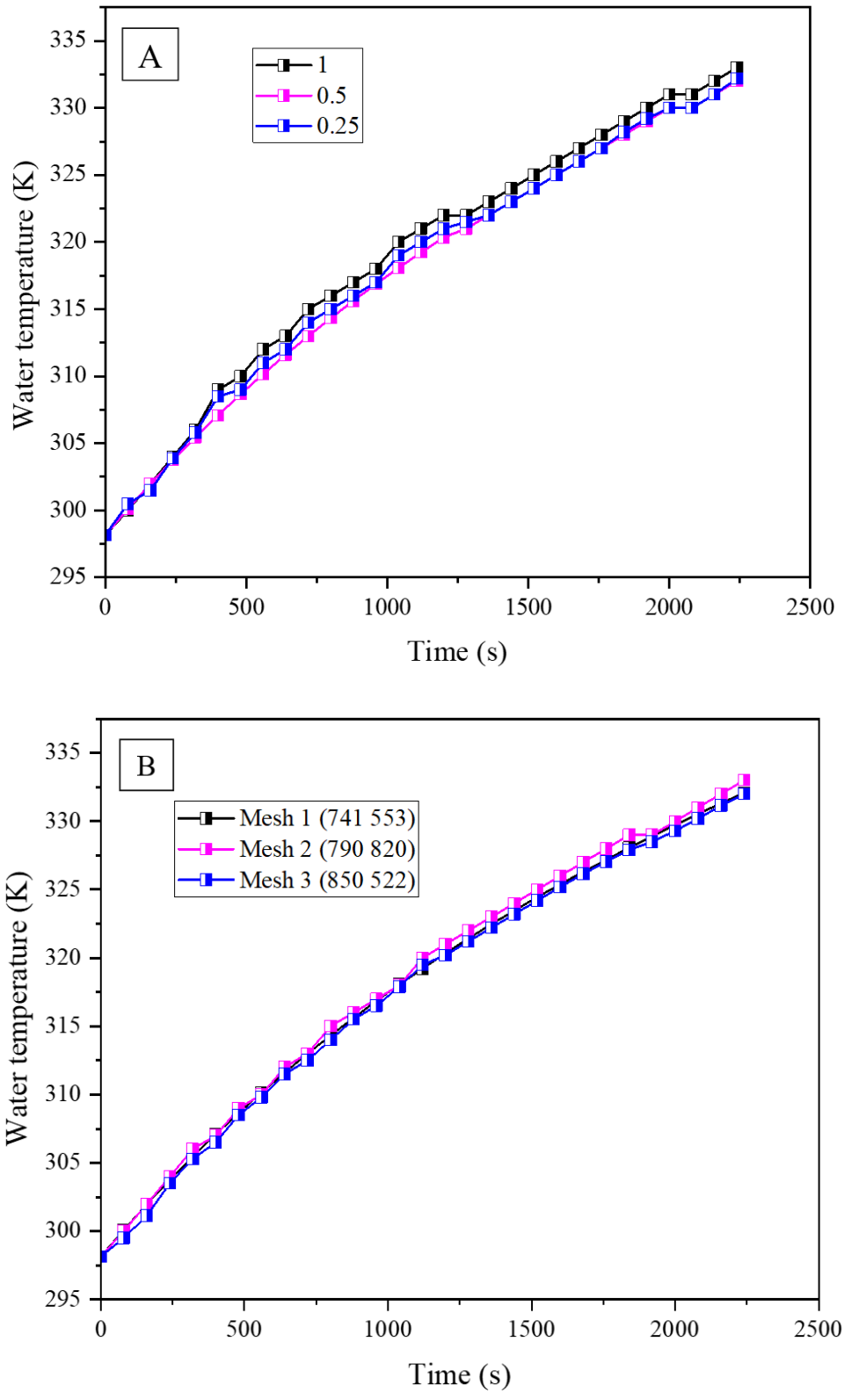

Figure IV. 5 : Independency study for tank 06: (A)-Time step independence, and (B)-Mesh independence.

IV.3-Results and discussion

IV.3.1-Temperature distribution

In **Figure IV.7**, reveals that Tank 06 achieves the most favorable water temperature distribution, while Tank 01 displays the least uniform distribution. Tank 06 outperforms the other tanks, maintaining a more consistent temperature profile. Tanks 02, 03, 04, and 05 exhibit temperature distributions that fall between those of Tank 01 and Tank 06, indicating varying levels of performance in terms of temperature uniformity.

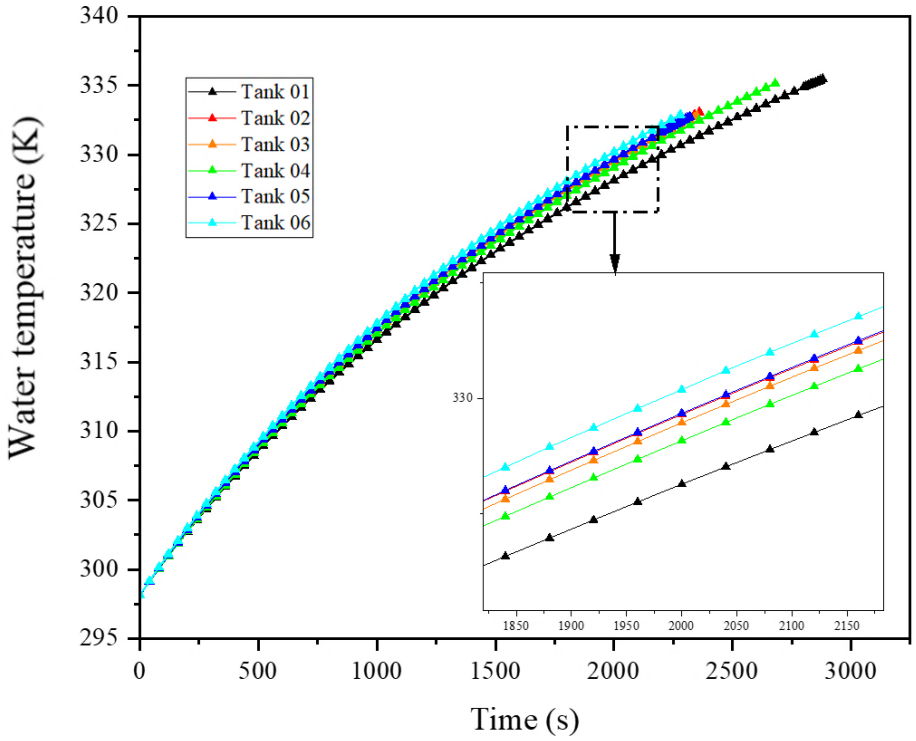

Figure IV. 6 : The temperature distribution within the tanks studied in this work.

In **Figure IV.8**, the PCM temperature in Tank 06 is the most optimal, consistently maintaining temperatures close to the desired target. This indicates efficient heat transfer and uniform thermal performance. Tanks 02, 03, 04, and 05 show higher PCM temperatures than Tank 01, yet remain lower than Tank 06, reflecting improved heat transfer and melting rates due to the modifications (**Figure IV.9**), though not as effectively as in Tank 06.

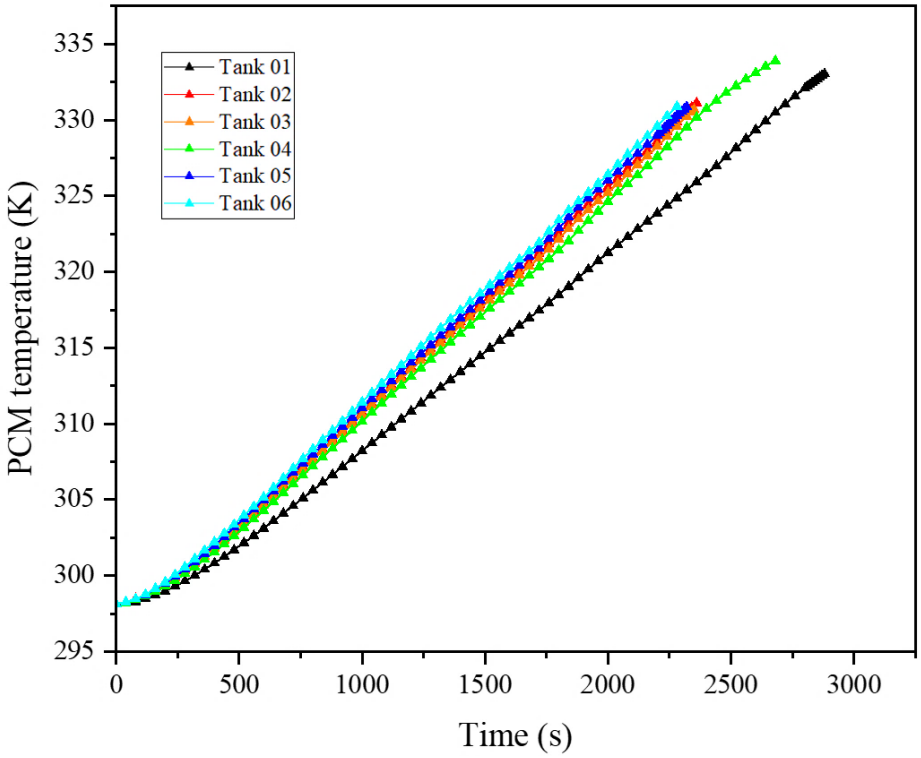

Figure IV. 7 : Temperature distribution of phase change materials for all tanks.

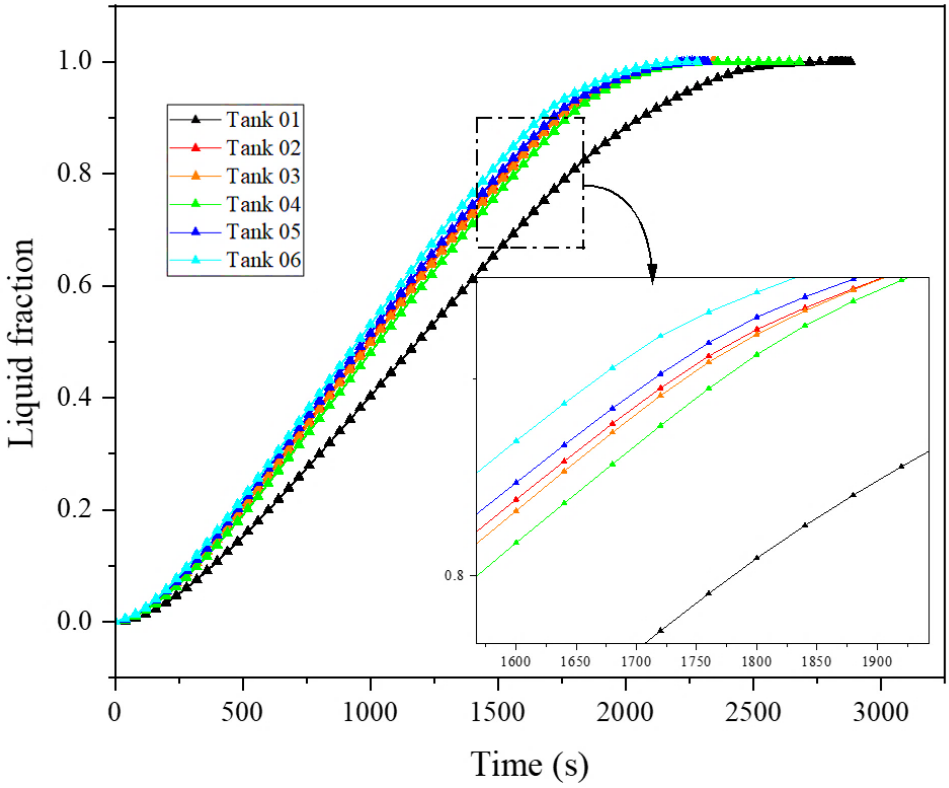

Figure IV. 8 : The melting process`s global liquid fraction.

In **Figure IV.10**, the outlet temperature analysis shows that Tank 01, without a baffle, has the highest outlet temperature, driven by the buoyancy effect, as hot water rises to the top and exits the tank. In contrast, Tanks 02, 03, 04, and 05, which include a baffle, exhibit lower outlet temperatures, indicating that the baffle's presence influences the outlet temperature. Tank 06, with its inclined baffle and perforations, displays fluctuating outlet temperatures due to the complex fluid flow and heat transfer patterns created by the baffle's design. The inclined baffle redirects hot water through the holes, adding complexity to the flow, which can cause temperature oscillations at the outlet. Tanks 02 through 04, lacking the inclined baffle, show more stable outlet temperatures compared to Tank 06.

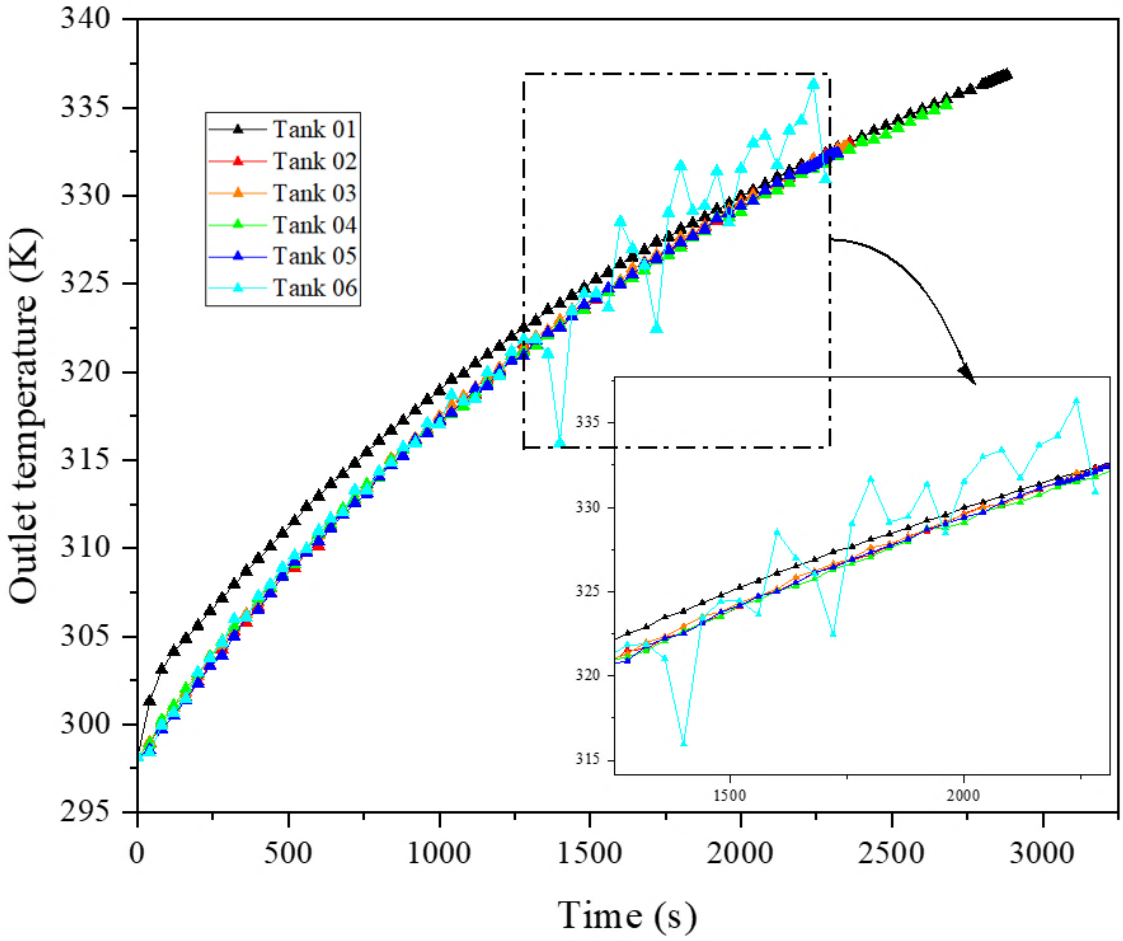

Figure IV. 9 : The outlet temperature for all tanks studied in this work.

The heat transfer blind zone issue in Tank 01, where the lower part of the tank experiences relatively lower temperatures due to natural convection, was addressed through strategic design modifications to improve fluid circulation and distribute heat more evenly. This blind zone results from hot water rising to the tank's upper section, leaving cooler water near the bottom. To mitigate this, a baffle with a diameter of 233.5 mm and seven 30 mm holes was introduced in Tank 02. These changes significantly reduced the blind zone and led to a more uniform internal temperature distribution compared to Tank 01. The improved fluid flow facilitated by the baffle design also enhanced the overall heat transfer efficiency, reducing temperature gradients and promoting greater thermal uniformity within the tank (**Figure IV.11)**.

However, the hot water primarily flowed through the hole directly aligned with the inlet, as well as the two adjacent holes near the inlet. In Tank 03, the hole diameter was increased to 32 mm in an attempt to promote a more uniform distribution of hot water across all the holes. Despite this modification, the flow remained concentrated through the hole facing the inlet and the two nearby holes on the right side of the tank. Consequently, Tank 03 displayed a marked temperature asymmetry, with the right side exhibiting significantly higher temperatures than the left. This uneven thermal distribution underscored the need for further optimization of the baffle design and hole arrangement to enhance fluid flow and ensure thermal uniformity throughout the tank (**Figure IV.12**).

In Tank 04, the hole diameter was further increased to 35 mm, which enhanced natural convection but also intensified the issue of heat transfer limitations in the blind zone. Despite the adjustment, hot water continued to flow predominantly through the same set of holes near the inlet, maintaining the original, uneven flow pattern. The stronger natural convection induced by the larger hole size further exacerbated the temperature imbalance within the tank. These results highlight that simply increasing hole diameter is insufficient to resolve the underlying issue of non-uniform temperature distribution. The findings emphasize the intricate interplay between baffle geometry, fluid flow, and thermal performance, suggesting that a more integrated design strategy is essential for achieving uniform heat transfer and optimal TES efficiency (**Figure IV.12**).

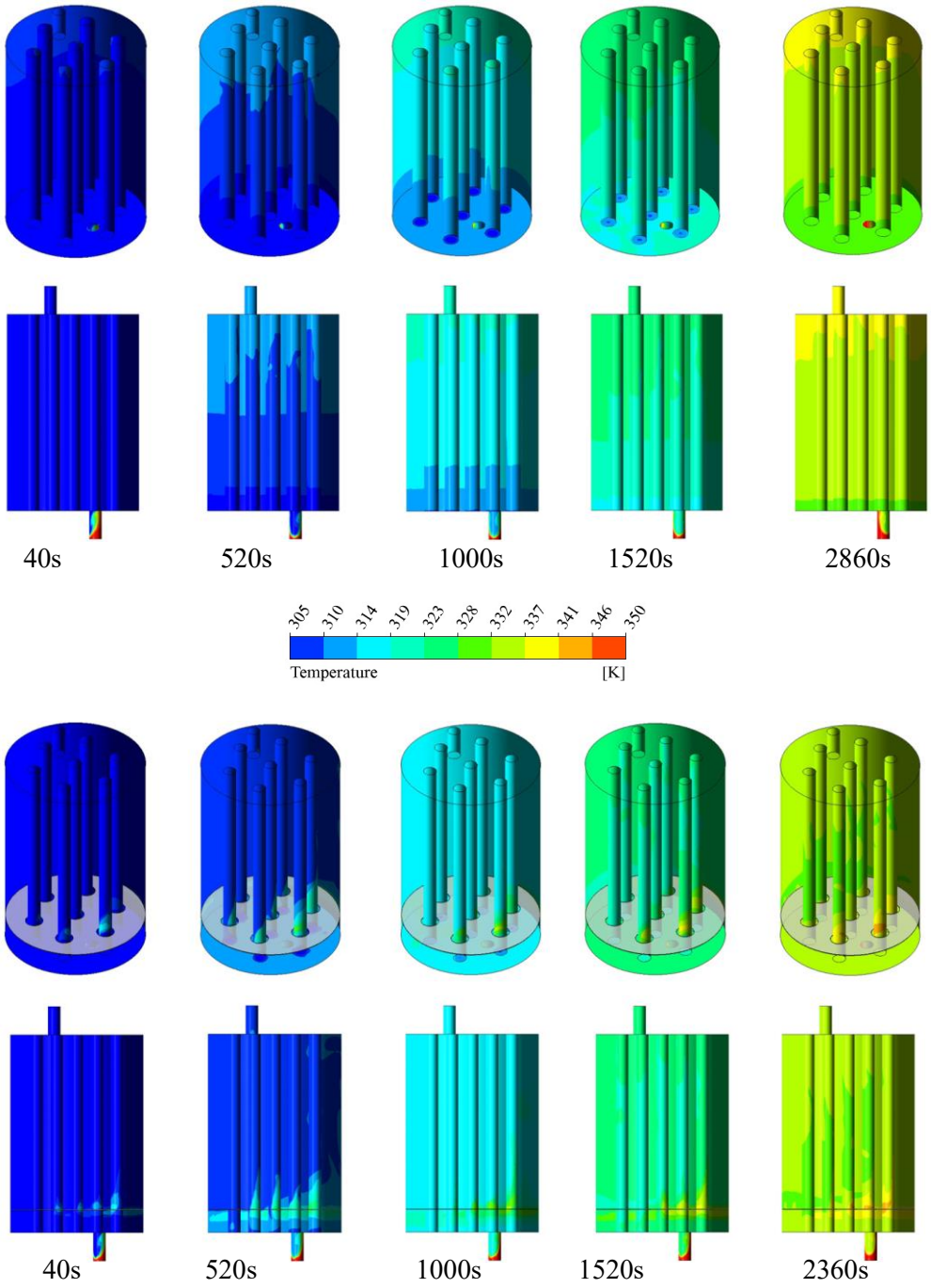

Figure IV. 10 : The temperature contours for tank 01 and tank 02.

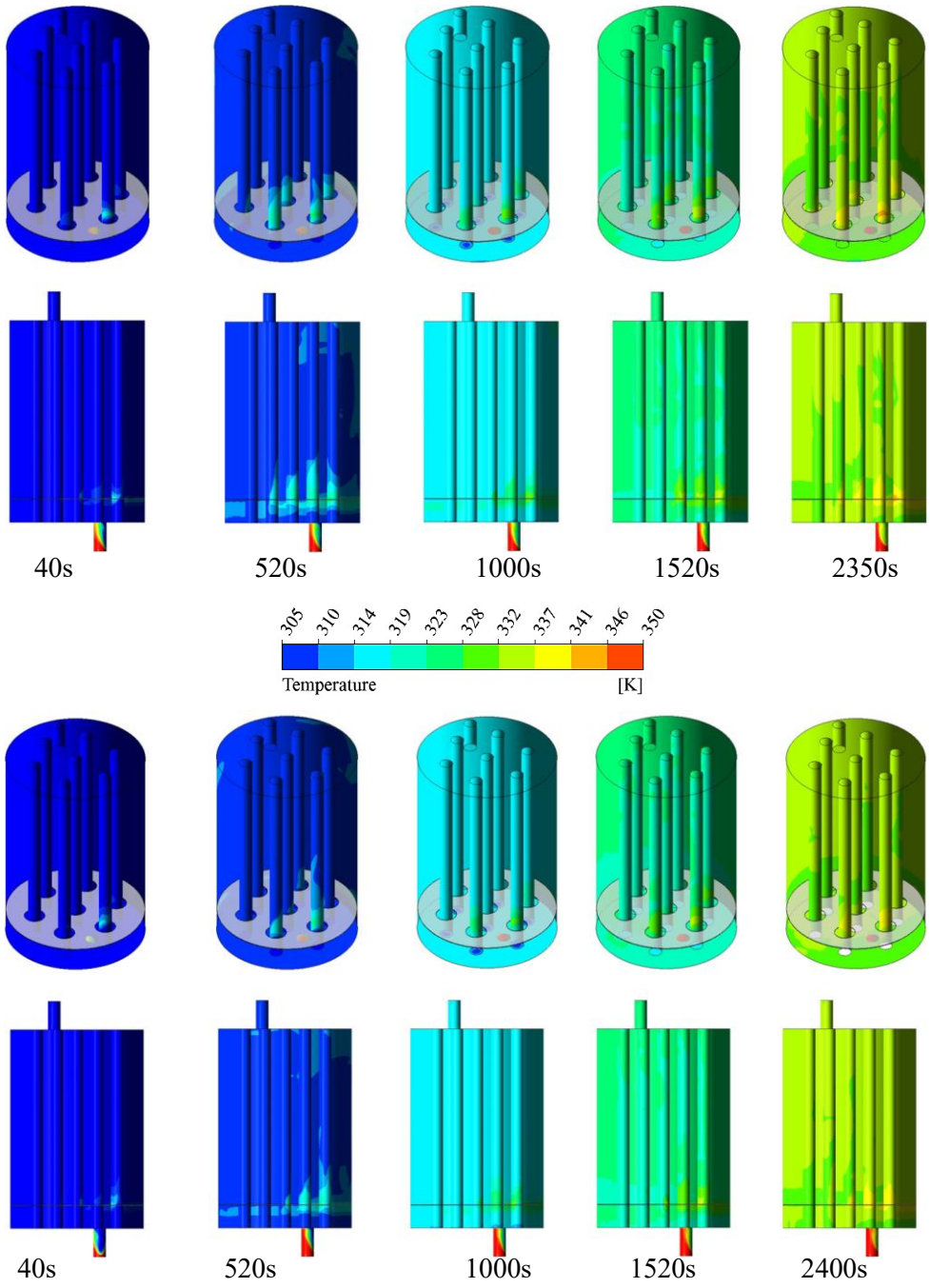

Figure IV. 11 : The temperature contours for tank 03 and tank 04.

In Tank 05, an inclined baffle with a 5° angle and seven 32 mm holes was introduced to enhance heat transfer and fluid flow. The 32 mm hole size was selected based on the results from Tank 03, which demonstrated faster PCM melting times compared to Tanks 02 and 04. This design modification helped redirect hot water to the left side of the tank, although the two holes near the

inlet continued to present challenges as hot water did not flow through them. The 5° inclination was chosen as the optimal angle to direct hot water toward the left side of the tank, with the PCM cylinders strategically positioned in the center of the holes. This adjustment aimed to enhance heat transfer by ensuring more uniform contact between the hot water and the PCM cylinders, thereby improving the overall efficiency of the TES system (**Figure IV.13**).

In Tank 06, which features a 5° inclined baffle, the final design solution involved enlarging the two critical holes near the inlet to 35 mm, while maintaining the remaining five holes at 32 mm. This adjustment enabled the hot water to pass uniformly through all seven holes, significantly enhancing heat transfer and ensuring direct contact with all PCM cylinders. As a result, melting times were reduced, temperature distribution became more uniform, and the previously identified heat transfer blind zone was effectively eliminated enhancing the tank's overall thermal performance (**Figure IV.13**).

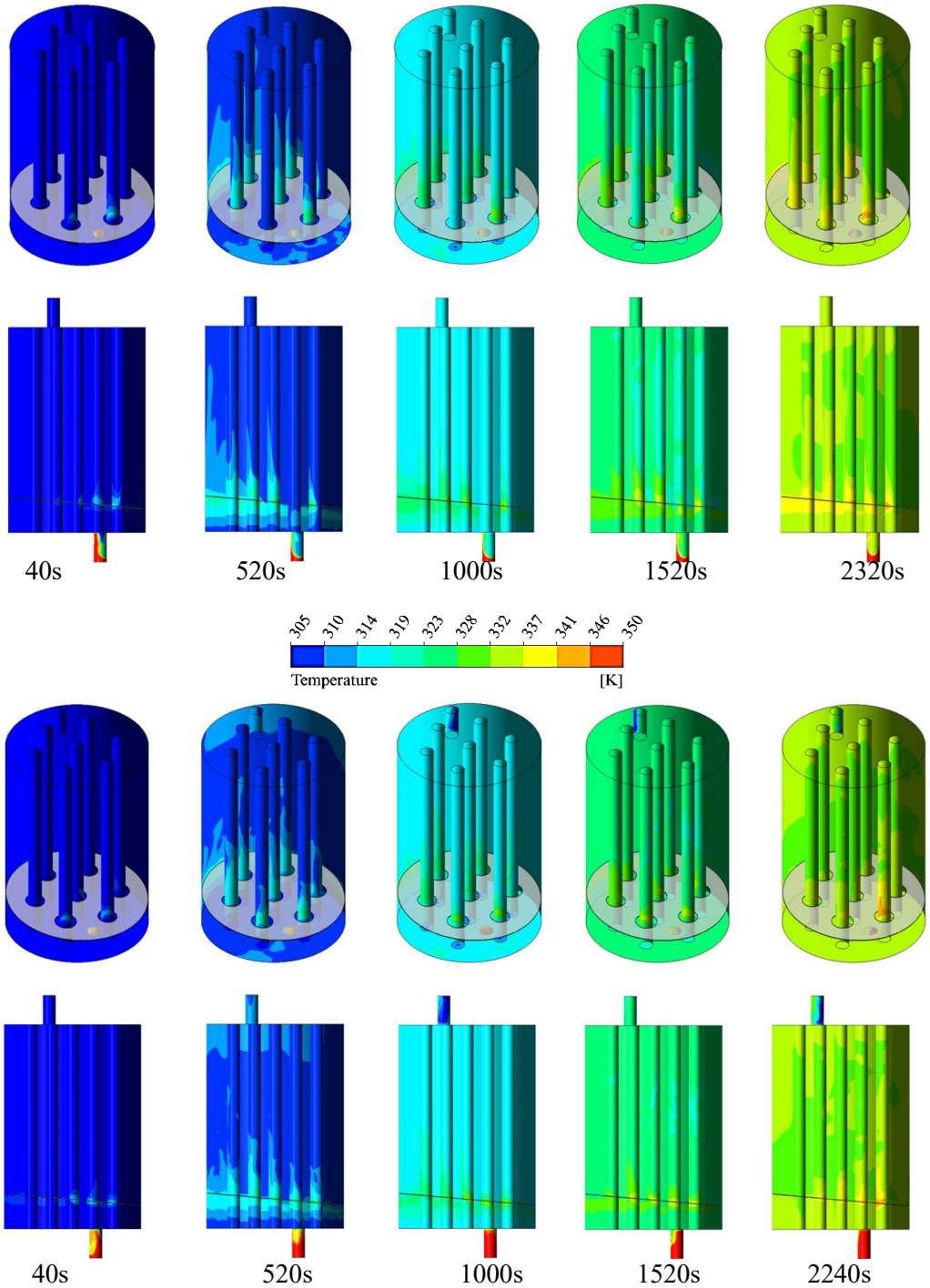

Figure IV. 12 : The temperature contours for tank 05 and tank 06.

In the original tank (Tank 01), a heat transfer blind zone was observed at the bottom of the tank, primarily due to buoyancy forces. As heated water entered the tank, it naturally rose to the top, resulting in delayed melting of the PCM cylinders located at the bottom (**Figures IV.11** and **IV.14)**.

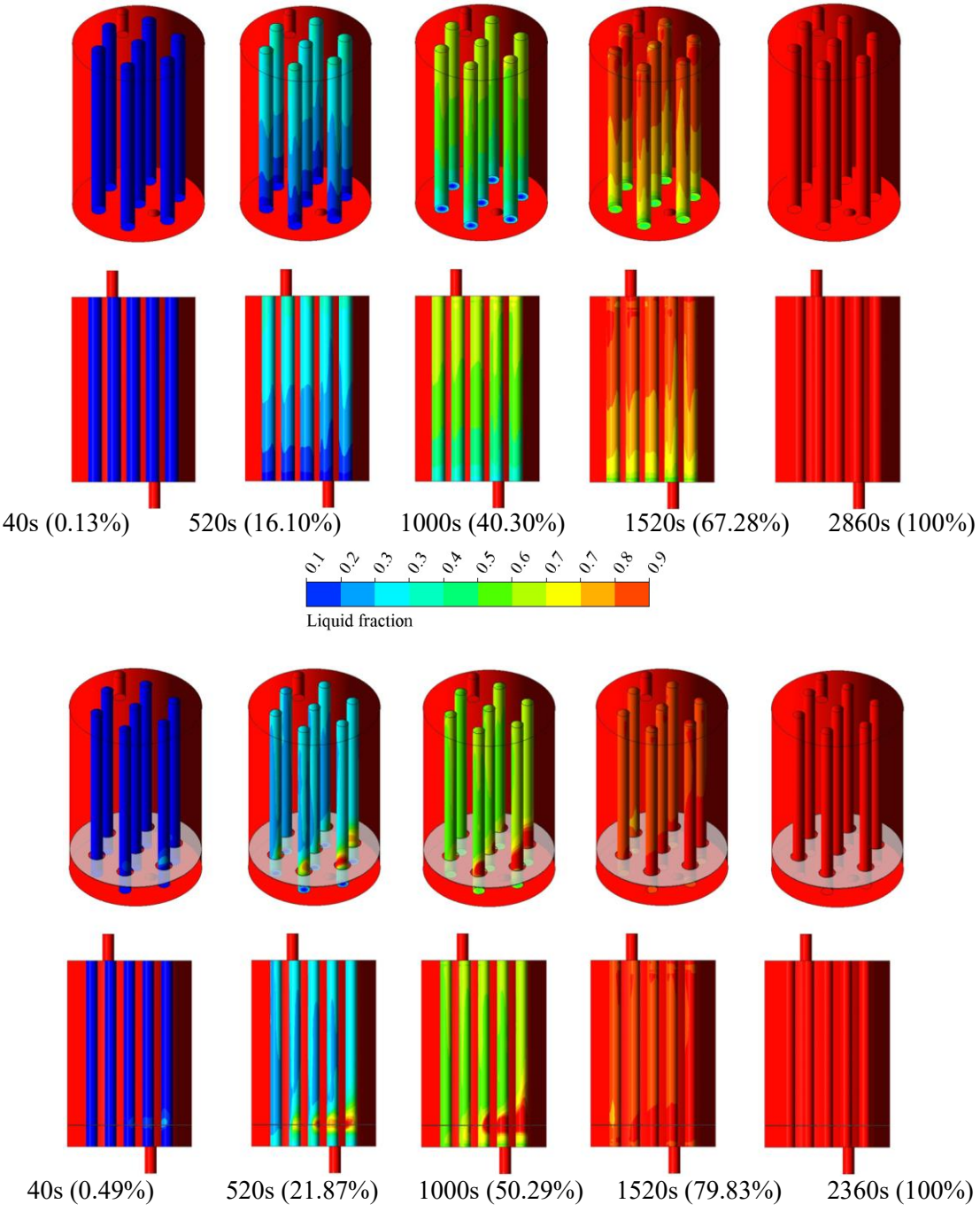

Figure IV. 13 : The liquid fraction contours for tank 01 and tank 02.

In Tank 02, a baffle with seven 30 mm holes was introduced to address the heat transfer blind zone at the bottom of the tank. This baffle acted as a barrier to prevent the hot water from rising too quickly, thereby improving heat transfer at the base. As a result, the hot water was redirected through the holes, making contact with the PCM cylinders and enhancing the overall heat

distribution. The melting time was significantly reduced from 2860 s to 2360 s, as illustrated in **Figures IV.11** and **IV.14**.

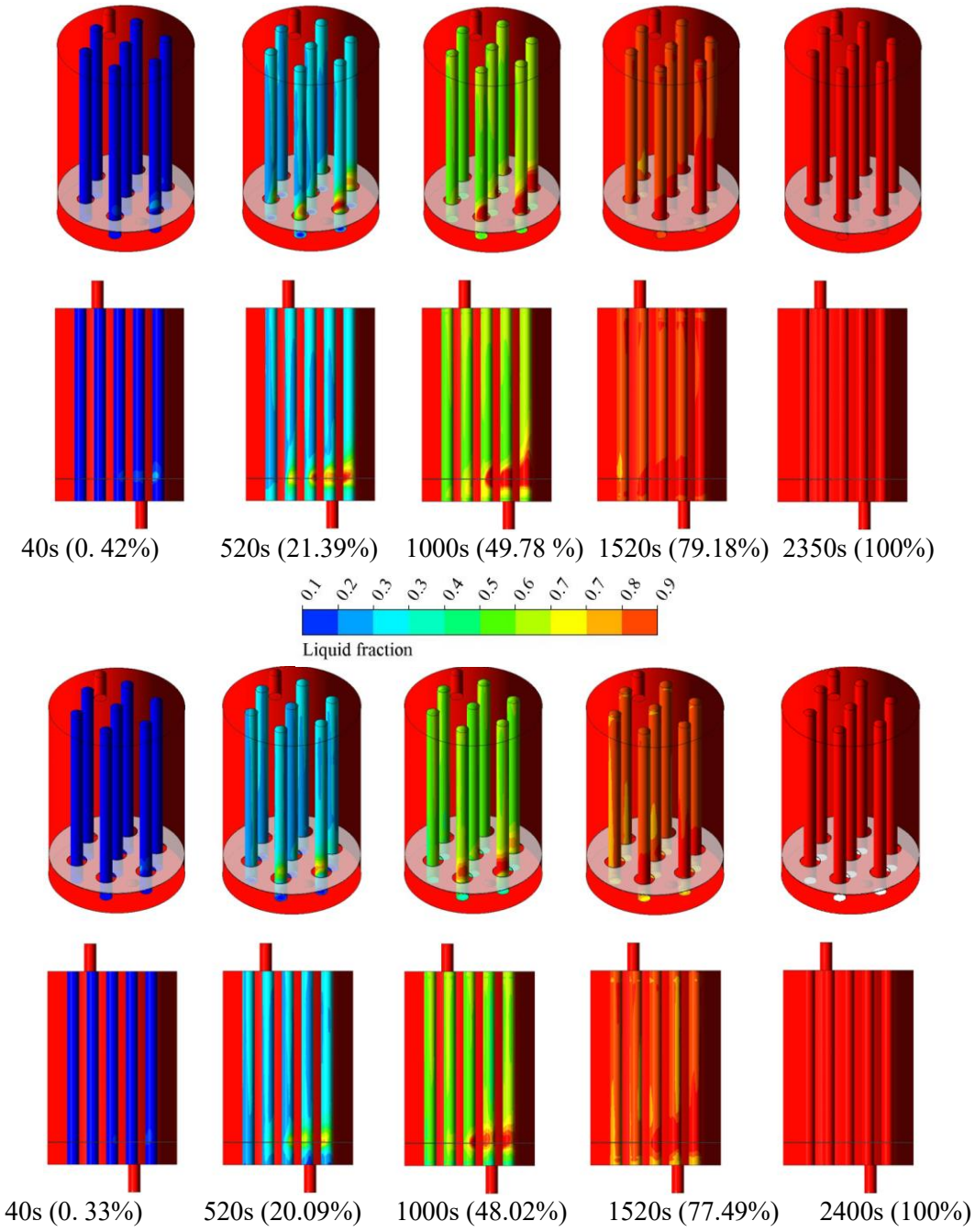

Figure IV. 14 : The liquid fraction contours for tank 03 and tank 04.

In Tanks 03 and 04, adjustments were made to the hole diameters in the baffle to further enhance heat diffusion. Increasing the hole diameter to 32 mm in Tank 03 led to slight

improvements in heat distribution, but the reduction in melting time was minimal, with a time of 2350s only slightly better than Tank 02. However, when the hole diameter was further increased to 35 mm in Tank 04, the hot water predominantly rose toward the top of the tank. This resulted in a longer melting time of 2400s, compared to Tanks 02 and 03. These variations highlighted the significant impact of the baffle design on fluid flow patterns and buoyancy forces, ultimately influencing the overall heat transfer within the tank (**Figures IV.12** and **15)**.

Introducing an Inclined Baffle (Tank 05): To improve heat transfer and resolve the flow imbalance near the inlet, Tank 05 was equipped with an inclined baffle angled at 5°. This design adjustment redirected the hot water flow to the holes on the left side of the tank, improving the distribution of heat and contact with all PCM cylinders. As a result, the PCM melting time was reduced to 2320s, demonstrating more efficient thermal performance (**Figures IV.13** and **16)**.

In Tank 06, the issue of limited water flow through the two right-side holes near the inlet was resolved by enlarging their diameters to 35 mm, while keeping the remaining holes at 32 mm. This adjustment facilitated more uniform hot water distribution across the tank, enabling consistent contact with all PCM cylinders. Consequently, the PCM melting process was accelerated, reducing the total melting time to 2240s, as illustrated in **Figures IV.13** and **IV.16**.

Analyzing melting durations across various baffle configurations provides critical insight into their impact on thermal efficiency. As detailed in **Table IV.4**, the inclusion of baffles in Tanks 02 to 06 led to melting time reductions ranging from 16.08% to 21.67%, highlighting their effectiveness in enhancing heat transfer and expediting energy storage. These results emphasize the importance of optimizing baffle geometry, hole size, and placement to improve thermal performance and ensure more uniform temperature distribution within PCM-based storage systems.

Shortened melting times indicate enhanced system performance and more effective energy utilization, which are essential for real-world TES applications. Accelerated heat storage not only improves responsiveness but also boosts the overall energy efficiency of the system.

Assessing the environmental impact of the proposed system is equally important. A life cycle assessment (LCA) offers valuable insights into energy consumption, emissions, and resource usage throughout the system's lifespan. Moreover, the environmental effects of PCM manufacturing and disposal should be carefully considered. Adopting sustainable production methods and exploring

eco-friendly PCM alternatives can significantly minimize the system's overall ecological footprint.

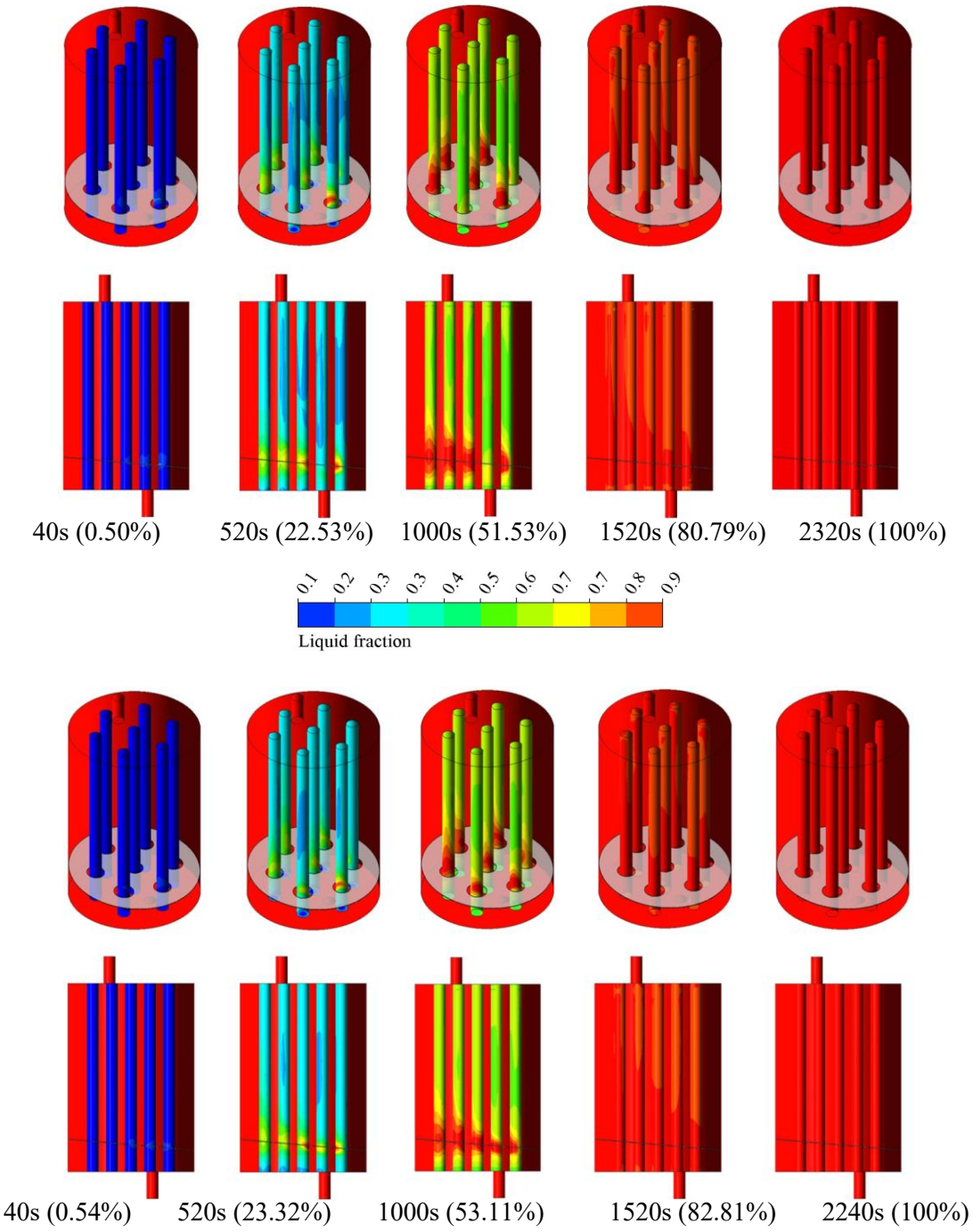

Figure IV. 15 : The liquid fraction contours for tanks 05 and 06.

Table IV. 3 : Summary of Total Melting Time, Decrease in Melting Time Ratio, and Maximum Thermal Storage Efficiency for All Tanks.

Tanks	Melting time	The reduction of the melting time	The maximum thermal storage efficiency
Tank 01	2860 s	-	67.55 %
Tank 02	2360 s	17.48 %	63.48%
Tank 03	2350 s	17.83%	62.97%
Tank 04	2400 s	16.08%	63.03 %
Tank 05	2320 s	18.88%	62.89%
Tank 06	2240 s	21.67%	62.51%

IV. 3.2-Heat flux

During the melting phase, the TES tank is supplied with hot water, which acts as the primary heat source to trigger the phase change of the solid PCM. This hot water enters the tank and directly interacts with the PCM, initiating the heat transfer process necessary for melting.

As the hot water interacts with the solid PCM, it transfers TES to the PCM, causing it to transition from a solid to a liquid state. This transfer of heat from the hot water to the PCM is termed the "water heat flux," which measures the rate at which the hot water loses heat as it provides the energy necessary to melt the PCM [199]. Concurrently, the PCM absorbs this heat, leading to a steady increase in its temperature. This absorbed energy enables the PCM to undergo a phase change and store thermal energy in its liquid form. The rate at which the PCM absorbs heat during this phase change is referred to as the "PCM heat flux."

IV.3.2.1-Water heat Flux

Tank 01 exhibits the highest water heat flux among all tanks due to the absence of a baffle. Without a baffle to control the flow, the hot water rises rapidly to the top and exits the tank quickly. As a result, Tank 01 requires a higher water heat flux to fully melt the PCM, necessitating greater hot water flow through the PCM region. The peak water heat flux observed in Tank 01 is 216.69 W/m^2.

In contrast, Tank 06 shows the lowest water heat flux, with a maximum value of 109.97 W/m². This is because the inclined baffle with holes effectively redirects the hot water flow and increases its contact with the PCM, facilitating efficient heat transfer and reducing the water heat flux needed to melt the PCM.

Tanks 02, 03, 04, and 05, which also include baffles, experience reduced water heat flux compared to Tank 01. The baffles in these tanks help control the upward movement of hot water, promoting a more controlled and uniform flow. This results in a more even distribution of heat and a lower water heat flux, contributing to a more efficient melting process (**Figure IV.17**).

The analysis of heat flux underscores its importance in evaluating the effectiveness of baffle modifications. It highlights how baffle design influences heat transfer efficiency and uniform temperature distribution within PCM tanks, ultimately facilitating and accelerating the PCM melting process.

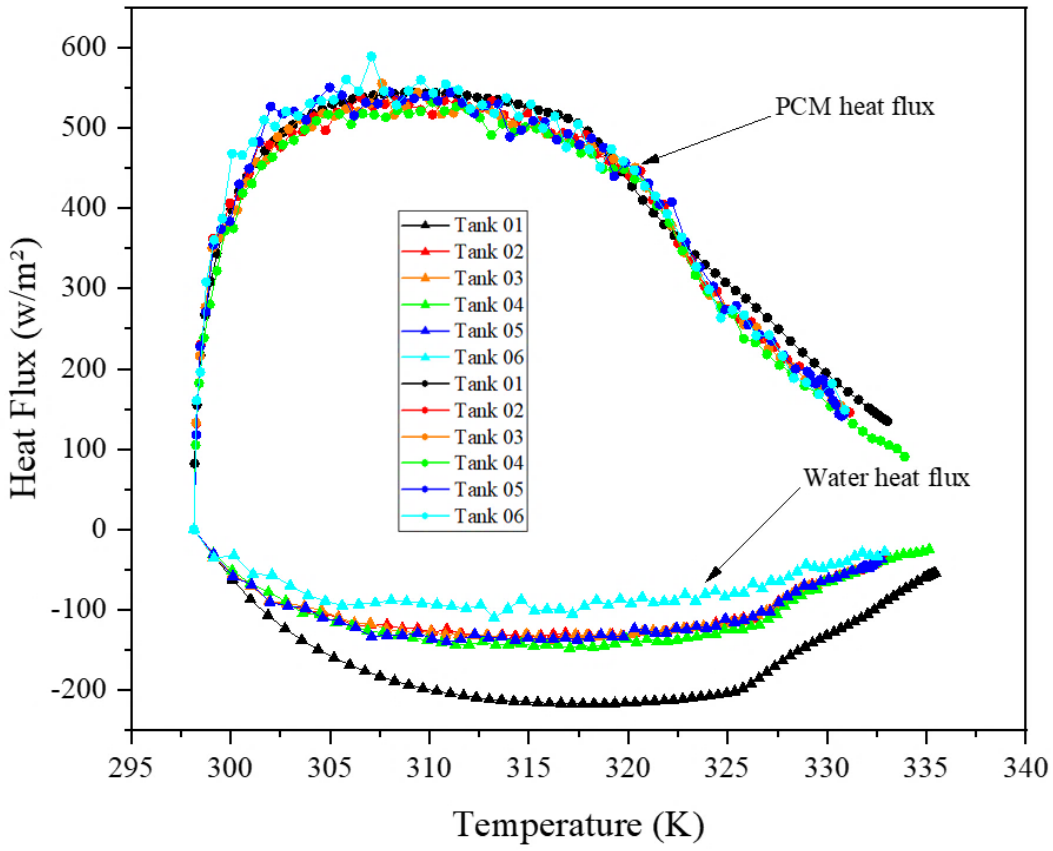

Figure IV. 16 : The PCM and water heat flux within the tanks.

IV.3.2.2-PCM heat Flux

Tank 06 demonstrates the highest PCM heat flux, indicating superior heat transfer and accelerated PCM melting. This performance is attributed to the inclined baffle design, which enhances contact between the hot water and PCM, leading to faster melting and reduced water-side heat flux. Likewise, Tanks 02 through 05 show notable PCM heat flux improvements due to the inclusion of baffles and structural adjustments that promote more effective thermal exchange within the tank.

In contrast, Tank 01, despite occasionally showing comparable PCM heat flux, experiences fluctuations because of the absence of a baffle. The uncontrolled flow of hot water in Tank 01 leads to varying PCM heat flux, making it less efficient in maintaining consistent heat transfer (**Figure IV.17**).

Variations in water and PCM heat flux across the tanks are closely linked to the influence of baffles and the resulting flow dynamics. In Tank 01, the absence of flow regulation leads to inefficient heat distribution, requiring higher water heat flux to achieve complete PCM melting. In contrast, Tank 06, equipped with an optimized baffle configuration, promotes uniform temperature distribution and minimizes the water heat flux needed. Tanks 02 to 05 show moderate improvements, offering enhanced thermal performance compared to Tank 01 but falling short of the efficiency observed in Tank 06. These results highlight the critical role of strategic flow control and thermal management in improving heat transfer and melting efficiency within TES systems.

The melting dynamics and heat exchange between the PCM and hot water in the TES tank offer valuable insight into the heat flux trends illustrated in **Figure IV.17**.

At the onset of the process, hot water enters the tank and immediately begins transferring thermal energy to the solid PCM. As this transfer occurs, the PCM starts to melt, absorbing heat from the hot water. During this phase, the water heat flux decreases because the hot water gradually loses heat to the PCM, as well as through the tank's outlet. This decline in water heat flux is a result of the decreasing temperature gradient between the hot water and the PCM as the PCM heats up.

Simultaneously, the PCM begins to absorb heat, leading to an increase in the PCM heat flux. This heat absorption intensifies as the PCM approaches its melting point, where the phase change from solid to liquid occurs. During this transition, the PCM absorbs a large amount of latent heat,

which is reflected in a peak in the PCM heat flux. The melting process sustains this elevated heat absorption rate until most of the PCM has transitioned to the liquid phase.

In summary, the initial decline in water heat flux, followed by a rise in PCM heat flux, is driven by the dynamic thermal exchange as the PCM absorbs heat during its phase change, illustrating the intricate interplay between heat transfer and phase change phenomena within the TES tank.

After a period of sustained heating, the PCM within the tank undergoes complete melting, resulting in a relatively uniform temperature distribution throughout the tank. At this stage, the phase change process is almost fully completed, and the PCM heat flux begins to decrease. This reduction in heat flux occurs because the remaining solid PCM gradually transitions into its liquid form, and as the PCM nears its fully melted state, the rate of heat absorption diminishes.

As the phase change concludes, the temperature difference between the hot water and the PCM decreases, further lowering the PCM heat flux. With the PCM now fully in its liquid state, its temperature remains relatively stable, assuming the continuous supply of hot water is maintained. At this point, the heat flux curves begin to stabilize, with both the water heat flux and PCM heat flux reaching relatively constant values. This indicates that the system has achieved a steady state, where the rate of heat transfer between the hot water and the now-liquid PCM has reached equilibrium.

IV.3.3-Velocity vectors

The velocity vector is crucial in understanding fluid flow dynamics and the impact of various tank modifications on heat transfer. Analyzing the velocity vectors for each tank, as shown in **Figure IV.18**, reveals distinct flow characteristics:

Tank 01: The velocity vectors illustrate a strong, direct upward movement of hot water entering the tank. This flow pattern is primarily due to buoyancy forces, where the hotter, less dense water naturally rises toward the surface. Additionally, natural convection, driven by temperature gradients within the tank, amplifies this upward flow, promoting the movement of high-temperature water.

Tanks 02, 03, and 04: The Adding a baffle with holes causes the velocity vectors to demonstrate that hot water predominantly flows through the openings on the right side of the tank, particularly

the hole facing the inlet and the two closest to it. This results in a concentrated flow pattern on the right side, enhancing heat transfer efficiency in that region. As the hot water rises, cooler water descends due to gravitational forces, creating a convection cycle with a counterclockwise flow pattern.

Tank 05: Including an inclined baffle, the velocity vectors reveal that the hot water is redirected toward the openings on the left side of the tank. This configuration allows the hot water to occupy more space on the left, resulting in a more evenly distributed flow. Consequently, the heat transfer is improved, with better contact between the hot water and the PCM cylinders.

Tank 06: The velocity vectors indicate that hot water flows through all the holes in the baffle, creating an optimized flow path that enhances heat transfer. This configuration ensures that the hot water comes into contact with all the PCM cylinders, leading to a uniform temperature distribution and a shorter melting time.

Overall, the velocity distribution within each tank demonstrates distinct characteristics that influence heat transfer performance. Tank 01 shows a strong upward flow of hot water, while Tanks 02, 03, and 04 have a concentrated flow on the right side. Tank 05 achieves a more balanced distribution with flow primarily on the left side, and Tank 06 offers optimal diffusion with hot water passing through all the holes. These distinct flow patterns are critical for understanding the heat transfer dynamics and overall efficiency of the TES tanks.

Figure IV.19 illustrates the velocity variation over time for Tank 03, highlighting the influence of temperature differences and natural convection on fluid flow:

Initially, at t = 40 s, the velocity of the hot water is very high, driven by the substantial temperature difference between the incoming hot water and the cooler water already in the tank. This sharp contrast in temperature generates strong buoyancy forces, leading to a vigorous upward flow through natural convection.

At t = 520 s, as the thermal energy is gradually transferred to the tank water, the overall temperature of the water increases. By this time, the temperature difference between the incoming hot water and the tank water has decreased compared to the initial state at t = 40 s. As a result, the

velocity begins to decrease, though it remains relatively elevated due to the ongoing effects of natural convection.

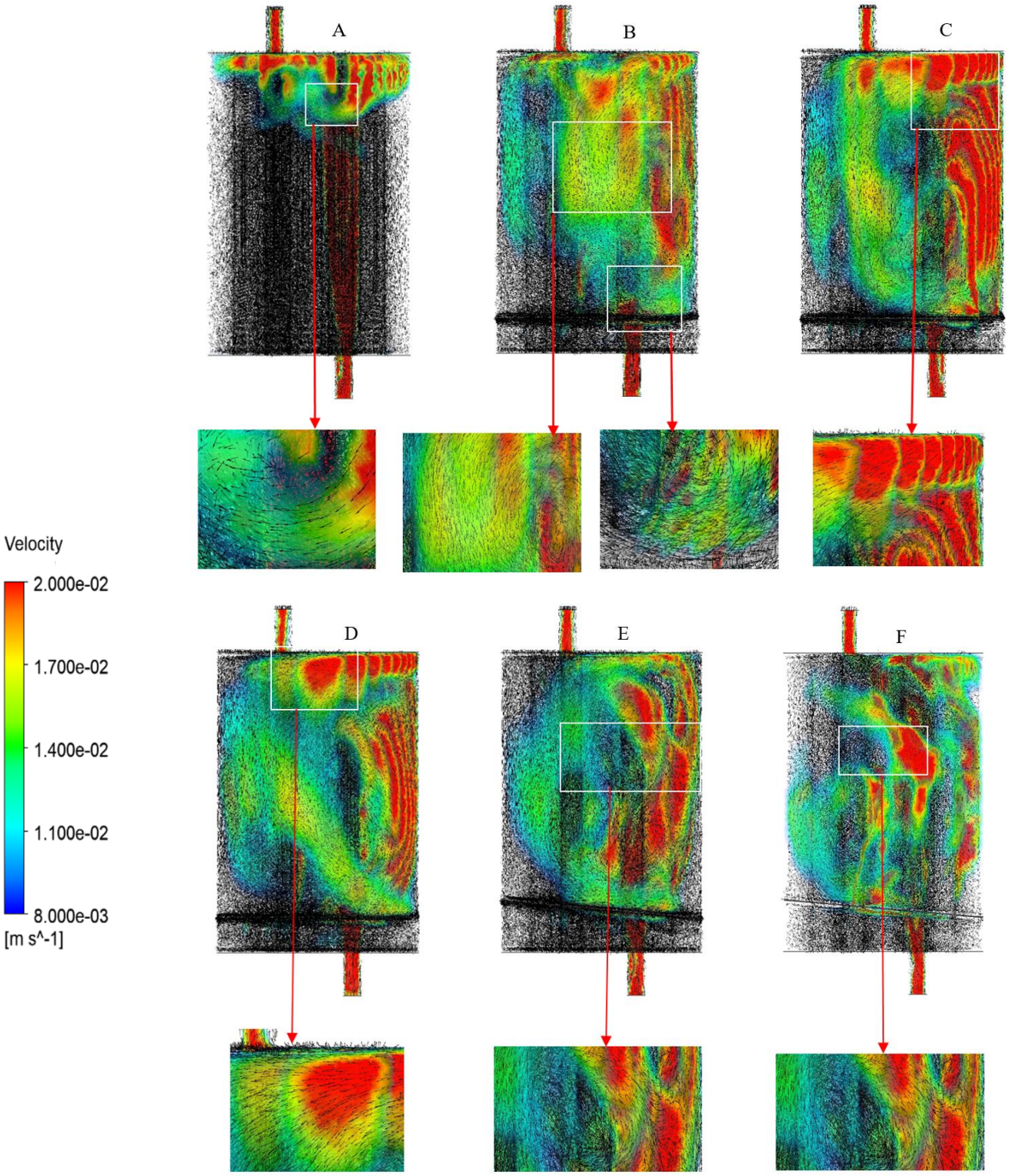

Figure IV. 17 : Three dimensions velocity vector profiles for all tanks at the 40 s: (A)-tank 01, (B)-tank 02, (C)-tank 03, (D)-tank 04, (E)-tank 05, (F)-tank 06.

At t = 1000 s, the velocity decreases further as the temperature difference between the incoming hot water and the water in the tank becomes even smaller. This reduced temperature gradient weakens the buoyancy forces and the natural convection currents they generate, resulting in a noticeable decline in velocity.

Likewise, at t = 1520 s and t = 2350 s, the velocity further declines due to the continued weakening of thermal gradients and reduced buoyancy effects. The temperature of the tank water is now much closer to that of the incoming hot water, which further reduces the driving force for natural convection. Throughout these intervals, the steady decline in velocity reflects the gradual balancing of temperatures between the incoming hot water and the water already in the tank. As this temperature difference continues to diminish, the strength of natural convection lessens, leading to a continuous decrease in velocity.

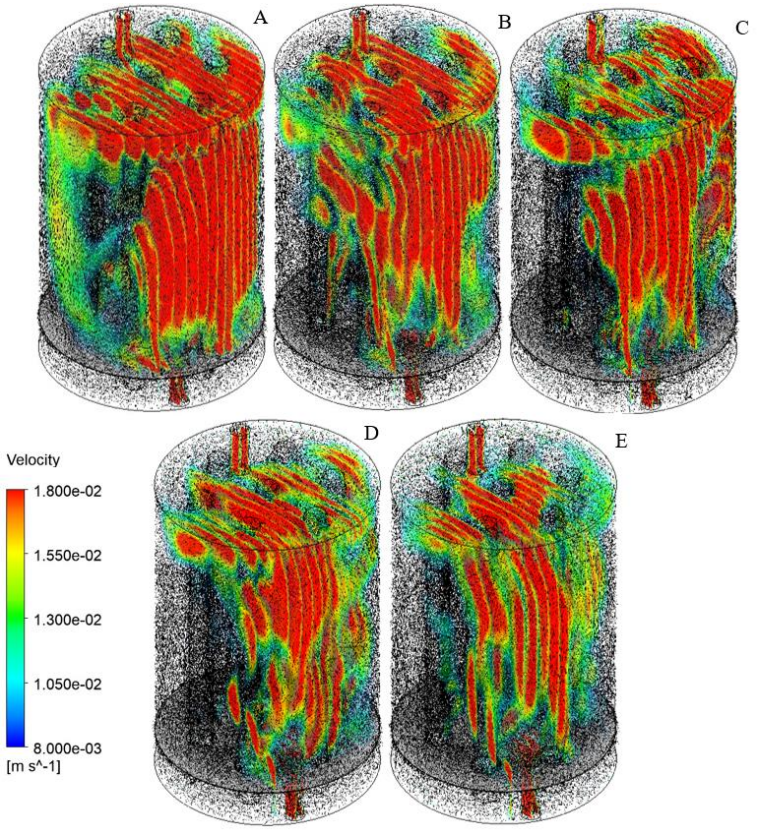

Figure IV. 18 : Velocity vector profiles for tank 03 at different times: A-at 40s, B-at 520s, C-at 1000s, D-at 1520s, E-at 2350s.

IV.3.4-Static enthalpy

Static enthalpy is a key thermodynamic property representing the total energy content of a fluid at a given temperature and pressure. It accounts for both the internal energy and the energy associated with pressure-volume work [208]. Within the scope of TES, static enthalpy plays a crucial role in quantifying the heat content of the PCM and the heat transfer fluid (typically water) in the storage system.

Tank 01 (**Figure IV.20-(a)**): The static enthalpy curves for both PCM and water in Tank 01 exhibit a slow, steady increase over time. In the absence of a baffle or any flow-guiding structure, hot water rises directly to the top due to buoyancy, limiting heat transfer to the PCM at the bottom. This uncontrolled flow leads to inefficient thermal distribution and delayed PCM melting. The PCM's enthalpy increases slowly, intersecting the water's enthalpy curve around 1000 seconds—after which it begins to rise more rapidly. This behavior reflects the PCM's limited and delayed heat absorption in Tank 01.

Tank 02 (**Figure IV.20-(b)**): Incorporating a baffle with seven 30 mm holes improves heat transfer by interrupting the vertical flow of hot water and promoting a more uniform thermal distribution. As a result, the PCM static enthalpy curve intersects the water enthalpy curve at approximately 750s, indicating earlier and more efficient heat absorption. Following this intersection, the PCM enthalpy rises more rapidly than the water’s, reflecting the enhanced heat transfer and faster melting enabled by the baffle design.

Tank 03 (**Figure IV.20-(c)**): Equipped with a baffle featuring seven 32 mm holes, Tank 03 exhibits improved flow control and thermal distribution. This design results in a rapid rise in both PCM and water static enthalpies. Similar to Tank 02, the PCM enthalpy curve intersects the water enthalpy curve around 750s, followed by a steeper increase in PCM enthalpy. This behavior confirms the enhanced heat transfer efficiency achieved through optimized baffle configuration, enabling faster PCM melting.

Tank 04 (**Figure IV.20-(d)**): Tank 04, which incorporates a baffle with seven 35 mm holes, demonstrates a slower increase in both PCM and water static enthalpy compared to Tanks 02 and 03. The enthalpy curves intersect at approximately 800s, after which the PCM enthalpy rises at a steeper rate. This delayed intersection indicates lower heat transfer efficiency. While the larger

hole diameter promotes stronger natural convection, it also leads to uneven heat distribution in some regions, thereby reducing the overall effectiveness of PCM heat absorption.

Tank 05 (**Figure IV.20-(e)**): Incorporating an inclined baffle angled at 5°, Tank 05 effectively channels hot water toward the left-side holes, improving thermal contact with the PCM cylinders. This results in a more uniform temperature distribution and enhanced heat transfer. The intersection of the PCM and water static enthalpy curves occurs at around 750s, followed by a steeper rise in PCM enthalpy. These trends indicate that Tank 05 delivers improved thermal performance and more efficient PCM melting compared to previous configurations.

Tank 06 (**Figure IV.20-(f)**): Tank 06 incorporates an optimized inclined baffle with two enlarged 35 mm holes near the inlet and five 32 mm holes distributed throughout. This strategic layout promotes uniform hot water flow across all PCM cylinders, maximizing thermal contact and improving heat transfer. The static enthalpy curves show a marked increase, with the PCM curve intersecting the water curve around 680s. Beyond this point, the PCM enthalpy rises more sharply, confirming that Tank 06 delivers the highest heat transfer efficiency and the fastest PCM energy absorption among all configurations.

Figure IV.21 presents the static enthalpy contours within Tank 06, illustrating the dynamic progression of heat absorption over time. At 40s, both water and PCM exhibit low enthalpy, marking the initial phase of melting. By 520s, the water's static enthalpy rises rapidly, reflecting increased heat absorption. Soon after, the PCM’s static enthalpy also begins to climb sharply, indicating active phase change. Notably, beyond 520 s, the PCM's enthalpy surpasses that of the water, highlighting its superior heat storage capacity. At 1000, 1520, and 2240s, the PCM shows significantly higher enthalpy values, confirming efficient latent heat absorption. These results underscore the effectiveness of PCM in thermal energy storage, as it progressively absorbs and retains more heat than water during the melting process.

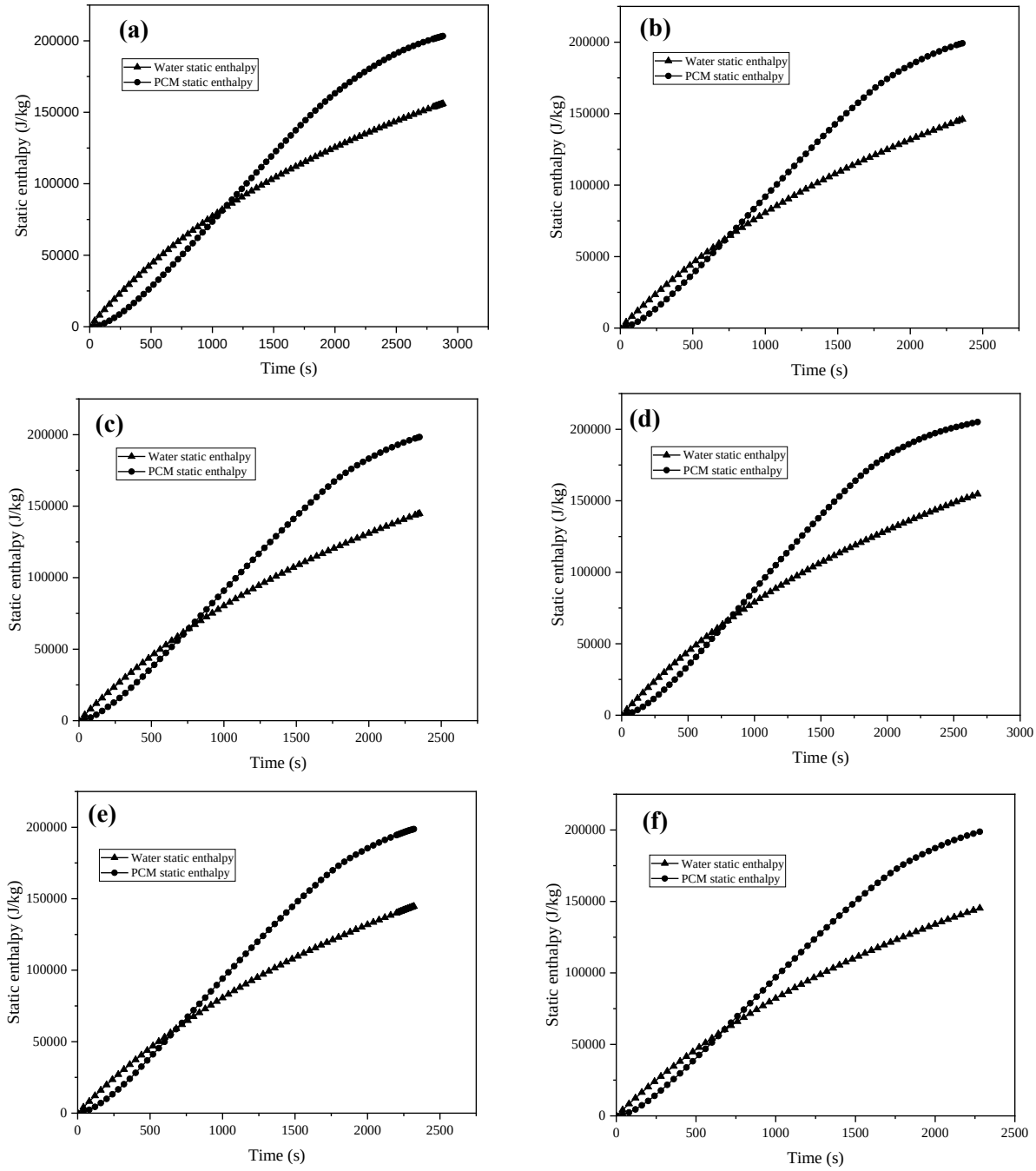

Figure IV. 19 : The variation of water static enthalpy and PCM static enthalpy for: (a)- Tank 01, (b)-Tank 02, (c)-Tank 03, (d)-Tank 04, (e)-Tank 05, (f)-Tank 06.

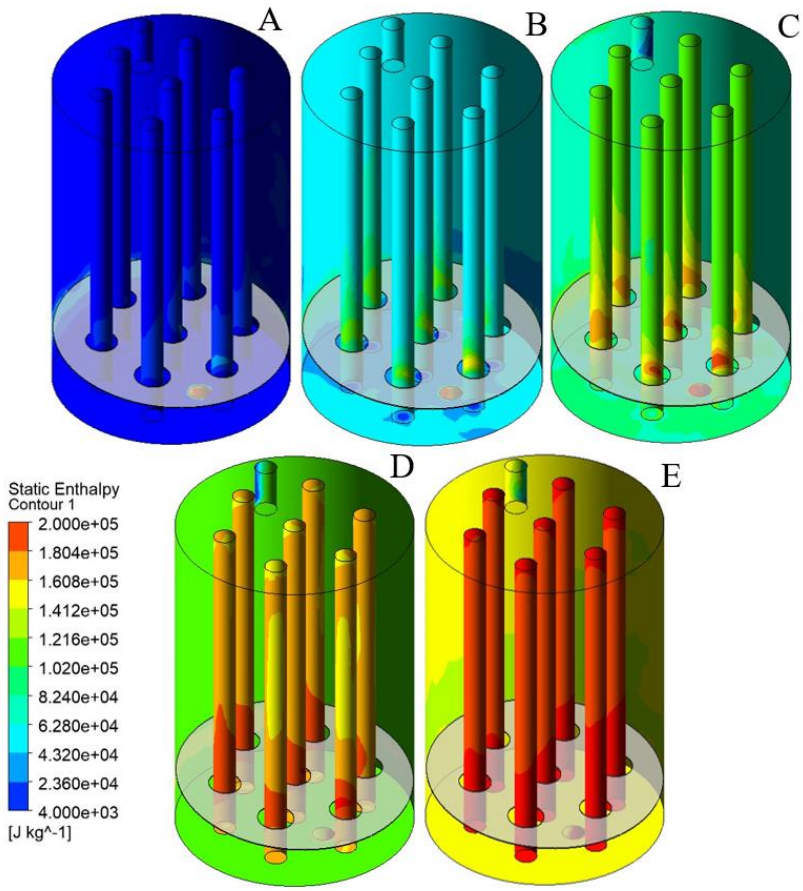

Figure IV. 20 : The static enthalpy contours for the thermal energy storage tank (tank 06) at different times: A-at 40s, B-at 520s, C-at 1000s, D-at 1520s, and E-at 2240s.

IV.3.5-Richardson number

The Richardson number (Ri) is a key dimensionless parameter that quantifies the interplay between buoyancy forces and viscous forces in fluid flow. It is frequently employed to assess natural convection and the stability of fluid flow within a tank.

Figure IV.22 shows that Tank 01, which lacks a baffle, allows for unrestricted upward flow of hot water. This absence results in a high Richardson number (*Ri*) of approximately 26, indicating a strong buoyancy-driven flow and significant natural convection pushing hot water towards the top of the tank. The prominent buoyancy forces create a stratified temperature distribution within the tank. Over time, as the tank heats up, the *Ri* value decreases, reflecting a reduction in thermal stratification. This trend suggests that while thermal stratification is initially high, it diminishes as the tank reaches a more uniform temperature distribution.

Tank 02 is equipped with a baffle featuring seven 30 mm holes, which partially restricts the upward flow of hot water. This design results in a significantly lower *Ri* compared to Tank 01, with a maximum value of around 3. The baffle's obstruction moderates the balance between buoyancy and viscous forces, leading to a more uniform temperature distribution within the tank. The Richardson number in Tank 02 shows some fluctuations and occasionally turns negative, indicating that at times, the temperature at the tank's bottom is higher than at the top.

Tank 03: Tank 03 features a baffle with seven 32 mm holes designed to enhance heat transfer and distribution. The presence of this baffle results in a *Ri* with a maximum value of around 5, and it fluctuates between approximately 1.5 and 4. This range indicates a well-balanced interaction between buoyancy and viscous forces. The baffle's holes facilitate efficient flow and heat transfer, leading to a relatively uniform temperature distribution within the tank.

Tank 04 utilizes a baffle with seven 35 mm diameter holes, designed to enhance thermal performance. *Ri* varies moderately between 2.5 and 7.5, indicating a relatively balanced interaction between buoyancy-driven and viscous forces. This configuration supports improved thermal convection and helps maintain a more consistent temperature profile throughout the tank.

Tank 05: Tank 05 includes an inclined baffle set at a 5° angle to optimize flow patterns and heat transfer. The *Ri* peaks around 5, with minor fluctuations. At times, the *Ri* may turn negative, suggesting that the temperature at the tank's bottom can exceed that at the top. Despite these variations, the inclined baffle enhances heat transfer efficiency and promotes a more uniform temperature distribution within the tank.

Tank 06 features an inclined baffle with five 32 mm holes and two 35 mm holes to optimize heat transfer and flow dynamics. The *Ri* peaks at around 6 and exhibits slight temporal variations. Intermittently, *Ri* values may become negative, indicating that the temperature at the tank's bottom can exceed that at the top. Despite these fluctuations, the improved design with multiple holes and the inclined baffle ensures efficient heat transfer, leading to a uniform temperature distribution within the tank.

In conclusion, the implementation of baffles in Tanks 02 to 06 significantly influenced the *Ri* by mitigating temperature stratification. In contrast to Tank 01 where the absence of baffles permits hot water to rise unimpeded to the top, resulting in pronounced thermal stratification and elevated Ri values the presence of baffles in the other tanks promotes a more uniform vertical flow. This improved flow distribution reduces temperature gradients within the tanks, leading to lower

and more stable Ri values. The uniform temperature distribution achieved in tanks with baffles contrasts sharply with the stratified distribution in Tank 01, highlighting the critical role of baffle design in enhancing thermal homogeneity and optimizing *Ri* values. Over time, as the temperature distribution becomes more uniform, the Ri value decreases, particularly in Tank 01, reflecting the reduced temperature gradient and improved thermal equilibrium.

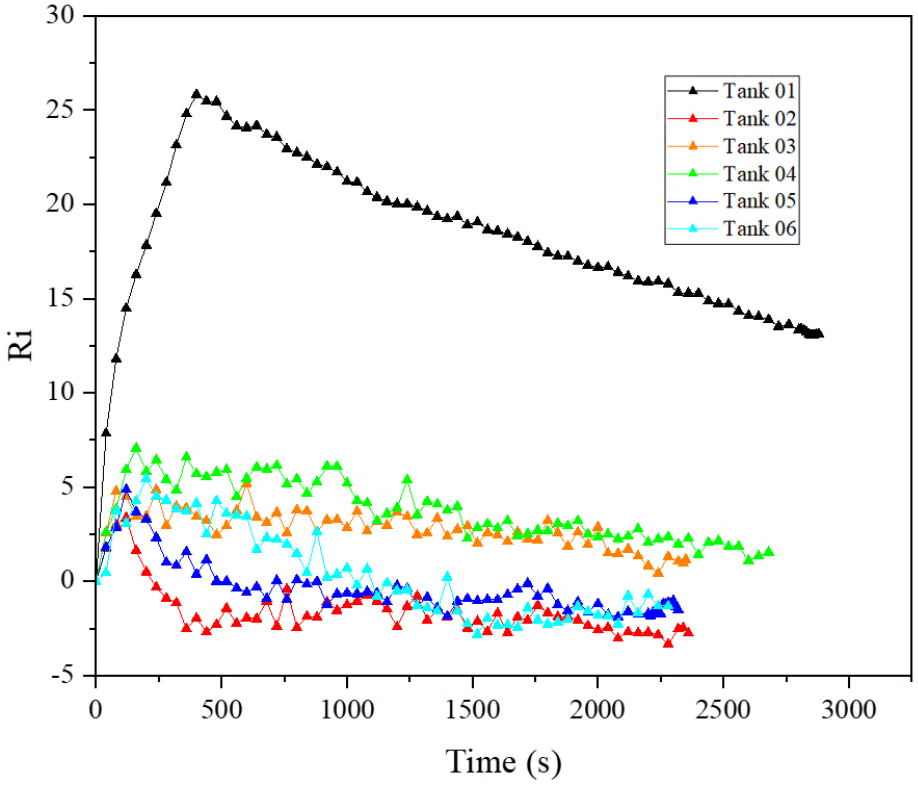

Figure IV. 21 : The influence of influence baffles on *Ri* number.

IV.3.6- Thermal storage efficiency

Thermal storage efficiency (η) measures the effectiveness of a TES system in absorbing and retaining heat. It is typically defined as the ratio between the temperature increase of the storage material and the temperature difference between the inlet hot water and the initial temperature of the material. A higher value of η indicates better thermal performance, reflecting greater heat absorption and retention by the PCM.

Figure IV.23 illustrates that Tank 06 exhibits the highest thermal storage efficiency among all the tanks (Tank 01, 02, 03, 04, and 05), demonstrating superior heat absorption and retention. This enhanced efficiency is due to the advanced design features and modifications implemented

in Tank 06, which improve heat transfer and ensure a uniform temperature distribution within the tank, thereby reducing temperature stratification.

In contrast, Tank 01 exhibits the lowest thermal storage efficiency due to the absence of a baffle. This lack of flow control results in uneven heat distribution and pronounced temperature stratification. As hot water naturally rises to the top, the PCM cylinders located at the bottom undergo delayed melting due to insufficient thermal contact. The reduced interaction between the hot water and the PCM leads to minimal temperature variation in the PCM, ultimately lowering the tank's overall thermal storage performance.

Although Tank 01 achieves a higher maximum thermal storage efficiency (67.55%) compared to Tanks 02, 03, 04, 05, and 06, this higher efficiency is realized only after a longer period due to its inefficient heat distribution. On the other hand, the baffles and design enhancements in Tanks 02, 03, 04, 05, and 06 facilitate quicker heat transfer and prompt improvements in thermal storage efficiency, even though their maximum efficiency levels are slightly lower than that of Tank 01 (**Table IV.4**).

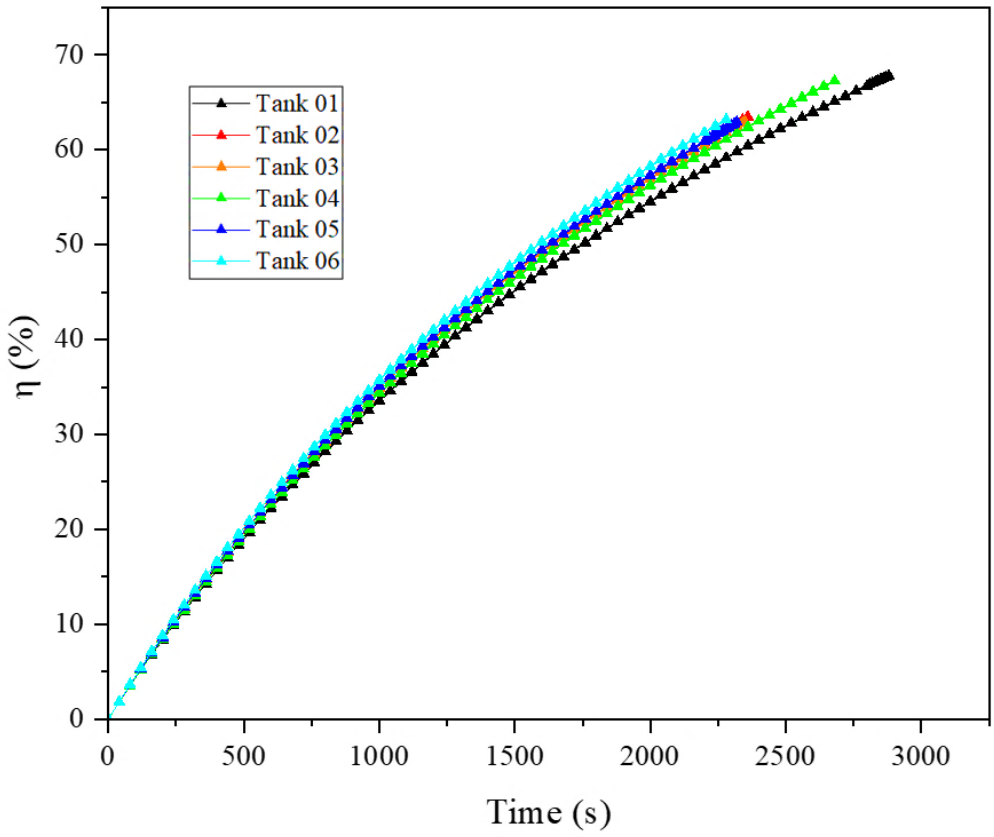

Figure IV. 22 : The thermal storage efficiency of all tanks.

IV.3.7- The economic analysis

IV.3.7.1- The total cost analysis

The total cost (C_{total}) includes the cost of the PCM within the cylinders (C_{PCM}) and the aluminum cost (C_{Al}), used for the tank, PCM cylinders, and baffles (for Tanks 02–06), using the formulation presented in Section II.4. Although the PCM mass is consistent across all designs, C_{Al} varies due to differences in the volume and configuration of aluminum components in each tank. Specifically, Tank 01 has an aluminum mass of 14.3 kg, while Tanks 02~06 have slightly varying aluminum masses. With the unit cost of paraffin set at \$2 USD/kg (C'_{PCM}) [209], and aluminum priced at \$18.40 USD/kg (C'_{Al}) [210]. Tank 01's total cost was \$265.40 USD, whereas each of Tanks 02–06 incurred a slightly higher cost of \$267.20 USD. Among them, Tank 06 stood out by achieving a 21.67% reduction in melting time, making it the most efficient configuration. Notably, this substantial performance improvement was accomplished with a minimal additional cost, amounting to less than \$2 USD/kg (as shown in Figure IV.24-(A)). This highlights the strong cost-

performance advantage of incorporating baffles, with Tank 06 serving as a compelling example of how minor design modifications can lead to major efficiency gains in TES systems.

IV.3.7.2-The economic performance

In real-world engineering applications, evaluating the TES capabilities of materials is crucial, but the economic aspect is equally important in determining project feasibility and overall costs [211].

Tank 01 has a P_c value of 0.2, reflecting its thermal energy storage efficiency relative to its cost. In contrast, Tanks 02 to 06 showcase higher Pc values, ranging from 0.24 to 0.26 (**Figure IV.24-(B)**). This indicates that these tanks offer a more favorable performance-to-cost ratio, providing better thermal energy storage capabilities for a similar investment. The increasing in P_c values from Tank 02 to Tank 06 demonstrate a trend towards improved economic performance as baffles and other design modifications are incorporated. These results highlight the importance of optimizing tank design to achieve a superior balance between performance and cost in thermal energy storage systems.

Tank 06 stands out as the optimal choice despite its $2 USD higher cost compared to Tank 01, due to its superior P_c value of 0.26 and a reduced melting time of 2240s. This highlights the crucial balance between cost and performance in optimizing thermal energy storage systems.

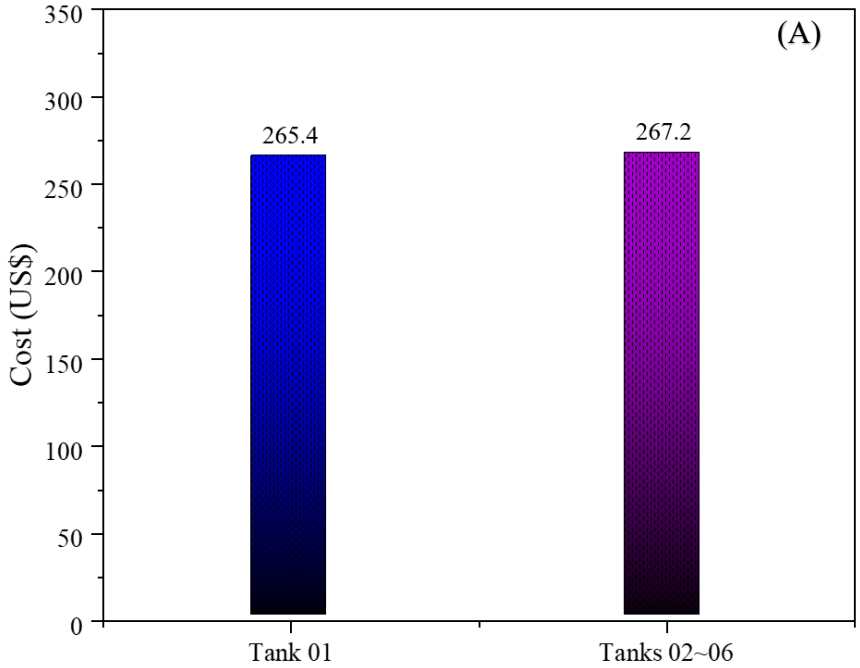

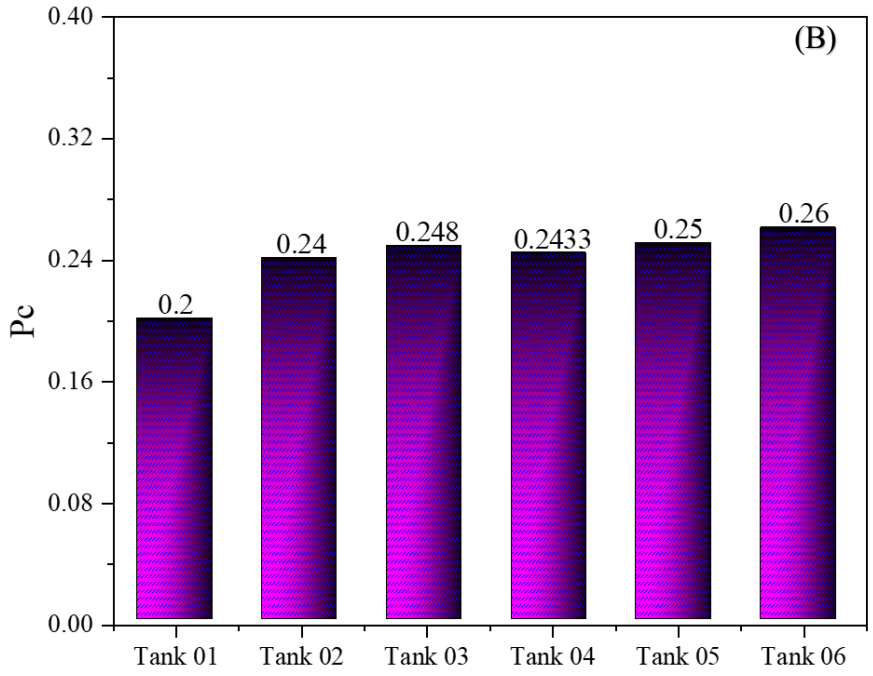

Figure IV. 23 : (A)- The total cost for all tanks, (B)- The economic performance for all tanks.

IV.4-Conclusion

This study investigated the impact of different baffle configurations on the thermal performance of PCM tanks by analyzing temperature profiles, liquid fraction evolution, heat flux distribution, velocity fields, Richardson numbers, and storage efficiency. The results demonstrated that incorporating baffles led to considerable improvements in thermal behavior, including better temperature uniformity, reduced thermal stratification, and enhanced heat transfer efficiency.

The addition of baffles also accelerated the melting process of the PCM, with Tanks 02 to 06 achieving shorter melting durations (between 2240 s and 2400 s) compared to the baseline Tank 01. Furthermore, the modified flow paths of hot water due to baffle presence increased the maximum heat flux within the PCM, reaching up to 560 W/m² in Tank 06, signaling improved thermal storage performance.

Flow visualization through velocity vectors showed that baffles improved natural convection, supported by lower Richardson numbers in baffle-equipped tanks. This indicates more active convective behavior, contributing to more efficient energy transfer. In conclusion, the findings emphasize the crucial role of strategic baffle design in enhancing the thermal performance,

shortening melting times, improving heat transfer, and increasing the overall feasibility of PCM-based thermal energy storage systems.

Among the evaluated configurations, Tank 06 with the inclined baffle containing holes of varying sizes proved to be the optimal design, achieving the shortest melting time (2240 s) and the highest economic performance with a Pc value of 0.26.

IV.5-Transition Between Hybrid and Shell-and-Tube Storage Systems

The work presented in Chapters III and IV focused on hybrid TES systems, which combine sensible and latent heat storage by integrating PCM containers into conventional water tanks. These chapters aimed to enhance the overall thermal capacity and system efficiency by leveraging the complementary characteristics of water and PCMs. Through numerical investigations, we assessed the impact of tank geometry, container placement, and flow configurations on thermal performance.

Building upon this hybrid approach, Chapters V and VI shift the focus exclusively to pure latent heat thermal energy storage systems, specifically through the use of PCM-based shell-and-tube heat exchangers. This transition reflects a more dedicated exploration of LHTES units, where the entire storage capacity relies on phase change processes. The insights gained from the hybrid systems particularly regarding heat exchange mechanisms, PCM behavior, and design constraints serve as a valuable foundation for the optimization strategies applied to shell-and-tube configurations. The objective in these latter chapters is to further enhance melting/solidification rates, energy density, and economic feasibility using innovative geometric and thermal control designs.

Part B
PCM Shell and Tube Heat Exchanger Systems

B.1-Validation of PCM Shell-and-Tube Heat Exchanger Models

Before presenting the numerical analysis in Chapters V and VI, the computational models are validated against experimental data to ensure accuracy and reliability. Two sets of validation studies were performed: (i) for Chapter V, assessing the impact of oval inner tube geometries, and (ii) for Chapter VI, evaluating wedge-shaped tubes and fin-enhanced PCM heat exchangers. The following subsections summarize the validation results.

B.1.1-Validation of Oval Inner Tube PCM Heat Exchanger (Chapter V)

This subsection presents the validation corresponding to Chapter V, focusing on the numerical analysis of PCM shell-and-tube heat exchangers with oval inner tube geometries. Al-Abidi et al. [213] investigated the solidification process of RT82 as a PCM within a TTHX, both with and without fins. Experimental trials were carried out for the finned case to authenticate their numerical model in both finned and non-finned models. The current computations were validated using their numerical findings of the changing liquid fraction over time for the non-finned case. As illustrated in **Figure B.1**, our results align closely with those stated by Al-Abidi et al. [213].

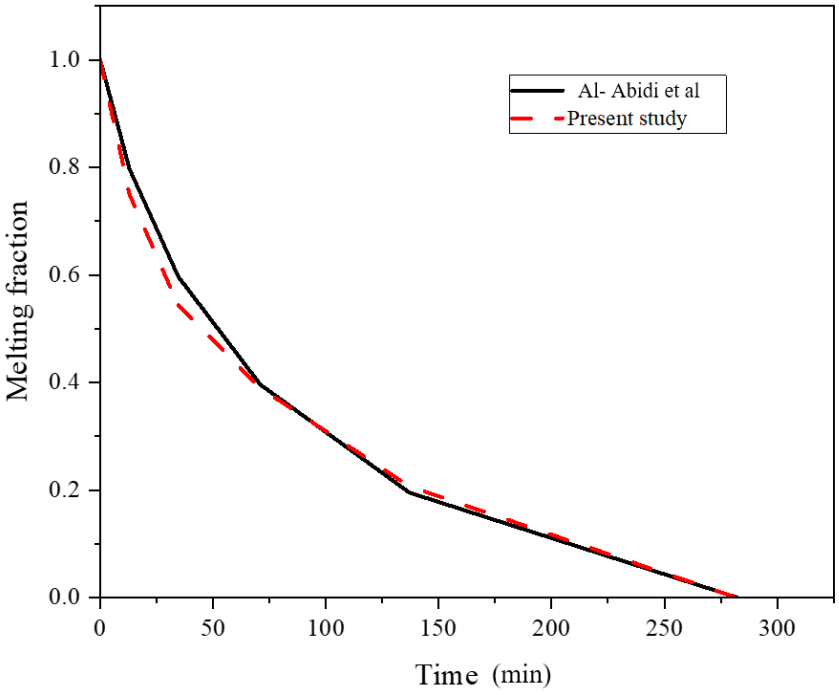

Figure B.1 : The liquid fraction variations for the solidification process: Experimental [213] vs CFD (present study).

B.1.2-Validation of Wedge-Shaped and Fin-Enhanced PCM Heat Exchanger (Chapter VI)

This subsection provides the validation corresponding to Chapter VI, addressing PCM units with wedge-shaped geometries and finned designs. Validating the numerical model through comparison with experimental data is essential. In this study, the experimental results from Al-Abidi et al. [231] are used to validate the current 2D numerical model. **Figure B.2** compares the average PCM temperature over time from both the numerical simulation and the experiment. The two curves show strong agreement, with relative deviations ranging from approximately 0.1% to 3.4%. These discrepancies may result from temperature measurement uncertainties or assumptions made in the numerical model. In particular, variations in PCM temperature are largely attributed to changes in thermal conductivity during the melting process. Overall, the numerical model demonstrates a reliable prediction of the PCM's thermal behavior.

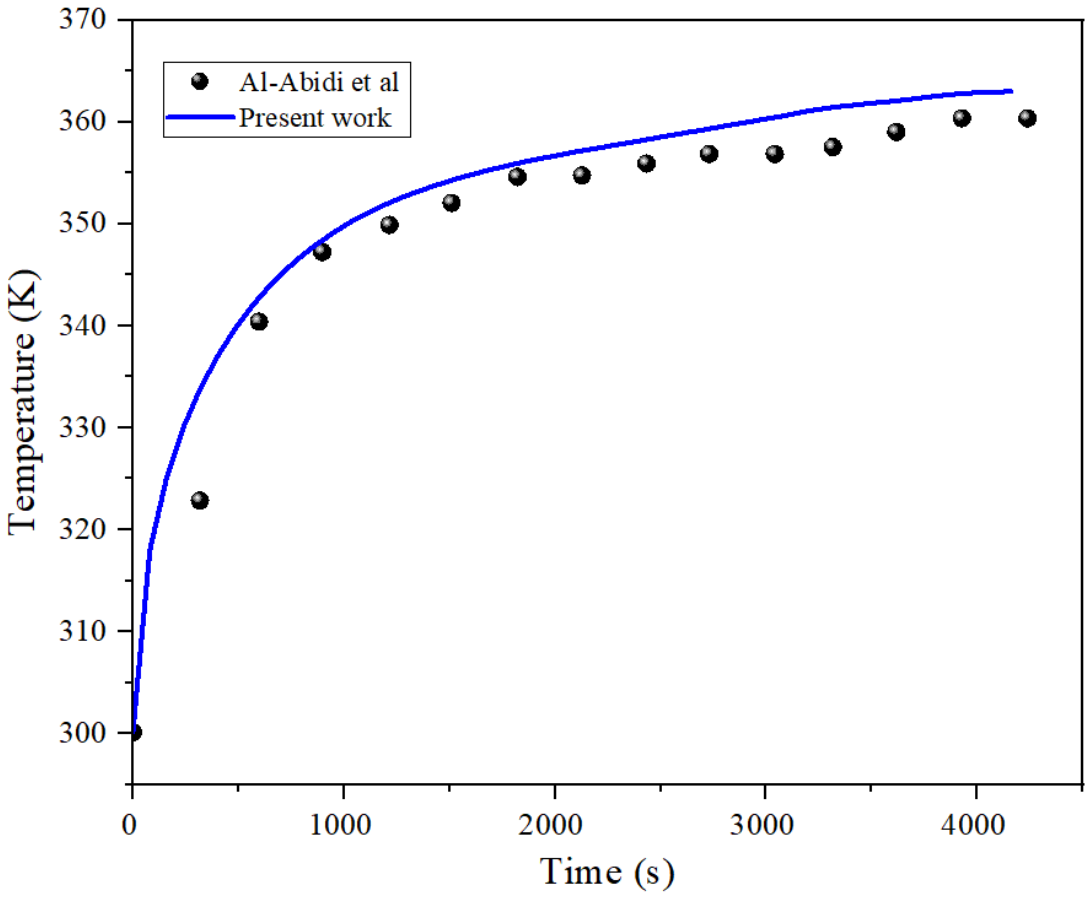

Figure B.2: Comparison of temperatures derived from CFD simulations (this study) with the experimental values documented by Al-Abidi et al [231].

Chapter V. Impact of oval inner tube shape on PCM thermal storage performance in shell-and-tube systems

V.1-Introduction

This chapter provides a systematic investigation into the melting and solidification processes of phase change material (PCM) units, comparing various inner tube geometries: horizontal oval, inclined oval (45°), vertical oval, and circular tubes. The study highlights that the vertical oval inner tube demonstrates superior efficiency, achieving complete melting and solidification in significantly shorter times compared to other designs. During melting, the circular inner tube completes the process in the 7560s, while both the horizontal and inclined oval units finish in the 7500s. In contrast, the vertical oval unit completes melting in the 7260s, showing a notable reduction in time, especially evident with a 3.96% improvement compared to other geometries. Similarly, in solidification, the circular inner tube takes 17760s, the horizontal oval 17160s, and the inclined oval 16080s, whereas the vertical oval unit completes in 14400s, marking an 18.91% decrease in solidification time.

V.2-Problem description and methodology

V.2.1-*The study of geometry and the imposition of boundary conditions*

This problem centers around the geometrical configuration of a triplex-tube heat exchanger (TTHX), as depicted in Figure 1. In **Figure V.1-(A)**, the TTHX is illustrated, and **Figures V.1-(B), 1-(C), 1-(D), and 1-(E)** depict the computational domains for the circular inner tube, H oval inner tube, In oval inner tube, and V oval inner tube, respectively. The TTHX configuration functions as a container for the storage of energy in a liquid desiccant air conditioning system powered by solar energy [213]. It includes three concentric tubes mounted horizontally, each with a length of 500 mm. The respective inner diameters, intermediate, and outer tubes are 50.8 mm, 150 mm, and 200 mm. The intermediate and outer tubes maintain a uniform thickness of 2 mm, while the inner tube is 1.2 mm thick. On the other hand, the oval inner tube has a major radius length of a =36 mm and a minor radius length of b = 16 mm (**Table V.1**); these specified dimensions for the oval inner tube are chosen intentionally to provide an equivalent surface area to that of a circular inner tube. This design decision allows for a fair and controlled comparison between the oval and circular shapes in our system. The annular space among the inner and intermediate tubes is filled with PCM (RT82) [214], the thermophysical characteristics of which are detailed in **Table V.2**, and a heat transfer fluid (HTF) circulates within the interior and outer tubes alike, with water serving as the HTF.

The computational domain is represented by an annular region, symbolizing the space containing the PCM (RT82), with R_o and R_i representing the radius of the intermediate and inner tubes, respectively. At the initial time t = 0s, the PCM is at a temperature of 350 K for the melting process and 366.15 K for the solidification process. The wall temperature, corresponding to the water temperature, is 363.15 K for the melting process and 341.15 K for the solidification process. These constant temperatures are crucial parameters that influence thermal dynamics, creating standardized conditions for a focused evaluation of the effect of inner tube shapes on PCM melting and solidification times. One can establish the initial condition as follows:

At $t = 0, T(x, y) = T_{initial} = 350K$, For the melting process. (V.1)

At $t = 0, T(x, y) = T_{initial} = 366.15K$, For the solidification process. (V.2)

For $t > 0$, the inner and intermediate walls of the annulus are subjected to a consistent temperature (T_w) for the entire duration of the solidification and melting processes (**Figures V.1-(B)** and **(C)**). Therefore, the boundary conditions can be expressed as follows:

At $r = R_i, T(x, y) = T_w = 363.15k$, For the melting process. (V.3)

At $r = R_o, T(x, y) = T_w = 341.15k$, or the solidification process. (V.4)

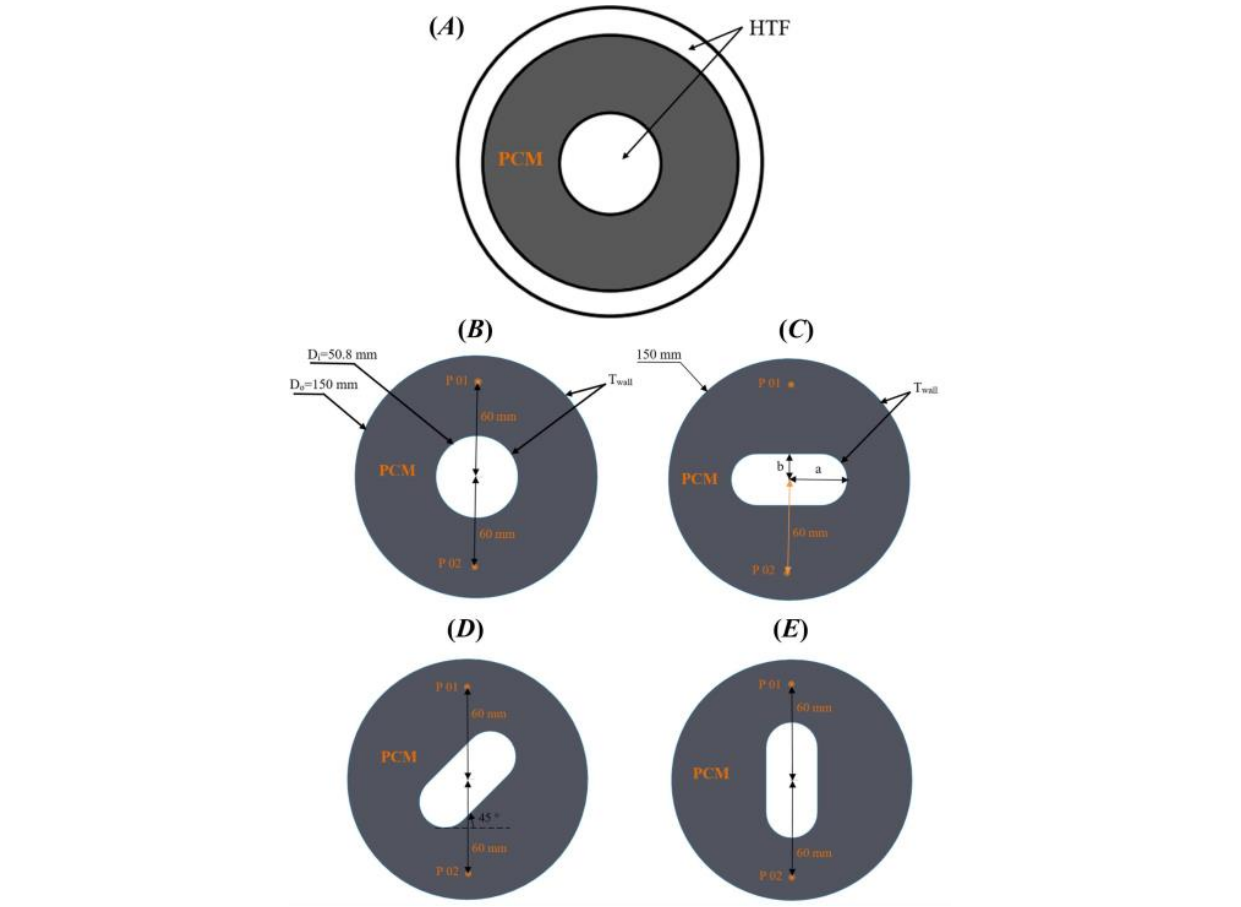

Figure V. 1 : (A) Schematic representation of TTHX. The geometry of the computational domain for all PCM units: (B) circular inner tube, (C) H oval inner tube, (D) In oval inner tube, (E) V oval inner tube.

Table V. 1: The computational dimensions.

Name	Symbol	Value (mm)
Circular outer diameter	D_o	50.8
Circular inner diameter	D_i	150
Oval major radius length	a	36
Oval minor radius length	b	16

Table V. 2: Thermophysical properties of RT82.

RT82 Properties	Value
Solidus density (Kg/m^3)	950
Liquidus density (Kg/m^3)	770
Specific heat capacity (J/Kg.K)	2000
Thermal conductivity (W/m.K)	0.2
Dynamic viscosity (N.s/m^2)	0.03499
Latent heat (KJ/Kg)	176
Solidus temperature (K)	350
Liquidus temperature (K)	358
Thermal expansion coefficient (1/K)	0.001

To formulate a mathematical framework depicting the process of solidification, the PCM is presumed to exist in a liquid state; however, for the melting process, PCM is assumed to be in a solid state initially, undergoing phase change with transient, laminar, and incompressible flow properties. The subsequent presumptions are taken into account:

1. The temperature fluctuation within the HTF is deemed insignificant, implying that the wall temperature (T_w) remains constant.

2. The flow was considered to be transient, incompressible, and governed by the Newtonian fluid model in a two-dimensional setting.

3. The flow of the melt is governed by buoyancy and remains in the laminar regime.

4. Dissipative effects due to viscosity are deemed negligible.

5. No-slip conditions.

6. Except for density, all PCM's thermophysical characteristics remain constant concerning temperature.

7. Adiabatic system.

8. To address the influence of natural convection, which is unavoidable, particularly throughout the melting phase, the simulations incorporated the Boussinesq approximation model [88]. This model assumes that the density of the fluid remains constant, except for a single term in the momentum equation. In this context, density is regarded as a function of temperature, as expressed by:

$$\rho = \rho_m \left(1 - \beta (T - T_m)\right) \tag{V.5}$$

Where, $T_m = \frac{T_s + T_l}{2}$, ρ_m is the density of the liquid PCM, while T_s and T_l represent the solidus and liquidus temperatures, respectively.

9. No supercooling effect.

V.2.2-*Governing equations*

Governing equations are used to characterize the fluid flow and temperature distribution within the annulus, as presented in Chapter II.

V.3-Numerical method and validation

V.3.1-*Numerical method*

A 2D CFD model was created in ANSYS FLUENT 22.2 to address the melting/solidification challenge. This approach utilizes the Enthalpy-porosity technique, first presented by Voller et al. [217]. This technique utilizes the concept of liquid phase fraction to indirectly represent the transition between solid and liquid states, accommodating both isothermal and nonisothermal phase change scenarios. The finite volume method (FVM) with a double precision solver was employed for discretizing the governing equations. The SIMPLE algorithm was chosen for pressure-velocity coupling [218], while a QUICK scheme was utilized for solving momentum and energy equations. The pressure correction equation was addressed using the PRESTO scheme. Transient terms were handled through a second-order implicit discretization scheme. The mesh

consisted of hexahedral elements, and inflation was applied for inner tubes (see **Figure V.2- (A)** and **(B)**). The under-relaxation factors for the velocity components, pressure correction, and thermal energy were 0.7, 0.3, and 1, respectively. Convergence criteria were set at 10^{-4} for continuity, 10^{-4} for momentum, and 10^{-6} for energy residuals.

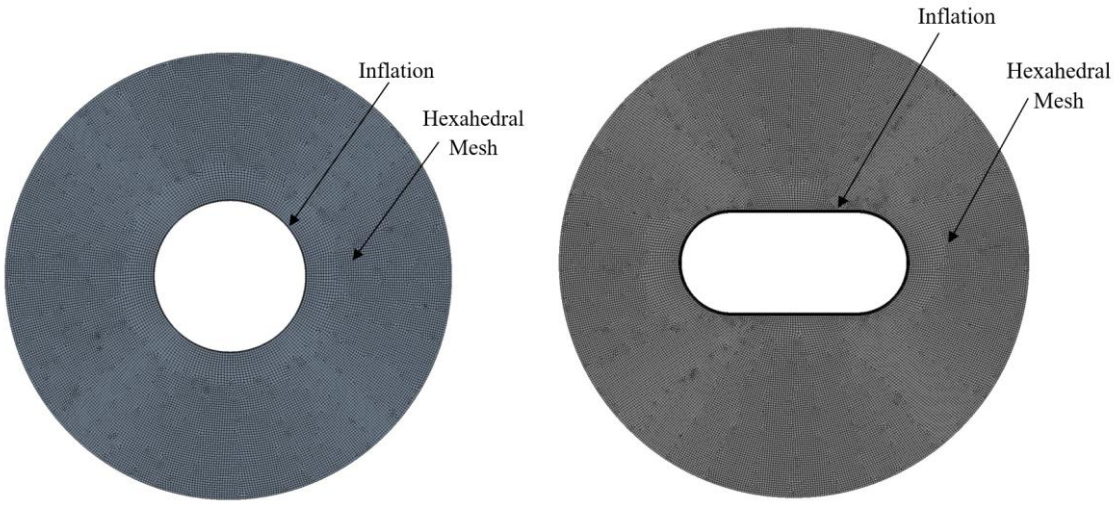

Figure V. 2 : Hexahedral Mesh distribution: (A)- Circular inner tube PCM units geometry, (B)-H oval inner tube PCM units geometry.

V.3.2-*Grid and time step independence study*

There are three separate grid resolutions to guarantee grid-independent outcomes for a model of a circular inner tube (N = 23474, 18613, and 15078) were assessed for discretizing the computational domain. Minor discrepancies were observed in the results, as shown in **Figure V.3-(A)**. Ultimately, all numerical simulations for the circular inner tube model in this study were conducted using a mesh number of 23474, while for the oval inner tube, the mesh number employed was 32689. Additionally, three distinct time steps (t = 0.2, 0.5, and 1.0 s) were examined for integrating time derivatives, as depicted in **Figure V.3-(B)**. A time step of 1 s proved to be sufficient in maintaining solution independence and stability. This choice not only streamlined computational time but also upheld a commendable level of simulation accuracy.

V.4-Results and discussion

This segment showcases the outcomes of PCM melting and solidification processes, along with the temperature evolution within the PCM unit. Key indicators such as temperature distribution and liquid ratio represent phase change events and numerically assess heat distribution. This analysis aims to anticipate opportunities for enhancing the thermal effectiveness of the PCM unit.

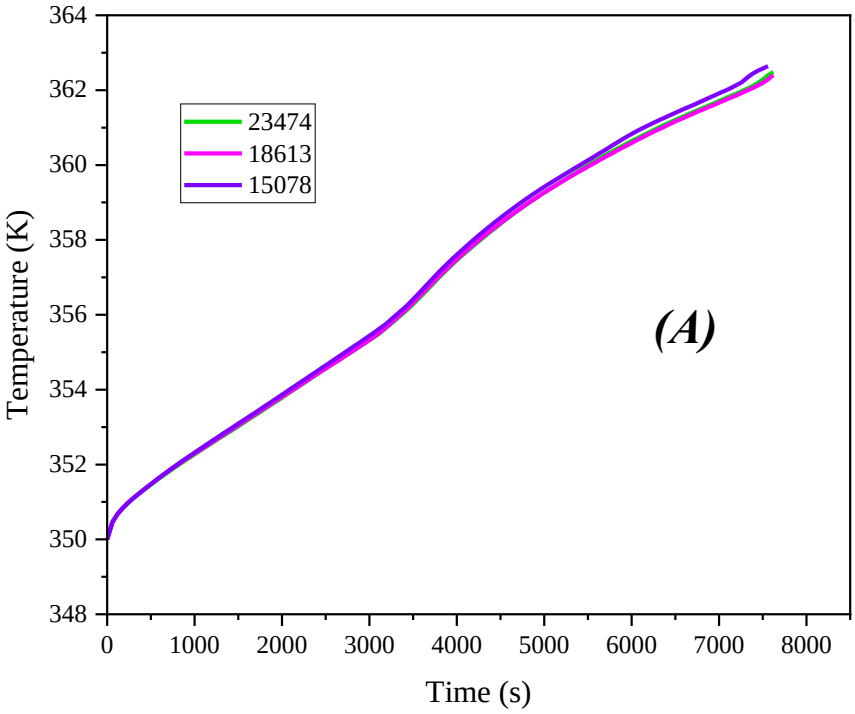

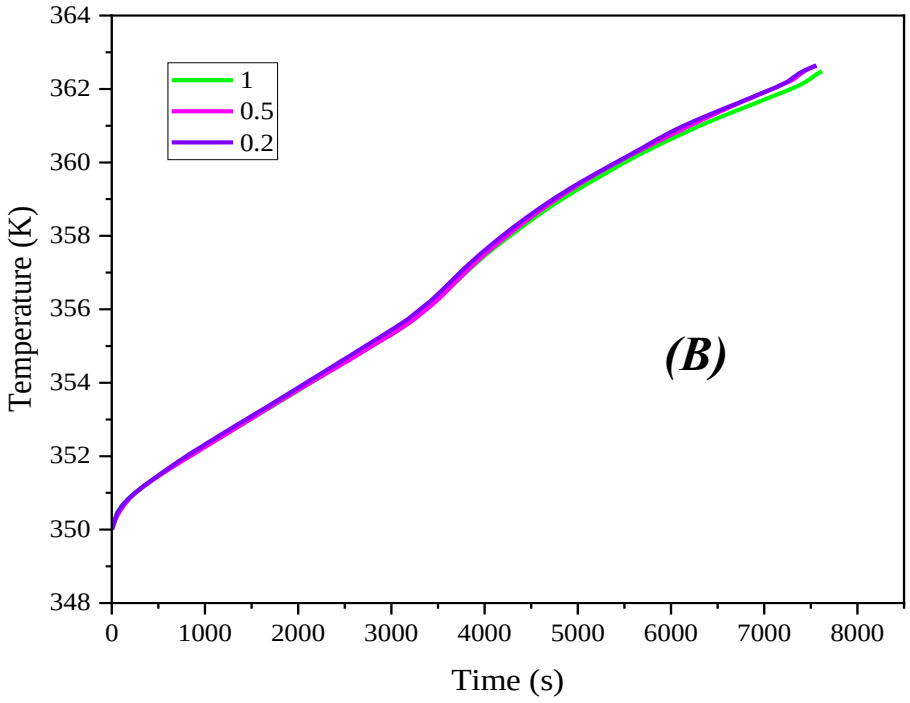

Figure V. 3 : Effects of (A) grid size and (B) time on the PCM temperature versus time for melting process (Circular inner tube).

V.4.1-*The PCM melting process*

V.4.1.1-*Progression of temperature and liquid fraction for the melting process*

Figure V.4 illustrates the temperature profile of the PCM, while **Figure V.5** presents the variation in total liquid fraction across the entire PCM unit. **Figures V.6-(A)**, **6-(B)**, **6-(C)**, and **6-(D)**, respectively, showcase the local temperature at points 1 and 2, as well as the local liquid fraction at points 1 and 2. Four distinct PCM units were established and labelled as Circular, H oval, In oval, and V oval. Despite alterations in the inner tube's geometry, the volume of each computational domain (PCM volume) remains consistent. This setup enables a comprehensive investigation into the influence of the inner tube shape on the melting dynamics. In all cases (Circular, H oval, In oval, and V oval), the PCM temperature rises due to its absorption of heat from the inner and middle walls, in parallel, the liquid fraction also increases. This occurs as the PCM starts undergoing melting when absorbing the heat. While the temperature rise is similar for all cases, there is a slightly more pronounced increase observed in V oval as the melting process nears completion. Consequently, the V oval shape takes the lead in the melting process, reaching f=1, due to its closer proximity to the bottom, which has a lower temperature compared to other

regions. As a result, it transfers more heat to the bottom compared to the other cases. This temperature gradient is a direct result of buoyancy-driven flow arising from density variations inside the PCM unit.

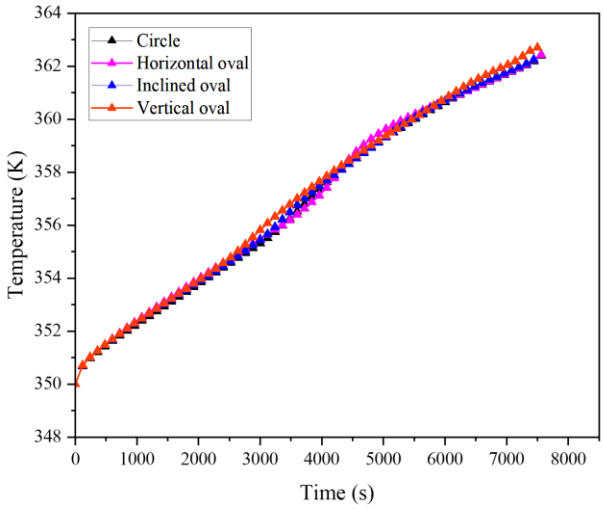

Figure V. 4: The PCM temperature distribution for the melting process.

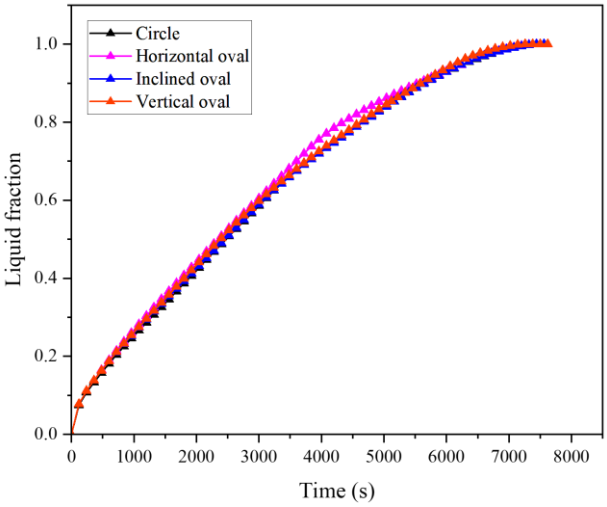

Figure V. 5: The liquid fraction distribution for the melting process.

Figure V.7-(A); for the local temperature at point 1, the temperature initially remains constant but then experiences an increase over time. Specifically, in the case of V oval, there is an initial rapid increase in temperature compared to the other cases. This is attributed to V oval's proximity to the top of the unit (point 1), allowing it to receive more heat and consequently exhibit a faster and sudden temperature rise compared to the other cases. In contrast, the H oval experiences a slightly delayed temperature increase due to its greater distance from this specific point at the highest part of the unit (point 1). The initial constancy in temperature is a result of the melting process commencing within both the inner and intermediary tubes. As the molten layer expands externally into the surrounding melt zone, it leads to the displacement of the solid-liquid interface towards the annular space, so to point 1.

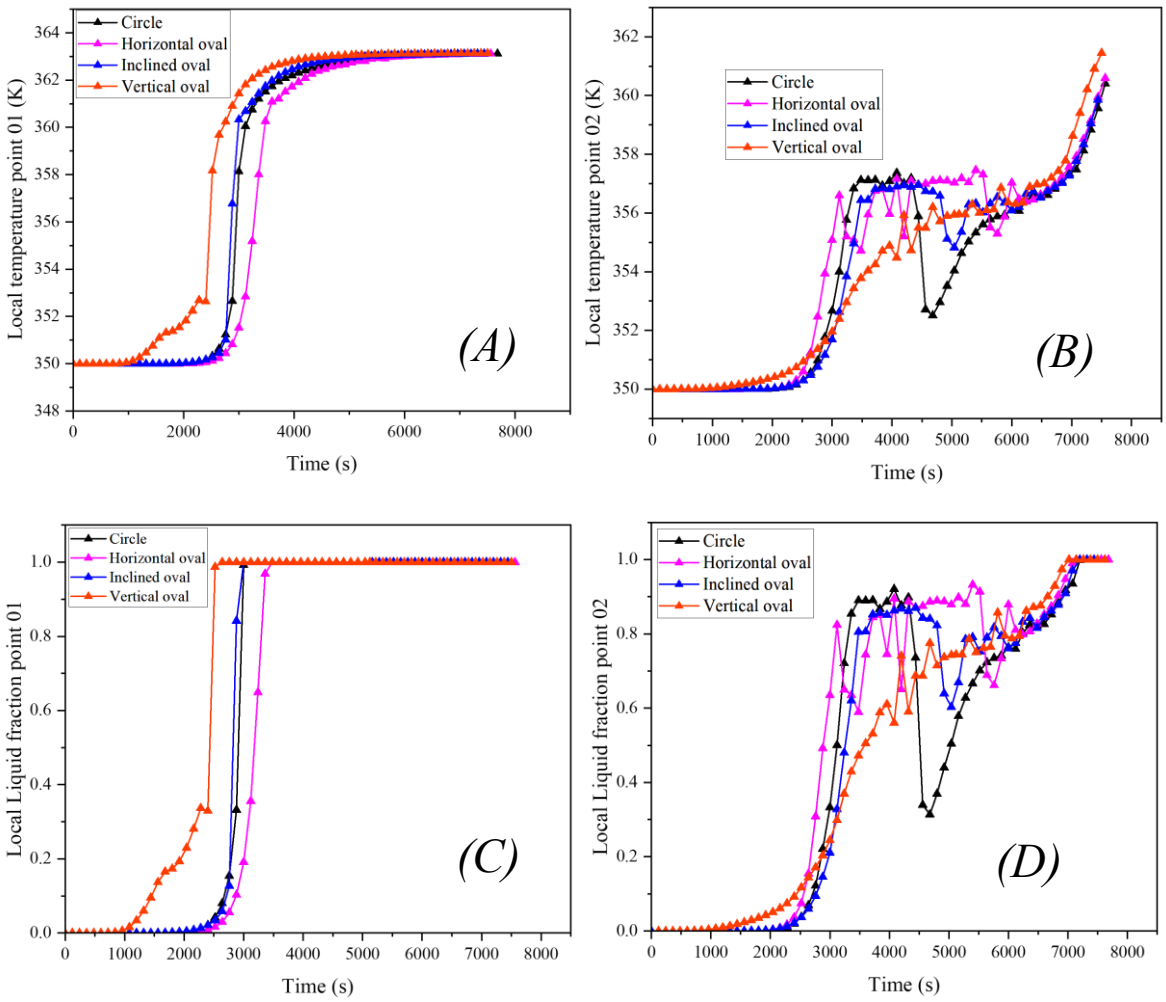

Figure V. 6 : The local PCM temperature distribution and the local liquid fraction distribution for the melting process: (A) the local PCM temperature distribution at point 1, (B) the local PCM temperature distribution at point 2, (C) the local liquid fraction distribution at point 1, (D) the local liquid fraction distribution at point 2.

Figure V.6-(B); for point 2, located at the bottom of the PCM units, the temperature remains constant for an extended period before eventually increasing. This behavior is attributed to the outset of the melting process, where the inner and intermediate tubes initiate the transformation then the molten layer expands outward into the surrounding melt zone, so it needs more time to reach the heat to point 2. It's worth noting that during this process, fluctuations in temperature are observed; the fluctuation in temperature at point 2 can be attributed to a combination of factors. Changes in heat transfer rates, variations in local flow patterns, and interactions among the PCM's solid and liquid states all play a role. Additionally, the impact of temperature gradients and

convective currents within the PCM further contribute to these fluctuations. These complex interactions collectively contribute to the dynamic nature of the temperature profile observed at point 2. Notably, in the case of V oval, the temperature increases at point 2 is more efficient. This can be attributed to the proximity of the heat source to this specific point. The shorter distance allows for a more direct and efficient transfer of heat, leading to a more significant temperature rise compared to other cases.

Figure V.6-(C); initially, at point 1, the local liquid fraction remains constant as the PCM undergoes the premature stages of the melting process. In the case of V oval, due to point 1 proximity to the heat source at the uppermost of the unit, the local liquid fraction at point 1 increases more rapidly compared to other cases; leading to a quicker transition from solid to liquid. For H oval, point 1 is farther from the heat source; there is a minor delay in the increase of local liquid fraction at point 1. However, it will eventually catch up as the melting process progresses.

Figure V.6-(D); at point 2, situated at the lower part of the PCM units, the local liquid fraction initially remains constant. Given its distance from the heat source, it necessitates more time for the molten layer to extend downwards and reach this location (point 2). Consequently, the local liquid fraction at point 2 experiences an increase after an extended period owing to differences in density; the liquid PCM tends to rise towards the top of the PCM unit. This behavior extends the duration required for heat to reach the bottom of the PCM unit (point 2). As a result, the increase in local liquid fraction at point 2 is delayed compared to other regions within the unit. In the case of V oval, due to point 2's proximity to the heat source at the lowest part of the unit, the local liquid fraction at point 2 increases more rapidly compared to other cases. This phenomenon is accompanied by fluctuations in the local liquid fraction, driven by various factors such as alterations in heat transfer rates, shifts in flow patterns, and interactions between the solid and fluid states of the PCM states.

V.4.1.2-*Temperature and liquid fraction contours for the melting process*

Figures V.8 and **9** present temperature and liquid fraction contours across all PCM units at various intervals. Within the temperature contours, the low-temperature area, depicted in green, corresponds to the solid phase and relates to the solid area in the liquid fraction. The liquid fraction contours illustrate the evolving form and advancement of the melting boundary throughout the

process. The PCM is represented in blue when solid (f = 0) and in red when completely liquid (f = 1), with the presence of a mushy zone providing a visual indicator of the advancing melting front.

In **Figure V.7**, at t = 0, the temperature is uniformly set at the initial value of 350 K for all cases. As time progresses to t = 1020 s, the heat spreads around the inner and middle tubes because they are heat sources. By t = 3000 s, it becomes evident that the heat starts concentrating in the unit's upper part. This phenomenon arises due to differences in density and the occurrence of natural heat convection. Consequently, the hotter PCM liquid rises while the cooler PCM remains at the lowest part of the unit. Similarly, at t = 5100 s, the top portion of the units becomes hotter than the bottom half. It's important to note that this behavior is typical in melting processes, where heat distribution and convection have a considerable role in shaping the temperature profile. Upon completion of the melting process, the temperature inside the PCM units is approximately uniform across all cases.

In **Figure V.8**, at t = 0, the PCM is in a solid state for all cases. As time progresses to t = 1020 s, melting commences within the inner and intermediate tubes. The molten layer expands outward into the surrounding melt region, displacing the solid-liquid interface towards the annular space. During the entirety of the melting procedure, heat transfer occurs through conduction exclusively within the solid PCM, while in the liquid PCM, it involves both conduction and convection. This is induced by temperature gradients, instigating buoyancy-driven flow due to density disparities across the annulus. By t = 3000 s, the concentration of heat becomes evident in the upper part of the units, resulting in more pronounced melting in this region. Similarly, at t = 5100 s, the top portion of the units becomes hotter than the bottom half, resulting in more extensive melting in the

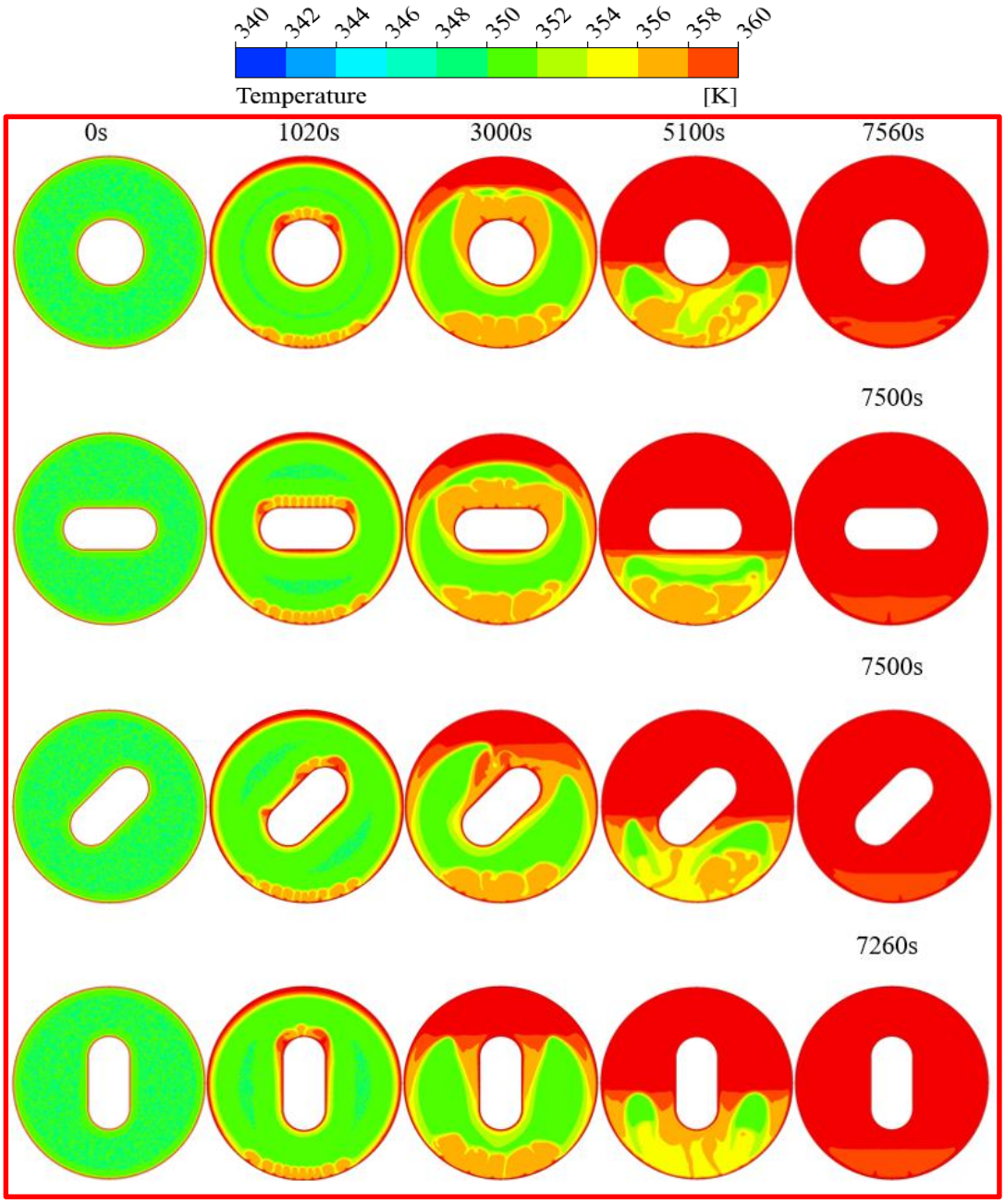

Figure V. 7 : Temperature contour plots for the melting process.

upper part. It's important to note that this behavior is typical in melting processes, where heat distribution and convection hold substantial importance in shaping the liquid fraction profile. Upon completion of the melting process, the liquid fraction inside the PCM units reaches f=1 across all cases. The unit with a V oval inner tube completes the melting process firstly due to the shape of its inner tube, which is nearer to the lower part of the PCM unit, thus allowing for a more efficient

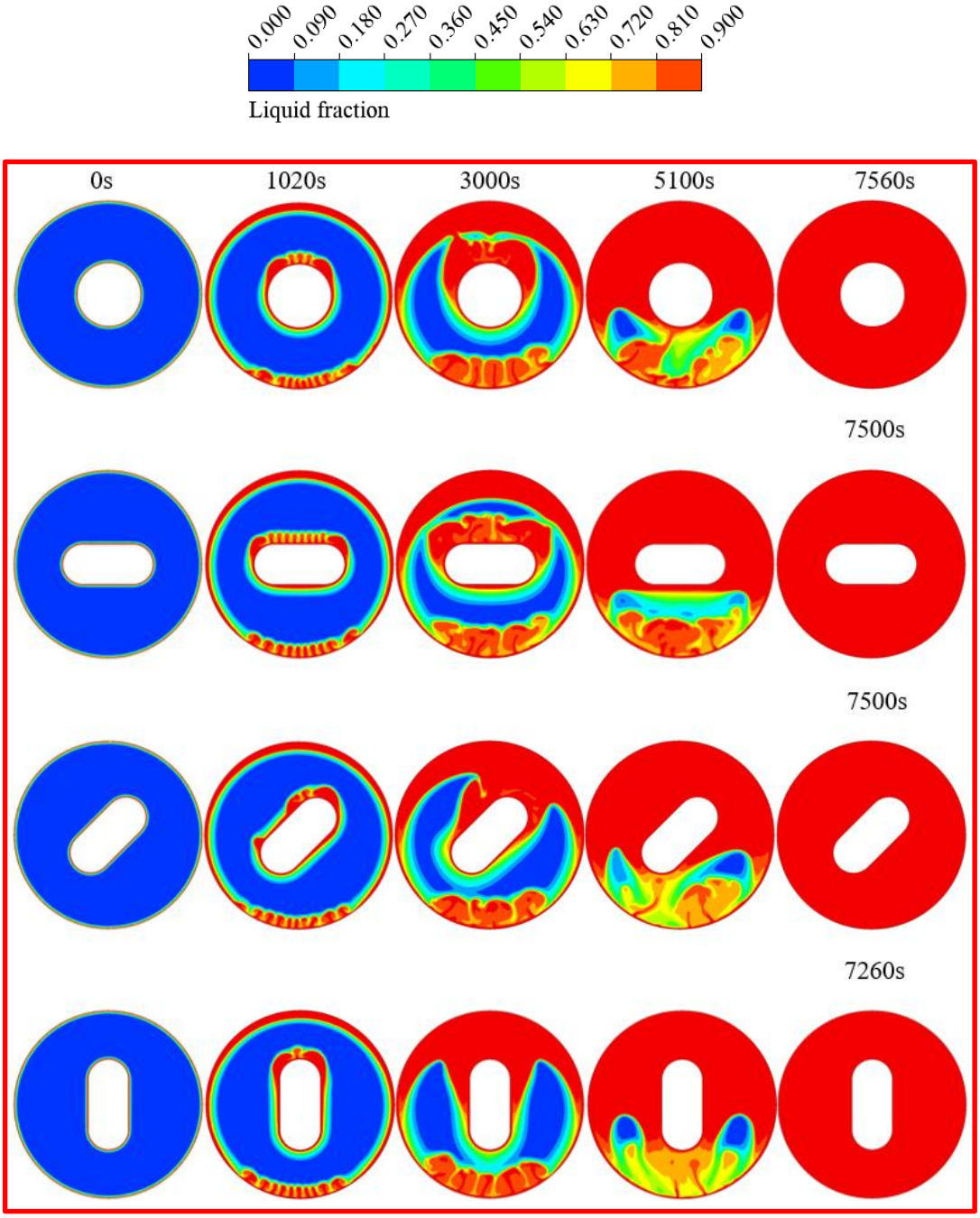

Figure V. 8 : Liquid fraction contour plots for the melting process.

transfer of heat to this region than other PCM units. **Figure V.9** illustrates the completion times for melting, with the Circular inner tube completing the melting process after 7560s, the H oval and In oval units completing after 7500 s, and the V oval unit completing after 7260s. The reduction in melting time for H oval and In oval is approximately 0.8%, whereas for V oval, it is notably greater at 3.96%.

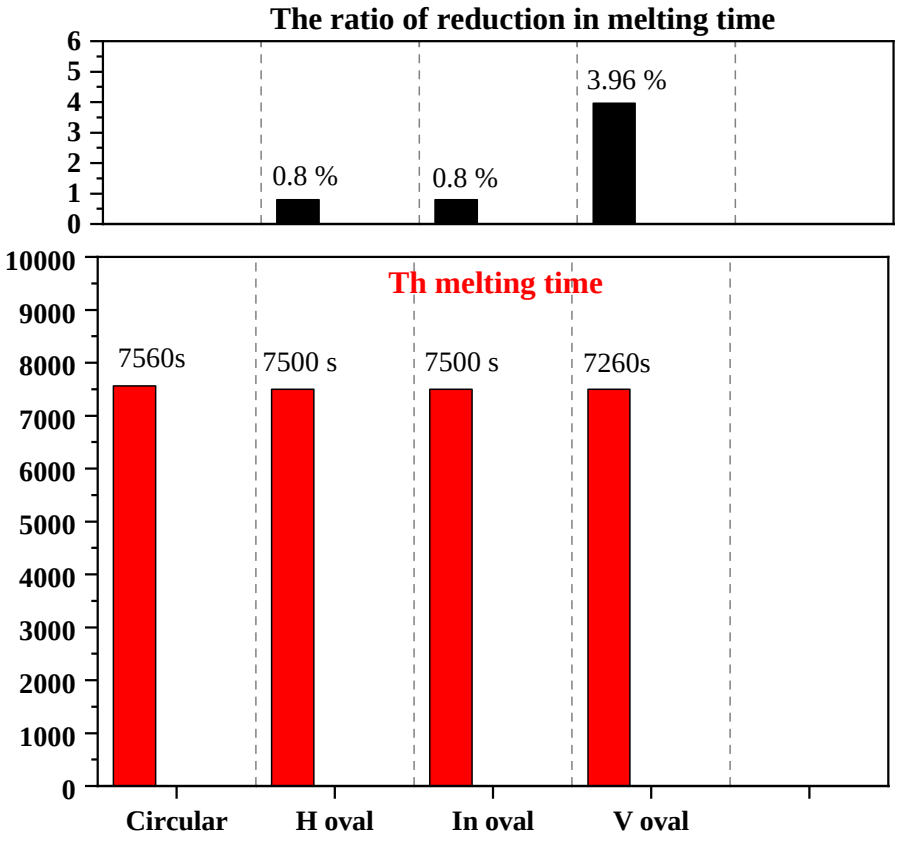

Figure V. 9 : The melting time and the reduction in melting time for all cases.

V.4.1.3-*The heat flux variation for the melting process*

Figure V.10 illustrates the transient heat flux comparison among various PCM units throughout the melting cycle. All curves exhibit complete overlap in the initial stage, indicating that the heat flux remains independent of the inner tube shape during this phase. This is likely due to the dominant influence of heat conduction, which tends to overshadow the impact of the inner tube's shape. As the process develops, natural convection comes into play, resulting in noticeable discrepancies among the curves. This signifies a shift in the heat transfer mechanism. The variations observed can be attributed to the evolving influence of convective heat transfer in conjunction with the specific geometry of the inner tube. In the case of the V oval inner tube case, the heat flux reaches its minimum value (approximately zero) earlier than in other cases. This is due to a larger portion of PCM being exposed to the heat transfer process, resulting in a more rapid reduction in heat flux. The specific geometry of the V oval inner tube facilitates this enhanced heat transfer.

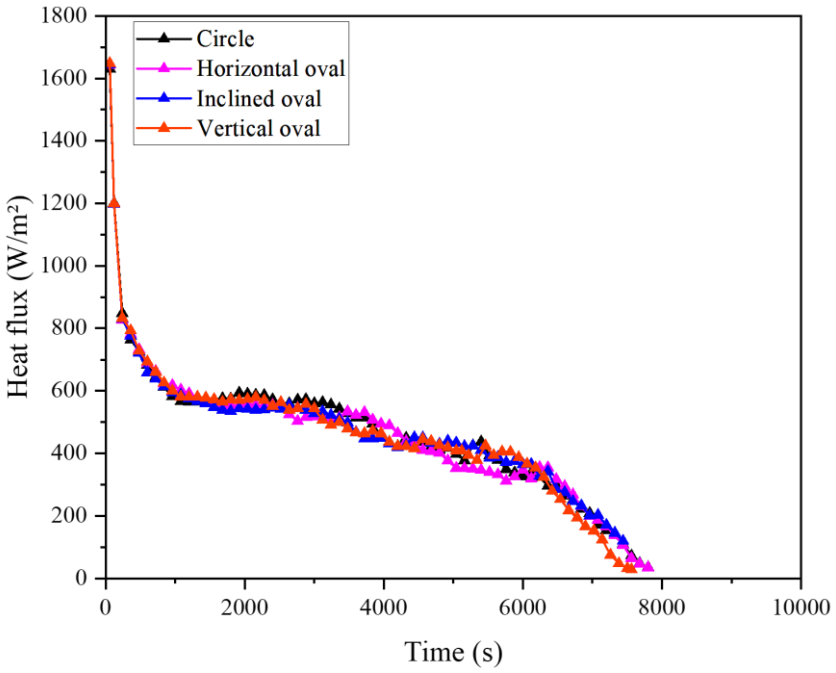

Figure V. 10 : The PCM heat flux distribution for the melting process.

V.4.2-*The PCM solidification process*

V.4.2.1-*Progression of temperature and liquid fraction for the solidification process*

Figure V.12 provides insight into the temperature profile of the PCM during the solidification process, while **Figure V.11** offers a visual representation of the variation in total liquid fraction across the entire PCM unit. Moving on to **Figures V.13-A**, **B**, **C**, and **D**, these curves display the local temperature at points 1 and 2 and the local solid fraction at these same points, respectively. For all cases, which include Circular, H oval, In oval, and V oval, the PCM temperature decreases as it releases heat to the inner and middle walls. Concurrently, the liquid fraction also experiences a decline. This transformation is indicative of the PCM transitioning into a solid state owing to the dissipation of heat. Notably, the rate of temperature decrease is slower in the case of the circular inner tube in comparison to the other configurations, which causes a slow decrease in liquid fraction compared to the other cases. During solidification, the V oval shape demonstrates superior efficiency by initiating solidification and reaching a fully solid-state (f=0) before other cases. This efficiency is attributed to its advantageous proximity to the upper part of the PCM unit, characterized by a higher temperature than other regions. The efficient heat transfer to the V oval inner tube results in a faster and more pronounced decrease in temperature compared to other configurations.

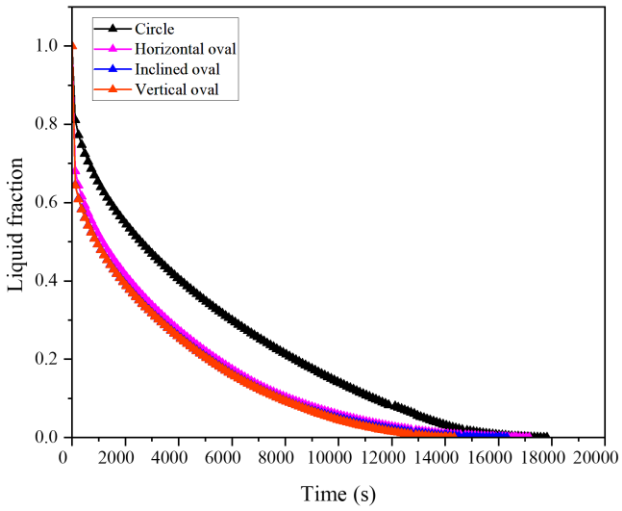

Figure V. 11: The PCM temperature distribution for the solidification process.

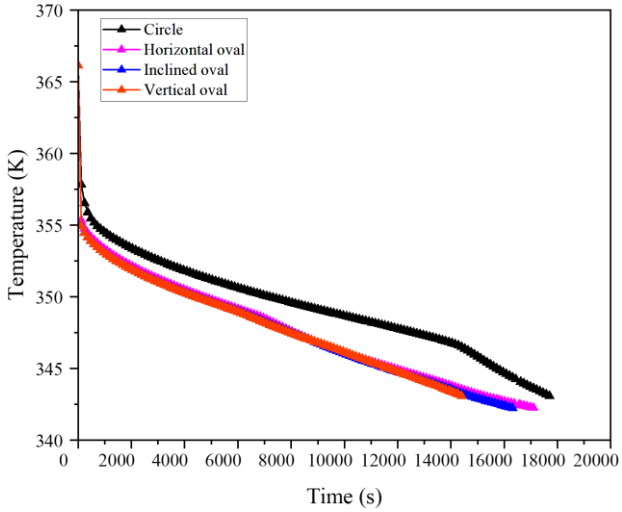

Figure V. 12: The liquid fraction distribution for the solidification process.

Figure V.13-(A); at point 1, the circular shape exhibits a slower decrease in the local temperature compared to the other cases. This is owing to the relatively weaker heat transfer from the PCM to the circular inner tube, leading to a slower solidification process in this configuration. On the other hand, the local temperature at point 1 experiences a rapid decrease initially during the solidification process for all cases. As time progresses, the temperature continues to decrease for all cases, but the H oval exhibits a delayed temperature decrease due to its greater distance from the specific point at the top of the unit (point 1). In contrast, V oval undergoes a rapid temperature decrease at point 1 because it is closer to the heat source than other cases, allowing it to absorb more heat.

Figure V.13-(B); at point 2, located at the bottom of the PCM units, there is an initial rapid decrease in the local temperature during the solidification process for all cases. As time advances, the temperature continues to decrease for all cases, and the circular shape exhibits a slower decrease in temperature in comparison to the other cases. Furthermore, with H oval shows a delayed temperature decrease at point 2 due to its greater distance from the specific location at the bottom of the unit (point 2). In contrast, V oval undergoes a swift temperature decrease at point 2 because of its proximity to the heat source compared to other cases, enabling it to absorb more heat.

Figure V.13-(C); at point 1, the initial stages of the solidification process witness a swift decrease in the local liquid fraction at point 1 for all cases. Over time, the local liquid fraction at point 1 continues to decrease across all instances, with H oval displaying a delayed decrease at point 1 due to its big distance from the specific location at the top of the unit (point 1). In contrast, V oval experiences a rapid temperature reduction at point 1, benefitting from its closer proximity to the heat source compared to other cases. This closer proximity enables V oval to absorb more heat, resulting in a faster transition into a solid state (f=0).

Figure V.13-(D); at point 2, positioned at the bottom of the PCM units, there is an initial rapid decrease in the local liquid fraction during the solidification process for all cases. Over time, the liquid fraction continues to decrease for all cases, with H oval displaying a delayed decline at point 2 due to its greater distance from the specific location at the bottom of the unit (point 2). Conversely, V oval undergoes a swift reduction in liquid fraction at point 2 owing to its proximity to the heat source compared to other cases. This proximity allows it to absorb more heat, facilitating a quicker transition into a solid state (f=0).

V.4.2.2-*Temperature and liquid fraction contours for the solidification process*

Figures V.14 and **15** showcase temperature and liquid fraction distributions across all PCM units at different time intervals. In the temperature contours, the red areas indicate high temperatures, signifying the liquid phase, and align with the liquid region displayed in the liquid fraction contours. These contours visually depict the changing shape and advancement of the solidification interface throughout the process. The PCM is portrayed in blue when solid (f = 0) and red when entirely liquid (f =1), and a mushy zone visually indicates the progressing solidification front.

In **Figure V.14**, at t = 0, the temperature is uniformly set at the initial value of 366.15 K for all cases. As time progresses to t = 2400 s, the inner and intermediate tubes begin to absorb heat, revealing variations in heat absorption between the circular inner tube and other configurations. Specifically, H oval, In oval, and V oval absorb more heat than the circular configuration, attributed to the larger lateral surface of the oval shapes. As time advances to t = 6000 s and t = 12000 s, it becomes evident that heat is concentrated more in the regions between the lines of the oval and the middle tube due to the larger space between them. The heat absorption

is maximized between the circular arc of the oval and the middle tube due to the smaller region between them.

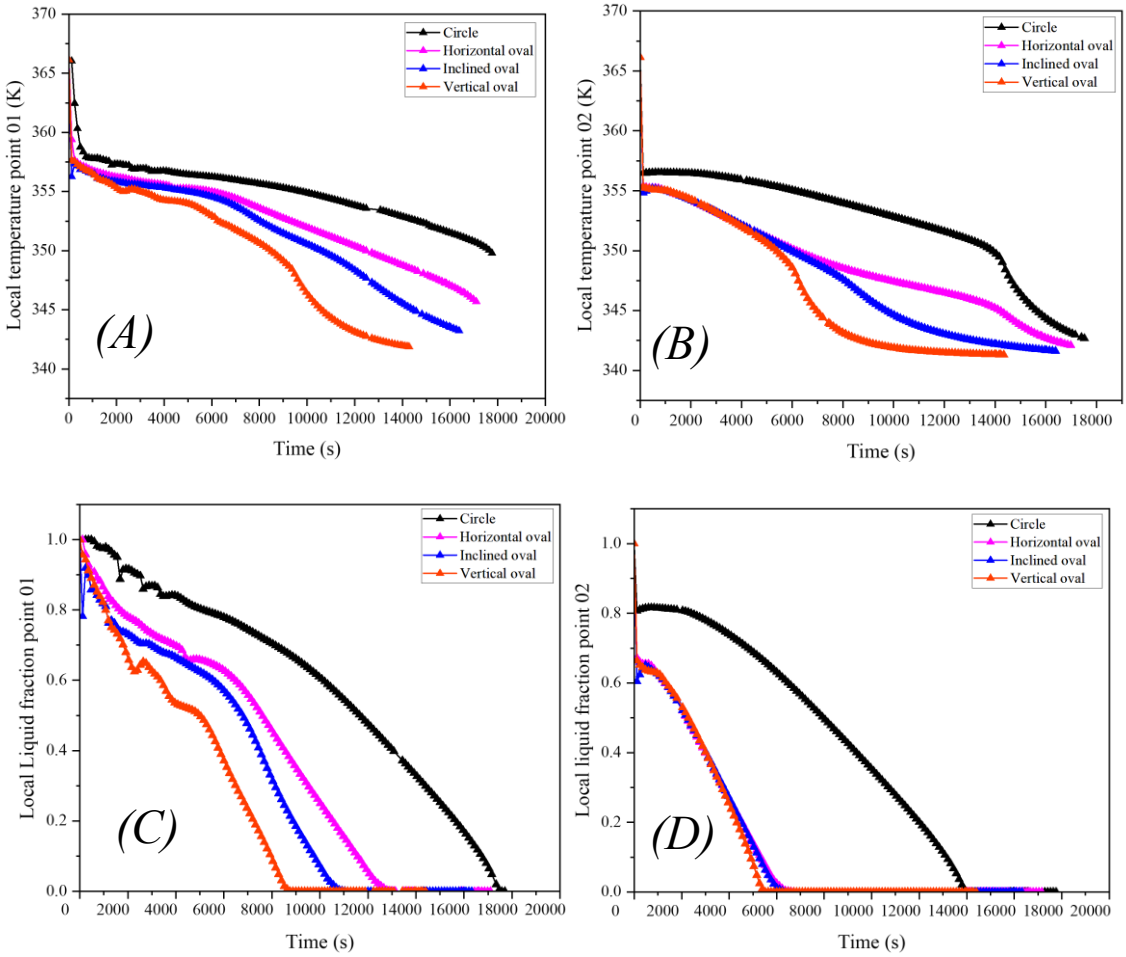

Figure V. 13: The local PCM temperature distribution and the local liquid fraction distribution for the solidification process: (A) the local PCM temperature distribution at point 1, (B) the local PCM temperature distribution at point 2, (C) the local liquid fraction distribution at point 1, (D) the local liquid fraction distribution at point 2.

In **Figure V.15**, at t = 0, the PCM is in a liquid state for all cases. Solidification commences with absorbing the heat by the inner and middle tubes as time progresses to t = 2400 s. Throughout the solidification process, heat transfer occurs through conduction exclusively within the solid PCM, while in the liquid PCM, it involves both conduction and convection. This is induced by temperature gradients, instigating buoyancy-driven flow due to density disparities across the PCM annulus. By t = 6000 s and t = 12000 s, the concentration of heat becomes evident between the oval lines and the middle tube, resulting in less solidification in this region. In contrast, between

the circular arc of the oval and the middle inner tube, it becomes cooler than the other regions, resulting in more rapid solidification in these regions. Upon completion of the solidification process, the liquid fraction inside the PCM units reaches f=0 across all cases. The unit with a V oval inner tube completes the solidification process firstly due to the shape of its inner tube, which is nearer to the top section of the PCM unit where the heat accumulates more, thus allowing for more efficient absorption of heat in this region.

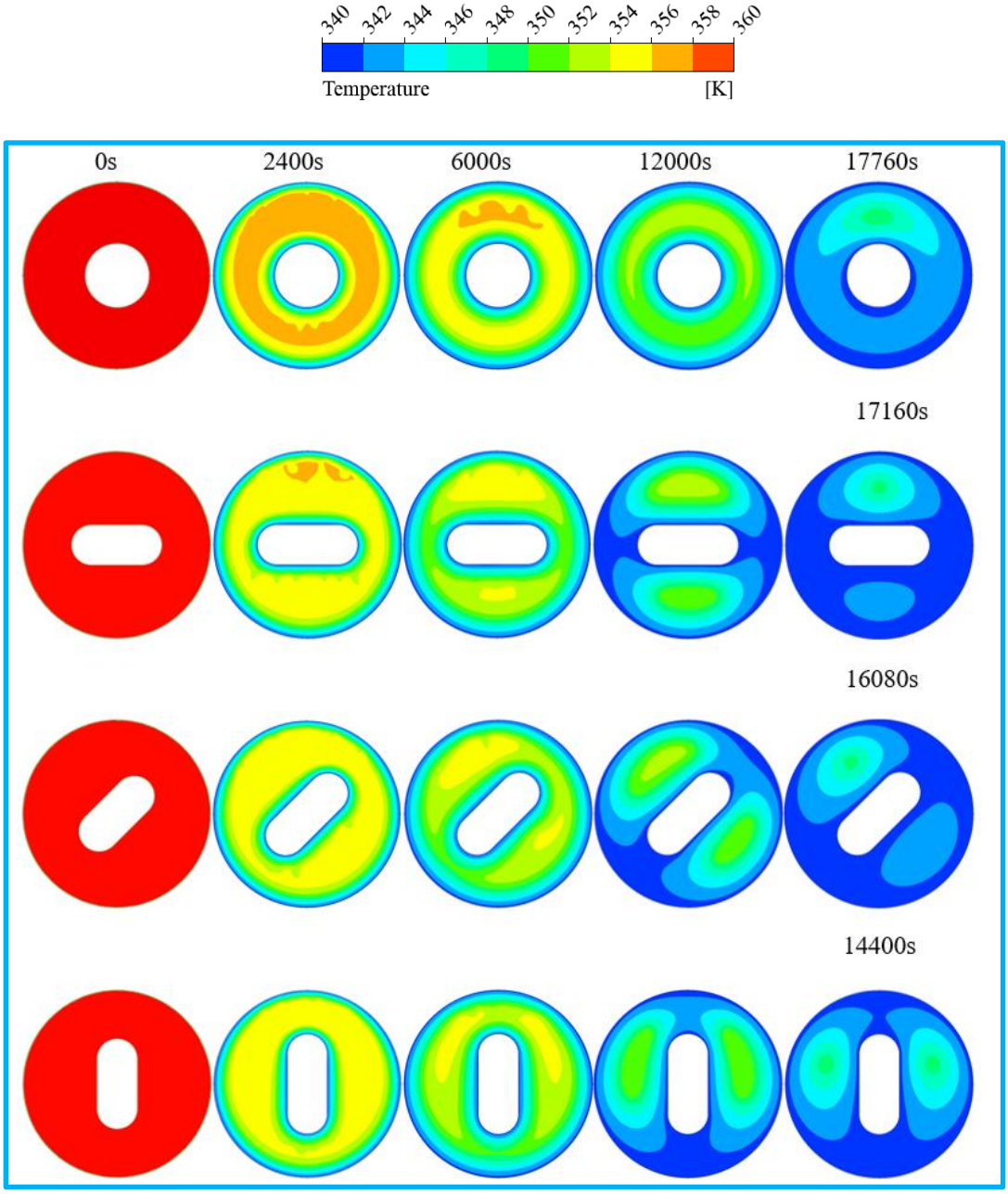

Figure V. 14 : Temperature contour plots for the solidification process.

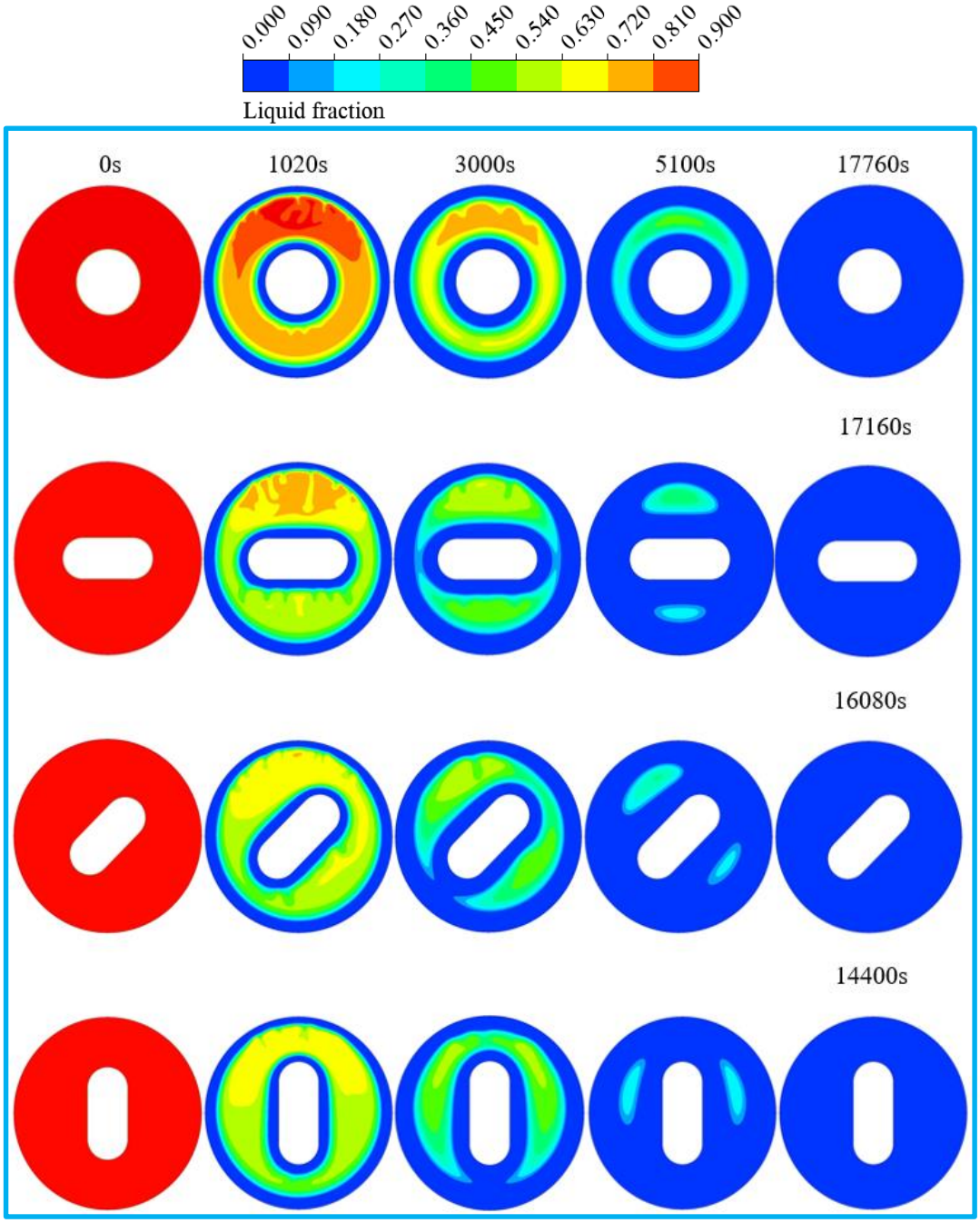

Figure V. 15 : Liquid fraction contour plots for the solidification process.

Figure V.16 illustrates the completion times for solidification, with the Circular inner tube completing the melting process after 17760s, the H oval completing after 17160 s, and In oval units completing after 16080 s, and the V oval unit completing after 14400s. The reduction in

melting time for H oval and In oval is 3.37% and 9.46%, respectively, whereas for V oval, it is notably greater at 18.91%.

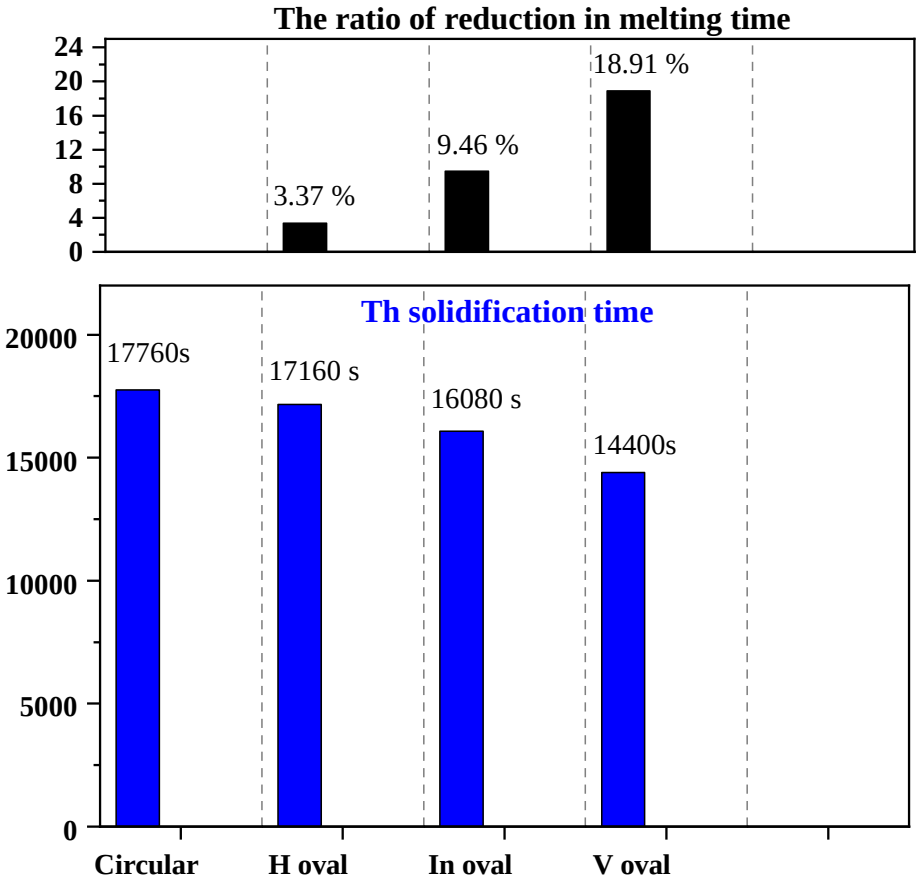

Figure V. 16: The solidification time and the reduction in solidification time for all cases.

V.4.2.3-*The heat flux variation for the solidification process*

Throughout the solidification process, the heat flux transitions to negative values. In the initial stages, the heat flux experiences a rapid decrease due to the swift drop in temperature differences between the cold walls and the liquid PCM. The detailed heat flux curve during solidification is represented in **Figure V.17**. Notably, no notable variations exist among the four configurations: circular, H oval, In oval, and V oval. The heat fluxes for all cases are nearly equal, with the oval cases slightly higher than the circular case towards the end of the solidification process. This phenomenon is owing to the larger perimeter of the oval shape than the circle, providing them with more heat absorption capacity. However, the weakened natural convection during solidification

enhances heat conduction efficiency, which tends to overshadow the impact of the inner tube's shape.

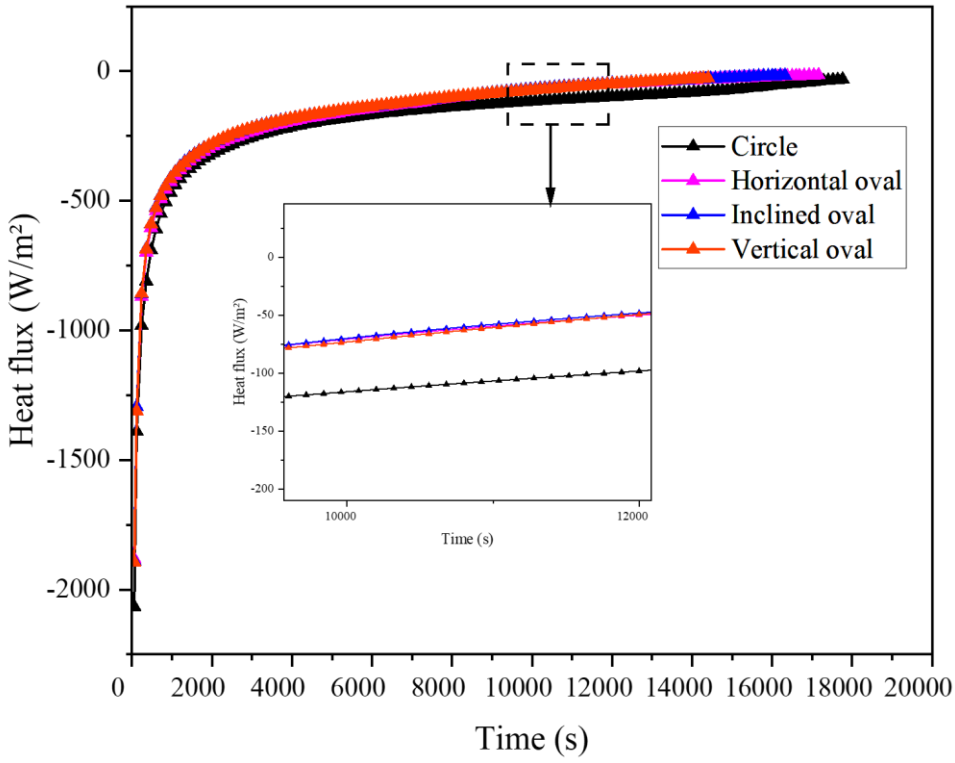

Figure V.17: The PCM heat flux distribution for the solidification process.

In the realm of PCM-based thermal storage, certain research limitations are notable, including simplified material properties, the inherent two-dimensional modeling assumption, and idealized boundary conditions. The reliance on precise material data, particularly during phase transitions, introduces uncertainties. The predominantly two-dimensional modeling approach may not fully capture spatial variations, while idealized boundary conditions may limit the study's applicability to real-world scenarios. Addressing these limitations poses challenges, such as the complexity of experimental validation due to the intricate nature of the systems and the difficulty in replicating real-world conditions. Parametric sensitivity and variability, coupled with the challenge of scaling up findings from small-scale models to larger systems, also require careful consideration. Looking ahead, prospects in the domain include exploring advanced modeling techniques like three-dimensional simulations for enhanced accuracy, innovations in PCMs through material science advancements, and the amalgamation of PCM-based storage with

renewable energy sources. Additionally, the development of smart control and monitoring systems presents opportunities for optimizing system performance under varying conditions, contributing to the evolution of efficient and sustainable energy solutions. On the other hand, Investigating the integration of metal foams, nanoparticles, fins, and multiple PCMs presents exciting opportunities for enhanced heat transfer and system performance. Assessing potential benefits or addressing specific challenges associated with each element could further guide and refine future research endeavors.

In conclusion, our study aimed to investigate the influence of changing the inner tube geometry to an oval shape on the melting time of the PCM. Through a comprehensive analysis of different inner tube geometries, we have provided insights into the thermal performance improvements associated with the adoption of an oval shape. The reduction in melting time observed in our results underscores the potential benefits of this geometric modification, contributing to the ongoing efforts in optimizing PCM-based thermal collectors for enhanced solar energy storage efficiency. While our study primarily focuses on the impact of changing the inner tube geometry from circular to oval shapes, it's important to acknowledge potential limitations in our investigation. Factors such as variations in PCM composition, container design, and environmental conditions were not explicitly addressed. These factors could potentially influence the generalization of our results to other scenarios or applications. Additionally, the experimental nature of our study may introduce variability in the observed reduction of melting and solidification times. Future research could explore these factors in greater detail to enhance the depth and applicability of our findings.

Among the compared geometries, the vertical oval inner tube was identified as the optimal design, reducing melting time to 7260 s (3.96% faster) and solidification time to 14,400 s (18.91% shorter) compared to other configurations.

V.5-Conclusion

In summary, this chapter demonstrates significant enhancements in PCM melting and solidification processes through innovative inner tube geometries. The H oval, In oval, and V oval designs exhibited notable performance improvements, including reduced melting and solidification times compared to the circular configuration. The vertical oval inner tube showed the fastest temperature increase during melting, reaching the melting point quicker than other

geometries. It completed melting in 7260 seconds, a 3.96% reduction compared to the circular tube. Additionally, the V oval inner tube reached its minimum heat flux value earlier, with a maximum heat flux of 1600 W/m². During solidification, the vertical oval inner tube reached solidification temperature faster and had a shorter solidification time (14400s) compared to the circular tube (17760s), an 18.91% reduction. Minimal differences in heat flux among all geometries during solidification were observed due to enhanced heat conduction efficiency.

These findings highlight the potential for optimizing PCM efficiency through strategic inner tube geometry design, enhancing the efficiency and reliability of solar energy systems. Quicker transitions between solid and liquid states optimize energy capture and extend stored energy availability, contributing to greater grid stability and advancing renewable energy goals.

Chapter VI. Enhancing TES Efficiency with Wedge-Shaped Geometries and Fins in PCM Heat Exchangers

VI.1- Introduction

This study investigates TES systems using PCM with ten cases involving modifications in inner tube and shell geometries, as well as fins. Starting from a circular shell and tube, designs progressed to vertical and horizontal wedge-shaped tubes, parallel shells, and integrated fins. Results show melting time reduced from 5920 s (original case) to 2560 s (three wedges with parallel shell and fins), achieving a 56.75% time-saving. Energy storage improved from 3050 kJ to 3070 kJ, with the highest value of 3076 kJ observed in the two-horizontal-wedge case. The three-wedge case also showed the highest Enhancement Ratio (*ER*) and strong convection currents. Economic analysis highlighted the three-wedge case as the most cost-effective, with P_c values ranging from 6.033 J/(s.$) to 10.6 J/(s.$). These findings emphasize the effectiveness of geometric modifications in enhancing TES performance and cost efficiency (**Figure V.1)**.

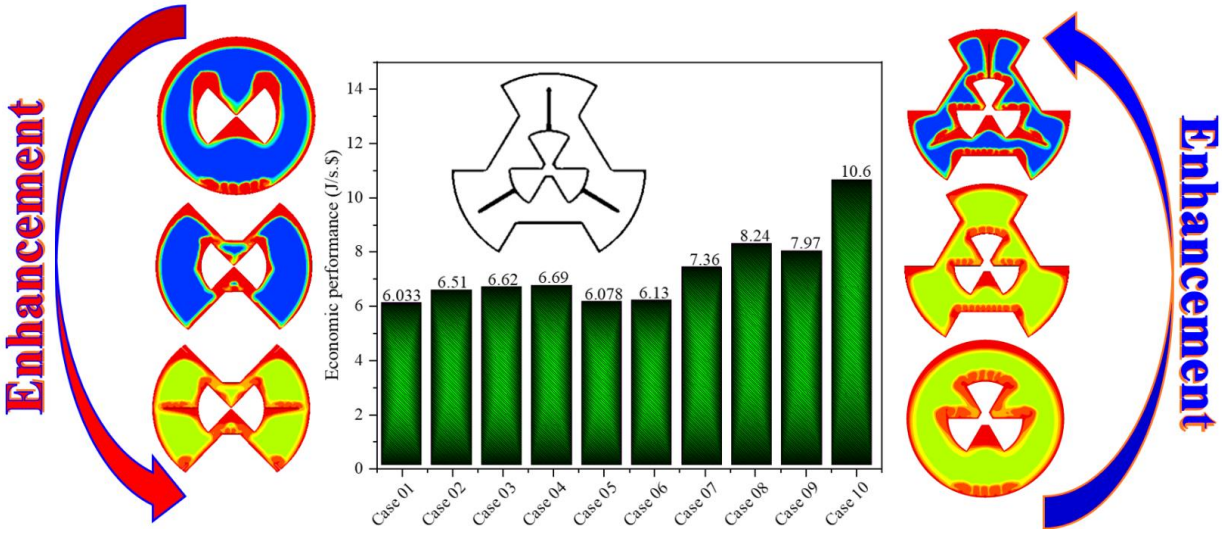

Figure VI. 1: Summary of chapter.

VI.2- Numerical Scheme

VI.2.1- Geometric representation

Ten distinct configurations were designed and analyzed, as illustrated in **Figure VI.2**. In the baseline model (Case 01), a circular shell with a diameter of 150 mm and a central inner tube with a diameter of 50.8 mm were used. Case 02 maintained the same circular shell but replaced the inner tube with two horizontally arranged wedge-shaped tubes, each having an equivalent circular diameter of 76 mm. In Case 03, the shell remained unchanged, while the inner tube was modified

to two vertically arranged wedges of the same diameter. Case 04 also retained the circular shell, incorporating three wedge-shaped inner tubes, each with a diameter of 71 mm.

In Case 05, the shell was reconfigured to be parallel to the wedge orientation, with a diameter of 184 mm, while the inner tube consisted of two horizontal wedges. Case 06 mirrored this configuration but in a vertical orientation. In Case 07, the inner tube comprised three wedges (71 mm diameter), and the shell was adjusted to be parallel, with a diameter of 180 mm. Case 08 built upon Case 05 by adding four short fins (10 mm length, 0.5 mm thickness) and two long fins (40 mm length, 0.5 mm thickness) to enhance heat transfer. Case 09 replicated Case 08 but in a vertical arrangement. Lastly, Case 10 was based on Case 07, with the addition of three long fins (40 mm length, 0.5 mm thickness).

Dimensional specifications are detailed in **Table VI.1** and visualized in **Figure VI.3**. Across all cases, the same volume of PCM was maintained. The PCM used in this study is RT82, selected for its negligible supercooling and long operational lifespan, with water employed as the HTF [41], rendering it the ideal PCM for this research. The thermophysical properties of RT82 are delineated in **Table VI.2** [214]. Notably, the surface area fraction of the fins (φ) is kept below 2%, and their total surface area remains constant across all configurations.

This consistency ensures that variations in thermal performance can be attributed to geometric and operational changes rather than differences in fin surface area.

Table VI. 1: Key geometric parameters of all PCM shell-and-tube heat exchangers.

Cases	Do (mm)	Di (mm)	ℓ (mm)	M (mm)	N (mm)
Case 01	150	50.8	-	-	-
Case 02	150	76	-	-	-
Case 03	150	76	-	-	-
Case 04	150	71	-	-	7
Case 05	184	76	61.5	20	-
Case 06	184	76	61.5	20	-
Case 07	180	71	58.5	32	7
Case 08	184	76	61.5	20	-
Case 09	184	76	61.5	20	-
Case 10	180	71	58.5	32	7

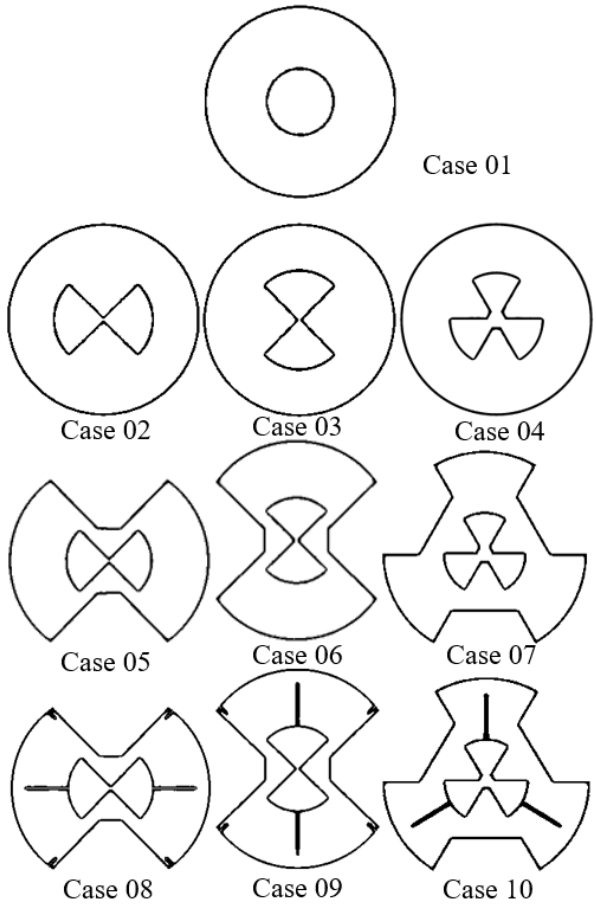

Figure VI. 2: Diagram of shell and tube heat exchanger configurations for all cases.

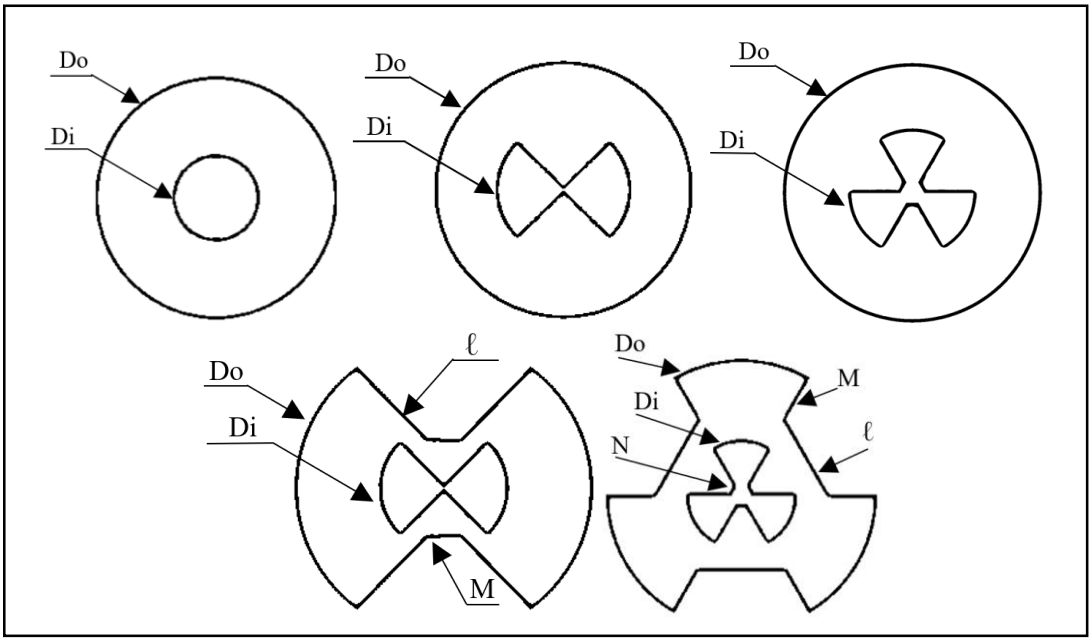

Figure VI. 3: Schematic representations of shell and tube heat exchanger dimensions for all cases.

A structured hexahedral mesh (**Figure VI.4**) was used for all cases, providing high-quality elements for accurate simulation results. The meshing strategy and grid resolution were uniformly applied throughout to maintain consistency in numerical accuracy.

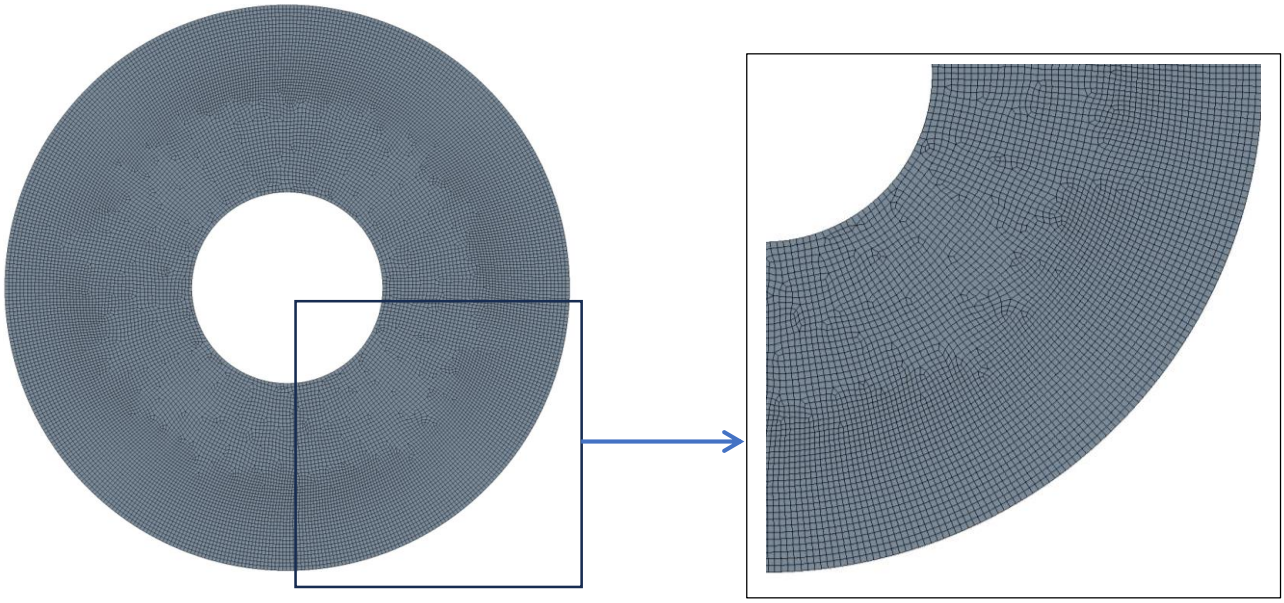

Figure VI. 4: Hexahedral grid for PCM shell and tube heat exchanger.

Table VI. 2: Thermophysical properties of RT82 and aluminum [214].

Property	Unit	RT82	Aluminum
Density	kg/m^3	950(s)/770(l)	2719
Specific heat capacity	kJ/kg.K	2	871
Thermal conductivity	W/m. K	0.2	202.4
Dynamic viscosity	kg/m.s	0.03499	-
Latent heat	kJ/kg	176	-
Temperature	K	350(s)/358(l)	-
Thermal expansion coefficient	1/K	0.001	-

VI.2.2- Assumptions and Governing Conditions

This section outlines the fundamental equations governing the PCM's thermal behavior. In the solid phase, heat transfer occurs primarily through conduction. As the PCM melts, both conduction

and natural convection become significant. The model assumes laminar, transient, and incompressible flow, along with additional assumptions described below. The widely adopted enthalpy-porosity method is used to simulate the melting process, which tracks the liquid fraction within each computational cell rather than explicitly following the moving phase-change interface [223]. In this model, the melting region is treated as a porous medium, where the local liquid fraction represents the porosity. A porosity of 0 indicates a fully solid state, while a value of 1 denotes a completely liquid state. The governing equations for fluid flow and temperature distribution are integrated within this enthalpy-porosity framework.

To develop a simplified mathematical model of the melting process, several assumptions were adopted. The analysis is carried out in a two-dimensional domain. No-slip conditions are applied along all solid boundaries. The HTF is assumed to have a constant temperature, and thermal variations within the fins are considered negligible, implying thermal equilibrium between the HTF, the fins, and the wall. Viscous dissipation effects are disregarded. The thermophysical properties of the PCM are treated as constant, except for the density in the momentum equations, where the Boussinesq approximation is applied [88]. Under this assumption, density is treated as temperature-dependent for buoyancy-driven flow modeling, as described in [224]:

$$\rho = \rho_m \left[1 - \beta \left(T_{ref} - T_m\right)\right] \tag{VI.1}$$

where, $T_m = \frac{T_s + T_l}{2}$, ρ_m represents the density of the liquid PCM, while T_s and T_l denote the solidus and liquidus temperatures, respectively.

Additionally, volume changes associated with phase transitions are neglected, and heat exchange with the surroundings is assumed to be nonexistent. The liquid phase is considered transient and incompressible. Thermal contact resistance at the interface between the inner tube and fins, as well as between the shell and fins, is assumed to be negligible. The modeling of viscous flow and heat transfer is governed by the Navier–Stokes equations, in conjunction with the energy conservation equation. These governing equations incorporate mass continuity, momentum conservation, and thermal energy balance, and collectively describe the transient behavior of the fluid and temperature fields during the melting process, as presented in Chapter II.

VI.2.3-Computational techniques and boundary conditions

The numerical simulations were carried out using ANSYS-FLUENT 2023-R1, where the governing partial differential equations were solved through a pressure-based solver, which is

well-suited for modeling incompressible flow conditions involved in PCM melting processes [97]. The momentum and energy equations were discretized using the finite volume method. For spatial discretization, the Second Order Upwind scheme was applied to the momentum equations, while the QUICK scheme was utilized for the energy equation. Pressure–velocity coupling was managed using the SIMPLE algorithm, and the pressure correction equation was solved via the PRESTO! scheme. Convergence thresholds were set at 10^{-4} for both continuity and momentum equations, and 10^{-6} for the energy equation.

To ensure the reliability of the numerical results, a mesh independence study was conducted. This involved comparing the liquid fraction across the entire PCM domain using three different mesh sizes: 0.6 mm, 0.7 mm, and 0.8 mm, corresponding to total cell counts of 27,040, 19,992, and 15,337, respectively. The results indicated that the 0.8 mm mesh size yielded dependable outcomes. Although smaller cell sizes gave similar results, they led to increased computational costs without significant improvements in accuracy. The results of the mesh independence study are shown in **Figure VI.5(A)**.

A time step independence analysis was conducted to identify the most suitable time increment for the simulations. Using a mesh consisting of 15,337 cells, three different time steps 0.1 s, 0.5 s, and 1 s were evaluated. As illustrated in **Figure VI.5(B)**, the resulting temperature profiles showed negligible differences across these time steps. Therefore, a time step of 1 s was chosen in conjunction with the 15,337-cell mesh, ensuring an optimal trade-off between computational accuracy and efficiency.

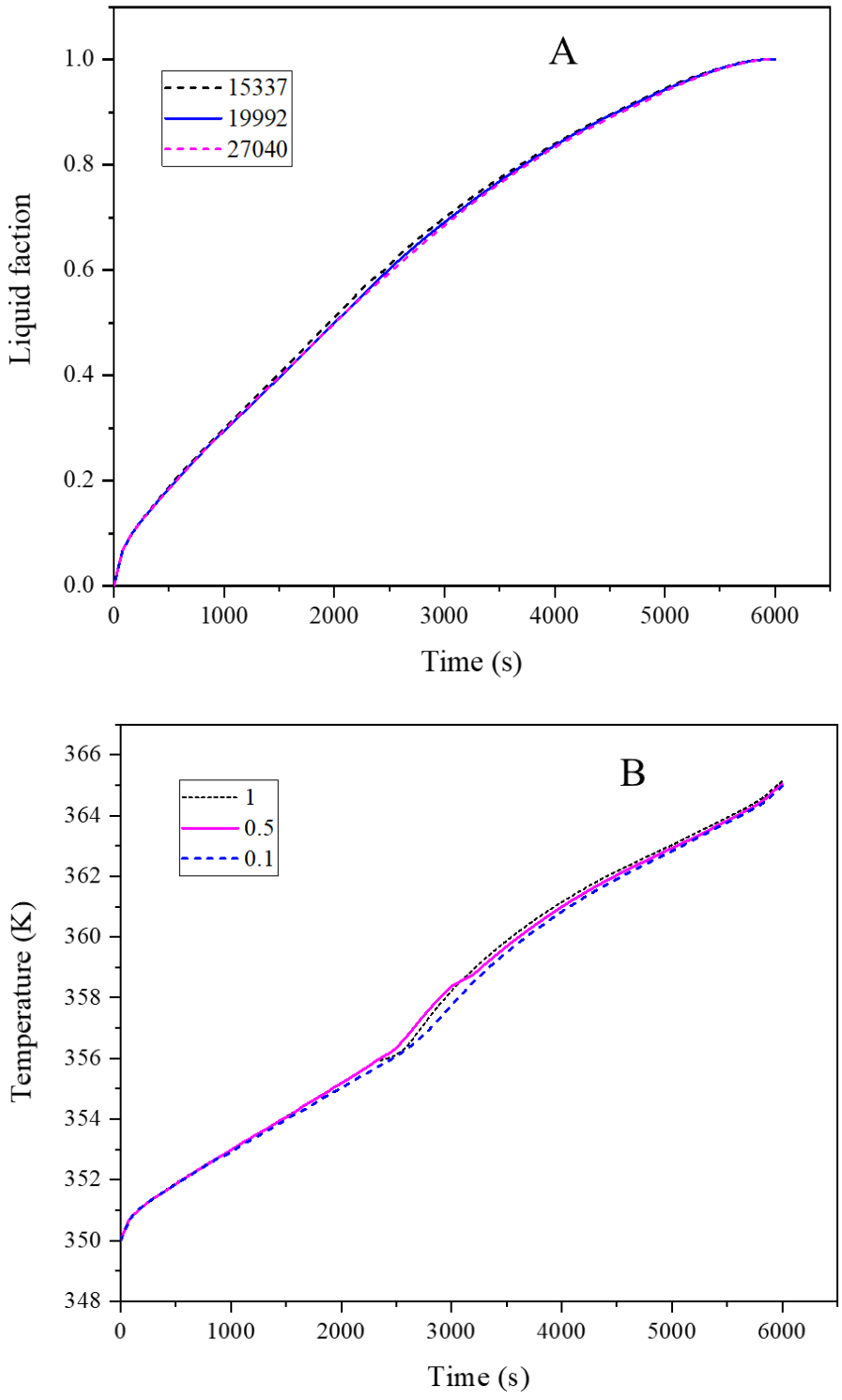

Figure VI. 5: (A) Mesh independence study, (B) Time step independence study.

The computational domain is designed as an annular section (**Figure V.6**), representing the region occupied by the PCM (RT82). At the start of the simulation (t = 0 s), the PCM is initialized at 350

K to model the melting behavior. The temperatures of both the inner wall and attached fins aligned with the temperature of the heat transfer fluid are kept constant at 366.15 K. These steady thermal boundary conditions provide a consistent framework for analyzing how variations in the inner and outer tube shapes, as well as the inclusion of fins, influence the melting duration of the PCM. The applied boundary conditions are summarized as follows:

At $r = R_{Shell}$ and $r = R_{tube}$, $T_{tube} = T_{Shell} = T_{Fins} = 366.15K$ (VI.2)

R_{tube} and R_{shell} represent the radius of the inner tube and the shell, respectively.

The initial condition is defined as follows:

At $t = 0, T(x, y) = T_{initial} = 350K$ (VI.3)

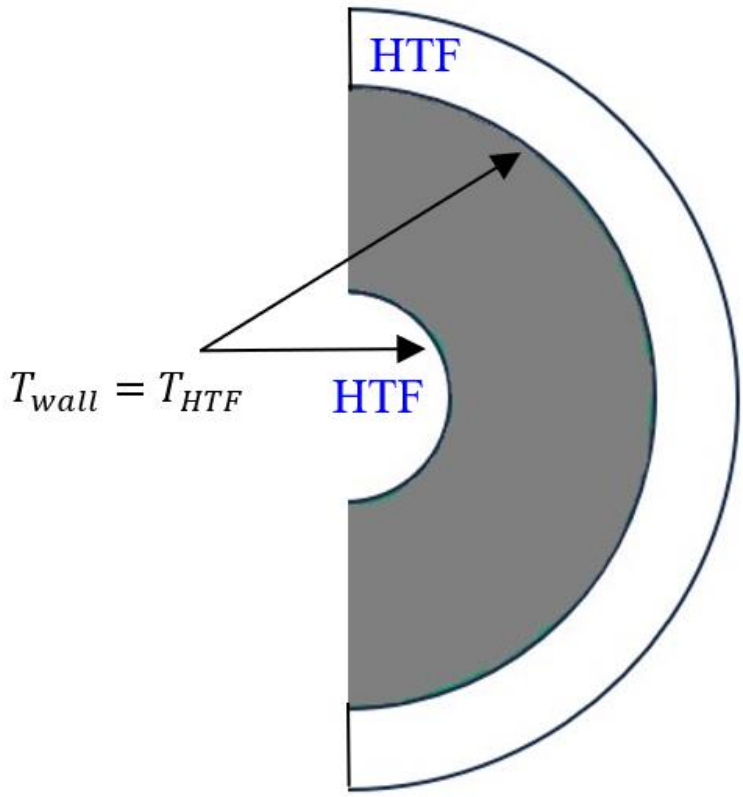

Figure VI. 6: Boundary conditions and computational domain for PCM.

VI.3- Results and discussion

VI.3.1-Tube geometry

This study evaluates four inner tube geometries within a circular shell to analyze their influence on PCM temperature distribution. All cases share the same outer shell, while the inner tube geometry varies as follows: Case 01 – circular tube (baseline); Case 02 – two horizontal wedges; Case 03 – two vertical wedges; and Case 04 – three wedges. **Figure VI.8** illustrates the average PCM temperature for each configuration. Among the designs, Case 04 exhibits the highest temperature rise due to the increased surface area provided by the three-wedge structure, which enhances heat transfer from the tube to the PCM. Cases 02 and 03 also outperform the baseline, though to a lesser extent, with their two-wedge geometries promoting better thermal contact than the simple circular tube. These results highlight the importance of inner tube surface area optimization in improving heat transfer efficiency within TES systems.

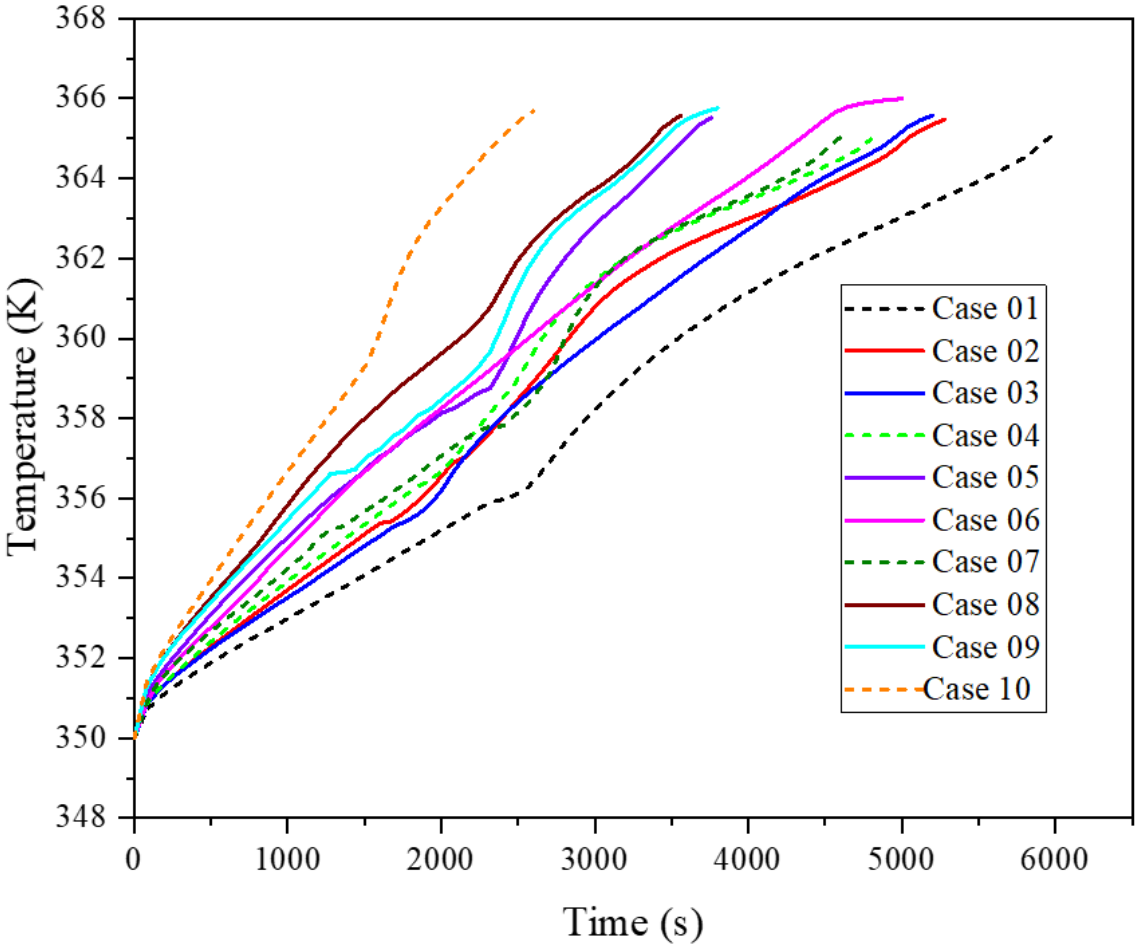

Figure VI. 7: The average temperature of the PCM across all cases.

Figure VI.9 presents the evolution of the liquid fraction for various inner tube geometries within a circular shell. Case 04 demonstrates the highest liquid fraction, followed by Cases 02 and 03, with all outperforming the baseline Case 01. The superior performance of Case 04 is attributed to its larger inner tube surface area, which enhances heat transfer and accelerates the phase change process. Similarly, the two-wedge configurations in Cases 02 and 03 improve melting efficiency over the circular design, albeit to a lesser extent than the three-wedge arrangement.

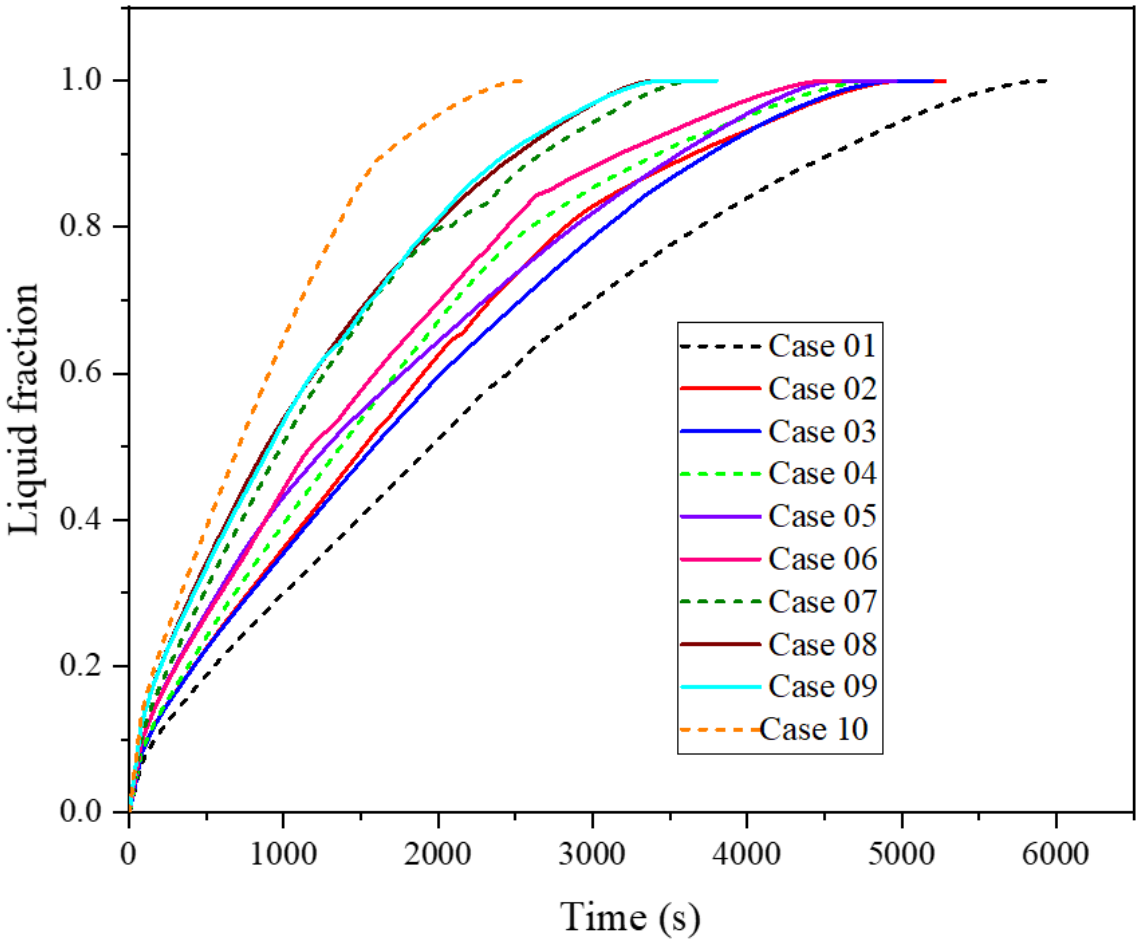

Figure VI. 8: The average liquid fraction of the PCM for all cases.

Figures VI.10 and **VI.11** illustrate the melt fraction and temperature contours, respectively, comparing the melting progress across different inner tube geometries relative to the base case. In each figure, columns represent temporal progression, while rows correspond to the four studied configurations, starting uniformly at t = 80 s. Initially, the melting process is governed by conduction from the heated surfaces to the adjacent PCM. At t = 80 s, all cases exhibit uniform melting around both the inner tube and outer shell. The recorded temperatures and liquid fractions

were as follows: Case 01 reached 350.7 K with 6.83% melting; Case 02 and Case 03 both reached 350.84 K with 8.12%; and Case 04 recorded 350.86 K with a liquid fraction of 8.38%. These early differences highlight the influence of increased surface area on accelerating the initial phase change.

As time progresses to t = 1040 s, melting intensifies due to buoyancy-driven convection, which enhances heat transfer beyond conduction. At this point, Case 01 exhibited a temperature of 353.07 K and a liquid fraction of 30.85%, while Case 02 reached 354.82 K and 37.22%. Case 03 registered 353.61 K with 36.52%, and Case 04 reached 354.04 K with the highest fraction at 40.56%.

By t = 4560 s, most of the PCM had melted, with a remaining solid region near the bottom, where heat transfer continues primarily through conduction. Case 01 achieved 362.26 K and 90.14% melting, whereas Cases 02, 03, and 04 recorded 363.91 K (97.99%), 364.16 K (98.29%), and 364.41 K (99.2%), respectively.

Overall, Case 04, having the largest heat transfer surface area, demonstrated the most efficient melting, completing the process in 4800 s. This is notably faster than Case 01, which required 5920 s. Case 02 and Case 03 followed, with complete melting times of 5040 s and 4960 s, respectively. The results confirm that enhanced surface area and geometric design significantly influence thermal performance and melting rate.

The melting process in PCM-based TES systems typically begins with heat transfer dominated by conduction near the heated surfaces, forming an initial molten layer around both the inner tube and the shell. As the phase change progresses and the liquid fraction increases, natural convection driven by buoyancy forces arising from temperature-induced density gradients becomes increasingly significant. These convective currents facilitate the upward movement of the heated liquid PCM, thereby accelerating the melting process and promoting a more uniform temperature distribution. The interplay between conduction at the solid–liquid interface and convective flow within the liquid region enhances the overall heat transfer efficiency. Notably, configurations that incorporate extended surfaces or geometrical modifications to increase heat transfer area further intensify this effect, resulting in faster and more homogeneous melting throughout the PCM domain. Additionally, optimizing the placement and orientation of heat sources can improve the effectiveness of natural convection, contributing to improved thermal performance and energy storage rates.

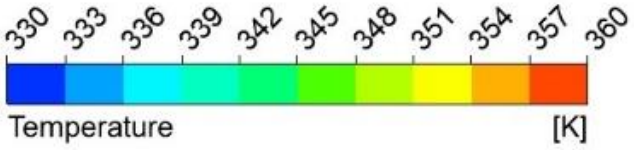

Time (s)	80	1040	2560	4560
Average temperature (K)	350.7	353.071	356.26	362.26
Case 01				
Average temperature (K)	350.84	354.82	358.74	363.91
Case 02				
Average temperature (K)	350.84	353.61	358.6	364.16
Case 03				
Average temperature (K)	350.86	354.04	359.39	364.41
Case 04				

Figure VI. 9: Temperature Contours for Cases 01, 02, 03, and 04.

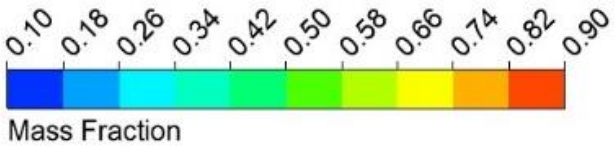

Time (s)	80	1040	2560	4560
Liquid fraction (%)	6.83	30.85	62.28	90.14
Case 01				
Liquid fraction (%)	8.12	37.22	74.80	97.99
Case 02				
Liquid fraction (%)	8.12	36.52	70.54	98.29
Case 03				
Liquid fraction (%)	8.38	40.65	79.41	99.2
Case 04				

Figure VI. 10: Liquid fraction Contours for Cases 01, 02, 03, and 04.

VI.3.2- Shell geometry

As illustrated in **Figure VI.8**, the average temperature profiles for Cases 05, 06, and 07 exhibit a nearly identical upward trend. These cases were specifically designed to investigate the influence of inner tube geometry on the temperature distribution within the PCM domain. In Case 05, the inner tube consisted of two horizontally aligned wedge-shaped fins, with the shell oriented parallel to these wedges. Case 06 maintained the same wedge configuration but rotated it vertically. In Case 07, the inner tube incorporated three wedge-shaped fins, again with the shell aligned parallel to their orientation. This specific geometric arrangement, where the shell surface runs parallel to the fins was selected to maximize the shell's surface area and promote a more uniform distribution of PCM. By ensuring that all regions of the PCM remain in close proximity to both the heated inner tube and the shell, this design enhances thermal accessibility across the entire volume. Consequently, each segment of the PCM is exposed to efficient heat transfer paths, allowing it to absorb thermal energy more uniformly and effectively, thereby accelerating the melting process and improving thermal performance.

Figure VI.9 clearly shows a consistent increase in the liquid fraction for Cases 05, 06, and 07, exceeding the levels observed in Cases 01 through 04. These improvements are the result of deliberate modifications to both the shell and inner tube geometries, aimed at evaluating their influence on phase change behavior. Among them, Case 07 exhibited the most favorable progression of the liquid fraction. This enhancement is primarily attributed to the inner tube's design, which incorporated three wedge-shaped extensions, thereby increasing the available surface area for thermal interaction. Furthermore, aligning the outer shell parallel to the geometry of the inner tube significantly expanded the shell's effective heat transfer surface. This configuration not only promoted more efficient heat delivery but also ensured a more homogeneous distribution of the PCM within the annular domain of the heat exchanger. As a result, thermal energy was absorbed more uniformly across the PCM volume, accelerating the melting process and leading to superior thermal performance in Case 07 compared to the other configurations.

Figures VI.12 and **VI.13** present the evolution of melt fraction and temperature contours, respectively, allowing for a comparative analysis between the proposed shell configurations and the reference design. In these figures, each column corresponds to a specific time step, while each row represents a distinct case. The melting process is tracked beginning from t = 80 s for all

configurations, providing a consistent temporal reference for assessing thermal performance and melting behavior.

Melting initially proceeds through heat transfer dominated by conduction from the heated surfaces to the adjacent PCM, marking the onset of phase change during the early period (t = 80–720 s). At this stage (t = 720 s), conduction remains the primary mechanism of heat transfer, leading to relatively uniform melting around both the inner tube and the shell in Cases 05, 06, and 07. In Case 05, the PCM temperature reached 353.60 K, corresponding to a liquid fraction of 35%. Case 06 exhibited a temperature of 353.34 K with a liquid fraction of 34.24%. In comparison, Case 07 achieved the highest temperature of 353.98 K and a liquid fraction of 39.66%, indicating superior melting performance. This enhancement is directly related to the increased heat transfer surface area provided by the three-wedge geometry of the inner tube in Case 07. The results clearly demonstrate that a larger effective surface area facilitates more rapid and extensive melting during the conduction-dominated stage.

At t=1440s, melting continues to progress as the PCM near the heated surfaces absorbs more thermal energy. At this stage, buoyancy-driven effects become increasingly significant, leading to the development of natural convective currents. These currents enhance the upward transport of heat within the molten PCM, accelerating the overall melting process. In Case 05, the PCM temperature reached 356.47 K, corresponding to a liquid fraction of 53.58%. Case 06 recorded a temperature of 355.51 K with a liquid fraction of 56.08%, while Case 07 exhibited a slightly higher temperature of 356.50 K and a significantly greater liquid fraction of 65.54%. The superior performance of Case 07 is attributed to its optimized geometry, which promotes stronger convective flow and better thermal distribution. As the melting front advances, most of the PCM surrounding the heat transfer surfaces becomes fully liquefied. However, a residual solid mass tends to persist at the base of the heat exchanger, where convective effects are weaker and melting relies primarily on conduction. By t=2160s, continued heat input further reduces this solid region. Case 05 reached a temperature of 358.73 K with a liquid fraction of 67.39%. Case 06 showed a temperature of 357.48 K and a liquid fraction of 73.54%. Case 07 again demonstrated the most effective melting behavior, achieving a temperature of 358.42 K and a liquid fraction of 81.44%. These findings reinforce the influence of enhanced geometry on accelerating both conduction and convection mechanisms within the PCM domain.

Case 07, featuring the largest heat transfer surface area, strategically distributes the PCM close to both the shell and inner tube surfaces, significantly enhancing thermal interaction. This configuration promotes stronger natural convection and results in the fastest melting among all cases, completing the phase change in just 3680s substantially shorter than the 5920 s required in the baseline case.

Cases 05 and 06, which incorporate enhanced heat transfer surfaces, achieved complete melting in 4640 s and 4560 s, respectively faster than Cases 01 through 04. Overall, the melting process begins with conduction near heated surfaces, forming an initial liquid layer. As the liquid fraction increases, buoyancy-driven convection develops, accelerating heat transfer and promoting uniform melting. Configurations with larger heat transfer areas, such as wedge-shaped geometries, strengthen this conduction-convection synergy, leading to significantly faster and more efficient phase change throughout the PCM domain.

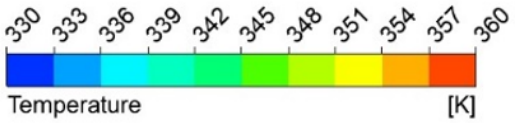

Time (s)	80	720	1440	2160
Average temperature (K)	350.88	353.60	356.47	358.73
Case 05				
Average temperature (K)	350.88	353.34	355.51	357.48
Case 06				
Average temperature (K)	351.09	353.98	356.50	358.42
Case 07				

Figure VI. 11: Temperature Contours for Cases 05, 06, and 07.

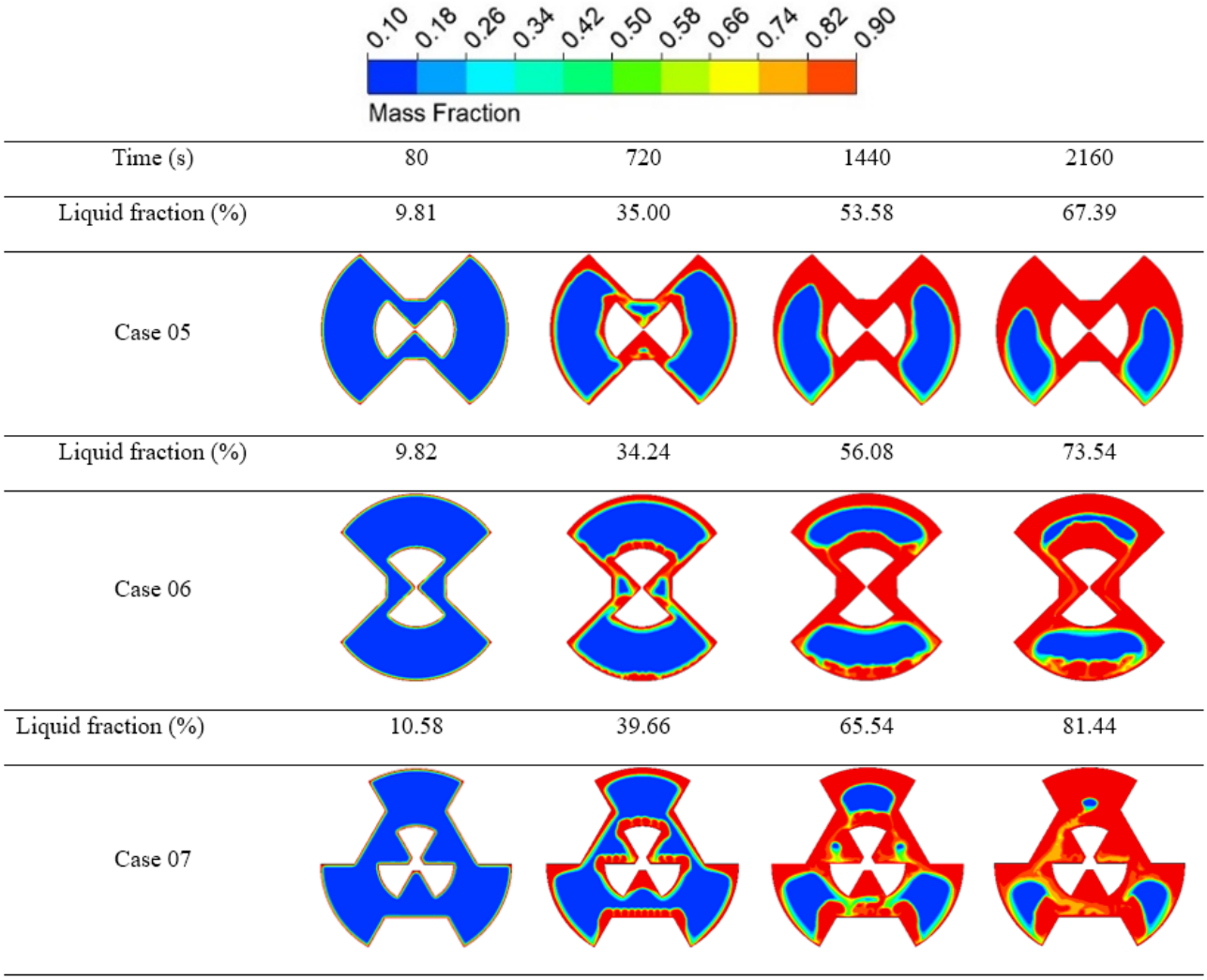

Figure VI. 12: Liquid fraction Contours for Cases 05, 06, and 07.

VI.3.3- Fins addition

Case 08 featured an inner tube composed of two horizontal wedges, each equipped with a long fin, along with four small fins positioned at the corners of the shell, which was aligned parallel to the wedges. Case 09 mirrored this design but with a vertical orientation. In Case 10, the inner tube included three wedges, each with a long fin, with the shell again oriented parallel to the wedge arrangement. These geometries were designed to increase the surface area of the shell and promote uniform PCM distribution by placing each PCM segment in close proximity to both the inner and outer heat transfer surfaces. The inclusion of fins in all configurations further enhanced thermal performance by expanding the effective heat exchange surface, ensuring that each region of the PCM received maximum thermal input.

Figures VI.8 and **VI.9** reveal that Cases 08, 09, and 10 exhibit notable improvements in both average temperature and liquid fraction compared to the earlier configurations (Cases 01–07). Among them, Case 10 demonstrates the most significant enhancement in thermal performance. These improvements are attributed to the optimized inner tube and shell geometries, along with strategically placed fins, which collectively enhance heat transfer, promote uniform temperature distribution, and accelerate the phase change process.

In Case 08, the use of two horizontal wedges in the inner tube with a parallel shell led to a moderate improvement in the liquid fraction compared to Cases 05, 06, and 07. The addition of fins enhanced heat transfer, promoting a more uniform melt distribution. Case 09, which employed a similar wedge design but with a vertical orientation, exhibited slightly better performance due to more effective utilization of the fins in directing heat throughout the PCM. Case 10, featuring three wedges and a parallel shell, delivered the highest liquid fraction among all configurations. Its geometry, combined with extended fins, maximized the heat transfer surface area and ensured close contact between the PCM and both the inner tube and shell. This facilitated uniform temperature distribution and efficient phase change, resulting in a superior and more evenly distributed liquid fraction. Consequently, Case 10 outperformed all prior cases in terms of melting behavior and heat transfer efficiency.

Figure VI.14 illustrates the temperature contours for Cases 08, 09, and 10. At the initial stage (t = 80 s), heat transfer is predominantly driven by conduction. The fins transfer heat from the walls into the solid PCM, raising its temperature, although minimal melting occurs at this point. As time advances to t = 720 s, the melting layer thickens and buoyancy-driven convection becomes more prominent, altering the temperature distribution. This results in irregular temperature contours due to fluid impingement on the solid PCM, as seen in **Figure VI.14**. Based on **Figures VI.14** and **VI.15**, Case 08 reached a temperature of 354.47 K with a liquid fraction of 43.47%. Case 09 followed with a temperature of 354.34 K and a liquid fraction of 42.55%. Case 10 exhibited the highest temperature at 355.18 K and the most advanced melting, with a liquid fraction of 50.67%. These values represent a notable enhancement compared to Cases 05, 06, and 07 at the same time interval (t = 720 s), confirming the positive impact of geometric modifications and fin integration on thermal performance.

At t = 1440 s, the interface between the solid and liquid PCM extends further into the upper and lower regions of the domain. This expansion results from the deformation of the remaining solid PCM and its partial protrusion into the liquid phase, which accelerates the melting process. According to **Figures VI.14** and **VI.15**, Case 08 reached a temperature of 357.78 K with a liquid fraction of 67.21%, while Case 09 recorded a temperature of 356.72 K and a liquid fraction of 66.39%. Case 10 exhibited the most significant improvement, achieving a temperature of 358.95 K and a liquid fraction of 83.92%. These values highlight a substantial enhancement in melting performance compared to Cases 05, 06, and 07 at the same time step. In the final stage, as the PCM becomes predominantly liquid, natural convection gradually weakens, and heat transfer is increasingly dominated by conduction. This behavior is particularly evident in Case 10, where the convective influence on the deformation of the solid PCM becomes minimal, and the remaining solid particles settle at the bottom of the enclosure.

Figure VI.15 illustrates the evolution of the solid-liquid interface (liquid fraction contours) for Cases 08, 09, and 10. Although the volume occupied by the fins is kept constant, ensuring a consistent PCM mass across these cases, the total surface area varies due to differences in shell and inner tube geometries. A fin thickness of 0.5 mm, uniformly dividing the PCM domain, provides a large surface area for heat dissipation, which contributes to faster melting. In the early stage (t = 80 s), heat transfer is primarily driven by conduction, leading to a relatively uniform melting pattern around both the inner tube and the shell. By t = 720 s, all fin configurations exhibit similar melting behavior, with layers of liquid PCM forming adjacent to the exchanger walls and the fins. The key distinction between the finned (Cases 08–10) and non-finned cases (Cases 01–07) lies in the thickness of the liquid PCM layers particularly beneath the inner tube and at the fin extremities which are significantly greater in the finned configurations. During this intermediate phase, conduction remains the dominant heat transfer mechanism, as the volume of melted PCM is still insufficient to support substantial natural convection.

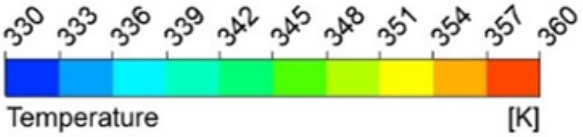

Time (s)	80	720	1440	2160
Average temperature (K)	351.26	354.47	357.78	360.12
Case 08				
Average temperature (K)	351.26	354.34	356.72	358.97
Case 09				
Average temperature (K)	351.4	355.18	358.95	364.04
Case 10				

Figure VI. 13: Temperature Contours for Cases 08, 09, and 10.

The increased presence of liquid PCM near the fin edges highlights the role of the fins in accelerating the onset of natural convection. The additional heat exchange area provided by the fins enhances thermal diffusion, leading to earlier formation of convection currents particularly in the lower region of the PCM annulus compared to the non-finned cases. As shown in **Figure VI.15**, convection currents become clearly visible in all finned configurations by 1440 seconds, reshaping the liquid–solid interface. Case 10 exhibits the most pronounced convection flows in the upper region of the PCM domain, attributed to its geometry offering the largest surface area and its evenly distributed fins across the three wedge-shaped segments of the shell and tube heat

exchanger. This configuration proves highly effective in promoting PCM melting. However, fins within the annulus somewhat restrict convection in the lower region of the domain.

At 1440 seconds, the finned cases achieve a melting range of approximately 67–83% of the PCM, in contrast to only 30–65% in the non-finned scenarios. This underscores the significant improvement in early-stage melting efficiency due to the incorporation of fins. The distribution of remaining solid PCM within the heat exchanger varies across Cases 08, 09, and 10, reflecting the influence of different geometrical configurations and fin placements on the phase change behavior.

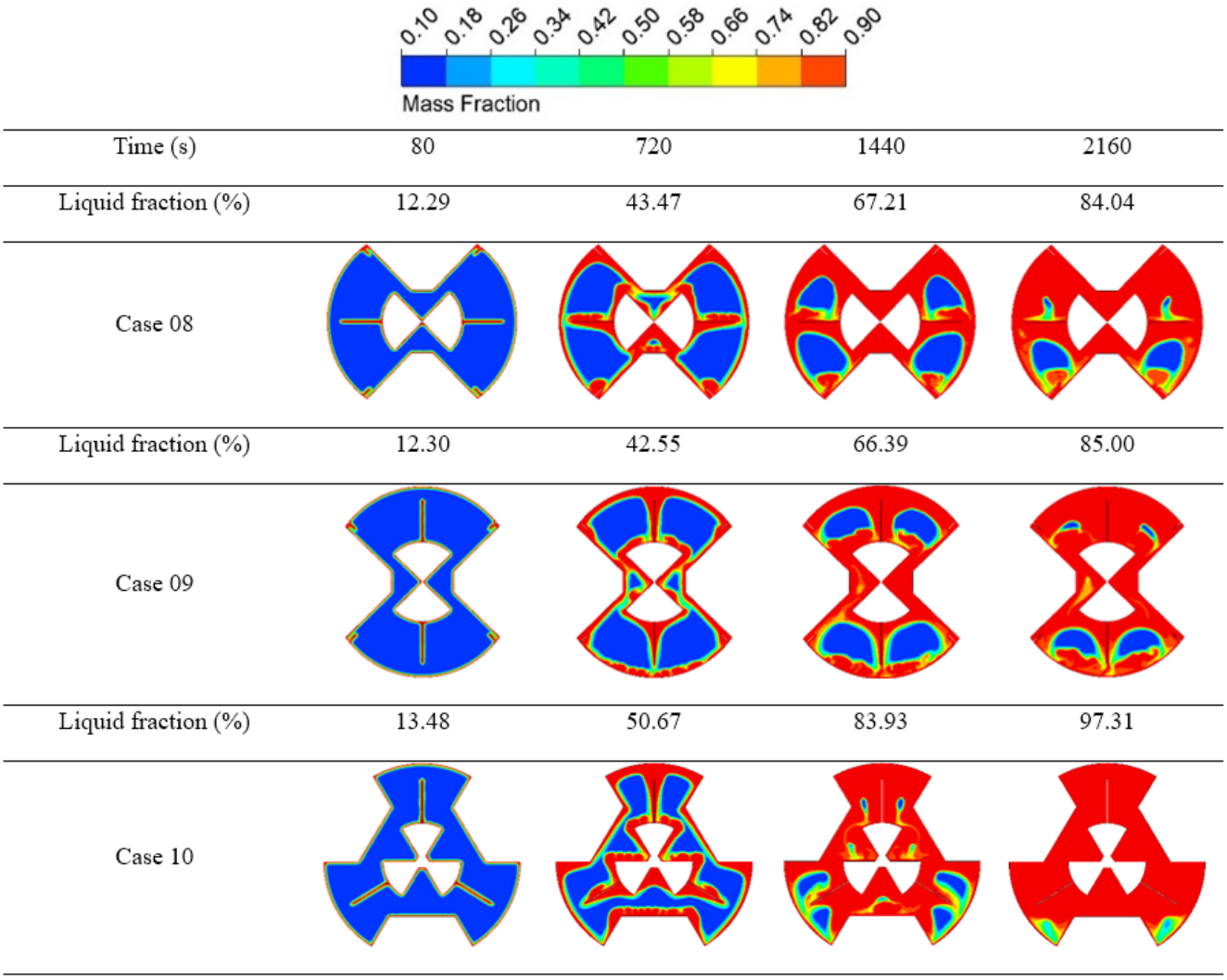

Figure VI. 14: Liquid fraction contours for Cases 08, 09, and 10.

.

Figure VI.16 presents the melting times for Cases 01 to 10, illustrating the influence of geometric modifications and fin integration on heat transfer efficiency. Case 01, used as the reference

configuration, recorded the longest melting time at 5920 seconds. Cases 02 to 04, featuring modifications to the inner tube geometry, demonstrated gradual improvements, with melting times of 5040 s, 4960 s, and 4800 s, respectively. Enhanced performance was observed in Cases 05 to 07, which combined changes in both the inner tube and shell geometries. These configurations further reduced the melting time to 4640 s, 4560 s, and 3680 s, respectively, with Case 07 showing the most substantial improvement within this group.

The greatest enhancements occurred in Cases 08 to 10, where the integration of geometric modifications with extended surfaces (fins) significantly boosted heat transfer. Cases 08 and 09 achieved melting times of 3400 s and 3520 s, while Case 10, with the most optimized configuration, attained the shortest melting time of 2560 s. These results clearly demonstrate that the combination of tailored geometrical designs and fin incorporation leads to notable reductions in melting time, highlighting the critical role of such strategies in improving the thermal performance of latent heat thermal energy storage systems.

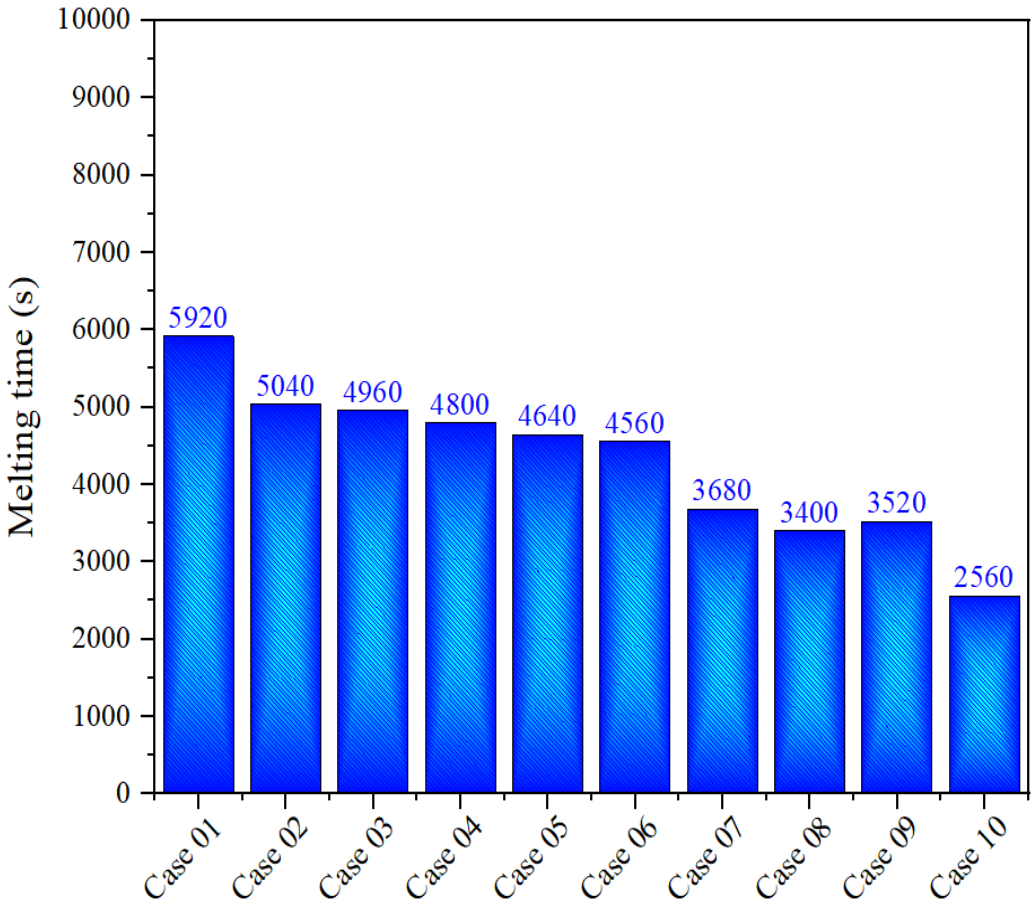

Figure VI. 15: Complete melting time for all cases.

VI.3.4- Enhancement ratio

The enhancement ratio (ER) quantifies the improvement in melting performance and is defined as the difference between the liquid fraction of a given modified case ($f_i(t)$) and that of the reference case ($f_{Case\ 01}(t)$), as expressed in Eq. (VI .4).

$$ER = \left(f_i(t) - f_{case01}(t) \right) \times 100 \quad \text{(VI.4)}$$

Figure VI.17 illustrates the time-dependent evolution of the enhancement ratio (ER) for all examined cases. Consistent with the previously discussed melting fraction trends, Case 10 exhibits the highest ER peak and the highest values of the enhancement function $f(t)$ throughout the melting process. For all cases (from Case 02 to Case 10), ER peaks are observed within the time interval of 1000 s to 3500 s, aligning with the period of intensified natural convection. This confirms that the enhanced convection currents during this stage play a pivotal role in accelerating the melting process. Following this dominant convection phase, the melting rate slows, leading to a gradual decline in ER values over time as the system approaches thermal equilibrium.

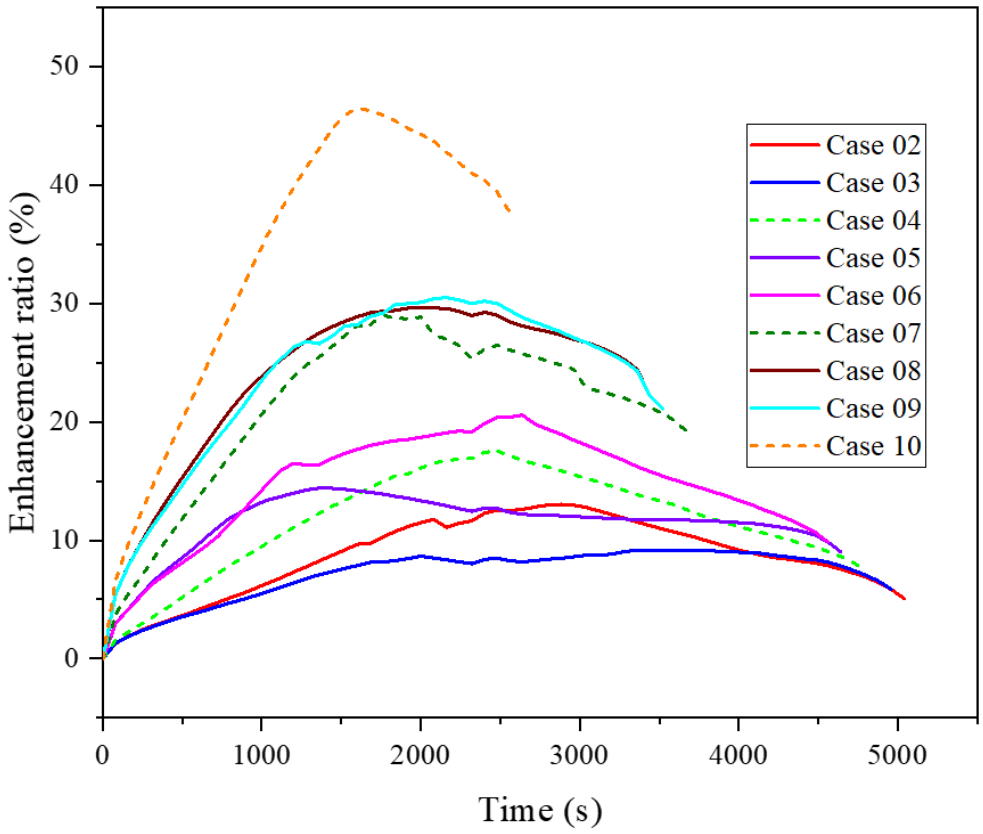

Figure VI. 16: Percentage enhancement ratio plotted against time melting process.

VI.3.5- Time-saving

The time-saving (τ) percentage is determined using Eq. (VI.5), where $t_{m,Case\ i}$ represent the melting times of $Case_i$ and the base case ($t_{m,Case_{01}}$), respectively.

$$\tau = \frac{t_{m,case_{01}} - t_{m,case_i}}{t_{m,case_{01}}} \quad \text{(VI.5)}$$

Figure VI.18 illustrates the time-saving percentages for all the evaluated cases. The influence of inner tube geometry, shell configuration, and the incorporation of fins is clearly reflected in the enhanced melting rates and corresponding time reductions. The observed time savings relative to the base case (Case 01) are as follows: 14.86% for Case 02, 16.2% for Case 03, 18.9% for Case 04, 21.62% for Case 05, 22.97% for Case 06, 37.83% for Case 07, 42.56% for Case 08, 40.45% for Case 09, and a substantial 56.75% for Case 10. These results highlight the effectiveness of combining geometric modifications with fin integration to improve thermal performance. Notably, the superior performance of Cases 08, 09, and especially Case 10 emphasizes the critical role of these design enhancements in accelerating the melting process and optimizing overall heat transfer efficiency.

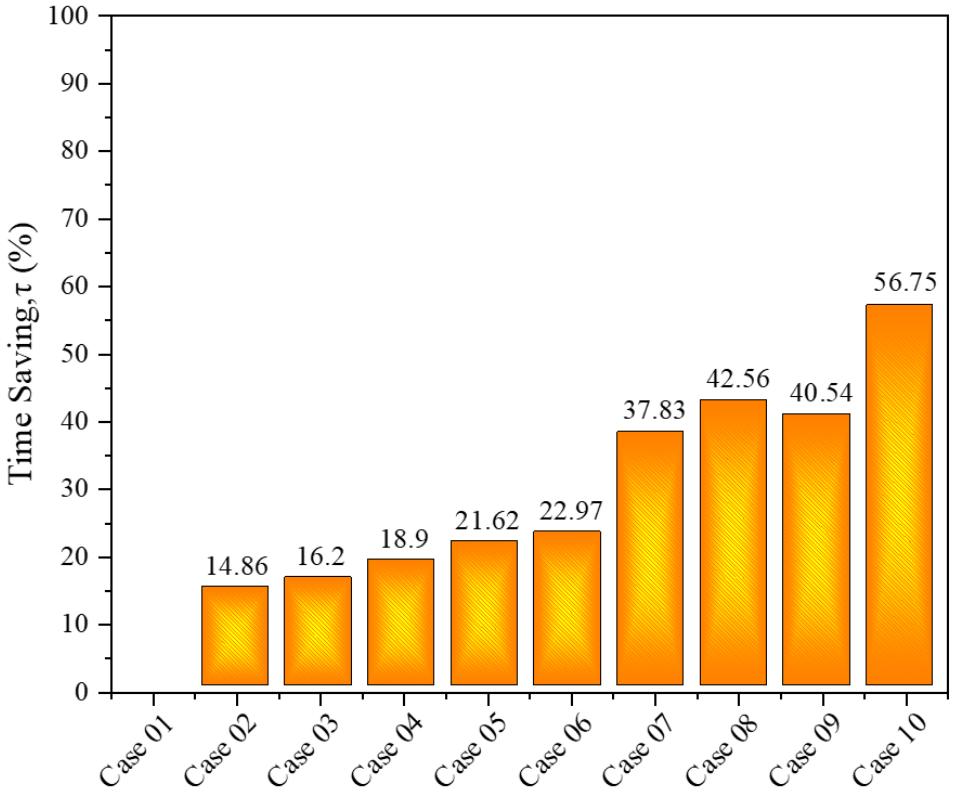

Figure VI. 17: Percentage Time Savings for all Cases.

VI.3.6- Thermal energy storage

The stored energy of the PCM was determined using the formulation presented in Section II.4. **Figure VI.19** demonstrates a positive correlation between the energy storage capacity and the geometrical modifications applied to the inner tube, shell, and the addition of fins. Enhancing the heat transfer surface area through these design changes leads to notable performance gains. Altering the inner tube from a circular form (Case 01) to two horizontal wedges (Case 02), vertical wedges (Case 03), and three wedges (Case 04) increases the energy storage from 3050 kJ to 3053 kJ, 3054 kJ, and 3052 kJ, respectively. Further, adapting the shell geometry in Cases 05 to 07 contributes to increased storage capacities of 3076 kJ, 3050 kJ, and 3063 kJ, respectively. When these geometric optimizations are combined with fins, energy storage further improves reaching 3055 kJ in Case 08, 3061 kJ in Case 09, and peaking at 3070 kJ in Case 10. These findings confirm that increasing the effective heat exchange surface area significantly enhances both thermal performance and overall energy storage capacity.

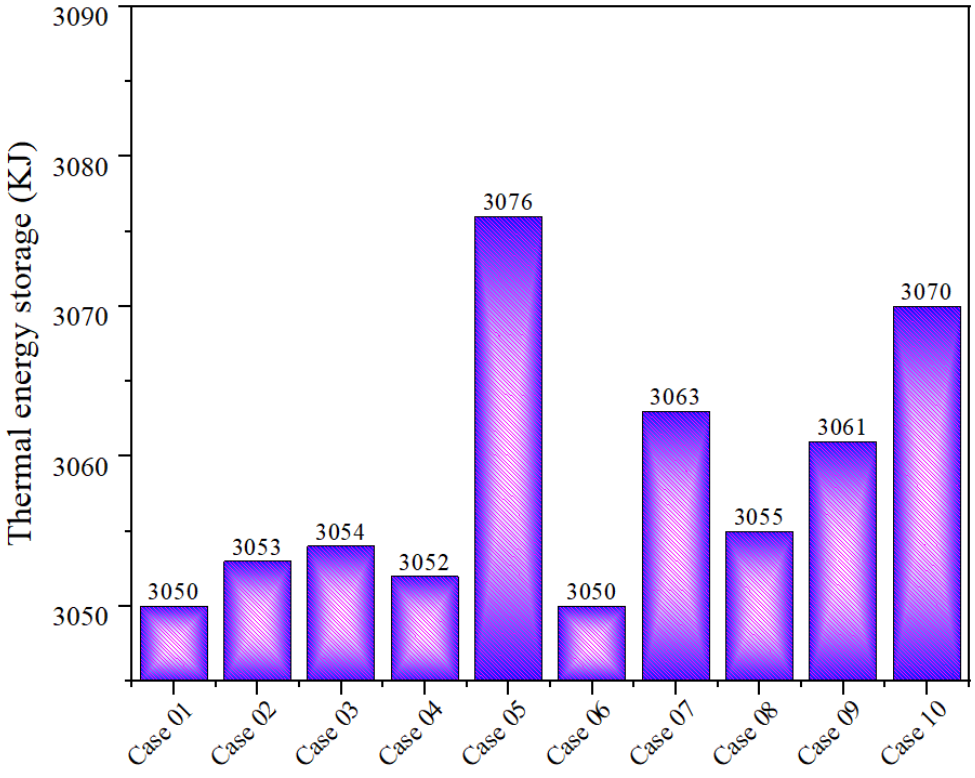

Figure VI. 18: The stored thermal energy for all cases.

VI.3.7- Nusselt number

The Nusselt number (Nu) is a dimensionless parameter used to characterize the prevailing heat transfer mechanism during the charging (melting) process. In this study, the Nu is evaluated along the heated surface to investigate the heat transfer behavior, using the formulation presented in Section II.4. This includes cases where the heated surface is divided into multiple segments.

Figure VI.20 presents the Nusselt number (Nu) evolution throughout the melting process for all ten configurations. The melting dynamics can be categorized into three distinct stages: an initial conduction-dominated phase, a period of intense natural convection, and a final stage marked by diminished convective activity. At the outset, high Nu values are recorded across all cases, attributed to the formation of a thin thermal boundary layer near the inner tube and shell, which reduces thermal resistance. As melting proceeds, the thickness of the liquid phase increases and the solid–liquid interface recedes, causing a sharp initial decline in the Nu number. This downward trend slows gradually and stabilizes as the system approaches thermal equilibrium. Additionally, transient spikes in the Nu curve appear during the process, reflecting brief instabilities and variations in convective flow.

As shown in **Figure VI.20**, cases exhibiting higher Nusselt numbers throughout the melting process are consistently associated with shorter melting times (**Figure VI.16**) and greater TES capacity (**Figure VI.19**), emphasizing the pivotal role of convective heat transfer in PCM systems. This correlation highlights that enhanced convective heat transfer significantly improves the phase change process by enabling more efficient heat distribution within the PCM. For example, Case 10 maintains a high Nusselt number and achieves the shortest melting time of 2560 seconds, while Case 5, with a similarly elevated Nusselt profile, records the highest thermal energy storage capacity of 3070 kJ. These observations indicate that a higher Nusselt number not only accelerates the melting process but also increases the amount of thermal energy stored, by facilitating rapid and uniform heating of the PCM. Therefore, optimizing the Nusselt number is essential for enhancing both melting performance and energy storage efficiency in latent heat thermal energy storage systems.

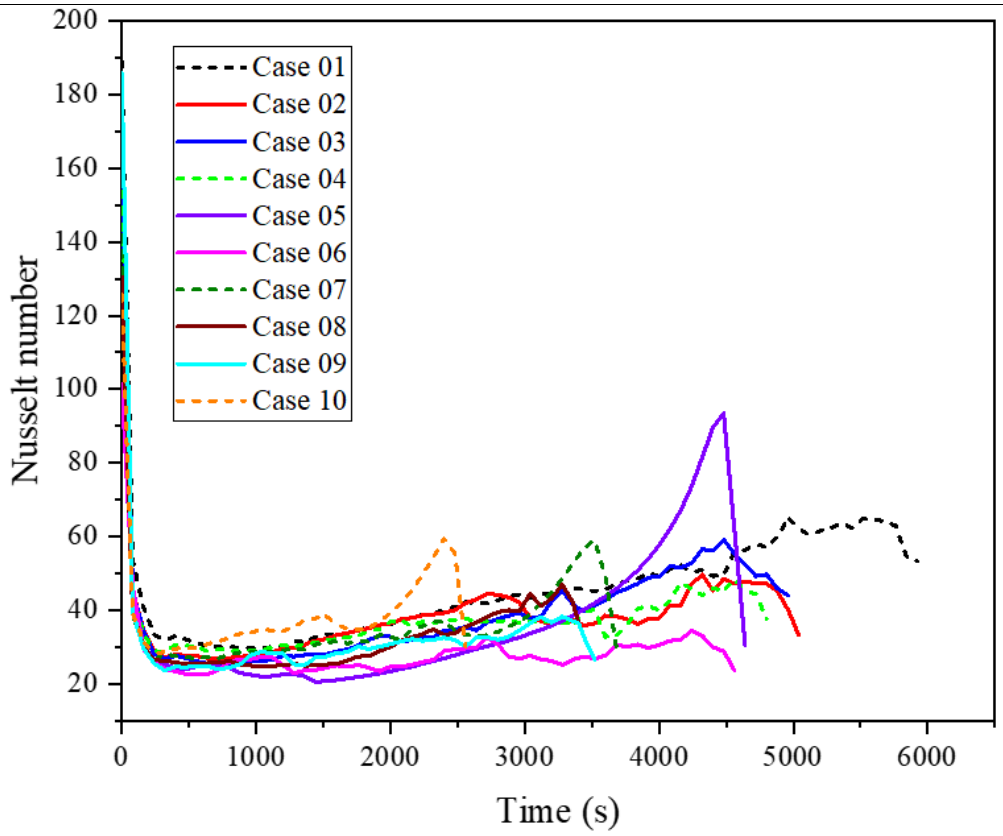

Figure VI. 19: Nusselt Number variation during the phase change process.

VI.3.8- Economic performance

In practical engineering applications, it is crucial not only to assess the TES potential of materials but also to evaluate their economic feasibility to ensure overall project viability.

Figure VI.21 illustrates the P_c evaluated for each case to evaluate the economic viability of the TES system. The results are as follows: Case 01 (Base Case) had P_c = 6.03$\frac{J}{s.\$}$, Case 02 had P_c = 6.51$\frac{J}{s.\$}$, Case 03 had P_c = 6.62$\frac{J}{s.\$}$, Case 04 had P_c = 6.69$\frac{J}{s.\$}$, Case 05 had P_c = 6.07$\frac{J}{s.\$}$, Case 06 had P_c = 6.13$\frac{J}{s.\$}$, Case 07 had P_c = 7.36$\frac{J}{s.\$}$, Case 08 had P_c = 8.24$\frac{J}{s.\$}$, Case 09 had P_c = 7.97$\frac{J}{s.\$}$, and Case 10, which exhibited the highest overall performance, achieved a cost-effectiveness value P_c = 10.6$\frac{J}{s.\$}$, indicating superior economic efficiency. This case not only recorded the shortest melting time but also ranked second in terms of total thermal energy storage, demonstrating an optimal balance between performance and cost. These results underscore those geometric modifications to the inner tube and shell, combined with the integration of fins, significantly improve both the thermal and economic performance of the system. The progressive improvements observed from

Case 01 to Case 10 reflect a consistent trend: strategic design enhancements contribute to more efficient and economically viable TES systems. The outstanding results in Case 10 serve as a clear example of how an integrated approach to geometry and heat transfer augmentation can deliver substantial benefits across multiple performance indicators.

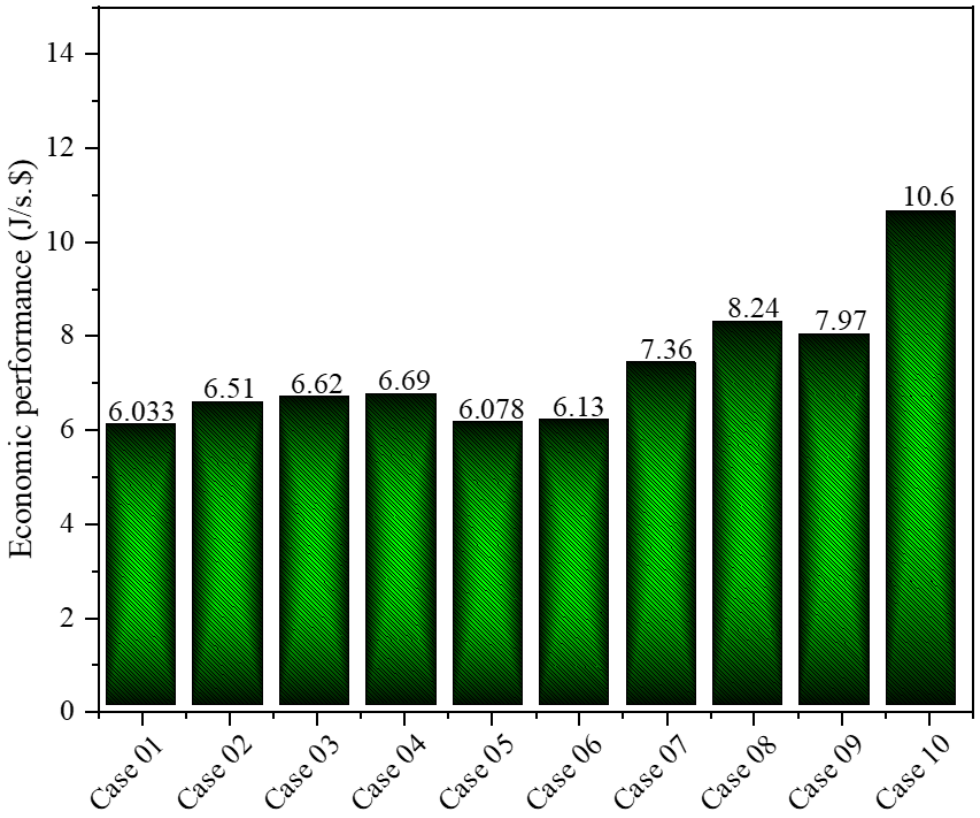

Figure VI. 20: Variations of economic performance over for all cases.

To consolidate and clearly compare the performance of all configurations studied in this chapter, a summary table has been added below (**Table 3**). This table presents a comprehensive overview of key performance indicators for the ten shell-and-tube cases, including melting time, time savings, total energy stored, and economic performance. It serves to highlight the impact of each geometric modification on thermal behavior and system efficiency, offering a clear comparison to support design selection. This synthesis provides the reader with a concise reference to evaluate which configurations deliver optimal thermal performance and economic viability.

Table VI. 3: Comparative Summary of Thermal and Economic Performance for the Ten Shell-and-Tube TES Configurations.

Cases	Melting time (s)	Time Savings (%)	TES (KJ)	Pc (J/(s.$))
Case 01	5920	-	3050	6.033
Case 02	5040	14.86	3053	6.51
Case 03	4960	16.20	3054	6.62
Case 04	4800	18.90	3052	6.69
Case 05	4640	21.62	3076	6.078
Case 06	4560	22.97	3050	6.13
Case 07	3680	37.83	3063	7.36
Case 08	3400	42.56	3055	8.24
Case 09	3520	40.54	3061	7.97
Case 10	2560	56.75	3070	10.6

The optimal configuration was Case 10 (three-wedge design with parallel shell and fins), which reduced melting time to 2560 s (56.75% time-saving) and achieved the highest economic performance with a Pc value of 10.6 J/(s.$).

VI.4-Conclusion

The study investigated ten TES configurations, focusing on variations in inner tube and shell geometries, as well as the addition of fins, to evaluate melting time, energy storage, heat transfer, and economic efficiency. Starting with a basic circular setup in Case 01, each subsequent case introduced design optimizations. Case 10, featuring a three-wedge inner tube, a parallel shell, and optimally placed fins, showed the best overall performance achieving the highest temperature (358.95 K), full melting in just 2560 s, and the greatest economic efficiency (P_c = 10.6 J/(s.$)). Nusselt number analysis revealed three melting stages conduction, strong convection, and weak convection with fluctuations due to convection instability. Energy storage increased from 3050 kJ in early cases to 3076 kJ in Case 05 and remained high in Case 10 (3070 kJ). These results highlight that combining geometric enhancements and fin integration can significantly improve both technical and economic performance.

Conclusions and perspectives

1- General conclusion

This thesis underscores the critical importance of PCMs in enhancing the effectiveness of TES systems, particularly in renewable energy applications where fluctuations in energy supply remain a significant limitation. By enabling the capture of surplus energy during peak generation and its release during periods of reduced availability, PCMs contribute substantially to improving system stability and operational efficiency.

The research delivers a detailed exploration of TES solutions, placing particular emphasis on latent heat storage and hybrid configurations. Latent heat storage systems stand out due to their high energy density and minimal volumetric variation during phase transitions, making them highly suitable for diverse thermal management scenarios. Meanwhile, hybrid systems that integrate PCMs with other storage media offer greater adaptability and improved system performance. A thorough overview is provided on PCM types, selection parameters, and their deployment across a range of temperature applications from domestic heating to large-scale industrial use. To address the inherent limitations of PCMs, the study examines several enhancement techniques, including the incorporation of fins, nanoparticle doping, and various encapsulation strategies aimed at boosting thermal conductivity, maintaining material stability, and enabling scalable designs. On the numerical side, the thesis identifies and evaluates key simulation methodologies including the Finite Difference Method (FDM), Finite Volume Method (FVM), Finite Element Method (FEM), and the Lattice Boltzmann Method (LBM). These computational tools are complemented by thermal modeling approaches such as the Enthalpy Method, Enthalpy-Porosity Method, Apparent Heat Capacity Method, and Molecular Dynamics Simulation. Together, these methods support accurate prediction of thermal behavior, improved system design, and performance assessment. Special attention is also given to mesh quality and boundary layer resolution to ensure the reliability and precision of numerical simulations.

In summary, this work offers valuable contributions to the advancement of PCM-based TES systems by providing practical design guidance, synthesizing best practices, and identifying key areas for future investigation. The findings and methodologies presented serve as a foundation for ongoing research efforts aimed at achieving more sustainable, resilient, and economically feasible energy storage technologies. The principal points of the thesis can be expressed as follows:

1. PCMs play a vital role in TES systems; however, their application requires innovative strategies to address challenges related to their inherent thermal instability and nonlinear phase transition behavior.
2. A thorough investigation of TES technologies especially those involving latent heat storage and hybrid configurations plays a key role in enhancing the performance and efficiency of PCM-based energy storage systems.
3. Innovative techniques such as fin integration, multi-PCM layering, nanoparticle enhancement, porous metal matrices, encapsulation, and shape-stabilization offer a comprehensive strategy for overcoming the limitations of PCMs and improving their thermal performance.
4. Numerical approaches such as the Finite Difference Method (FDM), Finite Volume Method (FVM), Finite Element Method (FEM), and Lattice Boltzmann Method (LBM) are fundamental for discretizing and solving the governing equations of heat transfer and fluid flow in PCM systems. These techniques facilitate precise simulation of temperature profiles, velocity fields, and phase change dynamics within complex geometries and under varying boundary conditions.
5. Thermal modeling techniques, including the Enthalpy Method, Enthalpy-Porosity Method, Effective Heat Capacity Method, and Molecular Dynamics, are critical for capturing the latent heat behavior, interface movement, and mushy zone formation during phase transitions in PCMs. These techniques allow for detailed representation of thermal responses and material properties throughout the melting and solidification processes.
6. The accuracy of numerical simulations heavily depends on mesh quality, with key parameters such as skewness, orthogonality, and element quality playing a critical role in ensuring reliable and stable computational results.

Future research in TES should focus on increasing sensible heat capacity through methods beyond temperature rise, optimizing fin configurations for PCM systems, and identifying the ideal number of PCM stages for maximum efficiency. Efforts should also address latent heat reduction from nanoparticles, enhance the accuracy of simulations involving complex structures like metal foams, and develop durable, cost-effective encapsulation materials. Improving numerical methods

to better capture phase change dynamics and melted PCM flow will further advance system design and performance reliability.

This thesis systematically explored various strategies to enhance the performance of PCM-based thermal energy storage systems. Chapter III revealed that the *L/D* ratio of storage tanks significantly impacts melting and solidification rates, with optimal *L/D* values enhancing thermal stratification and heat transfer. Chapter IV demonstrated the efficiency of strategically placed baffles in reducing melting time by up to 21.67%, while also improving economic performance, particularly in tanks with inclined baffles of varying hole diameters. Chapter V investigated different inner tube geometries, identifying the vertical oval tube as the most effective design, reducing solidification time by nearly 19%. Finally, Chapter VI showed that advanced geometric modifications, including multi-wedge tubes, parallel shells, and integrated fins, can decrease melting time by up to 56.75% and improve both energy storage capacity and cost efficiency. Collectively, these findings highlight the importance of design optimization in maximizing PCM performance for thermal energy storage applications.

In conclusion, our exploration of advanced TES technologies especially latent heat storage and hybrid systems highlights their potential to improve energy efficiency, lower operational costs, and strengthen energy security. These systems play a vital role in supporting climate goals by reducing greenhouse gas emissions and enhancing the integration of renewable energy. The study offers valuable insights for policymakers to establish effective standards and regulations for TES deployment. Moreover, these advancements align with global sustainability efforts, contributing to the UN Sustainable Development Goals focused on clean energy, industry innovation, and climate action.

2- Future perspectives

1. Leverage advanced numerical methods, including artificial intelligence, to enhance the accuracy and computational efficiency of simulations, particularly in modeling complex regions like mushy zones.

2. Investigate the integration of PCMs with other energy storage technologies such as batteries, thermal storage, or renewable systems to form hybrid configurations that offer superior flexibility and overall energy performance.

3. Develop optimization frameworks that consider material selection, structural design, and operational settings, supported by detailed techno-economic evaluations to identify the most viable solutions for different contexts.

4. Perform real-world experiments and pilot-scale applications to validate simulation results and understand how PCM systems perform under various operational and environmental conditions.

5. Carry out comprehensive environmental assessments, including life cycle analysis, to evaluate the sustainability of PCM systems, from raw material extraction through manufacturing and end-of-life disposal.

6. Explore scalable manufacturing techniques and modular designs to support the cost-effective expansion of PCM systems for commercial and industrial deployment, ensuring reliability and ease of implementation at larger scales.

7. Prioritize experimental validation of numerical models to ensure their reliability and applicability in real-world conditions. Future research should aim to bridge the gap between simulation and practice by designing controlled experiments that replicate operational environments, enabling accurate comparison and refinement of modeling approaches.

Pursuing these forward-looking strategies will support the ongoing advancement of PCM-based energy storage technologies, driving innovation and offering solutions to real-world implementation challenges. Nonetheless, several critical obstacles must still be addressed, such as tailoring PCM properties for targeted uses, ensuring long-term thermal stability, and achieving smooth integration within existing energy infrastructures. Overcoming these barriers will require coordinated efforts among researchers, industry professionals, and policy-makers. **Figure 1** presents a visual summary of key areas for future investigation along with corresponding recommendations.

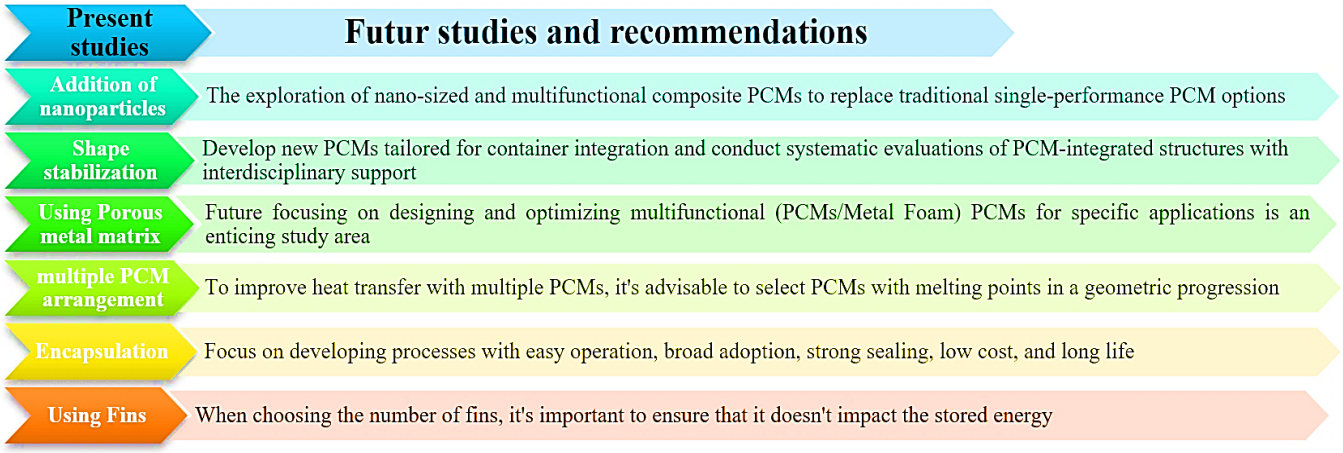

Figure 1: Future research directions in PCM integration.

Bibliographic references

References

[1] M. Arslan and A. A. Igci, “Thermal performance of a vertical solar hot water storage tank with a mantle heat exchanger depending on the discharging operation parameters,” *Sol. Energy*, vol. 116, pp. 184–204, 2015, doi: 10.1016/j.solener.2015.03.045.

[2] Y. Qin *et al.*, “The effect of phase change material balls on the thermal characteristics in hot water tanks: CFD research,” *Appl. Therm. Eng.*, vol. 178, no. April, 2020, doi: 10.1016/j.applthermaleng.2020.115557.

[3] D. Guerraiche, C. Bougriou, K. Guerraiche, L. Valenzuela, and Z. Driss, “Experimental and numerical study of a solar collector using phase change material as heat storage,” *J. Energy Storage*, vol. 27, no. November 2019, p. 101133, 2020, doi: 10.1016/j.est.2019.101133.

[4] G. S. Kumar, D. Nagarajan, L. A. Chidambaram, V. Kumaresan, Y. Ding, and R. Velraj, “Role of PCM addition on stratification behaviour in a thermal storage tank – An experimental study,” *Energy*, vol. 115, pp. 1168–1178, 2016, doi: 10.1016/j.energy.2016.09.014.

[5] G. Zsembinszki, C. Orozco, J. Gasia, T. Barz, J. Emhofer, and L. F. Cabeza, “Evaluation of the State of Charge of a Solid / Liquid Storage Tank,” *Energies*, vol. 13,1425, pp. 1–26, 2020.

[6] G. Dogkas *et al.*, “Development and experimental testing of a compact thermal energy storage tank using paraffin targeting domestic hot water production needs,” *Therm. Sci. Eng. Prog.*, vol. 19, no. May, p. 100573, 2020, doi: 10.1016/j.tsep.2020.100573.

[7] G. Feng *et al.*, “Simulation of a new phase change energy storage tank design with a vertical baffle,” *Energy Build.*, vol. 268, p. 112205, 2022, doi: 10.1016/j.enbuild.2022.112205.

[8] M. Fadl and P. C. Eames, “Numerical investigation of the influence of mushy zone parameter Amush on heat transfer characteristics in vertically and horizontally oriented thermal energy storage systems,” *Appl. Therm. Eng.*, vol. 151, no. November 2018, pp. 90–99, 2019, doi: 10.1016/j.applthermaleng.2019.01.102.

[9] S. ed D. Fertahi, A. Samaouali, T. Bouhal, and A. Arid, “Thermal energy storage

enhancement of a forced circulation solar water heater's vertical tank unit using phase change material," *Appl. Therm. Eng.*, vol. 215, no. November 2021, p. 118972, 2022, doi: 10.1016/j.applthermaleng.2022.118972.

[10] H. M. Teamah and M. F. Lightstone, "Numerical study of the electrical load shift capability of a ground source heat pump system with phase change thermal storage," *Energy Build.*, vol. 199, pp. 235–246, 2019, doi: 10.1016/j.enbuild.2019.06.056.

[11] M. Song, F. Niu, N. Mao, Y. Hu, and S. Deng, "Review on building energy performance improvement using phase change materials," *Energy Build.*, vol. 158, pp. 776–793, 2018, doi: 10.1016/j.enbuild.2017.10.066.

[12] K. Faraj, M. Khaled, J. Faraj, F. Hachem, and C. Castelain, "12 - Phase change materials (PCMs) in buildings," in *Woodhead Publishing Series in Composites Science and Engineering*, K. Pielichowska and K. B. T.-M. P. C. M. Pielichowski, Eds., Woodhead Publishing, 2023, pp. 507–567. doi: https://doi.org/10.1016/B978-0-323-85719-2.00003-1.

[13] H. Nazir *et al.*, "Recent developments in phase change materials for energy storage applications: A review," *Int. J. Heat Mass Transf.*, vol. 129, pp. 491–523, 2019, doi: 10.1016/j.ijheatmasstransfer.2018.09.126.

[14] M. M. Umair, Y. Zhang, K. Iqbal, S. Zhang, and B. Tang, "Novel strategies and supporting materials applied to shape-stabilize organic phase change materials for thermal energy storage–A review," *Appl. Energy*, vol. 235, no. November 2018, pp. 846–873, 2019, doi: 10.1016/j.apenergy.2018.11.017.

[15] Y. Lin, G. Alva, and G. Fang, "Review on thermal performances and applications of thermal energy storage systems with inorganic phase change materials," *Energy*, vol. 165, pp. 685–708, 2018, doi: 10.1016/j.energy.2018.09.128.

[16] B. M. Tripathi, S. K. Shukla, and P. K. S. Rathore, "A comprehensive review on solar to thermal energy conversion and storage using phase change materials," *J. Energy Storage*, vol. 72, no. PA, p. 108280, 2023, doi: 10.1016/j.est.2023.108280.

[17] J. Zhu, X. Zhang, W. Hua, J. Ji, and X. Lv, "Current status and development of research on

phase change materials in agricultural greenhouses: A review," *J. Energy Storage*, vol. 66, no. March, p. 107104, 2023, doi: 10.1016/j.est.2023.107104.

[18] I. Afaynou, H. Faraji, K. Choukairy, A. Arshad, and M. Arıcı, "Heat transfer enhancement of phase-change materials (PCMs) based thermal management systems for electronic components: A review of recent advances," *Int. Commun. Heat Mass Transf.*, vol. 143, no. March, p. 106690, 2023, doi: 10.1016/j.icheatmasstransfer.2023.106690.

[19] S. Jesumathy, M. Udayakumar, and S. Suresh, "Experimental study of enhanced heat transfer by addition of CuO nanoparticle," *Heat Mass Transf. und Stoffuebertragung*, vol. 48, no. 6, pp. 965–978, 2012, doi: 10.1007/s00231-011-0945-y.

[20] A. Arshad, M. Jabbal, and Y. Yan, "Thermal Performance of PCM-based Heat Sink with Partially Filled Copper Oxide Coated Metal-foam for Thermal Management of Microelectronics," *Intersoc. Conf. Therm. Thermomechanical Phenom. Electron. Syst. ITHERM*, vol. 2020-July, pp. 697–702, 2020, doi: 10.1109/ITherm45881.2020.9190574.

[21] M. Alhuyi Nazari *et al.*, "A review of nanomaterial incorporated phase change materials for solar thermal energy storage," *Sol. Energy*, vol. 228, no. November 2020, pp. 725–743, 2021, doi: 10.1016/j.solener.2021.08.051.

[22] T. Yang, W. P. King, and N. Miljkovic, "Phase change material-based thermal energy storage," *Cell Reports Phys. Sci.*, vol. 2, no. 8, p. 100540, 2021, doi: 10.1016/j.xcrp.2021.100540.

[23] H. Asgharian and E. Baniasadi, "A review on modeling and simulation of solar energy storage systems based on phase change materials," *J. Energy Storage*, vol. 21, no. December 2018, pp. 186–201, 2019, doi: 10.1016/j.est.2018.11.025.

[24] L. Kalapala and J. K. Devanuri, "Influence of operational and design parameters on the performance of a PCM based heat exchanger for thermal energy storage – A review," *J. Energy Storage*, vol. 20, no. July, pp. 497–519, 2018, doi: 10.1016/j.est.2018.10.024.

[25] T. Xiong, L. Zheng, and K. W. Shah, "Nano-enhanced phase change materials (NePCMs): A review of numerical simulations," *Appl. Therm. Eng.*, vol. 178, no. February, p. 115492,

2020, doi: 10.1016/j.applthermaleng.2020.115492.

[26] W. Cui *et al.*, "Heat transfer enhancement of phase change materials embedded with metal foam for thermal energy storage: A review," *Renew. Sustain. Energy Rev.*, vol. 169, no. August, p. 112912, 2022, doi: 10.1016/j.rser.2022.112912.

[27] T. Zhang, D. Huo, C. Wang, and Z. Shi, "Review of the modeling approaches of phase change processes," *Renew. Sustain. Energy Rev.*, vol. 187, no. March, p. 113724, 2023, doi: 10.1016/j.rser.2023.113724.

[28] B. Sun, Z. Liu, X. Ji, L. Gao, and D. Che, "Thermal energy storage characteristics of packed bed encapsulating spherical capsules with composite phase change materials," *Appl. Therm. Eng.*, vol. 201, no. PA, p. 117659, 2022, doi: 10.1016/j.applthermaleng.2021.117659.

[29] Y. Abbassi, E. Baniasadi, and H. Ahmadikia, "Transient energy storage in phase change materials, development and simulation of a new TRNSYS component," *J. Build. Eng.*, vol. 50, no. November 2021, p. 104188, 2022, doi: 10.1016/j.jobe.2022.104188.

[30] N. James, A. Mahvi, and J. Woods, "Optimizing phase change composite thermal energy storage using the thermal Ragone framework," *J. Energy Storage*, vol. 56, no. PA, p. 105875, 2022, doi: 10.1016/j.est.2022.105875.

[31] I. Al Siyabi, S. Khanna, T. Mallick, and S. Sundaram, "An experimental and numerical study on the effect of inclination angle of phase change materials thermal energy storage system," *J. Energy Storage*, vol. 23, no. September 2018, pp. 57–68, 2019, doi: 10.1016/j.est.2019.03.010.

[32] M. M. Farid, A. M. Khudhair, S. A. K. Razack, and S. Al-Hallaj, "A review on phase change energy storage: Materials and applications," *Energy Convers. Manag.*, vol. 45, no. 9–10, pp. 1597–1615, 2004, doi: 10.1016/j.enconman.2003.09.015.

[33] A. H. Elsheikh and M. Abd Elaziz, "Review on applications of particle swarm optimization in solar energy systems," *Int. J. Environ. Sci. Technol.*, vol. 16, no. 2, pp. 1159–1170, 2019, doi: 10.1007/s13762-018-1970-x.

[34] K. Faraj, M. Khaled, J. Faraj, F. Hachem, and C. Castelain, "A review on phase change

materials for thermal energy storage in buildings: Heating and hybrid applications," Jan. 01, 2021, *Elsevier Ltd*. doi: 10.1016/j.est.2020.101913.

[35] B. Chen, F. Kuznik, M. Horgnies, K. Johannes, V. Morin, and E. Gengembre, "Physicochemical properties of ettringite/meta-ettringite for thermal energy storage: Review," *Sol. Energy Mater. Sol. Cells*, vol. 193, no. August 2018, pp. 320–334, 2019, doi: 10.1016/j.solmat.2018.12.013.

[36] F. He, B. Yan, J. Zou, C. Hu, X. Meng, and W. Gao, "Experimental evaluation of the effect of perforated spiral fins on the thermal performance of latent heat storage units," *J. Energy Storage*, vol. 58, no. October 2022, p. 106359, 2023, doi: 10.1016/j.est.2022.106359.

[37] S. Mousavi, M. Siavashi, and A. Zadehkabir, "A new design for hybrid cooling of Li-ion battery pack utilizing PCM and mini channel cold plates," *Appl. Therm. Eng.*, vol. 197, no. May, p. 117398, 2021, doi: 10.1016/j.applthermaleng.2021.117398.

[38] R. Kumar *et al.*, "Simultaneous applications of fins and nanomaterials in phase change materials: A comprehensive review," *Energy Reports*, vol. 10, pp. 1028–1040, 2023, doi: 10.1016/j.egyr.2023.07.052.

[39] L. . Cabeza and H. Mehling, *Heat and cold storage with PCM. An up to date introduction into basics and applications*. 2008. [Online]. Available: http://www.springer.com/us/book/9783540685562

[40] M. Martinelli and M. Martinelli, "Stockage d ' énergie thermique par changement de phase – Application aux réseaux de chaleur To cite this version : HAL Id : tel-01412771 Stockage d ' énergie thermique par changement de phase – Application aux réseaux de chaleur," 2017.

[41] P. Yan, W. Fan, Y. Yang, H. Ding, A. Arshad, and C. Wen, "Performance enhancement of phase change materials in triplex-tube latent heat energy storage system using novel fin configurations," *Appl. Energy*, vol. 327, no. October, p. 120064, 2022, doi: 10.1016/j.apenergy.2022.120064.

[42] A. Bruch, J. F. Fourmigué, and R. Couturier, "Experimental and numerical investigation of a pilot-scale thermal oil packed bed thermal storage system for CSP power plant," *Sol.*

Energy, vol. 105, pp. 116–125, 2014, doi: 10.1016/j.solener.2014.03.019.

[43] Alsolen-Alcen, "No Title Heat solutions for life", doi: http://www.alsolen-alcen.com/fr.

[44] A. SOUPART-CARON, "Stockage de chaleur dans les Matériaux à Changement de Phase," *Univ. grenoble alpes*, p. 277, 2015, [Online]. Available: https://tel.archives-ouvertes.fr/tel-01266813/document

[45] F. L. Rashid *et al.*, "Recent Advances on The Applications of Phase Change Materials in Cold Thermal Energy Storage: A Critical Review," *J. Compos. Sci.*, vol. 7, no. 8, 2023, doi: 10.3390/jcs7080338.

[46] X. Jin, S. Zhang, M. A. Medina, and X. Zhang, "Experimental study of the cooling process of partially-melted sodium acetate trihydrate," *Energy Build.*, vol. 76, pp. 654–660, 2014, doi: 10.1016/j.enbuild.2014.02.059.

[47] R. Gulfam, P. Zhang, and Z. Meng, "Advanced thermal systems driven by paraffin-based phase change materials – A review," *Appl. Energy*, vol. 238, no. October 2018, pp. 582–611, 2019, doi: 10.1016/j.apenergy.2019.01.114.

[48] M. Freund, R. Csikós, S. Keszthelyi, and G. Y. Mózes, *Paraffin Products Properties, Technologies, Applications*, vol. Volume 14. 1982. [Online]. Available: http://www.sciencedirect.com/science/article/pii/S0376736108701481

[49] A. Arshad, M. Jabbal, L. Shi, and Y. Yan, "Thermophysical characteristics and enhancement analysis of carbon-additives phase change mono and hybrid materials for thermal management of electronic devices," *J. Energy Storage*, vol. 34, no. December 2020, p. 102231, 2021, doi: 10.1016/j.est.2020.102231.

[50] A. Arshad, "Assessment of nanomaterials in enhancing the thermophysical properties of phase change materials for thermal management," 2021, *University of Nottingham*.

[51] M. Schmidt and M. Linder, "A Novel Thermochemical Long Term Storage Concept: Balance of Renewable Electricity and Heat Demand in Buildings," *Front. Energy Res.*, vol. 8, no. July, pp. 1–12, 2020, doi: 10.3389/fenrg.2020.00137.

[52] G. Wei *et al.*, "Selection principles and thermophysical properties of high temperature phase change materials for thermal energy storage: A review," *Renew. Sustain. Energy Rev.*, vol. 81, no. March 2017, pp. 1771–1786, 2018, doi: 10.1016/j.rser.2017.05.271.

[53] J. Pereira da Cunha and P. Eames, "Thermal energy storage for low and medium temperature applications using phase change materials - A review," *Appl. Energy*, vol. 177, no. November, pp. 227–238, 2016, doi: 10.1016/j.apenergy.2016.05.097.

[54] A. Arshad, M. Jabbal, Y. Yan, and J. Darkwa, "The micro-/nano-PCMs for thermal energy storage systems: A state of art review," *Int. J. Energy Res.*, vol. 43, no. 11, pp. 5572–5620, 2019, doi: 10.1002/er.4550.

[55] T. Bauer, D. Laing, and R. Tamme, "Characterization of sodium nitrate as phase change material," *Int. J. Thermophys.*, vol. 33, no. 1, pp. 91–104, 2012, doi: 10.1007/s10765-011-1113-9.

[56] D. Haillot, T. Bauer, U. Kröner, and R. Tamme, "Thermal analysis of phase change materials in the temperature range 120-150 °c," *Thermochim. Acta*, vol. 513, no. 1–2, pp. 49–59, 2011, doi: 10.1016/j.tca.2010.11.011.

[57] R. Gulfam, P. Zhang, and Z. Meng, "Advanced thermal systems driven by paraffin-based phase change materials – A review," Mar. 15, 2019, *Elsevier Ltd*. doi: 10.1016/j.apenergy.2019.01.114.

[58] P. Bose and V. A. Amirtham, "A review on thermal conductivity enhancement of paraffinwax as latent heat energy storage material," *Renew. Sustain. Energy Rev.*, vol. 65, pp. 81–100, 2016, doi: 10.1016/j.rser.2016.06.071.

[59] R. A. Lawag and H. M. Ali, "Phase change materials for thermal management and energy storage: A review," *J. Energy Storage*, vol. 55, no. PC, p. 105602, 2022, doi: 10.1016/j.est.2022.105602.

[60] Q. Al-Yasiri and M. Szabó, "Paraffin As a Phase Change Material to Improve Building Performance: An Overview of Applications and Thermal Conductivity Enhancement Techniques," *Renew. Energy Environ. Sustain.*, vol. 6, p. 38, 2021, doi:

10.1051/rees/2021040.

[61] A. Sharma, A. Shukla, C. R. Chen, and T. N. Wu, "Development of phase change materials (PCMs) for low temperature energy storage applications," *Sustain. Energy Technol. Assessments*, vol. 7, pp. 17–21, 2014, doi: 10.1016/j.seta.2014.02.009.

[62] A. Sari and K. Kaygusuz, "Thermal performance of palmitic acid as a phase change energy storage material," *Energy Convers. Manag.*, vol. 43, no. 6, pp. 863–876, 2002, doi: 10.1016/S0196-8904(01)00071-1.

[63] S. Wang, P. Qin, X. Fang, Z. Zhang, S. Wang, and X. Liu, "A novel sebacic acid/expanded graphite composite phase change material for solar thermal medium-temperature applications," *Sol. Energy*, vol. 99, pp. 283–290, 2014, doi: 10.1016/j.solener.2013.11.018.

[64] M. Koschenz and B. Lehmann, "Development of a thermally activated ceiling panel with PCM for application in lightweight and retrofitted buildings," *Energy Build.*, vol. 36, no. 6, pp. 567–578, 2004, doi: 10.1016/j.enbuild.2004.01.029.

[65] J. Jia, B. Liu, L. Ma, H. Wang, D. Li, and Y. Wang, "Energy saving performance optimization and regional adaptability of prefabricated buildings with PCM in different climates," *Case Stud. Therm. Eng.*, vol. 26, no. May, p. 101164, 2021, doi: 10.1016/j.csite.2021.101164.

[66] T. Silva, R. Vicente, N. Soares, and V. Ferreira, "Experimental testing and numerical modelling of masonry wall solution with PCM incorporation: A passive construction solution," *Energy Build.*, vol. 49, pp. 235–245, 2012, doi: 10.1016/j.enbuild.2012.02.010.

[67] M. Mahdaoui *et al.*, "Building bricks with phase change material (PCM): Thermal performances," *Constr. Build. Mater.*, vol. 269, no. xxxx, p. 121315, 2021, doi: 10.1016/j.conbuildmat.2020.121315.

[68] A. M. Khudhair and M. M. Farid, "A review on energy conservation in building applications with thermal storage by latent heat using phase change materials," *Energy Convers. Manag.*, vol. 45, no. 2, pp. 263–275, 2004, doi: 10.1016/S0196-8904(03)00131-6.

[69] G. Alva, L. Liu, X. Huang, and G. Fang, "Thermal energy storage materials and systems

for solar energy applications," *Renew. Sustain. Energy Rev.*, vol. 68, no. February 2016, pp. 693–706, 2017, doi: 10.1016/j.rser.2016.10.021.

[70] S. I. Hussain, R. Dinesh, A. A. Roseline, S. Dhivya, and S. Kalaiselvam, "Enhanced thermal performance and study the influence of sub cooling on activated carbon dispersed eutectic PCM for cold storage applications," *Energy Build.*, vol. 143, pp. 17–24, 2017, doi: 10.1016/j.enbuild.2017.03.011.

[71] K. Hamid *et al.*, "Potential evaluation of integrated high temperature heat pumps: A review of recent advances," *Appl. Therm. Eng.*, vol. 230, no. PA, p. 120720, 2023, doi: 10.1016/j.applthermaleng.2023.120720.

[72] A. Arshad, H. M. Ali, M. Ali, and S. Manzoor, "Thermal performance of phase change material (PCM) based pin-finned heat sinks for electronics devices: Effect of pin thickness and PCM volume fraction," *Appl. Therm. Eng.*, vol. 112, pp. 143–155, 2017, doi: 10.1016/j.applthermaleng.2016.10.090.

[73] B. Palmer, A. Arshad, Y. Yang, and C. Wen, "Energy storage performance improvement of phase change materials-based triplex-tube heat exchanger (TTHX) using liquid–solid interface-informed fin configurations," *Appl. Energy*, vol. 333, no. August 2022, p. 120576, 2023, doi: 10.1016/j.apenergy.2022.120576.

[74] K. Du, J. Calautit, Z. Wang, Y. Wu, and H. Liu, "A review of the applications of phase change materials in cooling, heating and power generation in different temperature ranges," *Appl. Energy*, vol. 220, no. March, pp. 242–273, 2018, doi: 10.1016/j.apenergy.2018.03.005.

[75] C. Zeng, S. Liu, and A. Shukla, "Adaptability research on phase change materials based technologies in China," *Renew. Sustain. Energy Rev.*, vol. 73, no. November 2015, pp. 145–158, 2017, doi: 10.1016/j.rser.2017.01.117.

[76] B. P. Jelle and S. E. Kalnæs, *Phase Change Materials for Application in Energy-Efficient Buildings*. Elsevier Ltd, 2017. doi: 10.1016/B978-0-08-101128-7.00003-4.

[77] N. Kumar, P. K. S. Rathore, R. K. Sharma, and N. K. Gupta, "Integration of lauric

acid/zeolite/graphite as shape stabilized composite phase change material in gypsum for enhanced thermal energy storage in buildings," *Appl. Therm. Eng.*, vol. 224, no. January, p. 120088, 2023, doi: 10.1016/j.applthermaleng.2023.120088.

[78] C. Cárdenas-Ramírez, F. Jaramillo, and M. Gómez, "Systematic review of encapsulation and shape-stabilization of phase change materials," *J. Energy Storage*, vol. 30, no. 52, p. 101495, 2020, doi: 10.1016/j.est.2020.101495.

[79] J. Paul *et al.*, "Nano-enhanced organic form stable PCMs for medium temperature solar thermal energy harvesting: Recent progresses, challenges, and opportunities," *Renew. Sustain. Energy Rev.*, vol. 161, no. January, p. 112321, 2022, doi: 10.1016/j.rser.2022.112321.

[80] A. S, A. Sharma, and H. B. Kothadia, "Performance analysis of PCM melting in a fin-assisted thermal energy storage system – A numerical study," *Int. Commun. Heat Mass Transf.*, vol. 144, no. March, p. 106747, 2023, doi: 10.1016/j.icheatmasstransfer.2023.106747.

[81] R. V. Seeniraj and N. Lakshmi Narasimhan, "Performance enhancement of a solar dynamic LHTS module having both fins and multiple PCMs," *Sol. Energy*, vol. 82, no. 6, pp. 535–542, 2008, doi: 10.1016/j.solener.2007.11.001.

[82] Z. Liu, Y. Yao, and H. Wu, "Numerical modeling for solid-liquid phase change phenomena in porous media: Shell-and-tube type latent heat thermal energy storage," *Appl. Energy*, vol. 112, pp. 1222–1232, 2013, doi: 10.1016/j.apenergy.2013.02.022.

[83] A. K. Singh, P. K. S. Rathore, R. K. Sharma, N. K. Gupta, and R. Kumar, "Experimental evaluation of composite concrete incorporated with thermal energy storage material for improved thermal behavior of buildings," *Energy*, vol. 263, no. PA, p. 125701, 2023, doi: 10.1016/j.energy.2022.125701.

[84] Z. A. Qureshi, H. M. Ali, and S. Khushnood, "Recent advances on thermal conductivity enhancement of phase change materials for energy storage system: A review," *Int. J. Heat Mass Transf.*, vol. 127, pp. 838–856, 2018, doi: 10.1016/j.ijheatmasstransfer.2018.08.049.

[85] H. Faraji, M. Teggar, A. Arshad, M. Arıcı, E. Mehdi Berra, and K. Choukairy, "Lattice Boltzmann simulation of natural convection heat transfer phenomenon for thermal management of multiple electronic components," *Therm. Sci. Eng. Prog.*, vol. 45, no. September, p. 102126, 2023, doi: 10.1016/j.tsep.2023.102126.

[86] M. E. Zayed *et al.*, "Recent progress in phase change materials storage containers: Geometries, design considerations and heat transfer improvement methods," *J. Energy Storage*, vol. 30, no. February, p. 101341, 2020, doi: 10.1016/j.est.2020.101341.

[87] M. Kirincic, A. Trp, and K. Lenic, "Numerical evaluation of the latent heat thermal energy storage performance enhancement by installing longitudinal fins," *J. Energy Storage*, vol. 42, no. July, p. 103085, 2021, doi: 10.1016/j.est.2021.103085.

[88] C. Nie, S. Deng, and J. Liu, "Effects of fins arrangement and parameters on the consecutive melting and solidification of PCM in a latent heat storage unit," *J. Energy Storage*, vol. 29, no. March, p. 101319, 2020, doi: 10.1016/j.est.2020.101319.

[89] H. B. Mahood, M. S. Mahdi, A. A. Monjezi, A. A. Khadom, and A. N. Campbell, "Numerical investigation on the effect of fin design on the melting of phase change material in a horizontal shell and tube thermal energy storage," *J. Energy Storage*, vol. 29, no. March, p. 101331, 2020, doi: 10.1016/j.est.2020.101331.

[90] L. Wu, X. Zhang, and X. Liu, "Numerical analysis and improvement of the thermal performance in a latent heat thermal energy storage device with spiderweb-like fins," *J. Energy Storage*, vol. 32, no. July, p. 101768, 2020, doi: 10.1016/j.est.2020.101768.

[91] S. Baghaei Oskouei and Ö. Bayer, "Experimental and numerical investigation of melting and solidification enhancement using Fibonacci-inspired fins in a latent thermal energy storage unit," *Int. J. Heat Mass Transf.*, vol. 210, p. 124180, 2023, doi: 10.1016/j.ijheatmasstransfer.2023.124180.

[92] Z. Liu *et al.*, "Effect of phase change heat storage tank with gradient fin structure on solar energy storage: A numerical study," *Int. J. Heat Mass Transf.*, vol. 215, p. 124384, 2023, doi: 10.1016/j.ijheatmasstransfer.2023.124384.

[93] M. E. Nakhchi, M. Hatami, and M. Rahmati, "A numerical study on the effects of nanoparticles and stair fins on performance improvement of phase change thermal energy storages," *Energy*, vol. 215, p. 119112, 2021, doi: 10.1016/j.energy.2020.119112.

[94] R. Ge, Q. Li, C. Li, and Q. Liu, "Evaluation of different melting performance enhancement structures in a shell-and-tube latent heat thermal energy storage system," *Renew. Energy*, vol. 187, pp. 829–843, 2022, doi: 10.1016/j.renene.2022.01.097.

[95] J. Vogel and M. Johnson, "Natural convection during melting in vertical finned tube latent thermal energy storage systems," *Appl. Energy*, vol. 246, no. December 2018, pp. 38–52, 2019, doi: 10.1016/j.apenergy.2019.04.011.

[96] A. Sciacovelli, F. Gagliardi, and V. Verda, "Maximization of performance of a PCM latent heat storage system with innovative fins," *Appl. Energy*, vol. 137, pp. 707–715, 2015, doi: 10.1016/j.apenergy.2014.07.015.

[97] M. Ghalambaz *et al.*, "Intensifying the charging response of a phase-change material with twisted fin arrays in a shell-and-tube storage system," *Energies*, vol. 14, no. 6, 2021, doi: 10.3390/en14061619.

[98] L. N. N., "Assessment of latent heat thermal storage systems operating with multiple phase change materials," *J. Energy Storage*, vol. 23, no. February, pp. 442–455, 2019, doi: 10.1016/j.est.2019.04.008.

[99] L. Kalapala and J. K. Devanuri, "Influence of operational and design parameters on the performance of a PCM based heat exchanger for thermal energy storage – A review," *J. Energy Storage*, vol. 20, no. November, pp. 497–519, 2018, doi: 10.1016/j.est.2018.10.024.

[100] J. C. Kurnia, A. P. Sasmito, S. V. Jangam, and A. S. Mujumdar, "Improved design for heat transfer performance of a novel phase change material (PCM) thermal energy storage (TES)," *Appl. Therm. Eng.*, vol. 50, no. 1, pp. 896–907, 2013, doi: 10.1016/j.applthermaleng.2012.08.015.

[101] L. Gao, L. Dong, Z. Liu, Gegentana, D. Che, and B. Sun, "Thermal performance analysis and multi-objective optimization of thermal energy storage unit with cascaded packed bed

in a solar heating system," *Appl. Therm. Eng.*, vol. 219, no. PA, p. 119416, 2023, doi: 10.1016/j.applthermaleng.2022.119416.

[102] H. Faraji, M. El Alami, and A. Arshad, "Investigating the effect of single and hybrid nanoparticles on melting of phase change material in a rectangular enclosure with finite heat source," *Int. J. Energy Res.*, vol. 45, no. 3, pp. 4314–4330, 2021, doi: 10.1002/er.6095.

[103] J. M. Khodadadi and S. F. Hosseinizadeh, "Nanoparticle-enhanced phase change materials (NEPCM) with great potential for improved thermal energy storage," *Int. Commun. Heat Mass Transf.*, vol. 34, no. 5, pp. 534–543, 2007, doi: 10.1016/j.icheatmasstransfer.2007.02.005.

[104] A. Arshad, M. Jabbal, H. Faraji, M. A. Bashir, P. Talebizadehsardari, and Y. Yan, "Thermal process enhancement of HNCPCM filled heat sink: Effect of hybrid nanoparticles ratio and shape," *Int. Commun. Heat Mass Transf.*, vol. 125, 2021, doi: 10.1016/j.icheatmasstransfer.2021.105323.

[105] A. K. Gupta, G. Mishra, and S. Singh, "Numerical study of MWCNT enhanced PCM melting through a heated undulated wall in the latent heat storage unit," *Therm. Sci. Eng. Prog.*, vol. 27, p. 101172, 2022.

[106] F. Afsharpanah, G. Cheraghian, F. Akbarzadeh Hamedani, E. Shokri, and S. S. Mousavi Ajarostaghi, "Utilization of Carbon-Based Nanomaterials and Plate-Fin Networks in a Cold PCM Container with Application in Air Conditioning of Buildings," *Nanomaterials*, vol. 12, no. 11, 2022, doi: 10.3390/nano12111927.

[107] Y. Deng, J. Li, T. Qian, W. Guan, Y. Li, and X. Yin, "Thermal conductivity enhancement of polyethylene glycol/expanded vermiculite shape-stabilized composite phase change materials with silver nanowire for thermal energy storage," *Chem. Eng. J.*, vol. 295, pp. 427–435, 2016, doi: 10.1016/j.cej.2016.03.068.

[108] A. R. Alian, Y. Ju, and S. A. Meguid, "Comprehensive atomistic modeling of copper nanowires-based surface connectors," *Mater. Des.*, vol. 175, 2019, doi: 10.1016/j.matdes.2019.107812.

[109] R. P. Singh, S. C. Kaushik, and D. Rakshit, "Effect of inclination on the thermal response of composite phase change materials for thermal energy storage," *Energy Convers. Manag.*, vol. 163, no. November 2017, pp. 86–99, 2018, doi: 10.1016/j.enconman.2018.02.053.

[110] P. Mantilla Gilart, Á. Yedra Martínez, M. González Barriuso, and C. Manteca Martínez, "Development of PCM/carbon-based composite materials," *Sol. Energy Mater. Sol. Cells*, vol. 107, pp. 205–211, 2012, doi: 10.1016/j.solmat.2012.06.014.

[111] A. Arshad, H. Faraji, M. Jabbal, and Y. Yan, "A numerical study of HNCPCM filled metal-foam strips based heat sink for passive cooling," *Intersoc. Conf. Therm. Thermomechanical Phenom. Electron. Syst. ITHERM*, vol. 2021-June, pp. 524–530, 2021, doi: 10.1109/ITherm51669.2021.9503194.

[112] A. Sharma, P. Parth, S. Shobhana, M. Bobin, and B. K. Hardik, "Numerical study of ice freezing process on fin aided thermal energy storage system," *Int. Commun. Heat Mass Transf.*, vol. 130, no. December 2021, p. 105792, 2022, doi: 10.1016/j.icheatmasstransfer.2021.105792.

[113] X. Xiao, P. Zhang, and M. Li, "Preparation and thermal characterization of paraffin/metal foam composite phase change material," *Appl. Energy*, vol. 112, pp. 1357–1366, 2013, doi: 10.1016/j.apenergy.2013.04.050.

[114] M. Gaedtke *et al.*, "Total enthalpy-based lattice Boltzmann simulations of melting in paraffin/metal foam composite phase change materials," *Int. J. Heat Mass Transf.*, vol. 155, p. 119870, 2020, doi: 10.1016/j.ijheatmasstransfer.2020.119870.

[115] A. Parida, A. Bhattacharya, and P. Rath, "Effect of convection on melting characteristics of phase change material-metal foam composite thermal energy storage system," *J. Energy Storage*, vol. 32, no. September, p. 101804, 2020, doi: 10.1016/j.est.2020.101804.

[116] X. Yang, Z. Guo, Y. Liu, L. Jin, and Y. L. He, "Effect of inclination on the thermal response of composite phase change materials for thermal energy storage," *Appl. Energy*, vol. 238, no. October 2018, pp. 22–33, 2019, doi: 10.1016/j.apenergy.2019.01.074.

[117] X. Yang *et al.*, "Comparison of direct numerical simulation with volume-averaged method

on composite phase change materials for thermal energy storage," *Appl. Energy*, vol. 229, no. October 2017, pp. 700–714, 2018, doi: 10.1016/j.apenergy.2018.08.012.

[118] Y. Sheikh, M. O. Hamdan, and S. Sakhi, "A review on micro-encapsulated phase change materials (EPCM) used for thermal management and energy storage systems: Fundamentals, materials, synthesis and applications," *J. Energy Storage*, vol. 72, no. PC, p. 108472, 2023, doi: 10.1016/j.est.2023.108472.

[119] S. Karthikeyan, G. Ravikumar Solomon, V. Kumaresan, and R. Velraj, "Parametric studies on packed bed storage unit filled with PCM encapsulated spherical containers for low temperature solar air heating applications," *Energy Convers. Manag.*, vol. 78, pp. 74–80, 2014, doi: 10.1016/j.enconman.2013.10.042.

[120] D. Liu *et al.*, "Numerical evaluation of convective heat transfer properties of two-dimensional rotating PCM melt in the unilaterally heated rectangular container," *Renew. Energy*, vol. 193, pp. 920–940, 2022, doi: 10.1016/j.renene.2022.05.009.

[121] G. H. Feng, D. Liang, K. L. Huang, and Y. Wang, "Thermal performance difference of phase change energy storage units based on tubular macro-encapsulation," *Sustain. Cities Soc.*, vol. 50, no. August 2018, p. 101662, 2019, doi: 10.1016/j.scs.2019.101662.

[122] R. Fukahori, T. Nomura, C. Zhu, N. Sheng, N. Okinaka, and T. Akiyama, "Macro-encapsulation of metallic phase change material using cylindrical-type ceramic containers for high-temperature thermal energy storage," *Appl. Energy*, vol. 170, pp. 324–328, 2016, doi: 10.1016/j.apenergy.2016.02.106.

[123] P. B. Salunkhe and P. S. Shembekar, "A review on effect of phase change material encapsulation on the thermal performance of a system," *Renew. Sustain. Energy Rev.*, vol. 16, no. 8, pp. 5603–5616, 2012, doi: 10.1016/j.rser.2012.05.037.

[124] M. Neri, E. Chiavazzo, and L. Mongibello, "Numerical simulation and validation of commercial hot water tanks integrated with phase change material-based storage units," *J. Energy Storage*, vol. 32, no. July, p. 101938, 2020, doi: 10.1016/j.est.2020.101938.

[125] W. Su, J. Darkwa, and G. Kokogiannakis, "Development of microencapsulated phase

change material for solar thermal energy storage," *Appl. Therm. Eng.*, vol. 112, pp. 1205–1212, 2017, doi: 10.1016/j.applthermaleng.2016.11.009.

[126] M. Ghalambaz, A. J. Chamkha, and D. Wen, "Natural convective flow and heat transfer of Nano-Encapsulated Phase Change Materials (NEPCMs) in a cavity," *Int. J. Heat Mass Transf.*, vol. 138, pp. 738–749, 2019, doi: 10.1016/j.ijheatmasstransfer.2019.04.037.

[127] P. K. S. Rathore and S. K. Shukla, "Potential of macroencapsulated pcm for thermal energy storage in buildings: A comprehensive review," *Constr. Build. Mater.*, vol. 225, pp. 723–744, 2019, doi: 10.1016/j.conbuildmat.2019.07.221.

[128] K. Resch-Fauster and M. Feuchter, "Thermo-physical characteristics, mechanical performance and long-term stability of high temperature latent heat storages based on paraffin-polymer compounds," *Thermochim. Acta*, vol. 663, no. September 2017, pp. 34–45, 2018, doi: 10.1016/j.tca.2018.03.004.

[129] R. Gulfam, P. Zhang, and Z. Meng, "Advanced thermal systems driven by paraffin-based phase change materials – A review," *Appl. Energy*, vol. 238, no. June 2018, pp. 582–611, 2019, doi: 10.1016/j.apenergy.2019.01.114.

[130] Q. Zhang, H. Wang, Z. Ling, X. Fang, and Z. Zhang, "RT100/expand graphite composite phase change material with excellent structure stability, photo-thermal performance and good thermal reliability," *Sol. Energy Mater. Sol. Cells*, vol. 140, pp. 158–166, 2015, doi: 10.1016/j.solmat.2015.04.008.

[131] Q. Xiao, J. Fan, Y. Fang, L. Li, T. Xu, and W. Yuan, "The shape-stabilized light-to-thermal conversion phase change material based on CH3COONa·3H2O as thermal energy storage media," *Appl. Therm. Eng.*, vol. 136, no. December 2017, pp. 701–707, 2018, doi: 10.1016/j.applthermaleng.2018.03.053.

[132] Z. Hu, A. Li, R. Gao, and H. Yin, "Enhanced heat transfer for PCM melting in the frustum-shaped unit with multiple PCMs," *J. Therm. Anal. Calorim.*, vol. 120, no. 2, pp. 1407–1416, 2015, doi: 10.1007/s10973-014-4370-6.

[133] A. A. Rabienataj Darzi, M. Jourabian, and M. Farhadi, "Melting and solidification of PCM

enhanced by radial conductive fins and nanoparticles in cylindrical annulus," *Energy Convers. Manag.*, vol. 118, pp. 253–263, 2016, doi: 10.1016/j.enconman.2016.04.016.

[134] A. D. Korawan, S. Soeparman, W. Wijayanti, and D. Widhiyanuriyawan, "3D numerical and experimental study on paraffin wax melting in thermal storage for the nozzle-and-shell, tube-and-shell, and reducer-and-shell models," *Model. Simul. Eng.*, vol. 2017, 2017, doi: 10.1155/2017/9590214.

[135] M. Faghani, M. J. Hosseini, and R. Bahrampoury, "Numerical simulation of melting between two elliptical cylinders," *Alexandria Eng. J.*, vol. 57, no. 2, pp. 577–586, 2018, doi: 10.1016/j.aej.2017.02.003.

[136] A. Pourakabar and A. A. Rabienataj Darzi, "Enhancement of phase change rate of PCM in cylindrical thermal energy storage," *Appl. Therm. Eng.*, vol. 150, no. October 2018, pp. 132–142, 2019, doi: 10.1016/j.applthermaleng.2019.01.009.

[137] B. Kurşun and M. Balta, "Evaluation of the different inner and outer channel geometry combinations for optimum melting and solidification performance in double pipe energy storage with phase change material: A numerical study," *J. Energy Storage*, vol. 65, no. April, 2023, doi: 10.1016/j.est.2023.107250.

[138] S. Chatterjee and D. Bhanja, "Maximization of performance of a PCM latent heat storage system with innovative cavity shape and optimum heating tube position," *J. Therm. Anal. Calorim.*, vol. 148, no. 22, pp. 12549–12564, 2023, doi: 10.1007/s10973-023-12607-1.

[139] Z. Wang, H. Zhang, B. Dou, G. Zhang, and W. Wu, "Influence of inlet structure on thermal stratification in a heat storage tank with PCMs: CFD and experimental study," *Appl. Therm. Eng.*, vol. 162, no. November 2018, 2019, doi: 10.1016/j.applthermaleng.2019.114151.

[140] T. Bouhal, T. El Rhafiki, T. Kousksou, A. Jamil, and Y. Zeraouli, "PCM addition inside solar water heaters: Numerical comparative approach," *J. Energy Storage*, vol. 19, no. August, pp. 232–246, 2018, doi: 10.1016/j.est.2018.08.005.

[141] G. Feng, T. Wang, X. Li, N. He, G. Wang, and Y. Zhang, "Simulation of a composite latent heat storage tank with horizontal baffles and two phase-change temperatures," *Appl. Therm.*

Eng., vol. 225, no. December 2022, 2023, doi: 10.1016/j.applthermaleng.2023.120192.

[142] F. Wu, Z. Wang, H. Zhang, Y. Qin, X. You, and J. Lu, "Experimental and simulation analysis on thermal stratification characteristics in solar storage tanks with phase change materials," *J. Energy Storage*, vol. 46, no. November 2021, p. 103722, 2022, doi: 10.1016/j.est.2021.103722.

[143] T. B. Freeman *et al.*, "Advanced Materials and Additive Manufacturing for Phase Change Thermal Energy Storage and Management: A Review," *Adv. Energy Mater.*, vol. 13, no. 24, pp. 1–21, 2023, doi: 10.1002/aenm.202204208.

[144] L. Capuano, "Internatinal energy outlook 2018," *U.S. Energy Inf. Adm.*, vol. IEO2018, no. 2018, pp. 1–21, 2018, [Online]. Available: www.eia.gov/ieo%0Ahttps://www.eia.gov/outlooks/ieo/pdf/0484(2017).pdf

[145] X. Fang *et al.*, "Thermal energy storage performance of paraffin-based composite phase change materials filled with hexagonal boron nitride nanosheets," *Energy Convers. Manag.*, vol. 80, pp. 103–109, 2014, doi: 10.1016/j.enconman.2014.01.016.

[146] I. Baskar and M. Chellapandian, "Experimental and finite element analysis on the developed real-time form stable PCM based roof system for thermal energy storage applications," *Energy Build.*, vol. 276, p. 112514, 2022, doi: 10.1016/j.enbuild.2022.112514.

[147] H. M. Hoang *et al.*, "Heat transfer study of submicro-encapsulated PCM plate for food packaging application," *Int. J. Refrig.*, vol. 52, pp. 151–160, 2015, doi: 10.1016/j.ijrefrig.2014.07.002.

[148] H. I. Mohammed, P. Talebizadehsardari, J. M. Mahdi, A. Arshad, A. Sciacovelli, and D. Giddings, "Improved melting of latent heat storage via porous medium and uniform Joule heat generation," *J. Energy Storage*, vol. 31, no. August, p. 101747, 2020, doi: 10.1016/j.est.2020.101747.

[149] M. Mu, S. Zhang, S. Yang, and Y. Wang, "Phase change materials applied in agricultural greenhouses," *J. Energy Storage*, vol. 49, no. February, p. 104100, 2022, doi: 10.1016/j.est.2022.104100.

[150] Y. Zhao, X. Zhang, X. Xu, and S. Zhang, "Development of composite phase change cold storage material and its application in vaccine cold storage equipment," *J. Energy Storage*, vol. 30, no. February, p. 101455, 2020, doi: 10.1016/j.est.2020.101455.

[151] C. Hu, Z. Wang, R. Bo, C. Li, and X. Meng, "Effect of the cooling clothing integrating with phase change material on the thermal comfort of healthcare workers with personal protective equipment during the COVID-19," *Case Stud. Therm. Eng.*, vol. 42, no. January, p. 102725, 2023, doi: 10.1016/j.csite.2023.102725.

[152] M. Abu-Arabi, M. Al-harahsheh, M. Ahmad, and H. Mousa, "Theoretical modeling of a glass-cooled solar still incorporating PCM and coupled to flat plate solar collector," *J. Energy Storage*, vol. 29, no. March, p. 101372, 2020, doi: 10.1016/j.est.2020.101372.

[153] M. Y. Yazici, M. Avci, O. Aydin, A. Arshad, and M. Jabbal, "Effect of fin width ratio on thermal performance of fin based-heat sink with phase change materials," *Appl. Therm. Eng.*, vol. 227, no. February, p. 120425, 2023, doi: 10.1016/j.applthermaleng.2023.120425.

[154] C. Lin, S. Xu, G. Chang, and J. Liu, "Experiment and simulation of a LiFePO4 battery pack with a passive thermal management system using composite phase change material and graphite sheets," *J. Power Sources*, vol. 275, pp. 742–749, 2015, doi: 10.1016/j.jpowsour.2014.11.068.

[155] Z. Qin, C. Ji, Z. H. Low, W. Tong, C. Wu, and F. Duan, "Geometry effect of phase change material container on waste heat recovery enhancement," *Appl. Energy*, vol. 327, no. September, p. 120108, 2022, doi: 10.1016/j.apenergy.2022.120108.

[156] A. A. M. Omara, "Phase change materials for waste heat recovery in internal combustion engines: A review," *J. Energy Storage*, vol. 44, no. PB, p. 103421, 2021, doi: 10.1016/j.est.2021.103421.

[157] E. Guelpa and V. Verda, "Thermal energy storage in district heating and cooling systems: A review," *Appl. Energy*, vol. 252, no. June, p. 113474, 2019, doi: 10.1016/j.apenergy.2019.113474.

[158] K. Du, J. Calautit, P. Eames, and Y. Wu, "A state-of-the-art review of the application of

phase change materials (PCM) in Mobilized-Thermal Energy Storage (M-TES) for recovering low-temperature industrial waste heat (IWH) for distributed heat supply," *Renew. Energy*, vol. 168, pp. 1040–1057, 2021, doi: 10.1016/j.renene.2020.12.057.

[159] Y. Gao and X. Meng, "A comprehensive review of integrating phase change materials in building bricks: Methods, performance and applications," *J. Energy Storage*, vol. 62, no. November 2022, p. 106913, 2023, doi: 10.1016/j.est.2023.106913.

[160] D. Anderson, J. C. Tannehill, and R. H. Pletcher, *Computational fluid mechanics and heat transfer, Third edition*. 2016.

[161] M. Jourabian, M. Farhadi, and A. A. Rabienataj Darzi, "Accelerated melting of PCM in a multitube annulus-type thermal storage unit using lattice Boltzmann simulation," *Heat Transf. - Asian Res.*, vol. 46, no. 8, pp. 1499–1525, 2017, doi: 10.1002/htj.21286.

[162] Q. Li, K. H. Luo, Q. J. Kang, Y. L. He, Q. Chen, and Q. Liu, "Lattice Boltzmann methods for multiphase flow and phase-change heat transfer," *Prog. Energy Combust. Sci.*, vol. 52, pp. 62–105, 2016, doi: 10.1016/j.pecs.2015.10.001.

[163] R. Huang and H. Wu, "Phase interface effects in the total enthalpy-based lattice Boltzmann model for solid-liquid phase change," *J. Comput. Phys.*, vol. 294, pp. 346–362, 2015, doi: 10.1016/j.jcp.2015.03.064.

[164] V. V. R. & P. C., "A Fixed grid numerical modelling methodology for convection diffusion mushy region phase change problems," *Int. Jounal Heat Mass Transf.*, vol. 30, no. 8, pp. 1709–1719, 1978.

[165] A. Rakotondrandisa, G. Sadaka, and I. Danaila, "A finite-element toolbox for the simulation of solid–liquid phase-change systems with natural convection," *Comput. Phys. Commun.*, vol. 253, p. 107188, 2020, doi: 10.1016/j.cpc.2020.107188.

[166] L. Klimeš *et al.*, "Computer modelling and experimental investigation of phase change hysteresis of PCMs: The state-of-the-art review," *Appl. Energy*, vol. 263, no. January, p. 114572, 2020, doi: 10.1016/j.apenergy.2020.114572.

[167] Y. Allouche, S. Varga, C. Bouden, and A. C. Oliveira, "Dynamic simulation of an integrated

solar-driven ejector based air conditioning system with PCM cold storage," *Appl. Energy*, vol. 190, pp. 600–611, 2017, doi: 10.1016/j.apenergy.2017.01.001.

[168] K. Ghasemi, S. Tasnim, and S. Mahmud, "PCM, nano/microencapsulation and slurries: A review of fundamentals, categories, fabrication, numerical models and applications," *Sustain. Energy Technol. Assessments*, vol. 52, no. PB, p. 102084, 2022, doi: 10.1016/j.seta.2022.102084.

[169] V. R. Voller, "Numerical Heat Transfer , Part B : Fundamentals : An International Journal of Computation and Methodology FAST IMPLICIT FINITE-DIFFERENCE METHOD FOR THE ANALYSIS OF PHASE CHANGE PROBLEMS," *Numer. Heat Transf.*, vol. 17, no. September 2012, pp. 155–169, 1990.

[170] M. Fang and G. Chen, "Effects of different multiple PCMs on the performance of a latent thermal energy storage system," *Appl. Therm. Eng.*, vol. 27, no. 5–6, pp. 994–1000, 2007, doi: 10.1016/j.applthermaleng.2006.08.001.

[171] B. Başal and A. Ünal, "Numerical evaluation of a triple concentric-tube latent heat thermal energy storage," *Sol. Energy*, vol. 92, pp. 196–205, 2013, doi: 10.1016/j.solener.2013.02.032.

[172] F. S. dos Santos, K. A. R. Ismail, F. A. M. Lino, A. Arabkoohsar, and T. G. S. Lago, "Parametric investigation of the enhancing effects of finned tubes on the solidification of PCM," *Int. J. Heat Mass Transf.*, vol. 152, p. 119485, 2020, doi: 10.1016/j.ijheatmasstransfer.2020.119485.

[173] G. Worster, "Mathematical Modeling of Melting and Freezing Processes. By V. Alexiades and A. D. Solomon. Taylor & Francis, 1993. 323 pp. £35," *J. Fluid Mech.*, vol. 251, pp. 719–720, 1993, doi: 10.1017/S0022112093213593.

[174] Z. Younsi and H. Naji, "A numerical investigation of melting phase change process via the enthalpy-porosity approach: Application to hydrated salts," *Int. Commun. Heat Mass Transf.*, vol. 86, no. June, pp. 12–24, 2017, doi: 10.1016/j.icheatmasstransfer.2017.05.012.

[175] H. T. Modeling, "Lecture Heat Transfer Modeling g Introduction to ANSYS FLUENT,"

no. December, pp. 1–33, 2010.

[176] Y. T. Lee, L. H. Chien, F. B. Cheung, and A. S. Yang, "Numerical and experimental investigations on melting heat transfer performance of PCM in finned cold thermal energy storage," *Int. J. Heat Mass Transf.*, vol. 210, p. 124199, 2023, doi: 10.1016/j.ijheatmasstransfer.2023.124199.

[177] T. Bouzennada, F. Mechighel, T. Ismail, L. Kolsi, and K. Ghachem, "Heat transfer and fluid flow in a PCM-filled enclosure: Effect of inclination angle and mid-separation fin," *Int. Commun. Heat Mass Transf.*, vol. 124, no. April, p. 105280, 2021, doi: 10.1016/j.icheatmasstransfer.2021.105280.

[178] H. Xu, N. Wang, C. Zhang, Z. Qu, and M. Cao, "Optimization on the melting performance of triplex-layer PCMs in a horizontal finned shell and tube thermal energy storage unit," *Appl. Therm. Eng.*, vol. 176, no. November 2019, p. 115409, 2020, doi: 10.1016/j.applthermaleng.2020.115409.

[179] D. Heim, "Isothermal storage of solar energy in building construction," *Renew. Energy*, vol. 35, no. 4, pp. 788–796, 2010, doi: 10.1016/j.renene.2009.09.005.

[180] P. Han, X. H. Zheng, W. S. Hou, L. Qiu, and D. W. Tang, "Study on heat-storage and release characteristics of multi-cavity-structured phase-change microcapsules," *Phase Transitions*, vol. 88, no. 7, pp. 704–715, 2015, doi: 10.1080/01411594.2015.1014482.

[181] A. Artinov, M. Bachmann, and M. Rethmeier, "Equivalent heat source approach in a 3D transient heat transfer simulation of full-penetration high power laser beam welding of thick metal plates," *Int. J. Heat Mass Transf.*, vol. 122, pp. 1003–1013, 2018, doi: 10.1016/j.ijheatmasstransfer.2018.02.058.

[182] O. Mahian *et al.*, "Recent advances in modeling and simulation of nanofluid flows-part II: Applications," *Phys. Rep.*, 2018, doi: 10.1016/j.physrep.2018.11.003.

[183] S. M. Rassoulinejad-Mousavi and Y. Zhang, "Interatomic Potentials Transferability for Molecular Simulations: A Comparative Study for Platinum, Gold and Silver," *Sci. Rep.*, vol. 8, no. 1, pp. 1–10, 2018, doi: 10.1038/s41598-018-20375-4.

[184] C. Y. Zhao, Y. B. Tao, and Y. S. Yu, "Molecular dynamics simulation of nanoparticle effect on melting enthalpy of paraffin phase change material," *Int. J. Heat Mass Transf.*, vol. 150, 2020, doi: 10.1016/j.ijheatmasstransfer.2020.119382.

[185] F. J. Valdes-Parada, J. A. Ochoa-Tapia, and J. Alvarez-Ramirez, "Validity of the permeability Carman-Kozeny equation: A volume averaging approach," *Phys. A Stat. Mech. its Appl.*, vol. 388, no. 6, pp. 789–798, 2009, doi: 10.1016/j.physa.2008.11.024.

[186] B. Yang, A. Raza, F. Bai, T. Zhang, and Z. Wang, "Microstructural evolution within mushy zone during paraffin's melting and solidification," *Int. J. Heat Mass Transf.*, vol. 141, pp. 769–778, 2019, doi: 10.1016/j.ijheatmasstransfer.2019.07.019.

[187] A. S. Soliman, A. A. Sultan, and M. A. Sultan, "Effect of Mushy Zone Parameter on Phase Change Behavior of Different Configurations Storage Unit: Numerical Simulation and Experimental Validation," *Sustainability*, vol. 14, no. 21, p. 14540, 2022, doi: 10.3390/su142114540.

[188] M. Hameter and H. Walter, *Influence of the Mushy Zone Constant on the Numerical Simulation of the Melting and Solidification Process of Phase Change Materials*, vol. 38, no. 2012. Elsevier Masson SAS, 2016. doi: 10.1016/B978-0-444-63428-3.50078-3.

[189] A. Takudzwa Muzhanje, M. A. Hassan, and H. Hassan, "Phase change material based thermal energy storage applications for air conditioning: Review," *Appl. Therm. Eng.*, vol. 214, no. January, p. 118832, 2022, doi: 10.1016/j.applthermaleng.2022.118832.

[190] E. M. Alawadhi, "Meshing guide," *Finite Elem. Simulations Using ANSYS*, vol. 15317, no. November, pp. 407–424, 2020, doi: 10.1201/b18949-12.

[191] W. Li, Q. Li, X. Zhang, Y. Dong, and J. Zhao, "Experimental and numerical study on thermal performance and inlet and outlet structure optimization of phase change heat storage tank," *Int. J. Energy Res.*, vol. 46, no. 13, pp. 18146–18161, 2022, doi: 10.1002/er.8433.

[192] X. Yang, X. Yang, J. Ding, Y. Shao, F. G. F. Qin, and R. Jiang, "Criteria for performance improvement of a molten salt thermocline storage system," *Appl. Therm. Eng.*, vol. 48, pp.

24–31, 2012, doi: 10.1016/j.applthermaleng.2012.04.046.

[193] N. Rott, "Note On The History Of The Reynolds Number," *Annu. Rev. Fluid Mech.*, vol. 22, no. 1, pp. 1–11, 1990, doi: 10.1146/annurev.fluid.22.1.1.

[194] S. Seddegh, M. M. Joybari, X. Wang, and F. Haghighat, "Experimental and numerical characterization of natural convection in a vertical shell-and-tube latent thermal energy storage system," *Sustain. Cities Soc.*, vol. 35, no. July, pp. 13–24, 2017, doi: 10.1016/j.scs.2017.07.024.

[195] Q. Mao, N. Liu, L. Peng, and D. Liu, "A novel shell-and-tube thermal energy storage tank: Modeling and investigations of thermal performance," *Appl. Therm. Eng.*, vol. 159, no. June, p. 113964, 2019, doi: 10.1016/j.applthermaleng.2019.113964.

[196] ANSYS INC, "Lecture 3 Basic Overview of Using the FLUENT User Interface," *Cust. Train. Mater.*, no. December, pp. L3-13, 2010, [Online]. Available: https://imechanica.org/files/fluent_13.0_lecture03-solver-basics.pdf

[197] Q. Mao, N. Liu, and L. Peng, "Numerical investigations on charging/discharging performance of a novel truncated cone thermal energy storage tank on a concentrated solar power system," *Int. J. Photoenergy*, vol. 2019, 2019, doi: 10.1155/2019/1609234.

[198] Y. Li, G. Huang, H. Wu, and T. Xu, "Feasibility study of a PCM storage tank integrated heating system for outdoor swimming pools during the winter season," *Appl. Therm. Eng.*, vol. 134, pp. 490–500, 2018, doi: 10.1016/j.applthermaleng.2018.02.030.

[199] T. L. BERGMAN, A. S. LAVINE, F. P. INCROPERA, and D. P. DEWITT, *Fundamentals of Heat and Mass Transfer*, 7th ed., no. 1. John Wiley & Sons., 2011.

[200] T. Bouhal, S. ed-Dîn Fertahi, T. Kousksou, and A. Jamil, "CFD thermal energy storage enhancement of PCM filling a cylindrical cavity equipped with submerged heating sources," *J. Energy Storage*, vol. 18, no. May, pp. 360–370, 2018, doi: 10.1016/j.est.2018.05.015.

[201] H. Eddine, A. Belaadi, H. Alshahrani, M. K. A. Khan, and M. Bourchak, "Modeling three-dimensional flow in a thermal energy tank : Numerical analysis of the impact of tank shape

on the melting and solidification of phase change material," *J. Energy Storage*, vol. 72, no. PA, p. 108286, 2023, doi: 10.1016/j.est.2023.108286.

[202] A. D. Brent, V. R. Voller, and K. J. Reid, "Enthalpy-porosity technique for modeling convection-diffusion phase change: Application to the melting of a pure metal," *Numer. Heat Transf.*, vol. 13, no. 3, pp. 297–318, 1988, doi: 10.1080/10407788808913615.

[203] T. Bouhal, S. Fertahi, Y. Agrouaz, T. El Rhafiki, T. Kousksou, and A. Jamil, "Numerical modeling and optimization of thermal stratification in solar hot water storage tanks for domestic applications: CFD study," *Sol. Energy*, vol. 157, no. June, pp. 441–455, 2017, doi: 10.1016/j.solener.2017.08.061.

[204] Q. Mao, N. Liu, L. Peng, and D. Liu, "A novel shell-and-tube thermal energy storage tank: Modeling and investigations of thermal performance," *Appl. Therm. Eng.*, vol. 159, p. 113964, 2019, doi: 10.1016/j.applthermaleng.2019.113964.

[205] H. Mahgerefteh, Y. Rykov, and G. Denton, "Courant, Friedrichs and Lewy (CFL) impact on numerical convergence of highly transient flows," *Chem. Eng. Sci.*, vol. 64, no. 23, pp. 4969–4975, 2009, doi: 10.1016/j.ces.2009.08.002.

[206] G. Mazzucco, G. Xotta, V. A. Salomoni, M. Giannuzzi, and C. E. Maiorana, "Solid thermal storage with PCM materials. Numerical investigations," *Appl. Therm. Eng.*, vol. 124, pp. 545–559, 2017, doi: 10.1016/j.applthermaleng.2017.05.142.

[207] M. Y. Haller, C. A. Cruickshank, W. Streicher, S. J. Harrison, E. Andersen, and S. Furbo, "Methods to determine stratification efficiency of thermal energy storage processes - Review and theoretical comparison," *Sol. Energy*, vol. 83, no. 10, pp. 1847–1860, 2009, doi: 10.1016/j.solener.2009.06.019.

[208] J. P. Stark, *Fundamentals of classical thermodynamics (Van Wylen, Gordon J.; Sonntag, Richard E.)*, vol. 43, no. 5. 1966. doi: 10.1021/ed043pa472.1.

[209] A. Bland, M. Khzouz, T. Statheros, and E. I. Gkanas, "PCMs for residential building applications: A short review focused on disadvantages and proposals for future development," *Buildings*, vol. 7, no. 3, 2017, doi: 10.3390/buildings7030078.

[210] F. Wang *et al.*, "Comprehensive Evaluation of the Performances of Heat Exchangers with Aluminum and Copper Finned Tubes," *Int. J. Chem. Eng.*, vol. 2023, 2023, doi: 10.1155/2023/6666947.

[211] Q. Ying, H. Wang, and E. Lichtfouse, "Numerical simulation on thermal behavior of partially filled metal foam composite phase change materials," *Appl. Therm. Eng.*, vol. 229, no. October 2022, p. 120573, 2023, doi: 10.1016/j.applthermaleng.2023.120573.

[212] N. Ben Khedher *et al.*, "Geometry modification of a vertical shell-and-tube latent heat thermal energy storage system using a framed structure with different undulated shapes for the phase change material container during the melting process," *J. Energy Storage*, vol. 72, no. PB, p. 108365, 2023, doi: 10.1016/j.est.2023.108365.

[213] A. A. Al-Abidi, S. Mat, K. Sopian, M. Y. Sulaiman, and A. T. Mohammad, "Numerical study of PCM solidification in a triplex tube heat exchanger with internal and external fins," *Int. J. Heat Mass Transf.*, vol. 61, no. 1, pp. 684–695, 2013, doi: 10.1016/j.ijheatmasstransfer.2013.02.030.

[214] A. A. Al-Abidi, S. Mat, K. Sopian, M. Y. Sulaiman, and A. T. Mohammad, "Experimental study of PCM melting in triplex tube thermal energy storage for liquid desiccant air conditioning system," *Energy Build.*, vol. 60, pp. 270–279, 2013, doi: 10.1016/j.enbuild.2013.01.031.

[215] X. Cao, Y. Yuan, B. Xiang, L. Sun, and Z. Xingxing, "Numerical investigation on optimal number of longitudinal fins in horizontal annular phase change unit at different wall temperatures," *Energy Build.*, vol. 158, pp. 384–392, 2018, doi: 10.1016/j.enbuild.2017.10.029.

[216] J. Gasia, D. Groulx, N. H. S. Tay, and L. F. Cabeza, "Numerical study of dynamic melting enhancement in a latent heat thermal energy storage system," *J. Energy Storage*, vol. 31, no. January, p. 101664, 2020, doi: 10.1016/j.est.2020.101664.

[217] A. A. R. Darzi, M. Farhadi, and K. Sedighi, "Numerical study of melting inside concentric and eccentric horizontal annulus," *Appl. Math. Model.*, vol. 36, no. 9, pp. 4080–4086, 2012, doi: 10.1016/j.apm.2011.11.033.

[218] A. Abdi, V. Martin, and J. N. W. Chiu, "Numerical investigation of melting in a cavity with vertically oriented fins," *Appl. Energy*, vol. 235, no. November 2018, pp. 1027–1040, 2019, doi: 10.1016/j.apenergy.2018.11.025.

[219] M. M. Zaytoun, M. M. El-Bashouty, M. M. Sorour, and M. A. Alnakeeb, "Heat transfer characteristics of PCM inside a modified design of shell and tube latent heat thermal energy storage unit," *Case Stud. Therm. Eng.*, vol. 49, no. April, p. 103372, 2023, doi: 10.1016/j.csite.2023.103372.

[220] M. Ghalambaz *et al.*, "Melting process of the nano-enhanced phase change material (NePCM) in an optimized design of shell and tube thermal energy storage (TES): Taguchi optimization approach," *Appl. Therm. Eng.*, vol. 193, no. November 2020, p. 116945, 2021, doi: 10.1016/j.applthermaleng.2021.116945.

[221] S. S. Mousavi Ajarostaghi, A. Amirsoleymani, M. Arıcı, A. Dolati, and L. Amiri, "Thermal energy storage with PCMs: A comprehensive study of horizontal shell and multi-tube systems with finned design," *J. Energy Storage*, vol. 72, no. PE, p. 108762, 2023, doi: 10.1016/j.est.2023.108762.

[222] S. A. Zonouzi and A. Dadvar, "Numerical investigation of using helical fins for the enhancement of the charging process of a latent heat thermal energy storage system," *J. Energy Storage*, vol. 49, no. September 2021, p. 104157, 2022, doi: 10.1016/j.est.2022.104157.

[223] R. Qaiser, M. M. Khan, H. F. Ahmed, F. K. Malik, M. Irfan, and I. U. Ahad, "Performance enhancement of latent energy storage system using effective designs of tubes and shell," *Energy Reports*, vol. 8, no. March, pp. 3856–3872, 2022, doi: 10.1016/j.egyr.2022.03.028.

[224] M. Boujelbene *et al.*, "A comparative study of twisted and straight fins in enhancing the melting and solidifying rates of PCM in horizontal double-tube heat exchangers," *Int. Commun. Heat Mass Transf.*, vol. 151, no. January, p. 107224, 2024, doi: 10.1016/j.icheatmasstransfer.2023.107224.

[225] A. V. Arasu and A. S. Mujumdar, "Numerical study on melting of paraffin wax with Al 2O 3 in a square enclosure," *Int. Commun. Heat Mass Transf.*, vol. 39, no. 1, pp. 8–16, 2012,

doi: 10.1016/j.icheatmasstransfer.2011.09.013.

[226] S. Mat, A. A. Al-Abidi, K. Sopian, M. Y. Sulaiman, and A. T. Mohammad, "Enhance heat transfer for PCM melting in triplex tube with internal-external fins," *Energy Convers. Manag.*, vol. 74, pp. 223–236, 2013, doi: 10.1016/j.enconman.2013.05.003.

[227] B. Palmer, A. Arshad, Y. Yang, and C. Wen, "Energy storage performance improvement of phase change materials-based triplex-tube heat exchanger (TTHX) using liquid–solid interface-informed fin configurations," *Appl. Energy*, vol. 333, no. March, p. 120576, 2023, doi: 10.1016/j.apenergy.2022.120576.

[228] M. Fadl and P. C. Eames, "Numerical investigation of the influence of mushy zone parameter Amush on heat transfer characteristics in vertically and horizontally oriented thermal energy storage systems," *Appl. Therm. Eng.*, vol. 151, no. January, pp. 90–99, 2019, doi: 10.1016/j.applthermaleng.2019.01.102.

[229] W. B. Ye and M. Arıcı, "False diffusion, asymmetrical interface, and equilibrious state for pure solid-gallium phase change modeling by enthalpy-porosity methodology," *Int. Commun. Heat Mass Transf.*, vol. 144, p. 106746, 2023, doi: 10.1016/j.icheatmasstransfer.2023.106746.

[230] S. Seddegh, M. M. Joybari, X. Wang, and F. Haghighat, "Experimental and numerical characterization of natural convection in a vertical shell-and-tube latent thermal energy storage system," *Sustain. Cities Soc.*, vol. 35, pp. 13–24, 2017, doi: 10.1016/j.scs.2017.07.024.

[231] A. A. Al-Abidi, S. Mat, K. Sopian, M. Y. Sulaiman, and A. T. Mohammad, "Experimental study of melting and solidification of PCM in a triplex tube heat exchanger with fins," *Energy Build.*, vol. 68, no. PARTA, pp. 33–41, 2014, doi: 10.1016/j.enbuild.2013.09.007.

[232] K. S. Reddy, V. Mudgal, and T. K. Mallick, "Review of latent heat thermal energy storage for improved material stability and effective load management," *J. Energy Storage*, vol. 15, pp. 205–227, 2018, doi: 10.1016/j.est.2017.11.005.

[233] S. Deng, C. Nie, H. Jiang, and W. B. Ye, "Evaluation and optimization of thermal

performance for a finned double tube latent heat thermal energy storage," *Int. J. Heat Mass Transf.*, vol. 130, pp. 532–544, 2019, doi: 10.1016/j.ijheatmasstransfer.2018.10.126.

Annexes

Annex 1-(A): Flowchart of the PCM melting simulation algorithm.

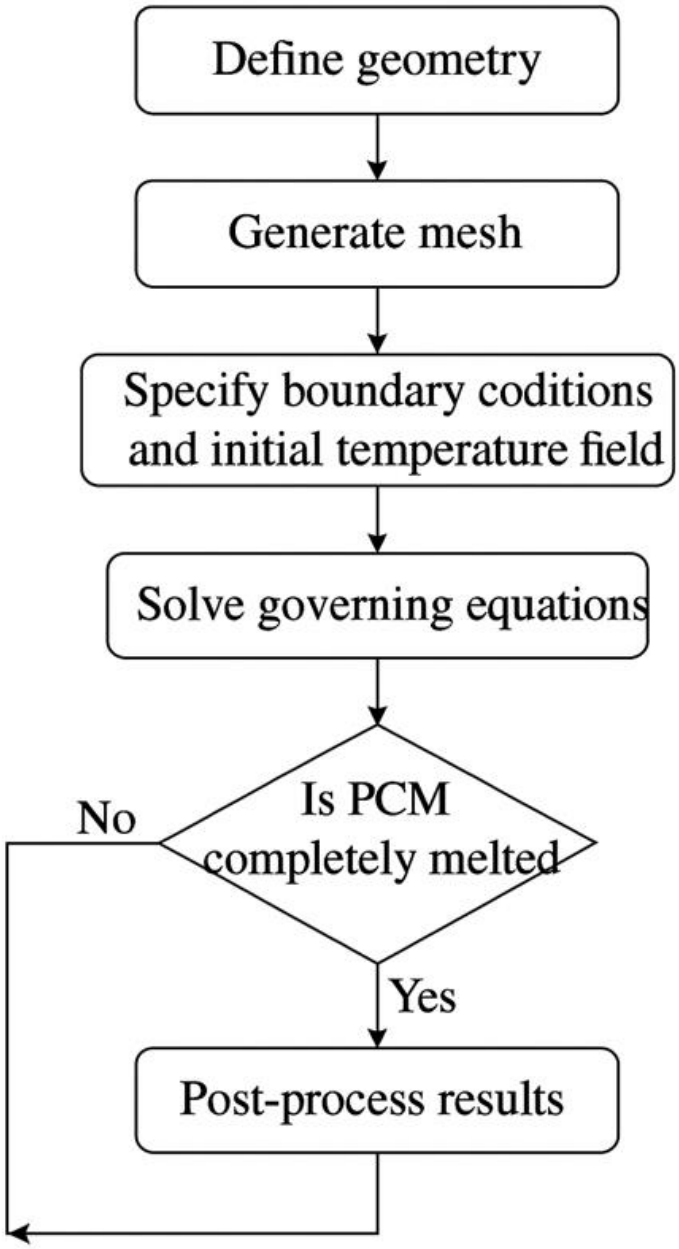

Annex 1-(B): Practical implementation steps in ANSYS Fluent.

1

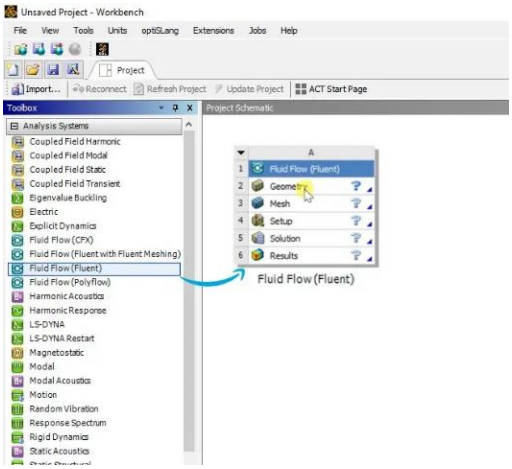

2

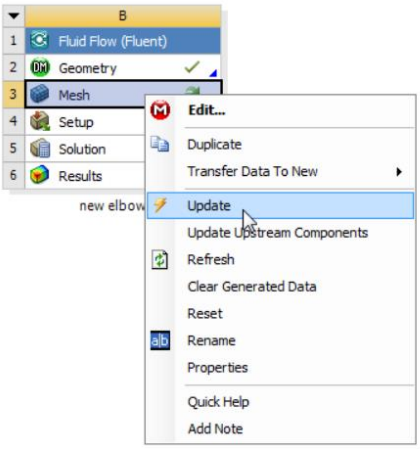

3

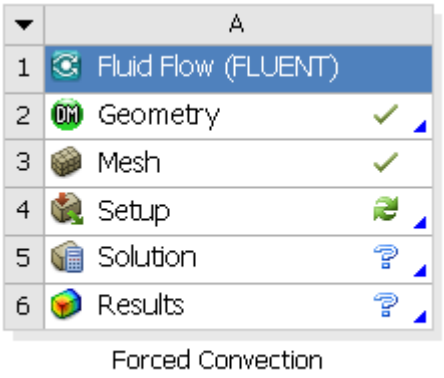

4

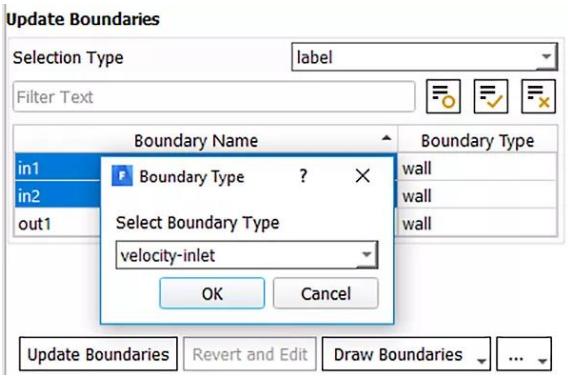

5

6

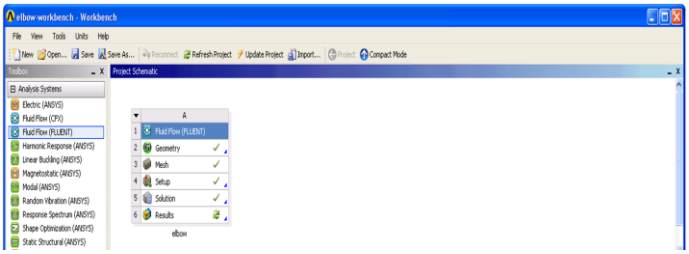

Annex 2: Water Properties at 80°C.

Property	Value
Density (kg/m³)	971.8
Viscosity (Pa·s)	0.000357
Thermal Conductivity (W/m·K)	0.668
Specific Heat (J/kg·K)	4182

Annex 3: Flowcharts of Numerical Solution Algorithms in CFD–PCM Simulation: (A)- Flowchart of CFD–PCM numerical solution algorithm (with equations, discretization, phase change), (B)- Flowchart of ANSYS Fluent numerical solution algorithm.

(A)

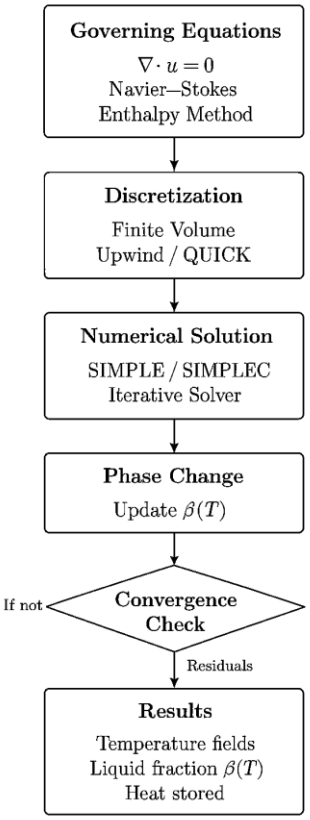

(B)

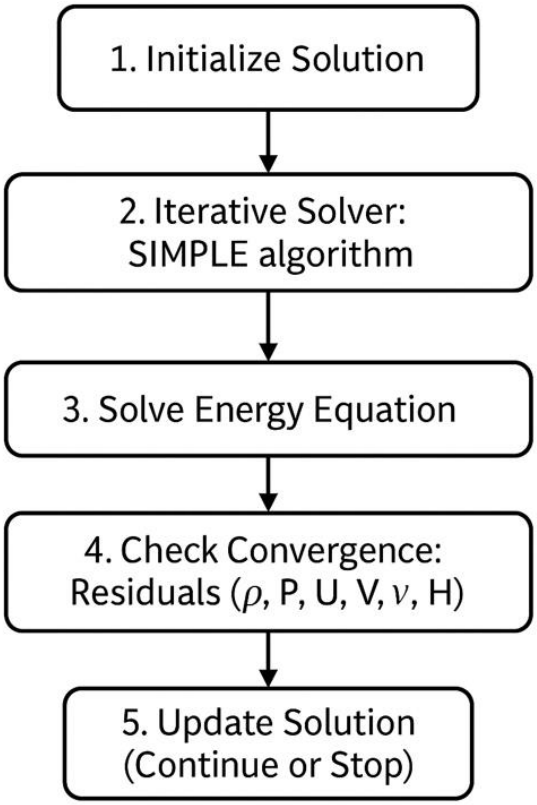

Annex 4: Numerical Methods Employed in CFD Simulations.

Numerical Method	Purpose/Description
SIMPLE Algorithm	Pressure-Velocity coupling to ensure mass conservation
SIMPLEC Algorithm	Enhanced version of SIMPLE, improves convergence rate
Second-Order Upwind	Discretization of momentum & energy equations for accuracy
QUICK Scheme	Used for energy equation to handle convection-dominated flows
PRESTO! Scheme	Pressure interpolation to enhance buoyancy-driven flow accuracy

Annex 5: Finite Volume Method Discretization of the Governing Equations.

$$\underbrace{\int_{V_P} \frac{\partial \rho\phi}{\partial t} dV}_{\text{Temporal derivative}} + \underbrace{\int_{V_P} \nabla \cdot (\rho \mathbf{u}\phi)\, dV}_{\text{Convective term}} - \underbrace{\int_{V_P} \nabla \cdot (\rho \Gamma_\phi \nabla\phi)\, dV}_{\text{Diffusion term}} = \underbrace{\int_{V_P} S_\phi(\phi)\, dV}_{\text{Source term}}$$

$$\int_V \nabla \cdot \mathbf{a} dV = \oint_{\partial V} d\mathbf{S} \cdot \mathbf{a}$$

$$\frac{\partial}{\partial t} \int_{V_P} (\rho\phi)\, dV + \oint_{\partial V_P} \underbrace{d\mathbf{S} \cdot (\rho \mathbf{u}\phi)}_{\text{convective flux}} - \oint_{\partial V_P} \underbrace{d\mathbf{S} \cdot (\rho \Gamma_\phi \nabla\phi)}_{\text{diffusive flux}} = \int_{V_P} S_\phi(\phi)\, dV$$

The governing transport equation is discretized using the Finite Volume Method (FVM), as applied in ANSYS Fluent. The equation is expressed in integral form, containing the transient, convective, diffusive, and source terms. By applying the Gauss divergence theorem, the volume integrals of fluxes are transformed into surface integrals, allowing evaluation at the control volume faces. This forms the basis for numerical schemes (Upwind, QUICK) used in ANSYS Fluent.